Springer Proceedings in Physics 278

Kusum Lata Pandey
Pradip Kumar Priya
Umesh Kumar Yadav
Prashanta Kumar Khandai *Editors*

Proceedings of the National Workshop on Recent Advances in Condensed Matter and High Energy Physics

CMHEP-2021

Springer

Springer Proceedings in Physics

Volume 278

Indexed by Scopus

The series Springer Proceedings in Physics, founded in 1984, is devoted to timely reports of state-of-the-art developments in physics and related sciences. Typically based on material presented at conferences, workshops and similar scientific meetings, volumes published in this series will constitute a comprehensive up-to-date source of reference on a field or subfield of relevance in contemporary physics. Proposals must include the following:

- name, place and date of the scientific meeting
- a link to the committees (local organization, international advisors etc.)
- scientific description of the meeting
- list of invited/plenary speakers
- an estimate of the planned proceedings book parameters (number of pages/articles, requested number of bulk copies, submission deadline).

Please contact:

For Americas and Europe: Dr. Zachary Evenson; zachary.evenson@springer.com
For Asia, Australia and New Zealand: Dr. Loyola DSilva; loyola.dsilva@springer.com

More information about this series at https://link.springer.com/bookseries/361

Kusum Lata Pandey · Pradip Kumar Priya ·
Umesh Kumar Yadav · Prashanta Kumar Khandai
Editors

Proceedings of the National Workshop on Recent Advances in Condensed Matter and High Energy Physics

CMHEP-2021

Springer

Editors
Kusum Lata Pandey
Department of Physics
Ewing Christian College
Prayagraj, India

Pradip Kumar Priya
Department of Physics
Ewing Christian College
Prayagraj, India

Umesh Kumar Yadav
Department of Physics
Ewing Christian College
Prayagraj, India

Prashanta Kumar Khandai
Department of Physics
Ewing Christian College
Prayagraj, India

ISSN 0930-8989 ISSN 1867-4941 (electronic)
Springer Proceedings in Physics
ISBN 978-981-19-2591-7 ISBN 978-981-19-2592-4 (eBook)
https://doi.org/10.1007/978-981-19-2592-4

This Springer imprint is published by the registered company Springer Nature Singapore Pte Ltd.
The registered company address is: 152 Beach Road, #21-01/04 Gateway East, Singapore 189721, Singapore

Preface

The first volume of this book contains papers presented at the workshop entitled "**Recent Advances in Condensed Matter and High Energy Physics (CMHEP-2021**)" on **March 5–6, 2021,** at the **Department of Physics, Ewing Christian College (ECC), Prayagaraj, India,** in collaboration with the **National Academy of Sciences (NASI), Prayagaraj, India**.

The objective of the workshop was to provide a well-organized platform to discuss the recent advancement in Condensed Matter and High Energy Physics among UG, PG and research students with the scientific community to enhance their knowledge. Recent theoretical and experimental developments in the Condensed Matter and High Energy Physics which include novel phases of matter, namely crystalline and non-crystalline phases, non-conventional superconducting phases, magnetic phases and quark-gluon plasma phases, etc., open a new path to the contemporary research. Understanding of these phases and their classification is an on-going collaborative effort involving High Energy Physicist, Condensed Matter Physicist as well as Mathematicians. The unique properties of these phases are also advantageous for the advancement for the future technologies.

Eminent speakers from various prestigious institutions of the country presented their recent research findings with the large number of participants from various universities, colleges and institutes in blended (online/offline) mode due to the restrictions imposed by the COVID-19 pandemic. Some of the participants also presented their research work in offline mode.

The present book contains contributed papers of the workshop. The works published in the book are contemporary and of recent interest from the Condensed Matter and High Energy Physics. We are very thankful to all the authors of contributed papers for their continuous efforts in preparing such outstanding manuscripts. We believe that present volume of the book will provide a wide range of recent research ideas to the reader in the field of Condensed Matter and High Energy Physics.

We are very thankful to the National Academy of Sciences (NASI), Prayagraj, India, for their financial as well as unconditional support. We are also very thankful to the college administration, convener and all the members of the Department of Physics for their generous support during the workshop.

Prayagraj, India

Kusum Lata Pandey
Pradip Kumar Priya
Umesh Kumar Yadav
Prashanta Kumar Khandai

Contents

Contributors

Imtiaz Ahmed Deparment of Chemistry, School of Basic Sciences, Central University of Punjab, Bathinda, India

Kalpana Awasthi Department of Physics, Kashi Naresh Government Post Graduate College, Gyanpur, Bhadohi, India

Pratima Chauhan Department of Physics, University of Allahabad, Prayagraj, India

Priyanka Chawla Department of Chemistry, CMP Degree College, University of Allahabad, Prayagraj, India

Sai Kumar Chirra Ewing Christian College, University of Allahabad, Prayagraj, India

Deeksha Department of Physics, School of Basic Sciences, Central University of Punjab, Bathinda, India

Ravindra Dhar Centre of Material Sciences, University of Allahabad, Prayagraj, India

Pooja Dwivedi Department of Physics, University of Allahabad, Prayagraj, India

Atul Kumar Gupta Department of Physics, Allahabad Degree College, University of Allahabad, Allahabad, India

Krishna Kanta Haldar Deparment of Chemistry, School of Basic Sciences, Central University of Punjab, Bathinda, India

S. Karmakar Department of Physics, Institute of Applied Sciences and Humanities, GLA University, Mathura, India

P. K. Khandai Department of Physics, Ewing Christian College, Prayagraj, India

Pawanpreet Kour Department of Physics, School of Basic Sciences, Central University of Punjab, Bathinda, India

Dheeraj Kumar Pandey Department of Physics, Vikramajit Singh Sanatan Dharama College, Kanpur, India

P. Kumar Department of Physics, Banaras Hindu University, Varanasi, India

Renil Kumar RIKEN, Saitama, Japan

Sandeep Kumar Raman Research Institute, Bengaluru, India;
Department of Chemistry, Nitte Meenakshi Institute of Technology, Bengaluru, India

Babita Kumari Department of Physics, Institute of Applied Sciences and Humanities, GLA University, Mathura, India

Ajit Kumar Maddheshiya Department of Physics, University of Allahabad, Allahabad, India

K. L. Pandey Department of Physics, Ewing Christian College, Prayagraj, India

M. B. Pandey Department of Physics, Vikramajit Singh Sanatan Dharama College, Kanpur, India

Prahalad Prasad Paroha Department of Basic Science and Humanities, Pranveer Singh Institute of Technology, Kanpur, India

Ashok Kumar Pathak Ewing Christian College, University of Allahabad, Prayagraj, India

Kumari Pooja Department of Chemistry, CMP Degree College, University of Allahabad, Prayagraj, India

Pradip K. Priya Department of Physics, Ewing Christian College, Allahabad, India

K. Saraswat Institute of Physics, Academia Sinica, Taipei, Taiwan

Ajaya Kumar Sharma Thin Film Laboratory, Department of Physics, Deen Dayal Upadhyaya Gorakhpur University, Gorakhpur, Uttar Pradesh, India

Anil Kumar Singh Ewing Christian College, University of Allahabad, Prayagraj, India

Birendra Singh Department of Basic Science and Humanities, Pranveer Singh Institute of Technology, Kanpur, India

D. Singh Department of Physics, Institute of Science, Banaras Hindu University, Varanasi, India

Hempal Singh Kirori Mal College, Department of Physics, University of Delhi, Delhi, India

M. K. Singh Department of Physics, Institute of Applied Sciences and Humanities, GLA University, Mathura, India;
Institute of Physics, Academia Sinica, Taipei, Taiwan

Prem Prakash Singh Ewing Christian College, University of Allahabad, Prayagraj, India

R. Singh Department of Physics, Institute of Applied Sciences and Humanities, GLA University, Mathura, India

U. B. Singh Department of Physics, Azim Premji University, Bhopal, India

V. Singh Department of Physics, School of Physical and Chemical Sciences, Central University of South Bihar, Gaya, India;
Department of Physics, Institute of Applied Science and Humanities, GLA University, Mathura, India;
Department of Physics, Institute of Science, Banaras Hindu University, Varanasi, India

Smriti Srivastava Ewing Christian College, University of Allahabad, Prayagraj, India

Anurag Tewari Department of Basic Science and Humanities, Pranveer Singh Institute of Technology, Kanpur, India

K. K. Tiwari Department of Physics, Allahabad Degree College, University of Allahabad, Allahabad, India

Mridula Tripathi Department of Chemistry, CMP Degree College, University of Allahabad, Prayagraj, India

Rahul Uttam Centre of Material Sciences, University of Allahabad, Prayagraj, India

Amit Kumar Verma Department of Physics, Allahabad Degree College, University of Allahabad, Allahabad, India

Ankit Kumar Vishwakarma Thin Film Laboratory, Department of Physics, Deen Dayal Upadhyaya Gorakhpur University, Gorakhpur, Uttar Pradesh, India

H. T. Wong Institute of Physics, Academia Sinica, Taipei, Taiwan

Lallan Yadava Thin Film Laboratory, Department of Physics, Deen Dayal Upadhyaya Gorakhpur University, Gorakhpur, Uttar Pradesh, India

Kamlesh Yadav Department of Physics, School of Basic Sciences, Central University of Punjab, Bathinda, India

Navneet Yadav Department of Physics, University of Allahabad, Allahabad, India

P. S. Yadav Department of Physics, University of Allahabad, Allahabad, India

R. R. Yadav Department of Physics, University of Allahabad, Allahabad, India

Sarita Yadav Physics Department, University of Allahabad, Prayagraj, India

Thakur Prasad Yadav Department of Physics, Hydrogen Energy Centre, Institute of Science, Banaras Hindu University, Varanasi, Uttar Pradesh, India

Umesh K. Yadav Department of Physics, Ewing Christian College, Allahabad, India

Gaurav Kumar Yogesh Department of Basic Science and Humanities, Pranveer Singh Institute of Technology, Kanpur, India;
Department of Physics, National Institute of Technology, Tiruchirappalli, India

Chapter 1
Ground State Properties of Spin-1/2 Falicov-Kimball Model on a Triangular Lattice with Uniform External Magnetic Field

Umesh K. Yadav and Pradip K. Priya

Abstract Electrons moving on a lattice in the presence of external magnetic field is always an interesting problem giving rise to many novel phenomena like flux quantization, quantum Hall effect and Hofsdter butterfly spectrum, etc. In addition to these exotic phenomena, inclusion of correlation between electrons moving on a triangular lattice makes the problem more complicated and one expects fairly complicated phases in the ground state in result of many novel phenomena like charge and magnetic order, non-Fermi liquid behavior and metal–insulator transitions in the system. Therefore, we have studied the ground state properties of spin-1/2 Falicov-Kimball model on a triangular lattice with an external uniform magnetic field using the classical Monte Carlo simulation algorithm and numerical diagnolization technique. We have found various charge and magnetic orders in the ground state configuration accompanying the metal–insulator transition with change in the magnetic field. These results will be applicable for a class of layered systems with triangular lattice, e.g., GdI_2, $NaTiO_2$ and $NaVO_2$, etc.

1.1 Introduction

Quantum Hall effect [1, 2], famous Hofstadter butterfly structure [3] and superconducting quantum flux phases [4, 5], etc., are phenomena of theoretical and experimental importance in contemporary condensed matter physics arising in the low-dimensional systems when electrons traverse on a lattice exposed to the external magnetic field. Electrons moving in the periodic potential (on underlying lattices) have a quantized energy spectrum, and the discrete energy bands are known as the Bloch bands. In an external magnetic field, the energy spectrum further splits into highly degenerate Landau levels. The interplay between these two effects leads to a complex fractal energy spectrum known as Hofstadter's butterfly [3]. The main hurdle in the realization of these effects is the requirement of extremely high, unfea-

U. K. Yadav (✉) · P. K. Priya
Department of Physics, Ewing Christian College, Allahabad 211003, India
e-mail: umeshyadav02@gmail.com

K. L. Pandey et al. (eds.), *Proceedings of the National Workshop on Recent Advances in Condensed Matter and High Energy Physics*, Springer Proceedings in Physics 278,
https://doi.org/10.1007/978-981-19-2592-4_1

sible large magnetic field. The recent proposals for Hofstadter's butterfly structure in some artificial super lattices by enhancing the lattice size to the order of magnetic length scale [6–11] bolster this research direction. Further in the above phenomenon, electron correlations are ignored. It is well known that electron correlations play an important role in governing the properties of systems in low dimensions [11, 12]. In the presence of electron correlations, very few results are known due to complexity of the problem.

Systems like cobaltates [13–15], GdI_2 [16] and its doped variant GdI_2H_x [17], $NaTiO_2$ [18–20], MgV_2O_4 [21], etc., have also attracted great interest as they exhibit a number of remarkable cooperative phenomena such as valence and metal–insulator transition, charge, orbital and magnetic order, excitonic instability and possible non-Fermi liquid states [16]. In these systems, different kinds of ordering are governed by interplay between kinetic and interaction energies of electrons on underlying lattice. These are layered and triangular lattice systems. The geometrical frustration from underlying triangular lattice coupled with strong quantum fluctuations gives rise to a huge degeneracy at low temperatures in result a competing ground states close by in energy. Therefore, for these systems one would expect a fairly complex phases in the ground state. There are also a class of correlated systems, namely rare-earth and transition metal compounds like $La_{1.6}Nd_{0.4}Sr_xCuO_4$, $YBa_2Cu_3O_{6+x}$ and $Bi_2Sr_2Cu_2O_{8+x}$ exhibit inhomogeneous charge ordering (e.g., phase separation) and high-temperature superconductivity [22, 23].

It is already shown that these systems may very well be described by different variants of the Falicov-Kimball model (FKM) [12, 16, 17, 24–28] on the triangular lattice. The FKM (having two kinds of states, namely itinerant states and localized states) was originally introduced to study the metal–insulator transition in the rare-earth and transition metal compounds [29, 30]. The model has also been extensively used to describe a variety of many-body phenomenon such as tendency of formation of charge and spin density wave, mixed valence, electronic ferroelectricity and crystallization in binary alloys [31–33].

Following the various intriguing results obtained on different variants of the FKM on different underlying lattices with or without external magnetic field and their validity for many physical systems of recent interest, it would be quite intriguing to uncover the following key questions: (1) *How external magnetic field affect the ground state properties of spin-dependent FKM? Whether orbital and spin degrees of freedom of electrons play crucial role in determining the properties of the FKM?* (2) *Can magnetic field produce metal to insulator transitions in the FKM?*.

In order to address these key questions, we have studied the ground state properties of the FKM on a triangular lattice in an uniform external magnetic field with various interaction terms between itinerant and localized electrons.

An ***uniform external magnetic field*** on a lattice can be set up by appropriately choosing the hopping of itinerant electrons position dependent. It is similar to the Hofstadter's approach [3], where one couples the magnetic field to the orbital degree of freedom of electrons via *the Peierls substitution* [34], by multiplying the hopping amplitude with a phase factor (A charge particle moving under the influence of an

external magnetic field is accompanied by a geometric phase known as *the Aharonov–Bohm phase* [35]) which depends on the field and on the position of electrons within the lattice [5, 12, 36].

We have studied the spin-1/2 FKM Hamiltonian ($\mathcal{H}$) on a triangular lattice with various interaction terms in the presence of finite external magnetic field given as

$$\begin{aligned}\mathcal{H} = &- \sum_{\langle ij\rangle,\sigma} \left[t_{ij} \exp\left\{ \frac{i\,e}{\hbar} \int_{\vec{R}_j}^{\vec{R}_i} \mathbf{A}(\vec{\mathbf{r}}).\mathbf{d}\vec{\mathbf{r}} \right\} + \mu\delta_{ij} \right] d^{\dagger}_{i,\sigma}\, d_{j,\sigma} \\ &+ U \sum_{i,\sigma} f^{\dagger}_{i,-\sigma}\, f_{i,-\sigma}\, d^{\dagger}_{i,\sigma}\, d_{i,\sigma} \\ &+ (U - J) \sum_{i,\sigma} f^{\dagger}_{i,\sigma}\, f_{i,\sigma}\, d^{\dagger}_{i,\sigma}\, d_{i,\sigma} \\ &+ U_f \sum_{i,\sigma} f^{\dagger}_{i,-\sigma}\, f_{i,-\sigma}\, f^{\dagger}_{i,\sigma}\, f_{i,\sigma} \\ &+ E_f \sum_{i,\sigma} f^{\dagger}_{i,\sigma}\, f_{i,\sigma}\end{aligned} \tag{1.1}$$

here $\langle ij\rangle$ denotes the nearest neighbor (NN) lattice sites. The $d^{\dagger}_{i,\sigma}$, $d_{i,\sigma}$ ($f^{\dagger}_{i,\sigma}$, $f_{i,\sigma}$) are, respectively, the creation and annihilation operators for d- (f-) electrons with spin $\sigma = \{\uparrow, \downarrow\}$ at the site i. First term is the band energy of spin-dependent d-electrons whose hopping is position dependent on the underlying lattice. In the second term, μ is the chemical potential for itinerant electrons. Third term is the on-site interaction between d- and f-electrons of opposite spins with coupling strength U. The fourth term is the on-site interaction between d and f-electrons of same spins with coupling strength $(U - J)$. Fifth term is the on-site Coulomb repulsion with strength U_f between f-electrons of opposite spins while the last term is the spin-independent, dispersionless energy E_f of the f-electrons.

It is quite interesting to note down that the Hamiltonian $\mathcal{H}$ (1.1) explicitly shows that the f-electrons act as an annealed disordered background or external charge and spin-dependent potential for the non-interacting moving d-electrons. This external potential of f-electrons can be 'annealed' to find the minimum energy of the system. It is also important to note that there is interlink between subsystems of f- and d-electrons. This connection between d- and f-electrons subsystems is responsible for the long-range ordered configurations and different magnetic ordered structures of f-electrons in the ground state [28, 31, 37] and also occurrence of metal–insulator transitions and band magnetism (finite magnetic moments for itinerant d-electrons) in the system [11].

Underlying lattice chosen to study the FKM is a triangular (non-bipartite) lattice and hence geometrically frustrated. Within the second-order perturbation theory, the FKM with extended interactions can be shown to map to an effective Ising model with antiferromagnetic (AFM) interactions in the large U limit. The AFM coupling

of Ising spins on triangular lattice is frustrated and leads to large degeneracies in the ground state configurations at low temperature. It turns out that this frustration is lifted in the higher-order perturbation in the order of $\frac{1}{U}$ [38].

Therefore, it would be quite interesting to study the role of spin degree of freedom of electrons on the ground state properties of the FKM on a triangular lattice with different set of parameters like U and α. Therefore in this present chapter, we would like to explore the ground state properties of the spin-dependent FKM on a triangular lattice with finite external magnetic field which affects the orbital (through Pierels substitution) degree of freedom of the itinerant d-electrons. These results will be very close to the recent theoretical and experimental findings on the triangular lattice [39–42]. Many other novel aspects of the correlated electron systems like non-trivial topology in band structure, charge, orbital and magnetic ordered configurations and their metallic or insulating nature are also expected to be uncovered.

Further, remarkable developments of the experimental techniques in the ultra-cold systems have also allowed to search for novel states of matter, which go beyond the possibilities, already offered by conventional condensed matter systems. Well-engineered optical lattices with laser-assisted tunnelings have enabled the realization of artificial high gauge fields with flexible tunability. One of the most interesting developments in ultra-cold atomic systems is the study of neutral atoms in the optical lattices [43]. Moreover, there are proposals for the realization of the various variants of the FKM in optical lattices with mixtures of light atoms and heavy atoms in the context of ultra-cold atomic systems [44–46].

1.2 Methodology

The Hamiltonian $\mathcal{H}$ (1.1) preserves the states of f-electrons, i.e., the d-electrons traveling through the lattice neither change spin nor occupation numbers of f-electrons. Therefore, local f-electron occupation number $\hat{n}_{fi,\sigma} = f^{\dagger}_{i,\sigma} f_{i,\sigma}$ is invariant and $\left[\hat{n}_{fi,\sigma}, \mathcal{H}\right] = 0$ for all i and σ. This also shows that $\omega_{i,\sigma} = f^{\dagger}_{i,\sigma} f_{i,\sigma}$ is a good quantum number taking values only 1 or 0 according to whether the site i is occupied or unoccupied by f-electron with spin σ, respectively.

Further, in order to create an uniform external magnetic field through the lattice, one can choose appropriate gauges. Here we have chosen the Landau gauge. For an external uniform magnetic field $\mathbf{B} = (0, 0, B)$, perpendicular to the plane of *triangular lattice*, the Landau gauge is considered as $\mathbf{A}(\vec{\mathbf{r}}) = B\,(0, x, 0)$. With this choice of gauge and following the local conservation of f-electron occupation, (1.1) can be written as follows:

$$\begin{aligned}\mathcal{H} = &\sum_{\langle ij\rangle,\sigma} \mathbf{h}_{ij,\sigma}(\{\omega_\sigma\}) d^{\dagger}_{i,\sigma}\, d_{j,\sigma} \\ &+ U_f \sum_{i,\sigma} \omega^{\dagger}_{i,-\sigma}\omega_{i,\sigma} + E_f \sum_{i,\sigma} \omega_{i,\sigma}\end{aligned} \tag{1.2}$$

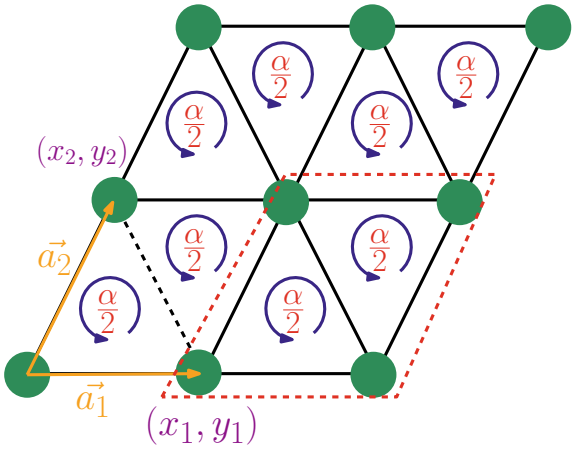

Fig. 1.1 (Color online) Schematic plot of a triangular lattice of size (3×3) exposed to an uniform magnetic flux α in each unit cell normal to the lattice. Circles filled with green color represent atoms arranged on the lattice points. A particular bond on a triangle is shown by dotted line in black color with coordinates (x_1, y_1) and (x_2, y_2). Direct primitive lattice vectors on a triangular lattice are shown in orange color and given by $\vec{a}_1 = a(1, 0)$ and $\vec{a}_2 = a(\frac{1}{2}, \frac{\sqrt{3}}{2})$, where a is the lattice constant. Arrow (shown in blue color) in each triangle represents path traversed by the itinerant electrons. After traversing on a closed triangular path, an electron will pick up a finite Aharonov–Bohm phase $\frac{\alpha}{2}$ in each triangles [8, 11, 47]

with,

$$\mathbf{h}_{ij,\sigma}(\{\omega_\sigma\}) = \Bigg[-t_{ij} \exp\left\{2\pi i \left(\frac{(x_2 + x_1)(y_2 - y_1)}{2}\right)\left(\frac{2}{\sqrt{3}a^2}\frac{\phi}{\phi_0}\right)\right\} + \Big\{U\omega_{i,-\sigma} + (U - J)\omega_{i,\sigma} - \mu\Big\}\delta_{ij}\Bigg] \tag{1.3}$$

here $\phi = \frac{\sqrt{3}a^2}{2}B$ is an uniform magnetic flux in each unit cell of triangular lattice and (x_1, y_1) and (x_2, y_2) are coordinates of a bond on a triangle (for details see Fig. 1.1). Choosing $\frac{\phi}{\phi_0} = \alpha \in (0, 1)$ as a dimensionless quantity and a as unity, $\mathbf{h}$ reduces to

$$\mathbf{h}_{ij,\sigma}(\{\omega_\sigma\}) = \Bigg[-t_{ij} \exp\left\{2\pi i \left(\frac{(x_2 + x_1)(y_2 - y_1)}{2}\right)\left(\frac{2}{\sqrt{3}}\alpha\right)\right\} + \Big\{U\omega_{i,-\sigma} + (U - J)\omega_{i,\sigma} - \mu\Big\}\delta_{ij}\Bigg] \tag{1.4}$$

It should also be noted down that this choice of gauge ensures that NN hopping of itinerant d-electrons in x-direction is $-t_{ij}$, while hopping in other directions is $-t_{ij} \exp\left\{2\pi i \left(\frac{(x_2+x_1)(y_2-y_1)}{2}\right)\left(\frac{2}{\sqrt{3}}\alpha\right)\right\}$, similar to *the Peierls substitution*. In this

way if an electron traverse on a complete plaquette of a triangle, it will pick up a finite *Aharonov–Bohm phase*, $\frac{\alpha}{2}$, in each triangle. In other words, electron will experience a finite magnetic flux α in each unit cell on the triangular lattice.

Our aim is to find the unique ground state configuration (state with minimum total internal energy) of f-electrons out of exponentially large possible configurations $\{\omega_\sigma\}$ for a chosen value of number of f-electrons N_f and for a set of values of parameters like U and α.

The method mainly involves the following steps:

1. We have set the scale of energy with $t_{\langle ij\rangle} = 1$.
2. The value of μ is chosen such that the filling of electrons ν is $\frac{(N_f + N_d)}{4N}$ (e.g., $N_f + N_d = N$ is one-fourth case ($\nu = \frac{1}{4}$) and $N_f + N_d = 2N$ is half-filled case ($\nu = \frac{1}{2}$), etc.), where $N_f = (N_{f_\uparrow} + N_{f_\downarrow})$, $N_d = (N_{d_\uparrow} + N_{d_\downarrow})$ and N are the total number of f-electrons, d-electrons and sites, respectively.
3. For a *triangular lattice* comprising of $N(= L^2, L = 12, 24, \ldots,$ etc.) sites, the $\mathcal{H}(\{\omega_\sigma\})$ is set up using the periodic boundary conditions (PBC).
4. In general, $\mathcal{H}(\{\omega_\sigma\})$ will be a $(2N \times 2N)$ matrix for a fixed configuration $\{\omega_\sigma\}$. Since there is no interaction considered between up and down spin d-electrons, one can set up the Hamiltonian matrix of size $(N \times N)$ for up and down spin d-electrons separately.
5. For one particular value of N_f, we have chosen values of $N_{f_\uparrow}$ and $N_{f_\downarrow}$ and their corresponding configurations $\{\omega_\uparrow\} = \{\omega_{1\uparrow}, \omega_{2\uparrow}, \ldots, \omega_{N\uparrow}\}$ and $\{\omega_\downarrow\} = \{\omega_{1\downarrow}, \omega_{2\downarrow}, \ldots, \omega_{N\downarrow}\}$.
6. Choosing the parameters U and J, U_f, and α the eigenvalues $\lambda_{i,\sigma}(i = 1, 2 \ldots, N)$ of $\mathbf{h}(\{\omega_\sigma\})$ are calculated using the numerical diagonalization technique.
7. The partition function (as system under consideration contains both itinerant and localized electrons, the grand canonical partition function is considered) of the system is written in the following form:

$$\mathcal{Z} = \sum_{\{\omega_\sigma\}} Tr\left(\exp\left\{-\beta\mathcal{H}(\{\omega_\sigma\})\right\}\right) \tag{1.5}$$

where the trace is taken over the d-electrons and $\beta = 1/k_B T$. The trace is calculated using the eigenvalues $\lambda_{i,\sigma}$. Further partition function can be recast in the following form:

$$\begin{aligned}\mathcal{Z} = \sum_{\{\omega_\sigma\}} \prod_i \left(\exp\left\{-\beta\left[U_f\omega_{i,\sigma}\omega_{i,-\sigma} + E_f\omega_{i,\sigma}\right]\right\}\right) \\ \times \prod_j \left(\exp\left\{-\beta\left[\lambda_{j,\sigma}(\{\omega_\sigma\}) - \mu\right]\right\} + 1\right)\end{aligned} \tag{1.6}$$

8. Now, the thermodynamic quantities can be calculated as averages over various configurations $\{\omega_\sigma\}$ with statistical weight $\mathcal{P}(\{\omega_\sigma\})$ is given by

$$\mathcal{P}(\{\omega_\sigma\}) = \frac{\exp\left\{-\beta\mathcal{F}(\{\omega_\sigma\})\right\}}{\mathcal{Z}} \tag{1.7}$$

where the corresponding free energy is given as follows:

$$\begin{aligned}\mathcal{F}(\{\omega_\sigma\}) = -\frac{1}{\beta}\Bigg[\ln\Bigg(\prod_i \exp\Big\{-\beta\Big[U_f\omega_{i,\sigma}\omega_{i,-\sigma} + E_f\omega_{i,\sigma}\Big]\Big\}\Bigg) \\ + \sum_j \ln\Bigg(\exp\Big\{-\beta\Big[\lambda_{j,\sigma}(\{\omega_\sigma\}) - \mu\Big]\Big\} + 1\Bigg)\Bigg]\end{aligned} \tag{1.8}$$

9. The total internal energy $\mathcal{E}(\{\omega_\sigma\})$ in the ground state is calculated as follows:

$$\begin{aligned}\mathcal{E}(\{\omega_\sigma\}) &= \lim_{T\to 0}\mathcal{F}(\{\omega_\sigma\}) \\ &= \sum_{i,\sigma}^{N_d}\lambda_{i,\sigma}(\{\omega_\sigma\}) + U_f\sum_{i,\sigma}\omega_{i,\sigma}\omega_{i,-\sigma} + E_f\sum_{i,\sigma}\omega_{i,\sigma}\end{aligned} \tag{1.9}$$

10. After this, classical Monte Carlo simulation algorithm is used to achieve an unique ground state configuration by annealing the static classical variables $\{\omega_\sigma\}$ ramping the temperature down from a high value to a very low value [24].

Here it also must be noted down that in the above Hamiltonian (1.1) vector potential, $\mathbf{A}$ is linear in position on the lattice along x-direction. Therefore, the translation corresponding to direct lattice vector shifts the phase of the wave function. This shift can also be compensated for a gauge transformation by introducing the magnetic translations. If the magnetic flux per unit cell ϕ is a rational multiple of the Dirac flux quantum ϕ_0, i.e., $\alpha = \frac{\phi}{\phi_0} = \frac{p}{q}$, where p and q are coprime integers, then in order to find the eigenfunctions which diagonalize the Hamiltonian (1.1) and the magnetic translation operators simultaneously, the number of sites chosen in the x-direction (L) must be integral multiple of q [5, 11].

1.3 Results and Discussion

In order to study the effects of on-site Coulomb interaction and magnetic field on the ground state properties of the FKM, various values of parameters like U, U_f, J, α and ν are chosen. In particular, we have calculated the results for $U = 1$ and 5, $U_f = 10$, $J = 0$, $\nu = \frac{1}{4}$ (with $N_{f_\uparrow} = N_{f_\downarrow} = 36$, $N_d = 72$) and for various values of α. Being chosen $J = 0$, on-site interaction between d- and f-electrons are same for all spins. U_f is also chosen a large value so that possibility of two f-electrons occupying the same site with opposite spins is discarded.

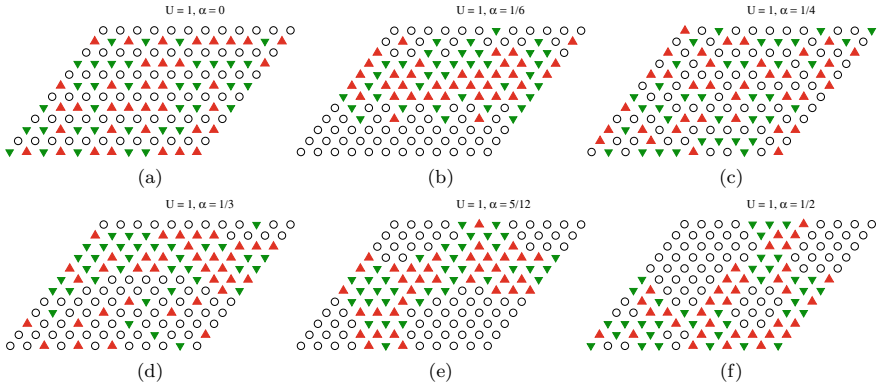

Fig. 1.2 (Color online) Ground state configurations of up and down spin localized f-electrons for $U = 1$, $N_{f_\uparrow} = N_{f_\downarrow} = 36$, $N_d = 72$ at **a**., $\alpha = 0$, **b**., $\alpha = 1/6$, **c**., $\alpha = 1/4$, **d**., $\alpha = 1/3$, **e**., $\alpha = 5/12$ and **f**. $\alpha = 1/2$. Here and onward up-triangles filled with black color and down-triangles filled with red color correspond to the sites occupied by spin-up and spin-down f-electrons, respectively, and open circles correspond to the unoccupied sites

We have found the ground state configurations of up and down spin f-electrons for the above-mentioned values of chosen parameters. In order to see the metal–insulator transition, energy gap ($\Delta = \lambda(N_d + 1) + \lambda(N_d - 1) - 2\,\lambda(N_d)$) around the Fermi energy (E_F) is calculated. It is shown that these results can be explained on the basis of density profile of d-electrons on each sites.

Nomenclature has been used for the various patterns [11, 12, 24] obtained in the ground state configurations of up and down spin f-electrons which are as follows: *Regular phase*: where the occupied sites are arranged in a long-range ordered pattern (Fig. 1.2a). *Quasi-regular phase*: where occupied sites arranged in nearly regular pattern with few defects (Fig. 1.3a). *Segregated phase*: where domains of occupied sites are segregated from the unoccupied sites (Fig. 1.2e). *Mixed phase*: where few occupied sites cluster together while remaining occupied sites are arranged in regular/quasi-regular pattern (Fig. 1.2d).

In Fig. 1.2, we have shown the ground state configurations of up and down spin f-electrons for $U = 1$ and for various values of α. A regular configuration is observed in ground state for f-electrons at $\alpha = 0$ (Fig. 1.2a). A mixed phase is observed in ground sate for $\alpha = 1/6$ (Fig. 1.2b). Nearly, regular phase is obtained for $\alpha = 1/4$ (Fig. 1.2c). Again mixed phase is seen for $\alpha = 1/3$ (Fig. 1.2d) and at large values of α segregated phase of f-electrons is found (Fig. 1.2c, f). These results show that the ground state configuration of f-electrons changes with change in α.

It is already mentioned that the AFM coupling on triangular lattice is frustrated and leads to large degeneracies at low temperatures. It turns out that this frustration is lifted in the higher-order perturbation in $\frac{1}{U}$. In order to see the effect of U on the ground state properties of the FKM in the presence of external magnetic field, we have obtained the ground state configurations and calculated energy gap around the Fermi energy at $U = 5$ and for different values of α.

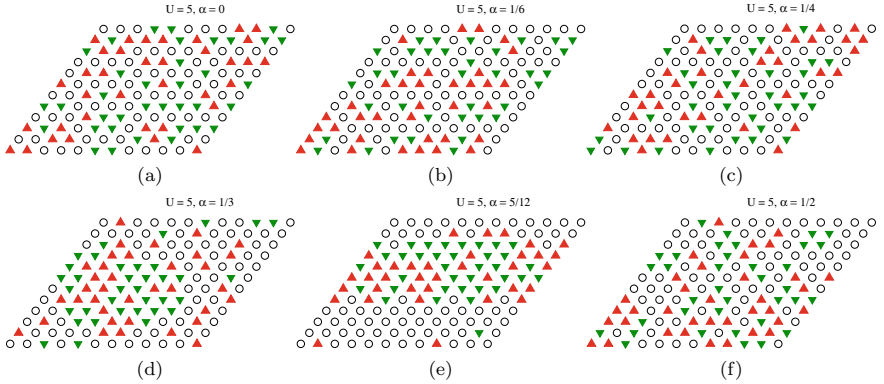

Fig. 1.3 (Color online) Ground state configurations of up and down spin localized f-electrons for $U = 5$, $N_{f\uparrow} = N_{f\downarrow} = 36$, $N_d = 72$ at **a**., $\alpha = 0$, **b**., $\alpha = 1/6$, **c**., $\alpha = 1/4$, **d**., $\alpha = 1/3$, **e**., $\alpha = 5/12$ and **f**. $\alpha = 1/2$

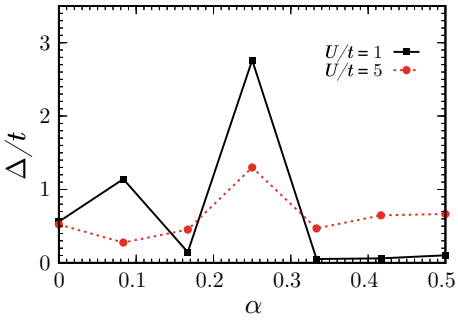

Fig. 1.4 (Color online) Flux (α) dependence of the gap Δ/t (calculated above the Fermi energy E_F) at $N_{f\uparrow} = N_{f\downarrow} = 36$, $N_d = 72$ and at different values of U. For certain values of α, Δ/t closes, and it is the signature of the metal to insulator transition in the system

In Fig. 1.3, we have shown the ground state configurations of up and down spin f-electrons at $U = 5$ and for various values α. Nearly, regular configurations are observed in ground state for f-electrons at $\alpha = 0, 1/6$ and $1/4$ (Fig. 1.3a–c). Mixed phases are observed in ground sate for $\alpha = 1/3$ and $5/12$ (Fig. 1.3d, e). Again a nearly regular phase is obtained for $\alpha = 1/2$ (Fig. 1.3f). These results clearly show that the ground state configuration changes with change in value of U. At $U = 5$, completely segregated phases are not obtained with α in contrast to the case of low values of $U = 1$ (Fig. 1.2).

In order to see the metal–insulator transition in the system, we have calculated the energy gap (Δ/t) around the Fermi energy (E_F) for d-electrons as function of α for $U = 1$ and 5 and shown it in Fig. 1.4.

Variation of Δ/t with α at different values of U (Fig. 1.4) clearly shows that there is **a metal to insulator transition in the system**. In particular in the case of

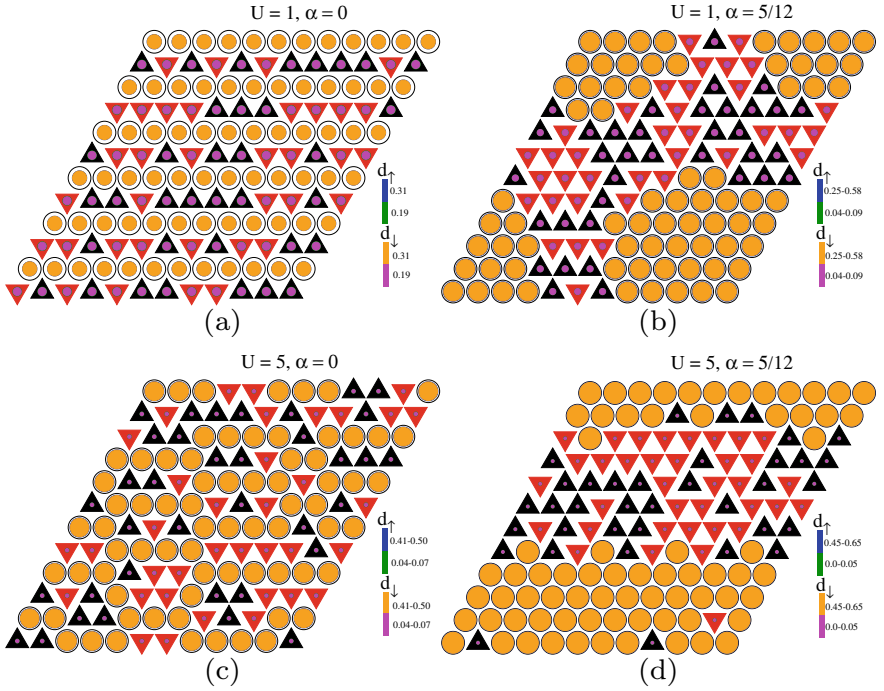

Fig. 1.5 (Color online) Up spin d-electron densities ($d_\uparrow$) and down spin d-electron densities ($d_\downarrow$) are shown on each sites for $N_{f_\uparrow} = N_{f_\downarrow} = 36$, $N_d = 72$ at different values of U and α. The color coding and the radii of the circles indicate the d-electron density profile. Cooperative effects of U and α can be seen on the variation of the d-electron densities on each site. At $U = 5$, d-electron densities are reduced on the occupied sites in comparison with the case of $U = 1$

$U = 1$ and $\alpha = 1/6, 1/3, 5/12$ and $1/2$, the Δ/t goes to zero. At $U = 1$ and for $\alpha = 0, 1/12$ and $1/4$, Δ/t remains finite. These results clearly indicate that choice of α is crucial to detect the metal to insulator transition in the ground state of the FKM.

In comparison with the case of $U = 1$, we find that for $U = 5$, Δ/t has also an irregular dependence on α. For all chosen values of α, Δ/t, unlike the case of $U = 1$, never closes. Thus, at $U = 5$ **no metal to insulator transition** is observed. These results are consistent with results already reported for the FKM with finite external magnetic field in the absence and the presence of Zeeman coupling terms for the large values of U [7, 11, 12].

These results can be understood by analyzing the up and down d-electrons densities on each site (Fig. 1.5) in combination with ground state configurations observed for the localized electrons (Figs. 1.2 and 1.3). Here, we have shown the up and down spin d-electron densities for $U = 1$ for $\alpha = 0$ and $5/12$ in Fig. 1.5a, b respectively. In Fig. 1.5c, d, results are shown for $U = 5$.

At $U = 1$ and $\alpha = 0$ (Fig. 1.5a), both up and down spin d-electrons are having the equal densities on all the sites. On the sites where f-electrons are already present, densities for both d-electron spins are equal but lesser in comparison with the unoccupied sites (as there is finite and same Coulomb repulsion for all types of d- and f-electron spins occupying the same site). Being the ground state configuration of localized f-electrons is regular, it is clear from Fig. 1.5a that the d-electron densities are trapped by the localized electrons. Hence, the d-electrons traveling through the lattice must overcome the potential raised by the localized electrons, and in this process, the d-electrons must lose their kinetic energy. Therefore, in this case there is a finite gap around the Fermi energy and system shows insulating nature. For $\alpha = 5/12$ (Fig. 1.5b), most of the up and down spin d-electron densities are spread on unoccupied sites. Since the ground state configuration is segregated, both types of d-electrons find enough space to hop through the entire lattice without any obstruction from the potential raised by the f-electrons. Therefore, in this case, gap closes around the E_F, and hence, system shows metallic nature.

Corresponding results for $U = 5$ and $\alpha = 0$ and $5/12$ (Fig. 1.5c, d), respectively, show that in comparison with the case of $U = 1$, here the density of d-electrons decreases on the sites already occupied by f-electrons and increases on unoccupied sites. Being the large value of U, the d-electrons are not able to move freely throughout the lattice, and hence, there is a finite gap around the E_F (irrespective of the ground state configurations of f-electrons) for all values of α. Hence, for $U = 5$ no metal to insulator transition is observed.

The results obtained above are applicable for a class of systems with layered structure and having underlying lattice as a triangular lattice. Metal–insulator transition phenomenon is of theoretical as well as experimental importance. The phase segregation of localized electrons obtained with magnetic flux at small values of U is observed in many experimental systems [13, 15, 24, 48, 49]. Here we propose that exposing such materials with the external uniform magnetic field may provide a new route to achieve the phase segregation. Metal to insulator transitions observed in these systems may be utilized to develop the sensors for the practical applications. In addition to these practical applications, our results may be a benchmark for many new theoretical investigations for these systems.

We have already said that there is recent proposal for the realization of the FKM in the context of ultra-cold atomic systems [11, 44–46]. These ultra-cold atomic systems provide a very clean and controlled artificial system where one can realize the unsolved quantum Hamiltonians to gain insight into the properties of the system which can otherwise be inaccessible in the conventional condensed matter systems. Hence, realization of the spin-1/2 FKM on a triangular lattice in the presence of external magnetic field using the ultra-cold atomic techniques may provide a new route to realize many novel phenomenon like quantum Hall effect [1, 2], famous Hofstadter butterfly structure [3] and superconducting quantum flux phases [4, 5].

In conclusion, we have studied the ground state properties of the spin-1/2 Falicov-Kimball model on a triangular lattice in the presence of uniform external magnetic field. Results are obtained using the numerical diagonalization technique and Monte Carlo simulation algorithm. It is found that for $U/t = 1$, the magnetic field produces

a phase transition from metal to insulator transitions accompanied by the phase segregation/mixed phases to the regular/quasi-regular phases in the system. At the large value of U/t (say $U/t = 5$), no metal to insulator transition is observed.

Acknowledgements UKY acknowledges the UGC, India, for a Faculty Research Start-Up grant No. F. 30-417/2018(BSR) under the BSR scheme.

References

1. K. Klitzing, G. Dorda, M. Pepper, Phys. Rev. Lett. **45**(6), 494–497 (1980)
2. D.J. Thouless, Phys. Rev. B **27**(10), 6083–6087 (1983)
3. D.R. Hofstadter, Phys. Rev. B **14**(6), 2239–2249 (1976)
4. P. Lederer, D. Poilblanc, T.M. Rice, Phys. Rev. Lett. **63**(14), 1519–1522 (1989)
5. M.M. Maśka, Phys. Rev. B **66**(5), 054533 (2002)
6. C. Albrecht, J.H. Smet, K. von Klitzing, D. Weiss, V. Umansky, H. Schweizer, Phys. Rev. Lett. **86**(1), 147–150 (2001)
7. S. Pradhan, J. Phys. Condens. Matter **28**, 505502 (2016)
8. S.K. Ghosh, U.K. Yadav, V.B. Shenoy, Phys. Rev. A (R) **92**(5), 051602 (2015)
9. S.K. Ghosh, U.K. Yadav, Phys. Rev. A **94**(4), 043634 (2016)
10. S.K. Ghosh, S. Greschner, U.K. Yadav, T. Mishra, M. Rizzi, V.B. Shenoy, Phys. Rev. A **95**(6), 063612 (2017)
11. U.K. Yadav, Eur. Phys. J. B **93**(12), 221, 505502 (2020)
12. U.K. Yadav, Solid State Commun. **249**(12–18), 0038–1098, 505502 (2017)
13. D. Qian, D. Hsieh, L. Wray, Y.D. Chuang, A. Fedorov, D. Wu, J.L. Luo, N.L. Wang, L. Viciu, R.J. Cava, M.Z. Hasan, Phys. Rev. Lett. **96**(21), 216405 (2006)
14. I. Terasaki, Y. Sasago, K. Uchinokura, Phys. Rev. B **56**(20), R12685–R12687 (1997)
15. K. Takada, H. Sakurai, E. Takayama-Muromachi, F. Izumi, R.A. Dilanian, T. Sasaki, Nature **422**(6927), 53–55 (2003)
16. A. Taraphder, M.S. Laad, L. Craco, A.N. Yaresko, Phys. Rev. Lett. **101**(13), 136410 (2008)
17. T. Maitra, A. Taraphder, A.N. Yaresko, P. Fulde, Eur. Phys. J. B **49**, 433–439 (2006)
18. S.J. Clarke, A.J. Fowkes, A. Harrison, R.M. Ibberson, M.J. Rosseinsky, Chem. Mater. **10**, 372–384, 505502 (1998)
19. H.F. Pen, J. van den Brink, D.I. Khomskii, G.A. Sawatzky, Phys. Rev. Lett. **78**(7), 1323–1326 (1997)
20. D.I. Khomskii, T. Mizokawa, Phys. Rev. Lett. **94**(15), 156402 (2005)
21. R. Kaur, T. Maitra, T. Nautiyal, J. Phys. Condens. Matter **25**, 065503 (2013)
22. H.A. Mook, P. Dai, F. Doğan, Phys. Rev. Lett. **88**(9), 097004 (2002)
23. R. Lemański, J.K. Freericks, G. Banach, Phys. Rev. Lett. **89**(19), 196403 (2002)
24. U.K. Yadav, T. Maitra, I. Singh, A. Taraphder, J. Phys. Condens. Matter **22**, 295602 (2010)
25. U.K. Yadav, T. Maitra, I. Singh, A. Taraphder, EPL (Europhys. Lett.) **93**, 47013, 295602 (2011)
26. U.K. Yadav, T. Maitra, I. Singh, Eur. Phys. J. B **84**, 365–370 (2011)
27. U.K. Yadav, T. Maitra, I. Singh, Solid State Commun. **164**(32–37), 0038–1098, 295602 (2013)
28. S. Kumar, U.K. Yadav, T. Maitra, I. Singh, Solid State Commun. **228**(1–5), 0038–1098, 295602 (2016)
29. L.M. Falicov, J.C. Kimball, Phys. Rev. Lett. **22**(19), 997–999 (1969)
30. R. Ramirez, L.M. Falicov, J.C. Kimball, Phys. Rev. B **2**(8), 3383–3393 (1970)
31. R. Lemański, Phys. Rev. B **71**(3), 035107 (2005)
32. H. Cencariková, P. Farkasovsky, N. Tomasovicova, M. Zonda, Phys. Status Solidi (B) **245**, 2593–2598, 1521–3951 (2008)
33. S. Pradhan, A. Taraphder, EPL (Europhys. Lett.) **116**, 57001, 295602 (2016)

34. R. Peierls, Z. Phys. **80**(763–791), 0044–3328, 295602 (1933)
35. Y. Aharonov, D. Bohm, Phys. Rev. **115**(3), 485–491 (1959)
36. M. Aidelsburger, *Artificial Gauge Fields with Ultracold Atoms in Optical Lattices* (Springer, Berlin, 2016)
37. S. Kumar, U.K. Yadav, T. Maitra, I. Singh, Solid State Commun. **189**(21–27), 0038–1098, 295602 (2014)
38. C. Gruber, N. Macris, A. Messager, D. Ueltschi, J. Stat. Phys. **86**(57–108), 1572–9613, 295602 (1997)
39. R.S. Khymyn, V.E. Kireev, B.O. Ivanov, Condens. Matter Phys. **17**(33701), 1–10, 295602 (2014)
40. R.S. Gekht, Sov. Phys. Usp. **32**, 871, 295602 (1989)
41. G. Li, P. Höpfner, J. Schäfer, C. Blumenstein, S. Meyer, A. Bostwick, E. Rotenberg, R. Claessen, W. Hanke, Nat. Commun. **4**, 1620, 295602 (2013)
42. H. Ishizuka, *Magnetism and Transport Phenomena in Spin-Charge Coupled Systems on Frustrated Lattices* (Springer, Berlin, 2015)
43. I. Bloch, J. Dalibard, W. Zwerger, Rev. Mod. Phys. **80**(3), 885–964 (2008)
44. C. Ates, K. Ziegler, Phys. Rev. A **71**(6), 063610 (2005)
45. L. Tomio, S. Adhikari, G. Krein, K. Ziegler, Nucl. Phys. A **790**, 718c–722c, 0375–9474 (2007)
46. M. Iskin, J.K. Freericks, Phys. Rev. A **80**(5), 053623 (2009)
47. D.P.A. Maurice, Proc. R. Soc. Lond. A **133**(60–72), 821 (1931)
48. D.S. Park, J.J. Mudd, M. Walker, A. Krupski, D. Seghier, N.F. Saniee, C.J. Choi, C.J. Youn, S.R.C. McMitchell, C.F. McConville, CrystEngComm **16**(11), 2136–2143, 295602 (2014)
49. D. Yong, H. He, L. Su, Y. Zhu, Z. Tang, X.C. Zeng, B. Pan, Nanoscale **7**(21), 9852–9858 (2015)

Chapter 2
Tuning the Morphology of Lanthanum Cobaltite Using the Surfactant-Assisted Hydrothermal Approach for Enhancing Oxygen Evolution Catalysis

Deeksha, Pawanpreet Kour, Imtiaz Ahmed, Krishna Kanta Haldar, and Kamlesh Yadav

Abstract The high consumption rate of fossil fuels to meet the global energy demands attracts the progress of innovative energy storage and conversion systems. Among them, water electrolysis shows major concern because of its great potential to produce clean hydrogen energy. The dawdling dynamics of the oxygen evolution reaction (OER) that occurs on the anode results in the low energy efficiency of the process. Perovskite oxide with transition metal on the B site possesses a high intrinsic as well as extrinsic activity toward OER. However, the low specific surface area restricts their catalytic activity. Here, we report on the synthesis of lanthanum cobaltite ($LaCoO_3$) nanoparticles and bundles of nanorods using glycine and PVP surfactants, respectively, via the hydrothermal method. Structural characterizations confirmed the pure phase synthesis of $LaCoO_3$ perovskite nanomaterials and further their electrocatalytic performance is investigated in an alkaline medium (1 M KOH). The results show that randomly oriented bundles of nanorods (average length 515 nm, average diameter 65 nm) exhibit smaller overpotential ($\eta = 420$ mV) at $j = 10$ mA cm^{-2} and the Tafel slope (99 mV dec^{-1}) compared with nanoparticles ($\eta = 450$ mV and Tafel slope ~ 110 mV dec^{-1}). The dramatically improved OER activity and larger electrochemical surface area (ECSA) of nanorods as compared to nanoparticles are because of the interconnected porous architecture of nanorods. Our work not only highlights the surfactant-assisted hydrothermal approach to synthesize the nanorods but also introduces the effect of a change in morphology on electrochemical activity.

Deeksha · P. Kour · K. Yadav (✉)
Department of Physics, School of Basic Sciences, Central University of Punjab, Bathinda 151401, India
e-mail: kamlesh.yadav@cup.edu.in

I. Ahmed · K. K. Haldar
Deparment of Chemistry, School of Basic Sciences, Central University of Punjab, Bathinda 151401, India

K. L. Pandey et al. (eds.), *Proceedings of the National Workshop on Recent Advances in Condensed Matter and High Energy Physics*, Springer Proceedings in Physics 278,
https://doi.org/10.1007/978-981-19-2592-4_2

2.1 Introduction

The advancement of clean, sustainable, and low-cost renewable energy sources to handle the environmental issues and diminish the global energy crisis is driving the attention of researchers today [1]. Among the numerous renewable energy technologies, the phenomenon of water electrolysis shows major concern because of its high purity hydrogen production capability. Two half-cell reactions are involved during the phenomenon of water electrolysis, one is hydrogen evolution (HER) and another is oxygen evolution reaction (OER) occurs on the cathode and anode, respectively [2]. OER follows more sluggish kinetics as compared to HER because of the involvement of four coupled electron-proton transfer processes, which results in lesser energy efficiency [3]. Although the commercial electrocatalysts for OER, such as IrO_2 and RuO_2 reduce the kinetic barrier, still the inadequacy of these precious metal oxides provoking to choose alternate materials with comparable efficiency and improved stability [4]. Recently, various cost-effective 3D-transition metal-based materials such as spinel oxides, simple perovskites, double perovskites, layered double hydroxides, sulfides, phosphides have been studied widely for efficient OER activity to replace the noble metals [5–10]. Among them, perovskite structure of ABO_3 type, where A is larger cation generally lanthanides or rare earth metals with 12-fold coordination occupy the corner of the unit cell, B is a smaller cation having sixfold geometry coordinated with six face-centered oxygen (O) anions have attracted more attention [11]. The flexibility and tunability of perovskite nanomaterials display the diversity of modified properties and facilitate the formation of the M–OH bond, which promotes the evolution of oxygen. Various activation strategies such as non-stoichiometry on A or B site, cation and anion doping, creation of oxygen vacancies, nanocomposites have been employed to boost the intrinsic and extrinsic activity of materials for efficient OER [12–14]. Despite the enormous efforts, perovskite nanostructures with a large surface area are in a demand to enhance the extrinsic activity for easy conduction of electron and mass transfer [15, 16]. It has been widely reported that altering the morphology of nanostructures is an efficient way for enrichment of active sites, which further increases the specific surface area for the catalytic reaction. Morphology can be altered via adopting different synthesis methods, the varying concentration of precursors, synthesis time, different pH values, etc. [17, 18]. For example, Zhao et al. designed vertically aligned nanosheets of lanthanum cobaltite ($LaCoO_3$) grown on conductive nickel foam (denoted as $LaCoO_3$/NF) using the hydrothermal method of synthesis with further annealing. It was analyzed that $LaCoO_3$/NF nanosheets exhibit lower overpotential with excellent electrochemical stability due to enlarged specific surface area and surface wettability for the rapid evolution of molecules of gas [19]. Nanostructure engineering can also modify the intrinsic reaction kinetics to enhance the efficiency of OER. For example, Liu et al. synthesize $SrNb_{0.1}Co_{0.7}Fe_{0.2}O_{3-\delta}$ nanofibers with diameter 80 and 135 nm through the electrospinning method and reported that engineering of nanofibers architecture with excessive oxygen vacancies shifted the path of the reaction and promote the process of oxygen evolution [20]. The nanostructures of cobalt-based perovskite

oxide such as $LaCoO_3$ show superior performance for OER in alkaline solutions as the intermediate spin state of cobalt ions in perovskites possess $e_g \approx 1$, which is one of the activity descriptors described by Shao-Horn et al. [21, 22].

Herein, we report the influence of morphology and specific surface area on the catalytic performance of cobalt-based perovskite oxide synthesized using the surfactant-assisted hydrothermal method. We have used different surfactants to synthesize the bundles of nanorods (NR) and nanoparticles (NP) of $LaCO_3$. The prepared $LaCoO_3$ bundles of nanorods exhibit enhanced OER activity with lower overpotential compared to nanoparticles. This result is because of the higher electrochemically active surface area possessed by one-dimensional porous nanorods compared to spherical nanoparticles.

2.2 Experimental Section

2.2.1 Materials

Lanthanum (III) nitrate hexahydrate ($La(NO_3)_3.6H_2O$, 99.995%), cobalt (II) nitrate hexahydrate ($Co(NO_3)_3.6H_2O$, 99%), and 5 wt% Nafion 117 solution were used (Sigma-Aldrich). Polyvinylpyrrolidone (PVP) k-30 (M.W-40,000), glycine ($C_2H_5NO_2$), ethanol (analytical grade), and ammonia solution (99.98%) were used in he the synthesis. All experiments were performed in the double-distilled water (18.2 MΩ cm).

2.2.2 Synthesis of Catalysts

A hydrothermal approach with different surfactants was utilized to synthesize the distinct morphologies of the $LaCoO_3$. For the synthesis of nanoparticles, initially, precursor solution was obtained by dissolving 20 mmol of $La(NO_3)_3.6H_2O$ and $Co(NO_3)_3.6H_2O$ in 60 ml of double-distilled water with magnetic stirring for one hour. After this, glycine was added in the ratio 1:4 (total nitrate ratio: glycine) and sonicated for 15 min using an ultrasonicator. Next, the pH was maintained at 8.2 using an ammonia solution resulted in a dark pink color solution. Then, the suspension was transferred to the stainless-steel Teflon-lined autoclave and heated up at 180 °C for 24 h in the furnace. After this, the precipitates were collected from the autoclave and rinsed several times with ultrapure water and ethanol. Further, these precipitates were dried in an oven for 10 h at 70 °C. Then, the final product was formed after sintering in a muffle furnace at 800 °C for 2 h with a ramping rate of 3 °C/min. After this, the black color powder was collected and named NP. For the synthesis of $LaCoO_3$ nanorods, PVP (K-30) was used instead of glycine and the time of the hydrothermal

process was changed from 24 to 15 h. The synthesized $LaCoO_3$ nanorods were named NR.

2.2.3 Structural Characterization

To confirm the phase purity of the samples, X-ray diffraction (XRD) pattern was obtained on PANalytical Empyrean instrument using Cu-K_α radiation of wavelength $\lambda = 1.5406$ Å from 10° to 90°. The morphological feature of the electrocatalysts was carried out using Model Merlin Compact couple field emission scanning electron microscope (FESEM). The FTIR spectra of prepared electrocatalysts were obtained by a Bruker Tensor 27 Model: NEXUS-870 spectrometer with KBr pellets in the range 4000–600 cm^{-1}.

2.2.4 Electrode Preparation

For the working electrode, catalyst ink was prepared by dissolving five milligrams of as-synthesized catalyst into 1000 μl of water/ethanol solution in the ratio of 3:1 and sonicated for 30 min. After that, 20 μL of 5 wt% Nafion solution was added to the dispersion and again sonicated for half an hour to form homogeneous ink. The 5 μL as-prepared catalyst ink was pipetted onto glassy carbon (GC) electrode (geometric surface area 0.07065 cm^2). The loaded mass of the catalyst was 0.34 mg/cm^2. Finally, the coated electrode was dried overnight in a vacuum desiccator and reserved for further electrochemical measurements.

2.2.5 Electrochemical Measurements

OER performance of the synthesized electrocatalysts was examined on Metrohm auto lab (multichannel-204) using Nova 2.1.4 software. The standard three-electrode system consists of a Platinum counter electrode, Ag/AgCl (3 M KCl) reference electrode, and the glassy carbon working electrode of 3 mm diameter was used to carry out all the experiments. 1 Molar KOH electrolyte prepared from KOH pellets and deionized was used for electrochemical testing. Linear sweep voltammetry was carried out from 0 to 1 V potential range at the scan rate of 10 mV/s. Cyclic voltammetry curves (CV) were obtained at various scan rates in the potential range of 1.26–1.37 V versus reversible hydrogen electrode (RHE). To normalize the measured potential versus RHE, the Nernst equation was used given below:

$$E_{(\mathrm{RHE})} = (0.059 * \mathrm{pH}) + E_{(\mathrm{Ref})} + E_{(\mathrm{Ag/AgCl})} \tag{2.1}$$

where pH represents the pH of electrolyte used in the experiment. $E_{(\mathrm{RHE})}$ and $E_{(\mathrm{Ag/AgCl})}$ indicate the measured potential versus reversible hydrogen electrode and potential versus Ag/AgCl, respectively. The applied potentials were also *iR* corrected using the formula written below

$$E_{\mathrm{actual}} = E_{\mathrm{applied}} - iR \tag{2.2}$$

where i and R represent the measured value of current and ohmic resistance due to electrolyte, respectively.

2.3 Results and Discussion

2.3.1 Structural Characterization

Figure 2.1a depicts the X-ray diffraction pattern of $LaCoO_3$ NP and NR. The peaks are well-matched with standard JCPDS card: 48-0123 and confirmed the fabrication of the rhombohedral structure of $LaCoO_3$. The presence of the intense narrow peaks in the XRD refers to the formation of highly crystalline $LaCoO_3$ NP and NR. The FTIR spectra of $LaCoO_3$ NP and NR are shown in Fig. 2.1b. The dips appearing at 1136, 1384, 1489, 1628 cm^{-1} are related to vibrations of $LaCoO_3$ crystal lattice, and the peak at 748 cm^{-1} is due to the vibrations of metal–oxygen bonds [23], which further confirms the formation of $LaCoO_3$.The band at 3705 cm^{-1} corresponds to the stretching vibration of O–H because of the H_2O molecules adsorbed on the $LaCoO_3$ surface [23].

FESEM images of $LaCoO_3$ revealed the formation of irregularly shaped nanoparticles when glycine is used as a surfactant (Fig. 2.2a). It changes into randomly oriented bundles of nanorods when the PVP precursor is used (Fig. 2.2b). The inset

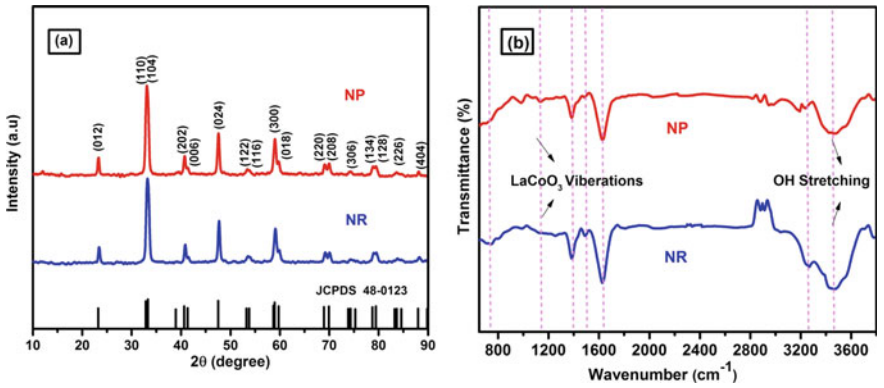

Fig. 2.1 **a** XRD of $LaCoO_3$NP and NR, **b** FTIR spectra of $LaCoO_3$NP and NR

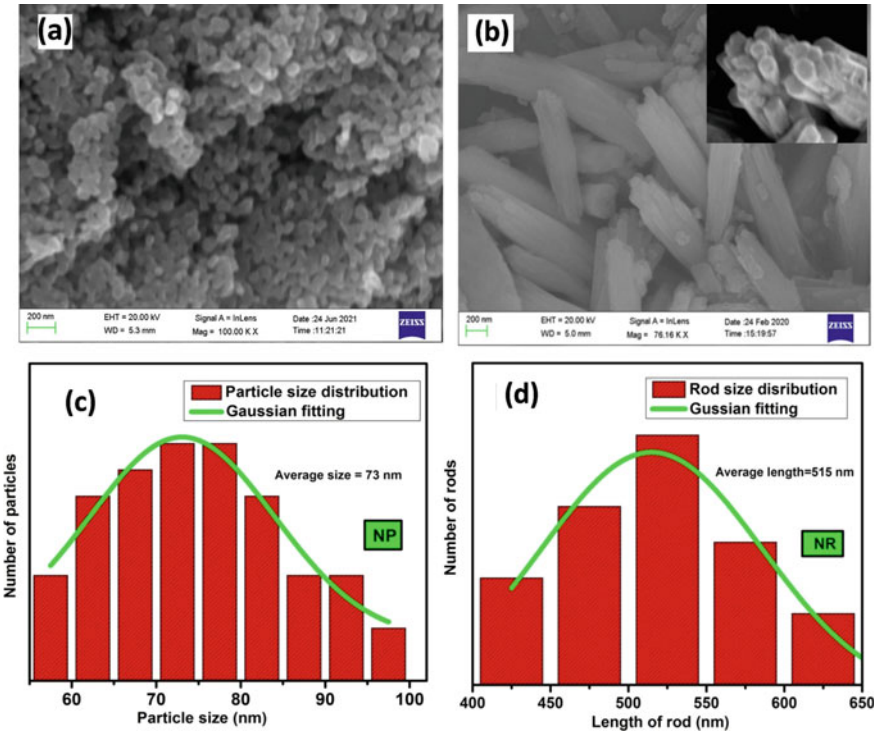

Fig. 2.2 FESEM images of NP (**a**), and NR (**b**); histogram of NP (**c**), and NR (**d**). The inset of **b** shows the front facet of nanorods

of Fig. 2.2c displays the front facet of a bundle of nanorods. Besides that, the FESEM images indicate that the NR sample has a more porous architecture compared to NP [24]. The histogram is drawn between the size of nanomaterial and frequency of event with Gaussian fitting to estimate the average size. The calculated value of the average particle size is 73 nm for the NP sample, while the average length of NR is 515 nm. It is because of the amphiphilic nature of PVP that increases the crystal growth of $LaCoO_3$ and leads to the formation of NR [24].

2.3.2 OER Activity

Figure 2.3a shows the LSV curve (E vs. RHE and current density) for NP and NR. A rapid rise in current density with an increase in potential is observed. Overpotential (η) is calculated at $j = 10$ mA cm^{-2} (current density) from the following equation

$$\text{Overpotential}(\eta) = E_{\text{RHE}} - 1.23\,\text{V} \tag{2.3}$$

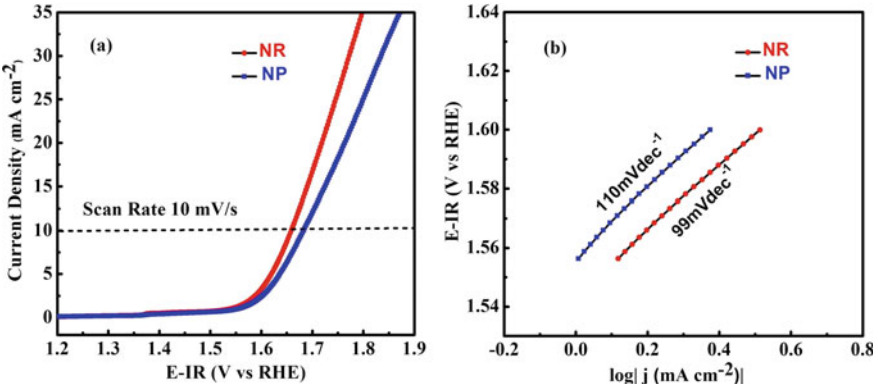

Fig. 2.3 **a** LSV OER curves for $LaCoO_3$ NP and NR and **b** Tafel plots of $LaCoO_3$NP and NR in 1 M KOH at the scan rate of 10 mV s^{-1}

NP achieves an overpotential of 450 mV, whereas NR displays a comparatively lower overpotential of 420 mV. To understand the reaction kinetics, Tafel slope is calculated by plotting a graph between log |*j*| and voltage versus RHE shown in Fig. 2.3b. Meanwhile, the nanorods of $LaCoO_3$ have a smaller value of 99 mV dec^{-1} than nanoparticles of 110 mV dec^{-1}. Thus, this result confirms that NR displays superior OER activity than the NP sample. This result is because of the enhancement of the transfer of electrons and ions through the direct transfer pathway facilitated by the interconnected architecture of nanorods. Moreover, this network also supports rapid mass transport, which promotes the efficiency of OER [15].

Figure 2.4a, b shows the CV plot performed at different scan rates for both the sample NP and NR, respectively. To expose the origin of the improved catalytic activity of NR as compared to NP, the electrochemical surface area (ECSA) is determined via double-layer capacitance (C_{dl}) from cyclic voltammetry curves at different scan rates. To evaluate the C_{dl}, both the anodic and cathodic charge current densities at 1.31 V versus RHE are plotted versus scan rate as represented is shown in Fig. 2.4c, d for NP and NR, respectively. The value of C_{dl} is found to be 0.72 mF cm^{-2} and 1.105 mF cm^{-2} for NP and NR samples, respectively. The ECSA is calculated using the following formula:

$$\text{ECSA} = \frac{\text{Double Layer Capacitance } (C_{dl})}{\text{Specific Capacitance}(C_s)} \tag{2.4}$$

The value of C_s used in this work is 40 μF cm^{-2} reported in the literature. The value of ECSA is 18 cm^2 and 27.62 cm^2 for NP and NR, respectively. Thus, this result confirms that NR has a larger ECSA than NP, which indicates the relatively large number of active sites because of the more porous architecture of NR, which further promotes the process of OER.

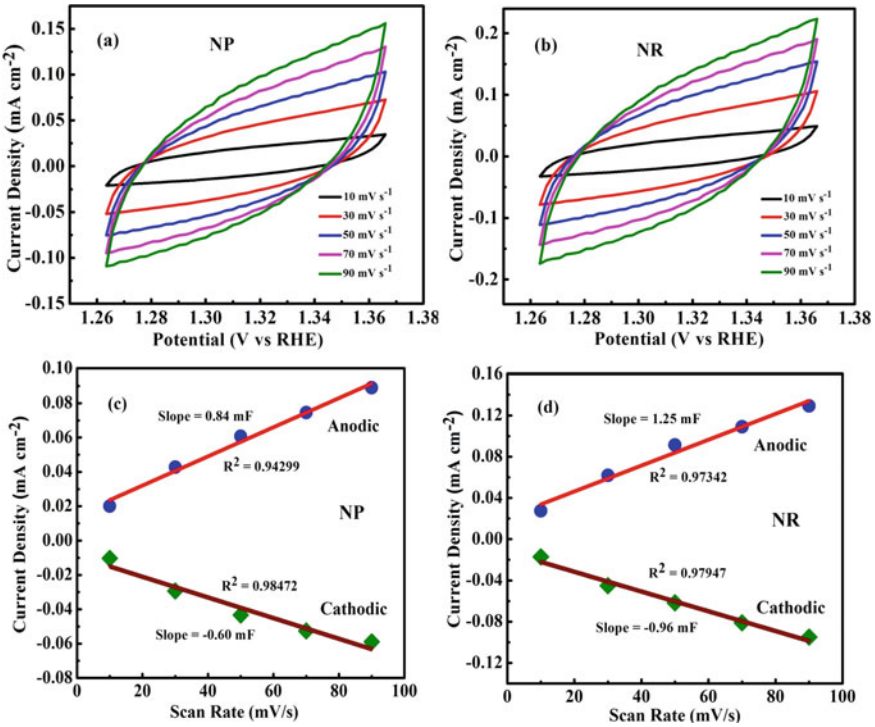

Fig. 2.4 Cyclic voltammograms of NP (**a**), NR (**b**) at different scan rates; variation of the anodic and cathodic current density of NP (**c**), NR (**d**) with scan rate for the determination of C_{dl} of the electrocatalysts

2.4 Conclusion

In summary, $LaCoO_3$ NP and NR are successfully synthesized through the hydrothermal process using different surfactants and investigated their electrocatalysts properties for OER activity in an alkaline medium (KOH). FESEM studies confirmed the formation of $LaCoO_3$ nanorods of average length 515 nm with 65 nm diameters and $LaCoO_3$ NP of average size 73 nm. This also shows the formation of a more porous structure of nanorods compared to nanoparticles. Electrochemical study reveals that nanorods exhibit better OER activity than nanoparticles possessing lower overpotential (η) of 420 mV with a small Tafel slope of 99 mV dec^{-1} as compared to NP (450 mV, 110 mV dec^{-1}). The boosted oxygen evolution activity is because of the more porous and interconnected architecture of NR, which enhanced the ECSA of NR. Thus, the rational modification of morphology is beneficial for efficient OER.

Acknowledgements The authors are grateful to the Central Instrumentation Laboratory (CIL), and the Department of Physics, Central University of Punjab (CUP), Bathinda, for providing research facilities. Two of the authors (Deeksha and Imtiaz Ahmed) acknowledge the Council of Scientific

and Industrial Research (CSIR) and one author (Pawanpreet Kour) acknowledges the University Grants Commission (UGC), Delhi, India for funding support.

References

1. F. Naseem, P. Lu, J. Zeng, Z. Lu, Y.H. Ng, H. Zhao, Y. Du, Z. Yin, Solid nanoporosity governs catalytic CO_2 and N_2 reduction. ACS Nano **14**(7), 7734–7759 (2020)
2. S. Wang, A. Lu, C.J. Zhong, Hydrogen production from water electrolysis: role of catalysts. Nano Convergence **8**(1), 1–23 (2021)
3. E. Fabbri, T.J. Schmidt, Oxygen evolution reaction—the enigma in water electrolysis. ACS Catal. **8**(10), 9765–9774 (2018)
4. Y. Lee, J. Suntivich, K.J. May, E.E. Perry, Y. Shao-Horn, Synthesis and activities of rutile IrO_2 and RuO_2 nanoparticles for oxygen evolution in acid and alkaline solutions. J. Phys. Chem. Lett. **3**(3), 399–404 (2012)
5. Y. Zhang, T. Lu, Y. Ye, W. Dai, Y.A. Zhu, Y. Pan, Stabilizing oxygen vacancy in entropy-engineered $CoFe_2O_4$-type catalysts for Co-prosperity of efficiency and stability in an oxygen evolution reaction. ACS Appl. Mater. Interfaces **12**(29), 32548–32555 (2020)
6. M. Qu, X. Ding, Z. Shen, M. Cui, F.E. Oropeza, G. Gorni, V.A. de la Peña O'Shea, W. Li, D.C. Qi, K.H. Zhang, Tailoring the electronic structures of the La_2NiMnO_6 double perovskite as efficient bifunctional oxygen electrocatalysis. Chem. Mater. **33**(6), 2062–2071 (2021)
7. J.W. Zhao, Z.X. Shi, C.F. Li, Q. Ren, G.R. Li, Regulation of perovskite surface stability on the electrocatalysis of oxygen evolution reaction. ACS Mater. Lett. **3**(6), 721–737 (2021)
8. Y. Cao, T. Wang, X. Li, L. Zhang, Y. Luo, F. Zhang, A.M. Asiri, J. Hu, Q. Liu, X. Sun, A hierarchical CuO@ NiCo layered double hydroxide core–shell nanoarray as an efficient electrocatalyst for the oxygen evolution reaction. Inorg. Chem. Front. **8**(12), 3049–3054 (2021)
9. J.F. Qin, M. Yang, T.S. Chen, B. Dong, S. Hou, X. Ma, Y.N. Zhou, X.L. Yang, J. Nan, Y.M. Chai, Ternary metal sulfides MoCoNiS derived from metal organic frameworks for efficient oxygen evolution. Int. J. Hydrogen Energy **45**(4), 2745–2753 (2020)
10. W. Li, D. Xiong, X. Gao, L. Liu, The oxygen evolution reaction enabled by transition metal phosphide and chalcogenide pre-catalysts with dynamic changes. Chem. Commun. **55**(60), 8744–8763 (2019)
11. C. Sun, J.A. Alonso, J. Bian, Recent advances in perovskite-type oxides for energy conversion and storage applications. Adv. Energy Mater. **11**(2), 2000459 (2021)
12. R. Xie, Z. Nie, X. Hu, Y. Yu, C. Aruta, N. Yang, Pr-doped $LaCoO_3$ toward stable and efficient oxygen evolution reaction. ACS Appl. Energy Mater. **4**(9), 9057–9065 (2021)
13. D. Guan, G. Ryu, Z. Hu, J. Zhou, C.L. Dong, Y.C. Huang, K. Zhang, Y. Zhong, A.C. Komarek, M. Zhu, X. Wu, Utilizing ion leaching effects for achieving high oxygen-evolving performance on hybrid nanocomposite with self-optimized behaviors. Nat. Commun. **11**(1), 1–10 (2020)
14. S. Bhowmick, A. Dhankhar, T.K. Sahu, R. Jena, D. Gogoi, N.R. Peela, S. Ardo, M. Qureshi, Low overpotential and stable electrocatalytic oxygen evolution reaction utilizing doped perovskite oxide, $La_{0.7}Sr_{0.3}MnO_3$, modified by cobalt phosphate. ACS Appl. Energy Mater. **3**(2), 1279–1285 (2020)
15. G. Nie, Z. Zhang, T. Wang, C. Wang, Z. Kou, Electrospun one-dimensional electrocatalysts for oxygen reduction reaction: insights into structure-activity relationship. ACS Appl. Mater. Interfaces **13**(32), 37961–37978 (2021)
16. R. Biswas, P. Thakur, G. Kaur, S. Som, M. Saha, V. Jhajhria, H. Singh, I. Ahmed, B. Banerjee, D. Chopra, T. Sen, Interfacial engineering of $CuCo_2S_4$/g-C_3N_4 hybrid nanorods for efficient oxygen evolution reaction. Inorg. Chem. **60**(16), 12355–12366 (2021)
17. Deeksha, Anu, K. Yadav, Effect of changing morphology of $BiFeO_3$ from nanoparticles to nanosheets on electrochemical properties, in *AIP Conference Proceedings*, vol. 2220 (2020), p. 020145

18. C. Zhang, W. Zhang, X. Li, Z. Zhu, Q. Wang, S. Luo, A. Xie, Honeycomb $LaMnO_3$ perovskite synthesized by a carbon sphere as a self-sacrificing template for supercapacitors. Energy Fuels **35**(16), 13457–13465 (2021)
19. T. Zhao, Y. Wang, X. Chen, Y. Li, Z. Su, C. Zhao, Vertical growth of porous perovskite nanoarrays on nickel foam for efficient oxygen evolution reaction. ACS Sustain. Chem. Eng. **8**(12), 4863–4870 (2020)
20. Q. Liu, C. Jia, M. Zhou, Z. He, Z. Gong, Y. Ling, X. Wang, K. Yashiro, Y. Chen, Modulating reaction pathways on perovskite cobaltite nanofibers through excessive surface oxygen defects for efficient water oxidation. Energy Fuels **35**(17), 13967–13974 (2021)
21. J. Suntivich, K.J. May, H.A. Gasteiger, J.B. Goodenough, Y. Shao-Horn, A perovskite oxide optimized for oxygen evolution catalysis from molecular orbital principles. Science **334**(6061), 1383–1385 (2011)
22. B. Xia, T. Wang, J. Ran, S. Jiang, X. Gao, D. Gao, Optimized conductivity and spin states in N-doped $LaCoO_3$ for oxygen electrocatalysis. ACS Appl. Mater. Interfaces **13**(2), 2447–2454 (2021)
23. S. Tasleem, M. Tahir, Constructing $La_xCo_yO_3$ perovskite anchored 3D g-C_3N_4 hollow tube heterojunction with proficient interface charge separation for stimulating photocatalytic H_2 production. Energy Fuels **35**(11), 9727–9746 (2021)
24. K.M. Koczkur, S. Mourdikoudis, L. Polavarapu, S.E. Skrabalak, Polyvinylpyrrolidone(PVP) in nanoparticle synthesis. Dalton Trans. **44**(41), 17883–17905 (2015)

Chapter 3
Synthesis of Novel Complex Metallic Alloys

Thakur Prasad Yadav and Kalpana Awasthi

Abstract The structural complexity of the alloys depends on the composition and number of atoms per unit cell. The intermetallic complex metallic materials have attracted research interest over the last several decades due to their interesting structural complexity, unusual physical, mechanical properties, and futuristic hope of potential applications. One example is quasicrystals, which appear ultimate complexity with lack of periodicity anymore in the usual three-dimensional space. The properties of the quasicrystal change dramatically with lattice complexity and can be tune in metal like as well as semi-conductors like behavior that may be exploited in various applications. In present book chapter, we have discussed the comprehensive different synthesis process of the complex metallic alloys which provide to the readers the most up-to-date information on the synthesis, chosen for their relevance to possible technical applications.

3.1 Introduction

From a very long time, materials were used by various cultures. The anthropologists find the traces of materials on basis of which they define the civilization. An innovative division among the different civilizations was shown by the progressive use of more sophisticated materials. The era of colligation came after the stage of survival when men learnt how to process the natural occurring materials and how to change them into useful form. Historically, the progress and development of societies have been intimately related to materials and its development. With the passes of

T. P. Yadav
Department of Physics, Hydrogen Energy Centre, Institute of Science, Banaras Hindu University, Varanasi, Uttar Pradesh 221005, India
e-mail: thakurp.yadav@bhu.ac.in

K. Awasthi (✉)
Department of Physics, Kashi Naresh Government Post Graduate College, Gyanpur, Bhadohi 221304, India
e-mail: awasthi.k@gmail.com

K. L. Pandey et al. (eds.), *Proceedings of the National Workshop on Recent Advances in Condensed Matter and High Energy Physics*, Springer Proceedings in Physics 278,
https://doi.org/10.1007/978-981-19-2592-4_3

time, new techniques were found out for the processing materials and had the superior properties than naturally occurring materials. The progression in the science provides us the facility to understand the structure–property correlation of the material and introduce a new discipline, and the evolution of many new technologies demands the new type of materials having superior chemical and physical properties. Many new materials were synthesized from the existing materials, reveals different properties (structural, magnetic, electrical, etc.) by means of alloying. Therefore, the microstructure was considered to be a determinative parameter in governing the several properties as electrical, magnetic, and mechanical properties. The availability of the high-resolution technique (electron and field ion microscopy) and advent of the theory of lattice defect (especially dislocation theory) give a remarkable boost in the understanding the mechanism by which ultra-fine microstructures affects the properties of solids. These developments facilitate the basic understanding of the correlation of microstructure and structure sensitive properties of the solid. The nice example is complex metallic alloys (CMA), a family of intermetallic compounds [1]. The concept deals with the phenomena that take place is an essentially metallic medium when the range of the interactions become small, or very small, in comparison to the period of the system, although the system is well ordered [2]. A large number of chemical combinations that may participate to the complexity of the compounds can be synthesized by using the 80 metals present in the periodic table. Such large choices of the metals open the possibility for the discovery of huge number of new ternary, quaternary CMAs [3]. Generally, due to the large number of independent atomic positions in the unit cell, it is considered that the complexity arises due to a difficulty to explain the crystal lattice arrangement. However, lots of CMAs do not need many independent lattice positions to be accounted for. In general, CMAs belong to the family of the intermetallics, are crystalline compounds. CMAs are characterized by the occurrence of well-defined clusters (most often of icosahedral symmetry), large unit cells (containing up to thousands atoms), and some disorder (essentially due to the fact that icosahedra do not fill three-dimensional space). Hence, the quasicrystals also belong with this family of novel complex metallic alloys [4, 5].

3.2 Synthesis of Complex Metallic Alloys

Complex metallic alloys can be made using three processes such as (i) solid phase mixing, (ii) liquid phase mixing, and (iii) gas phase mixing as shown in Fig. 3.1. In solid phase mixing, the mechanical alloying and mechanical milling techniques are most suitable. In liquid phase mixing, several melting processes can be use such as induction melting, arc melting, laser melting; laser cladding, however, in gas phase mixing the technique such as sputter deposition, pulse-laser deposition, atomic layer deposition. The sequential approach for the synthesis of complex metallic alloys has been thoroughly addressed below.

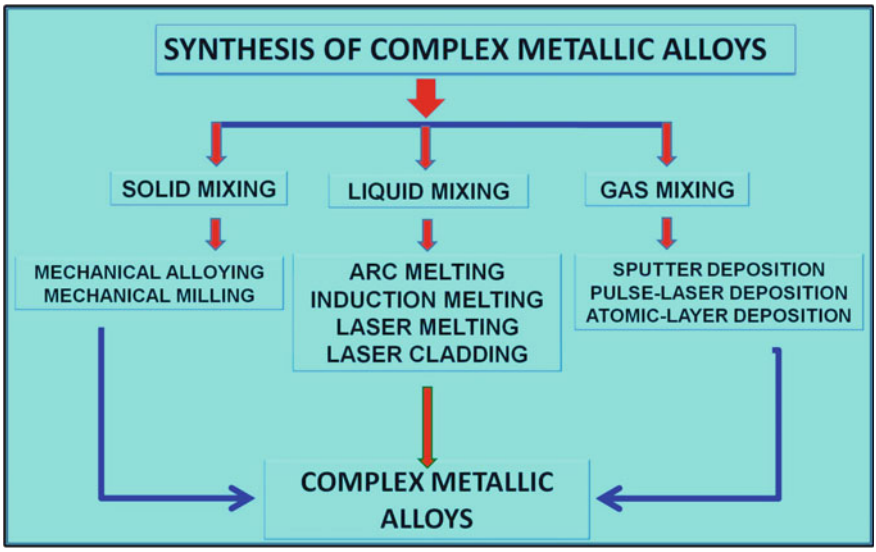

Fig. 3.1 Synthesis processes of complex metallic alloys

3.2.1 Mechanical Milling

Now-a-days, the most popular technique for synthesis of complex metallic alloys/composites in nano order complex metallic alloys is high-energy milling/mechanical milling (MM) [6]. This is a very safe, efficient, and low-cost technique [7]. Mechanical milling (MM)/mechanical alloying (MA) is processed by high-energy ball milling to ensure for homogeneity of materials. In the MM, continuous deformation, facture, and particle welding lead to amorphization or nano crystallization [8]. It is also used for processing route for intermetallic, amorphous materials, and nanocomposites [9]. A single-phase Al_3Ni_2-type nanocrystalline tau3 phases in the Al–Cu–Ni system has been synthesized by MA [10]. At Hydrogen Energy Centre, Banaras Hindu University, we are using planetary ball mill (Retsch PM 400) (Fig. 3.2) for mechanical alloying of the materials with different synthesis parameters.

3.2.1.1 High-Energy Ball Milling: Equipment and Process Variables

In MM, a suitable powder charge (typically, a blend of elemental, or prealloyed powders) is placed in a high-energy mill, along with a suitable milling medium (typically, hardened steel balls). The objective of milling is to reduce the particle size and provide proper mixing or blending of particles. The typical mill used for these purposes has been the tumbler ball mill (or for small charges the jar mill) which is a cylindrical container rotated about its axis in which balls impact upon the powder

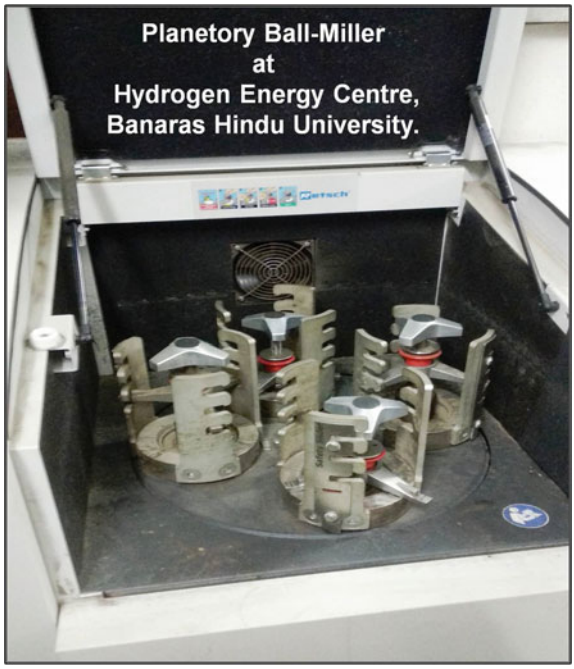

Fig. 3.2 Planetory ball miller (Retsch PM 400) at Hydrogen Energy Centre, Banaras Hindu University

charge. The balls may roll down the surface of the chamber in a series of parallel layers, or they may fall freely and impact the powder and balls beneath them. The tumbler ball mill is illustrated in Fig. 3.3a. The tumbler ball mill is operated closed to the critical speed beyond which the balls are pinned to the inner walls of the mill because of the centrifugal force dominating over centripetal force. For large scale production, tumbler mills are more economical when compared with the attritor and other high-energy ball mills [11]. Another type of mill that has been used for pilot-size production is the vibratory tube mill (Fig. 3.3b). The motion of the balls and particles in a vibratory mill is complicated. The cylindrical container is vibrated, and the impact forces acting on the powders are function of the rate of milling, amplitude of vibration, and mass of the milling medium. High-energy milling forces can be obtained by using high vibrational frequencies and small amplitudes of vibration. The details of the tumbler ball mill, the attritor mill, and the vibratory mill construction and operation are given in details in the review [12]. In addition to these mills, several other mills such as a single large ball in a vibrating frame mill, rod mill, modified rod mill, and other specially designed mills have been used for mechanical milling or alloying [13–20].

While a number of ingenious milling devices were developed early in the century, the one high-energy ball mill that has been adopted by industry was invented by Szegvari [12], in order to quickly attain fine sulfur dispersion for use in vulcanization of rubber. This mill is called an attritor or attrition mill and is illustrated in Fig. 3.4. The attritor has a vertical cylindrical tank, in which the powder and balls

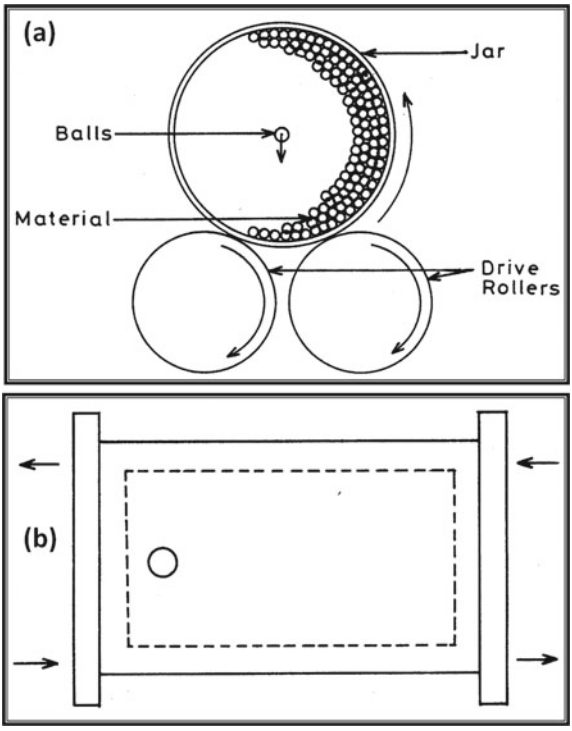

Fig. 3.3 Schematic cross-section of a tumbler (**a**) and vibratory (**b**) ball mills

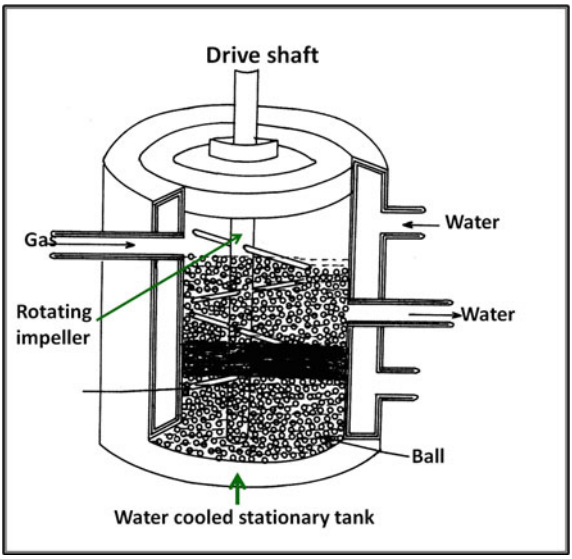

Fig. 3.4 Schematic diagram of an attritor ball mill chamber

are charged. The movement of the balls and powder is achieved by the horizontal impellers attached to a vertical shaft which is made to rotate. Set progressively at right angles to each other, the impellers energize the balls causing the size reduction of powder by impact. Tumbler mills may also be considered high-energy mills if of sufficiently large diameter (of the order of meters) and operated just short of the critical rotational speed at which centrifugal force "pins" the balls to the mill chamber wall. For large scale production of commercial materials, attritor mills have been largely replaced by the large tumbler ball mills [13].

The kinetics of mechanical milling or alloying depends on the energy transferred to the powder from the balls during milling. The energy transfer is governed by many parameters such as the type of mill, the powder supplied to drive the milling chamber, milling speed, size and size distribution of the balls, dry or wet milling, temperature of milling and the duration of milling. Since the kinetic energy of the balls is a function of their mass and velocity, dense materials (steel or tungsten carbide) are preferable to ceramic balls, and the size and size distribution should be optimized for the given mill. Too dense packing of balls reduces the mean free path of the ball motion, while a dilute distribution minimizes the collision frequency. The temperature during milling can depend on the kinetic energy of the ball and the material characteristics of the powder and milling media. The temperature of the powder influences the diffusivity and defect concentration in the powder influencing the phase transformations induced by milling. Higher temperatures are expected to result in phases which need higher atomic mobility (intermetallics) while at lower temperatures the formation of amorphous phases is expected if the energy is sufficient. Low temperature can also enhance the formation of nanocrystalline phases.

3.2.1.2 The Mechanics of Mechanical Milling

The mechanics milling or alloying is characterized by collisions between ball and powder which result in powder fragmentation and coalescence. There are several possible geometries for such collisions. For example, powder may be trapped between two colliding balls or caught between a ball and the wall of the container. In the case of attritor ball mill, powder may be impacted between the grinding media balls and the rotating impellers. On geometrical considerations, it is clear that the greatest numbers of collision events in this system are of the ball-powder-ball type. This kind of impact has been the basis for qualitative descriptions of the mechanical milling or alloying process [21, 22]. On this model, the powder particles (there are many particles involved in a single collision of the kind illustrated) trapped between the colliding balls undergo severe plastic deformation, causing them to flatten and work harden Fig. 3.5. If a surface film is present on the particles and is ruptured, atomically clean surface areas result [13]. Cold welding (coalescence) can result when two such flattened particles overlap so that their clean surface regions contact. In addition, the high strain-rate deformation and cumulative strain accompanying these collisions lead to particle fracture. These competing fracture and coalescence events continue throughout processing. Indeed, a suitable balance between them is required

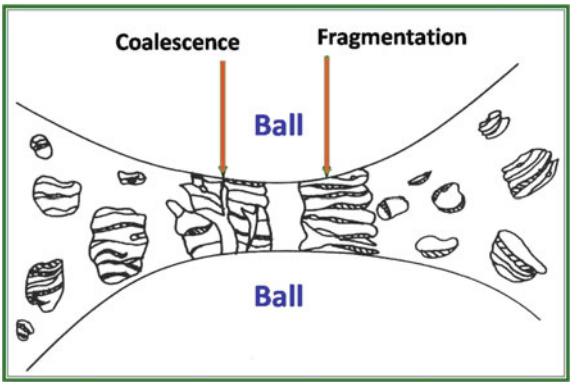

Fig. 3.5 Ball powder collision of powder mixture during mechanical milling

for success with the mechanical milling or alloying process. In most application, the balance is such that an approximate steady-state powder size distribution is obtained. In this stage, the particles are often shaped like flakes, and even through a steady-state powder size are found, continued microstructural refinement occurs as a result of the repetitive fragmentation and coalescence events.

3.2.2 Radio Frequency Induction Melting

It is a well-known synthesis method of alloys. This method frequently used in R and D research labs as well as in industries for melting any pure metal or alloy. For this purpose, various melting techniques such as gas blast, arc melting, and induction melting are used. Induction melting and arc melting methods are frequently used for synthesis of the alloys in small quantity. Generally, arc melting method is suitable for the melting the refractory materials such as molybdenum, tungsten, and niobium. due to the very high-power density of arc. Radio frequency (RF) induction heating is a non-contact method of providing fast, consistent heat for manufacturing applications which involve bonding or changing the properties of metals or other electrically conductive materials. The process involves on induced current within the material to produce heat through induction coil of the furnace. In induction furnace, the maximum electrical energy converts into heat through inductor coil and minimize the losses. Here, eddy current loss is more prominent than hysteresis loss. For induction heating purpose, the eddy currents the only way in which the electrical energy converted into the heat. There are two basic things for induction heating.

3.2.2.1 Historical Developments

In 1831, Michael Faraday demonstrated an experiment in which two coils of wire wound on an iron ring providing the first transformer on record, and the first realization of the phenomenon of "electromagnetic induction." Shortly after 1850, a large number of patents were issued covering high frequency apparatus for the heating of metals. General interest and use at that time was for melting, wherein a metallic crucible was heated by induction, and the heat of the crucible was transmitted the charge by conduction. In 1853, Fizeau added condensers to the interrupter circuits which increased the life of the spark gaps. Following this development, Colby demonstrated that a charge carrying conducting material, which could be made the secondary of the induction heating circuit, heat could be generated directly, therein when using a non-conducting crucible. Just prior to 1900, Tesla presented theoretical calculations in explanations of the use of Hertzian wave for high frequency processes. In the middle of 1980s the Ohio Crankshaft Company, one of the largest manufacturers of diesel engine crankshafts, took advantage of the surface heating effect of high frequencies for crankshaft bearings, developed the Tocco process which was the first high production application of induction heating for surface treating of metals. In spite of its present wide applications, induction heating, with external and internal types are still in not fully mature. Its ultimate utilization for the heat treating and surface hardening of metals, heating for forging and brazing or soldering of similar and dissimilar metals, and for processing of metallic parts for a variety of other reasons challenges the imagination.

3.2.2.2 Principles of Induction Heating

An induction heating circuit is fundamentally a transformer, wherein the inductor carrying the alternating current is a primary, and the substance to be heated is made the secondary by merely placing it within the confines of the loop formed by the inductor, there being no contact or connection between the two. The photograph showing R.F. induction furnace (12 kW) was used to synthesize novel CMA materials and is given in Fig. 3.6. The current flowing through the inductor sets up magnetic lines of force in a circular pattern which thread through the surface of the material being heated and induce a flow of energy therein. If a magnetic material is involved, it may be assumed to be made up of many small particles of iron which tend to become polarized with a North and South Pole lined up with the polarity of the field produced within the inductor by the flow of current. The polarity of this field changes many times per second with the alternation of the current necessary for high frequency heating. The tendency for these small magnets to realign themselves with the changing field polarity is resisted by the metal and internal molecular friction is developed which dissipates itself in the form of heat. Hence, this heating effect also takes place due to "*hysteresis*." A further source of heat is that resulting from the eddy currents which are produced in the area affected because of the intensity of the induced current much the same as the eddy swirls set up along the bank of a rapidly moving stream

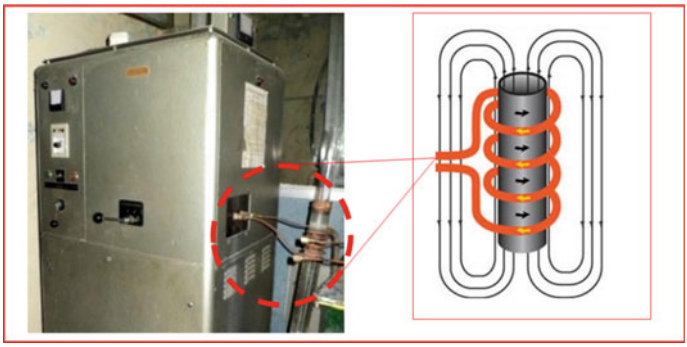

Fig. 3.6 Optical picture of 18 kW with 100 MHz RF induction furnace employed for melting of hydrogen storage materials

of water. The relationship of the amount of heat generated by these two phenomena is dependent upon both frequency and flux density, with hysteresis losses being of lesser significance. It can also be concluded that the role played by hysteresis in induction heating is of negligible importance. Since the substance which carried the current is acting as a conductor, it also has an electrical substance to this flow of energy. Then, we may compare induction heating to ordinary resistance heating and establish it likewise as that heat which is liberated as a result of I^2R losses. There is a flow of current (I) and a resistance to this current flow (R), both of which are responsible for the generation of heat. The magnetic lines of force which induce the flow of energy are more concentrated at the midpoint of the width of the inductor and near its inside face.

3.2.2.3 Induction Heating Circuits and Frequency Generation

The basic idea of inductive heating dates back to 1884 when Oliver Heaviside published a paper dealing with the theory. In 1906, Schneider proposed an induction furnace comprising a crucible surrounded by an inductor coil energized direct from an AC generator operating at high frequencies. In 1919, Northrup published a paper on principles of inductive heating with high frequency currents in which the electrical problems are discussed from a mathematical standpoint and practical information is given pertaining to coil and furnace design. Further, developments of designing induction heating furnace were carried out over number of years' span.

Induction heating practice hinges on the art of converting the customary forms of power into high frequency power on an industrial scale with reasonable efficiency. The basic elements of the circuit are capacitors for storing electrical energy electrostatically and inductors for storing it electromagnetically. The energy so stored can be caused to surge to and fro between capacitor and inductor and produce high frequency magnetic and electrostatic fields of sufficient intensity to produce very useful heating effects.

There are two basic types of induction heating circuit, namely the parallel resonant and the series resonant.

In each case, the frequency is determined primarily by the inductance 'L' and the capacitance 'C' and may be calculated from the formula

$$\omega^2 = \frac{1}{LC}$$

where

$\omega = 2\pi x$	frequency in cycles per second.
L	Inductance in Henries.
C	Capacitance in Farads.

In the parallel-resonant circuit, the current through the inductor coil and capacitor at resonance is determined by the "effective resistance", other things being the same. This is the sum of the high frequency resistance of the actual conductors plus an apparent resistance due to the transfer of power from the coil to the charge. In the low-resistance parallel-resonance circuit, the capacitor coil current may be many times that flowing in the external circuit to the generator. In the series-resonant circuit, on the other hand, the current is the same in all parts of the circuit and is again limited by the effective resistance. With low resistance, large currents may flow and the capacitor and coil voltages may be times that of the generator.

3.2.2.4 Vacuum-Tube Oscillation Generators

Another class of high frequency generators which replaced the spark-gap oscillator and vacuum-tube oscillators. This is a device function like a valve which may be electrically controlled to allow intermittent flow of electrons through the tube from filament to anode and thus provide the timed power impulses which maintain the high frequency oscillatory currents in the resonant part of the circuit. The filament heated to a suitable temperature by the passage of current supplied the electrons whose flow toward the anode is controlled by varying the potential of the grid with reference to that of the filament.

3.2.2.5 Comparison Between Induction Heating with Other Methods of Heating

High frequency induction heating has been used for heat treating steel for a number of years. However, that high frequency induction current is a source of energy capable of heating steel or other metals to a desired temperature. They are in the same category as a flame, a furnace or other sources of heat energy which are used for heat treating. The essential difference between induction heating and the other types of heating is the fact that the heat is generated under the surface of the piece subjected to the

high frequency magnetic flux. In all other types of heating, one has to depend on conduction to carry the heat from the surface skin into the piece being heated. This peculiarity makes induction heating extremely fast. It is also a fact that this high frequency magnetic flux will concentrate on the outside of the conductor or piece being heated; thus, the induction heating is very much applicable to surface hardening of metals.

3.2.3 Melt-Spinning Techniques

The widely used technique for rapid solidification of the metals/alloys in the form of ribbon or wire is melt-spinning technique (Fig. 3.7). In this technique, molten metal's or metallic alloys are squirted on to a fast rotating conducting metallic (copper) wheel which cools the molten material very fast. The main objective of the rapid solidification is to get round of the limitations associated with conventional solidification processing. The cooling rate associated with this technique is very fast as 105–106 K/s with rapid solidification process. Such a high cooling rate is desired in order to prevent nucleation of the high-temperature equilibrium phases. For requires such a high cooling rate through the specimen, it is desirable that at least in the one direction the dimension should have to very small. Thus, the synthesized alloys through this method are generally in the form of ribbons. So, we can use this technique for synthesis of alloys for various applications such as high-temperature materials, catalytic and storage materials, high-strength structural materials, corrosion resistant, magnetic and electrical materials, and metallic glasses. The alloy which is subjected to rapid solidification is kept inside a quartz nozzle tube of 14 mm diameter having an orifice of ~1 mm and is melted by RF induction furnace. By using the continuous pressure of argon, this molten alloy is ejected onto a fast-rotating copper wheel of

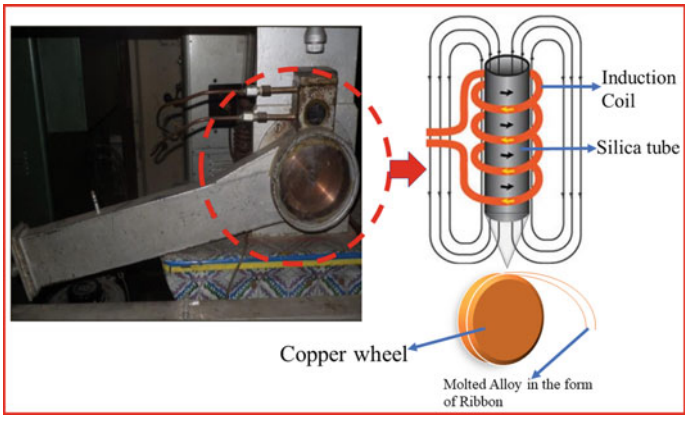

Fig. 3.7 Schematic picture of melt-spinning apparatus

the diameter of 14 cm. Chamber was fully evacuated before the induction melting of the alloy and then filled with high purity argon gas to avoid the contaminations and oxidation. The obtained ribbons are 2–4 mm wide with thickness of 30–40 and several centimeters long.

The ribbon dimensions such as thickness, widths, and the cooling rate are affected by the certain factors. These factors are given out as follows:

- Diameter of the orifice of the nozzle.
- Smoothness of the surface, thermal conductivity, and temperature of the wheel: An increase in the wheel temperature causes the change in the morphology and increase in the average thickness of the ribbons.
- The striking angle of the melt jet with the wheel.
- Rotating speed of the wheel: with increasing in the wheel speeds the average thickness of the ribbons decreases.
- The pressure of the gas is used to push the molten alloy onto the nozzle.

The above parameters are needed to be optimized to synthesize a good quality CMA ribbon.

3.2.4 Arc Melting Method

In the system of vacuum arc melting furnace sample heated by an electric arc which also known as tungsten inert gas (TIG) unit struck between material present in the crucible in the copper hearth. The chamber of the vacuum arc is evacuated, then it filled by non-reactive inert gases like argon gas so we can say that all steps performed in arc furnace in presence of argon atmosphere in this chamber repeated melting also performed for improving the homogeneity of the sample alloy material. The picture of arc melting system has been shown in Fig. 3.8.

3.2.5 Plasma Sputtering Method

Vapor state base-contented CMA synthesis processes are quite popular. Plasma nitriding and magnetron sputtering are two methods for processing CMA in the vapor state route. Sputtering technique uses for deposited the thin film on to the substrate by target under the bombard charged ions. We use for the produced thin film for CMA to get improve wear resistance, facture, oxidation resistance, and also for corrosion resistance. DC sputter technique requires a high voltage approx. 10^{12} V for sputter deposition magnetron sputtering also used for coating technique of CMA.

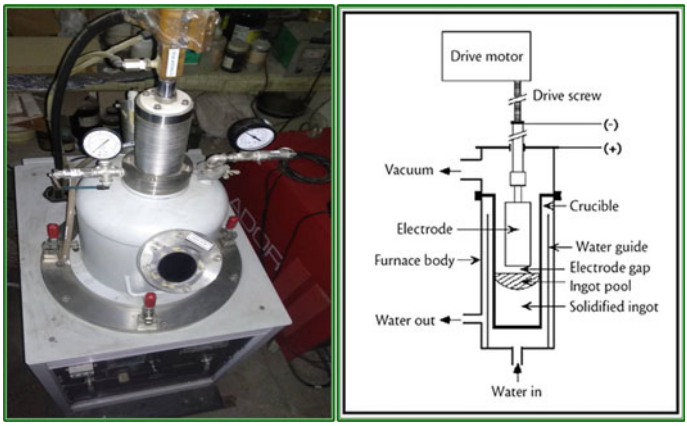

Fig. 3.8 Optical image and a schematic diagram of the arc melting method

3.3 Conclusion

Since several research articles have discussed about different type of CMA and their properties, therefore, the present article focuses on the synthesis processes of CMA. It was suggested that a non-equilibrium processing technique such as mechanical milling, melt spinning with controlled parameters could be used for the synthesis of CMA materials, CMA-nano-composite materials. Mechanical milling can induce defects and activate the frozen state of nanomaterials configuration and lead to the formation of a stable or metastable CMA composition.

Acknowledgements The authors gratefully acknowledge the discussion with all their collaborators, who have immensely contributed to the collaborative research work, a part of which has been discussed in this chapter. TPY would like to record his deep sense of gratitude to Prof. N. K. Mukhopadhyay who introduced and inspired him in this fascinating area of Physics of Metals and Materials, and to thank Prof. R. S. Tiwari and Prof M. A. Shaz for their encouragements and discussion. Authors would like to thank Prof R. K. Mandal and Prof B. S. Murty for many collaborative work and stimulating discussions. TPY would like to dedicate this book chapter to the memory of his beloved and respected Father the late Palloo Yadav, who succumbed prematurely to the dictum of dreadful illness during the writing of this book chapter. KA greatly acknowledge the financial support from Higher Education Department, Uttar Pradesh.

References

1. K. Urban, M. Feuerbacher, Structurally complex alloy phases. J. Non Cryst. Solids **143**, 334–335 (2004)
2. J.-M. Dubois, An introduction to complex metallic alloys and to the CMA network of excellence, in *Book Series on Complex Metallic Alloys: Basics of Thermodynamics and Phase Transitions in Complex Intermetallics* (2008), pp. 1–29

3. D.K. Rai, T.P. Yadav, V.S. Subrahmanyam, O.N. Srivastava, Structural and Mössbauer spectroscopic investigation of Fe substituted Ti–Ni shape memory alloys. J. Alloy Compd. **482**, 28–32 (2009)
4. T.P. Yadav, R.S. Tiwari, O.N. Srivastava, Effect of Cu substitution in Al–Co–Ni decagonal quasicrystals. J. Non-Cryst. Solids **334–335**, 39–43 (2004)
5. T.P. Yadav, S.S. Mishra, O.N. Srivastava, Copper nanocubes on $Al_{65}Cu_{20}Fe_{15}$ quasicrystalline surface. J. Alloy Compd. **712**, 134–138 (2017)
6. T.P. Yadav, R.M. Yadav, D.P. Singh, Mechanical milling: a top down approach for the synthesis of nanomaterials and nanocomposites. Nanosci. Nanotechnol. **2**, 22–48 (2012)
7. T.P. Yadav, N.K. Mukhopadhyay, M.A. Shaz, R.S. Tiwari, O.N. Srivastava, Phase transformation in $Al_{70}Ni_{24}Fe_6$ decagonal system during high energy ball milling. Phil. Mag. **86**(3–5), 397–404 (2006)
8. T.P. Yadav, N.K. Mukhopadhyay, R.S. Tiwari, O.N. Srivastava, Characterization of mechanically milled $Al_{65}Cu_{20}Fe_{15}$ icosahedral quasicrystalline alloy. Trans. Indian Inst. Met. **56**(6), 577–581 (2003)
9. T.P. Yadav, N.K. Mukhopadhyay, R.S. Tiwari, O.N. Srivastava, Studies on the formation and stability of nanocrystalline $Al_{50}Cu_{28}Fe_{22}$ alloy synthesized through high energy ball milling. Mater. Sci. Eng. A **393**(1–2), 366–373 (2005)
10. T.P. Yadav, N.K. Mukhopadhyay, R.S. Tiwari, O.N. Srivastava, Formation of Al_3Ni_2-type nanocrystalline T3 phases in the Al–Cu–Ni system by mechanical alloying. Philos. Mag. Lett. **87**(10), 781–789 (2007)
11. B.S. Murty, S. Ranganathan, Novel materials synthesis by mechanical alloying/milling. Int. Mater. Rev. **43**, 101–141 (1998)
12. C. Suryanarayana, Mechanical alloying and milling. Prog. Mater. Sci. **46**, 1–184 (2001)
13. C. Suryanarayana, Powder metal technologies and applications, in *ASM Handbook*, vol. 7 (ASM International, Materials Park, OH, 1998), pp. 80–90
14. C. Suryanarayana, *Bibliography on Mechanical Alloying and Milling* (Cambridge Interscience Publications, Cambridge UK, 1995)
15. J.S. Benjamin, T.E. Volin, The mechanism of mechanical alloying. Metall. Trans. **5**, 1929–1934 (1974)
16. J.S. Benjamin, Mechanical alloying. Sci. Am. **234**(5), 40–48 (1976)
17. T.P. Yadav, D. Singh, N.K. Mukhopadhayay, O.N. Srivastava, Synthesis and mechanical behavior of mechanically activated carbon-quasicrystal composite (2011) (Unpublished)
18. P.S. Gilman, J.S. Benjamin, Mechanical alloying. Annu. Rev. Mater. Sci. **13**, 279–300 (1983)
19. L. Schultz, Formation of amorphous metals by mechanical alloying. Mater. Sci. Eng. **97**, 15–23 (1988)
20. C.C. Koch, Materials synthesis by mechanical alloying. Annu. Rev. Mater. Sci. **19**, 121–143 (1989)
21. C.C. Koch, J.D. Whittenberge, Mechanical milling/alloying of intermetallics. Intermetallics **4**, 339–355 (1996)
22. R.S. Tiwari, T.P. Yadav, N.K. Mukhopadhyay, O.N. Srivastava, Nanocrystallization and structural correlation in quasicrystalline and crystalline phases during mechanical milling. Zeitschrift fur Kristallographie **224**(1–2), 26–30 (2009)

Chapter 4
A TiO_2-Based Gas Sensor for Liquefied Petroleum Gas

Ankit Kumar Vishwakarma, Ajaya Kumar Sharma, and Lallan Yadava

Abstract In this work, we reported TiO_2 and CdS-TiO_2 films for gas sensing properties such as the response of the sensor, response/recovery time, and sensing mechanism for liquefied petroleum gas (LPG) at room temperature. The samples TiO_2 and CdS-TiO_2 were fabricated on an alumina substrate with a finger electrode pattern. The response of the fabricated sensor was measured with exposure to LPG of varied concentrations (0–5000 ppm) in ambient air. It was found that an optimized CdS-TiO_2 extends the highest response, i.e., 42% for 5000 ppm LPG, which is 1.57 times more than the TiO_2 film. The response and recovery times were improved from 110 to 85 s and 210 to 180 s, respectively, for LPG (5000 ppm). The experimental results of fabricated sensors are verified, and it is in good agreement with the earlier reported paper.

4.1 Introduction

In the gas sensor field, semiconductor technology has been a major subject of intensive research and continuous development occurred during the last few decades. But due to the complexity and high cost of functioning these instruments, interest has been developed to produce simple low-cost gas sensing elements using microelectronic technologies [1–5]. Today, the world is still facing various problems such as environmental pollution, analysis of food and drug for health safety, detecting and tracing of explosive materials in military applications. Thus, for controlling and monitoring these, demand is still growing for small and IC compatible sensors using microelectronic technology with fast response (data accessing) and low price. Liquefied petroleum gas (LPG) is highly inflammable and yet, widely used in domestic purposes, automobiles, and industrial requirements. Accidental explosions due to leakage of LPG have been increased, which urgently demands the development

A. K. Vishwakarma · A. K. Sharma · L. Yadava (✉)
Thin Film Laboratory, Department of Physics, Deen Dayal Upadhyaya Gorakhpur University, Gorakhpur, Uttar Pradesh 273009, India
e-mail: ncfm16@gmail.com

K. L. Pandey et al. (eds.), *Proceedings of the National Workshop on Recent Advances in Condensed Matter and High Energy Physics*, Springer Proceedings in Physics 278,
https://doi.org/10.1007/978-981-19-2592-4_4

of a reliable sensor having utmost sensitivity to monitor such major leakages for preventing fatal accidents. Several works have been done to fabricate a suitable LPG detector based on tin oxide material [6–9]. Srivastava et al. [10] reported the sensing mechanism of Pd-doped SnO_2 sensor for LPG detection, and they found that 1 wt% Pd-SnO_2 sensor showed maximum sensitivity of 72% for LPG (5000 ppm). Yadava et al. [11] investigated sensing properties of CdS-doped SnO_2 thick film gas sensor for methanol, LPG, and acetone detection. They observed that the CdS-doped SnO_2 sensor is highly sensitive more selectivity and fast response/recovery time for methanol gas. In this article, we report the sensing properties of TiO_2 and CdS-TiO_2 samples for LPG. The maximum response reaches 42% for LPG of 5000 ppm at room temperature, which is higher than reported earlier [11].

4.2 Experimental Setup

We fabricated two sensors undoped TiO_2 and CdS-TiO_2 films on an alumina substrate with a finger electrode pattern on the front side and a resistor heater pattern on the backside. The finger electrode pattern was printed using a silver conductor paste (paste FD6176) on the front side and a heater electrode pattern using a ruthenium oxide-based resistor paste (paste NTC 2413 ESL) on the backside of the substrate. The resistance of the fabricated sensors in the air and gas environment is measured with the help of a dual DC power supply (LD-3202) and digital multimeter (Aplab 107N) as shown in Fig. 4.1.

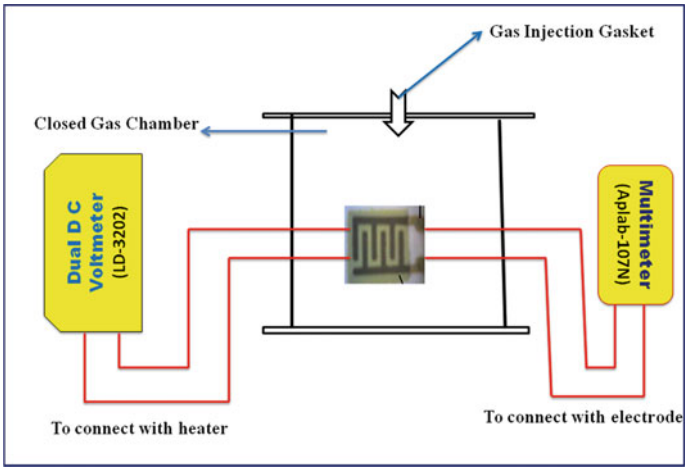

Fig. 4.1 Block diagram of the measurement setup

4.3 Results and Discussion

4.3.1 Sensing Response

The change in electrical resistance in the sample on exposure to an LPG is defined as a response as follows:

$$R = \frac{R_a - R_g}{R_a} \times 100$$

where R_a = resistance in air and R_g = resistance in the presence of target gas [12, 13]. The resistance of the fabricated sensors in the air and gas environment is measured with the help of a dual DC power supply (LD-3202) and digital multimeter (Aplab 107N).

The maximum response of the sensor TiO_2 and CdS-TiO_2 obtained for LPG is given in Table 4.1. The response values for LPG are 27% and 42% for sensors TiO_2 and CdS-TiO_2, respectively, which are shown in bar diagram in Fig. 4.2. We observed from Fig. 4.2 that, the response of LPG for CdS-TiO_2 is 1.57 times the TiO_2 sensor.

Table 4.1 Sensing response and transient time for LPG (5000 ppm)

Sample	Response (%)	Response time (s)	Recovery time (s)
TiO_2	27	110	210
CdS-TiO_2	42	85	180

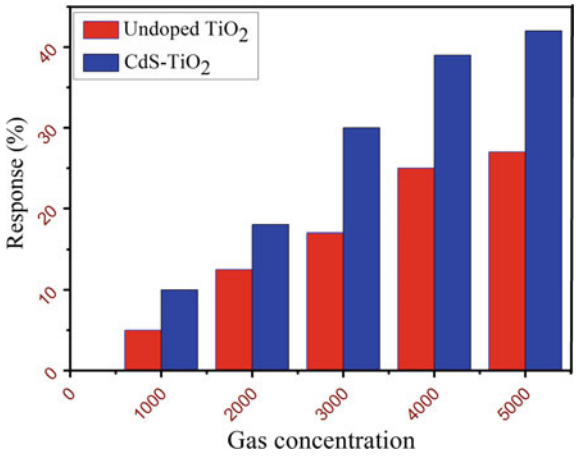

Fig. 4.2 The response of LPG gas for the undoped and CdS-TiO_2 sensor

4.3.2 *Transient Response and Mechanism*

The time required for the gas response to reach 90% of the final equilibrium value after a test gas was injected, and recovery time was the time recorded for the gas response to decrease by 90% its maximum value when the gas sensor was exposed in ambient air. Figure 4.3 shows that in sensor CdS-TiO_2 the response time and recovery time reduce from 110 to 85 s and 210 to 180 s, respectively, for LPG (5000 ppm) at room temperature (Table 4.1).

We plot log (C) with log (R) for the varying concentration of the LPG (0–5000 ppm) which is shown in Fig. 4.4. It is clear from Fig. 4.4, sensor exhibits a linearly logarithmic response ($R^2 = 0.98$ with $Y = 1.07X - 2.49$) and ($R^2 = 0.98$ with $Y = 0.94X - 1.82$) with LPG concentration for TiO_2 and CdS-TiO_2, respectively. The variation of log (C) with log (R) produces a straight line. Thus, the experimental data are in good agreement with the model proposed by the earlier worker [14, 15].

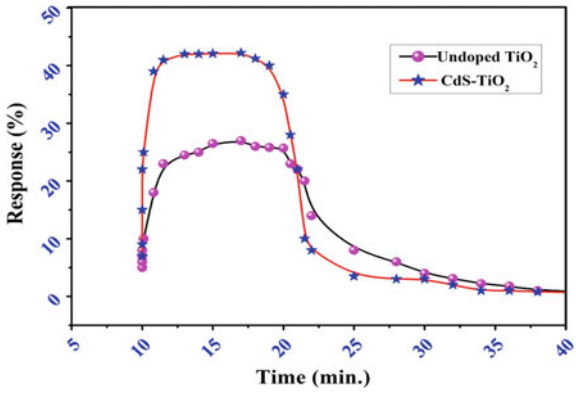

Fig. 4.3 Response and recovery time for undoped and CdS-TiO_2 sensor for LPG (5000 ppm)

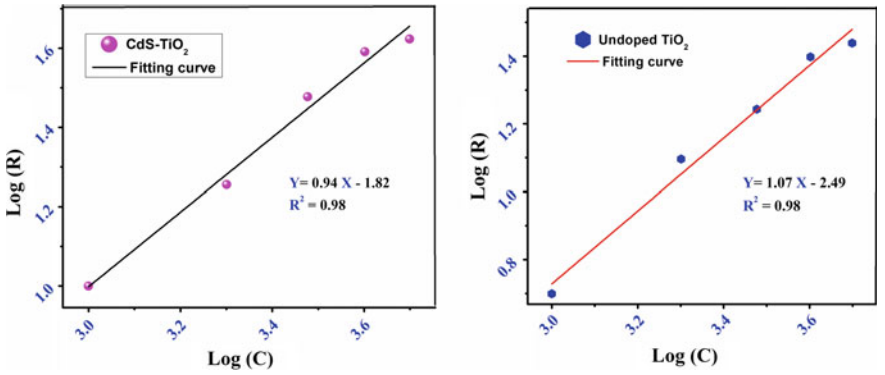

Fig. 4.4 Plot log (C) versus log (R) of the LPG (0–5000 ppm) for TiO_2 and CdS-TiO_2 sensor

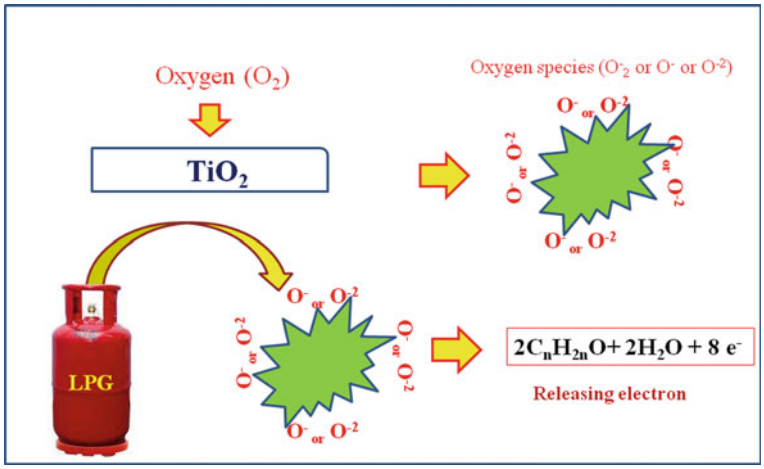

Fig. 4.5 The proposed reaction model of the sensing mechanism for ethanol

The response behavior of the fabricated sensor to exposed LPG gas can be explained based on adsorbing oxygen species. It is observed that LPG suffers extreme oxidation with chemisorbed ionic O_2 species and, thereby, supplies electrons to the conduction band. A possible model is shown in Fig. 4.5. The highest response of the sensor CdS-TiO_2 for LPG may be due to more free electrons being released when exposed to LPG gas.

4.4 Conclusions

Undoped and CdS-TiO_2 sensors have been fabricated and characterized for sensing LPG gas. The sensing properties show that the maximum response of LPG is found to be 27% and 42% for TiO_2 and CdS-TiO_2 films at 5000 ppm, respectively. Also, we observed the response and recovery time and are 85 s and 180 s for CdS-TiO_2. Our experimental results of fabricated sensors were verified, and it is in good agreement with the earlier reported paper.

Acknowledgements We are thankful to HoD of Physics, D D U Gorakhpur University, Gorakhpur Uttar Pradesh, to give me experimental measurement facilities.

References

1. M. Prudeziati, B. Morten, Thick-film sensors: an overview. Sens. Actuators **10**, 65–82 (1986)
2. R. Srivastava, R. Dwivedi, S.K. Srivastava, Development of high sensitivity tin oxide-based sensors for gas/odor detection at room temperature. Sens. Actuators B Chem. **50**, 175–180 (1998)
3. A.K. Vishwakarma, A.K. Sharma, N.K. Yadav, L. Yadav, Development of CdS-doped TiO_2 nanocomposite as acetone gas sensor. Vacuum **191**, 110363 (2021)
4. A.K. Vishwakarma, N.K. Yadav, L. Yadav, Detection of toluene gas using CdS-TiO_2 thin film gas sensor. Sens. Lett. **17**, 803–806 (2019)
5. A.K. Sharma, A.K. Vishwakarma, L. Yadava, Sensing and structural characteristics of TiO_2 thick film for LPG sensor. Mater. Today Proc. **38**(5), 2123–2126 (2021)
6. Z. Tianshu, P. Hing, Y. Li, Z. Jiancheng, Selective detection of ethanol vapor and hydrogen using Cd-doped SnO_2-based sensors. Sens. Actuators B **60**, 208–215 (1999)
7. K. Jain, R.P. Pant, S.T. Lakshmikumar, Effect of Ni doping on thick film SnO_2 gas sensor. Sens. Actuators B **113**, 823–829 (2006)
8. L.D. Feng, X.J. Huang, Y.K. Choi, Dynamic determination of domestic liquefied petroleum gas down to several ppm levels using a Sr-doped SnO_2 thick film gas sensor. Microchim. Acta **156**, 245–251 (2006)
9. T.D. Senguttwan, R. Rai, S.T. Laxmikumar, Gas sensing properties of lead doped tin oxide thick films. Mater. Lett. **61**, 582–584 (2007)
10. J.K. Srivastava, P. Pandey, V.N. Mishra, R. Dwivedi, Sensing mechanism of Pd-doped SnO_2 sensor for LPG detection. Solid State Sci. **11**, 1602–1605 (2009)
11. L. Yadava, R. Verma, R. Dwivedi, Sensing properties of CdS-doped tin oxide thick film sensor. Sens. Actuators B Chem. **144**, 37–47 (2010)
12. A.K. Vishwakarma, L. Yadava, Detection of propanol gas using titanium dioxide-based thick film. IOP Conf. Ser. Mater. Sci. Eng. **404**, 012020 (2018)
13. P. Yadav, A.K. Sharma, S.K. Yadav, A.K. Vishwakarma, L. Yadava, Sensing response of toluene gas and structural properties of CdS-SnO_2 thick films sensor. Mater. Today Proc. **38**(5), 2792–2796 (2021)
14. A.K. Vishwakarma, L. Yadava, Structural and sensing properties of ethanol gas using Pd-doped SnO_2 thick film gas sensor. Environ. Sci. Pollut. Res. **28**(4), 3920–3927 (2021)
15. A.K. Vishwakarma, A.K. Sharma, L. Yadava, Theoretical modeling of Pd-SnO_2 based ethanol gas sensor. J. Phys. Conf. Ser. **1921**, 012118 (2021)

Chapter 5
A Study of the Solar Cycle 21–24 and the Starting Phase of Solar Cycle 25

Smriti Srivastava, Sai Kumar Chirra, and Ashok Kumar Pathak

Abstract The manuscript deals with the study related to the last four solar cycles 21–24 along with the starting phase of solar cycle 25 based on online available astronomical data. Data related to solar cycles 21–24 (1976–2020) have been analyzed. And we could infer how the solar activities are affected with average sunspot counts. The results based on 27-day-averaged data of three parameters—10.7 cm solar flux, sunspot number, and solar wind proton density—are reported to observe their dependence on each other and how they varied during the starting phase of solar cycle 25. The data for the daily total sunspot number for the 1st day of 2020 to 223rd day of 2020 have also been analyzed and reported. On the basis of our analysis, we observe that the variation in number of sunspots leads to the quasi-periodicity and the difference in the strength of the solar cycle.

5.1 Introduction

Thermonuclear processes occur in the core of the Sun which results in the very hot temperature of the Sun's atmosphere because of which, our Star acts as a dynamo ejecting out the solar wind, magnetic charged particles, and plasma that travels throughout the interplanetary medium. The release of charged particles and plasma is responsible for the occurrence of prominences, solar flares, coronal mass ejections (CME), and geomagnetic storms, which may or may not have a hazardous impact on the Earth depending upon the intensity of solar event. The interaction of the Solar Energetic Particles (SEP) with the Earth's magnetosphere is responsible for space weather events such as geomagnetic storms [1].

Solar flares are sudden brightening of the Sun's photosphere, observed in close proximity to the sunspot group, erupt from the active regions of the Sun where the magnetic field is much stronger and classified as A, C, B, M, and X according to its peak flux in W/m^2 of X-rays. The reconfiguration and reconnection of the

S. Srivastava · S. K. Chirra (✉) · A. K. Pathak
Ewing Christian College, University of Allahabad, Prayagraj, India
e-mail: chskis4u@gmail.com

K. L. Pandey et al. (eds.), *Proceedings of the National Workshop on Recent Advances in Condensed Matter and High Energy Physics*, Springer Proceedings in Physics 278,
https://doi.org/10.1007/978-981-19-2592-4_5

magnetic field lie in the active regions of the solar interior results in heating the Sun's atmosphere locally and the acceleration of the charged particles to high speeds [2]. A coronal mass ejection is considered as an important form of solar activity that relates the changes observed in the coronal structure in a time interval from a few minutes to several hours [3]. A plausible important cause behind the generation of CME is magnetic reconnection. When two oppositely charged magnetic fields come together, rearrangement takes place and immediately after this rearrangement, the energy stored in the oppositely directed magnetic field lines is released. This sudden release of energy assumed responsible for solar flares drives the CME [4].

The energetic particles ejected out from the Sun driven by the magnetized, dynamic nature of the Sun, and variability in the number of sunspots. Sunspots are the darkened, magnetically active patches on the solar surface that acts as an origin for the coronal mass ejection and solar flares [5]. Sunspots vary in number, intensity, and the covered surface area. They emerge at mid-latitudes (approximately 35°) at the beginning of a cycle and move closer to the equator as the cycle progresses. This behavior of the Sun is termed as the Sporer Law of Zones [6].

The occurrence of sunspots varies with the 11-year periodicity, leading to the sunspot cycle. The cycle starts with the solar minimum period, that is, when the number of sunspots is very low. The cycle continues with sunspots reaching its peak termed as the solar maximum. Few years, after the solar maximum period is reached, sunspots again start to decline and the Sun becomes quiet [7].

The month of April of 2014 occurred as a maximum count month for the number of sunspots during the solar cycle 24, which commenced during the December of 2008, with minimal activity of the Sun and ended in the late 2019, witnessing the Sun to enter in its silent mode, announcing our Star to enter the solar cycle 25, and is expected to increase in its activity around 2025 with the sharp rise in the number of sunspots. The numbering of the solar cycle by Rudolf Wolf in 1843 has eased the tracking of the periodicity of solar activities. From 1755 to 2019, we had seen 24 solar cycles and have entered into the 25th solar cycle, in the end of 2019, as predicted by the Sun's activity [8]. The plot in Fig. 5.1 shows the maximum and the minimum sunspot counts from solar cycle 1–24. The plot in Fig. 5.2 shows the start and the end dates from SC 21 to SC 25. According to various predictions and researches, the SC 25 is expected to end by 2030.

The present paper aims at studying the solar cycles (SC) from SC 21 to the rising phase of solar cycle 25. The data for the total number of sunspots from 1976 to 2020, total number of CMEs from 1996 to 2020, 27-day-averaged of solar parameters, and the daily total sunspot number during the year 2020 are presented and plotted. The focus is on the analysis of data of sunspots, CMEs, and 27-day-averaged of solar activity parameters.

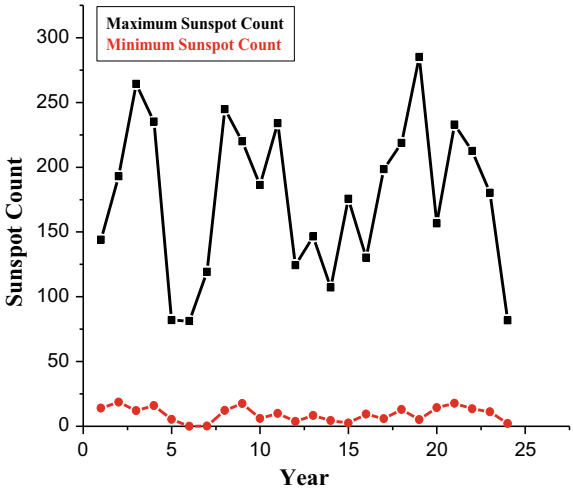

Fig. 5.1 Maximum and minimum sunspot count from solar cycle 1–24

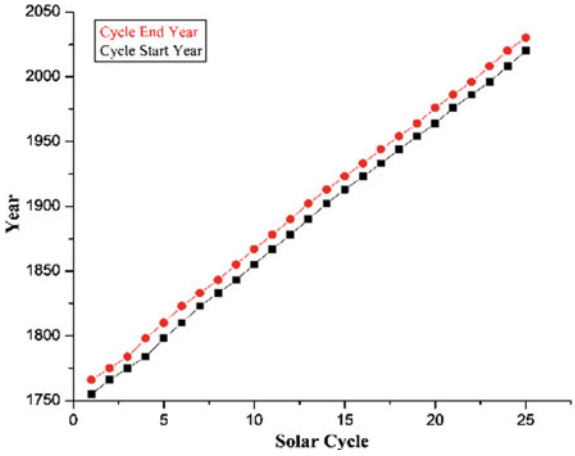

Fig. 5.2 The start and end dates for solar cycle 1–25

5.2 Observations and Data Analysis

Solar cycles from the year 1976–2019 are of great importance and crucial interest, which leads to the broad band of researches. In this section of the paper, the data for the total yearly average sunspot number (SSN) from the year 1976–2020 (solar cycle 21 to solar cycle 24) and the number of coronal mass ejections (N_{CME}) for the year 1996–2020 (solar cycle 23 to solar cycle 24) are plotted and analyzed. The plots related to these analyzes are shown in Figs. 5.3 and 5.4. The data for the sunspot number have been collected from the new version of the sunspot number data upgraded on July 1st, 2015, from version 1.0 to version 2.0, of the Sunspot Index and Long-term Solar Observations (SILSO), World Data Center (WDC), Royal University of Belgium,

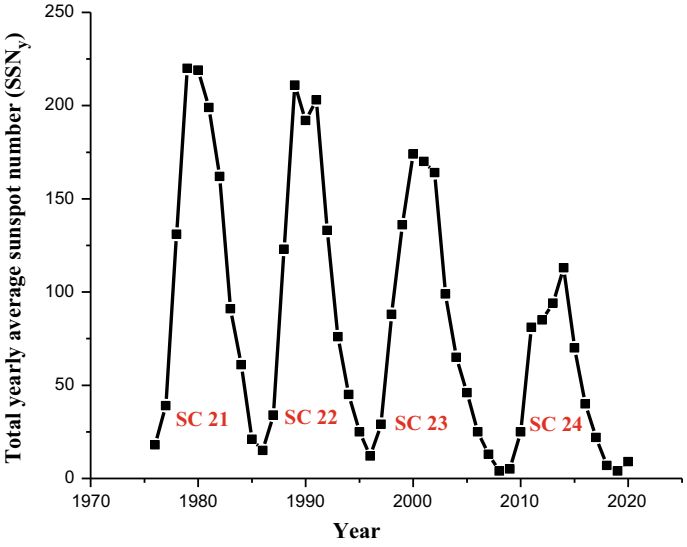

Fig. 5.3 Total yearly average sunspot counts from 1976 to 2020

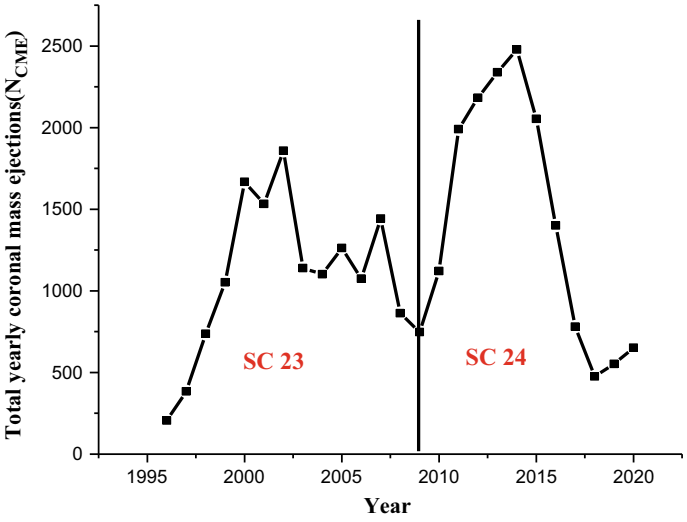

Fig. 5.4 Total yearly coronal mass ejections from 1996 to 2020

Brussels (https://wwwbis.sidc.be/silso/datafiles). The data for the number of coronal mass ejections (CME) are acknowledged to the CME catalog (https://cdaw.gsfc.nasa.gov/CME_list/), which contains monthly information about the number of CMEs, their position angle, halo CMEs, kinetic energy, and other details, identified since 1996 from Large Angle and Spectrometric Coronagraph (LASCO) on-board Solar

and Heliospheric Observatory (SOHO). Also, the catalog contains data gaps (search for the data gap) of 3 h or more, making it difficult to know about the existence of CMEs during that period. The catalog is generated and maintained at the CDAW Data Center by NASA and The Catholic University of America in cooperation with the Naval Research Laboratory. SOHO is an international cooperation between ESA and NASA. The monthly information about the number of CME of all the months of a particular year is collected and summed to get the total number of CME events during a year.

As can be seen from the graph in Fig. 5.3, the yearly average number of sunspots was very low during the year 1976, which marked the beginning of the solar cycle 21 with the minimal activity of the Sun.

The total yearly average sunspot counts (SSN_y) of 18.4 in the year 1976 geared up to 220 in the year 1979, announcing it as a solar maximum. After the year 1979, there occurred a continuous downfall in sunspots till the year 1986. The cycle ended in the year 1986 with a sunspot count of 15. The 7th day of November of 1978, prior to the solar maxima, recorded a solar flare with the X-ray class of X15.0 because of which occurred the large geomagnetic storm on 24th to 25th November of 1978 [9].

The year 1987 witnessed an increase in the number of total yearly average sunspots, giving evidence to the occurrence of solar cycle 22. The 21/22 minimum had 15 sunspots in 1986 and the sunspot number rose to 211 in 1989 with a downfall to 192 in 1990, but again increased to 203 in 1991. This was different from the total yearly sunspot number data of 1976–1986 where sunspots continuously showed a decrease in value after the solar maxima. Three flares with the X-ray class of X20.0, X15.0, and X13 occurred during 1989 and five flares on the 1st, 4th, 6th, 11th, and 15th day of the month of June of 1991, thus contributing to eight flares during the year. The X15.0 class solar flare on March 6, 1989, was followed by the CME on March 9, 1989 as a consequence of which there occurred a geomagnetic storm on March 13, 1989 at 2:44 A.M. EST, and the storm was powerful enough to cause electric disruptions in Quebec [10].

The trend of decrease and increase of sunspot number continued and came up with the ending phase of the solar cycle 22 to the starting phase of solar cycle 23. The minimum of sunspots occurred in 1996 with a total yearly sunspot number of 12, further increasing during 1997 and the maxima of sunspots reached in the year 2000, followed by the continuous decrease in sunspots similar to the period of the solar cycle 21. The launch of LASCO on-board SOHO spacecraft provided knowledgeable information about the occurrence of CME during period. As the graph in Fig. 5.4, 1700 CMEs occurred during the year 2002, contributing to, 13,750 CMEs during the solar cycle 23.

The most powerful solar flare of solar cycle 23 was observed on Bastille Day Event. An X5.7 flare originated from the sunspot termed as Active region 9077, hit Earth as radiation storm, the powerful ever since 1980 and the reason behind the Halo-CME and a geomagnetic storm of July 15–July 16. The geomagnetic storm peaked at the extreme level, G5 in the late hours of July 15. Other X-ray class flares of X20.0, X14.0 occurred on April 4, 2001, X17.2 and X10.0 on October 28 and 29 of 2003, and on September 7, 2005, with the class of X17.0. Geomagnetic storms

of DST min of −105 nT, −85 nT, −47 nT, and −74 nT occurred during the year 2003–2005 [11–13]. The sunspot counts reduced to 13 in 2007 and to 4 in 2008, thus marking the beginning of the next cycle.

The solar cycle 24 started in the year 2008. Sun gave no signs of sunspots for 817 days in beginning of 23/24 minimum and then a sunspot count of four during 2008, and peaked at the sunspot count of 113 in the year 2014. A total of 17,236 CMEs occurred during the cycle. St. Patrick's Day Geomagnetic storm, the most intense geomagnetic storm during the rising maximum phase of solar cycle 24 occurred on March 17th, 2015 with a DST min of −223 nT and continued till March 19 [14]. Based on above discussion and analysis we could infer followings:

1. The rate of occurrence of the coronal mass ejections varies directly with the sunspot number. Higher the sunspot numbers, higher is the number of coronal mass ejections.
2. Decline in the total yearly sunspot number during the maxima of 1979, 1989, 2000, and 2014.
3. However, the number of sunspots declined, but the total number of CME had increased from solar cycle 23 to solar cycle 24.
4. Although, amplitude of the cycle 24 was very low compared to cycle 23, but 2012–2014 saw a steep rise in the number of CMEs. Never had the total number of CMEs been so high during any year since 1996–2019.
5. Period of 1986–1996 shows a different behavior than any of the periods from 1976 to 1986, 1996 to 2008, and 2008 to 2019, in terms of the total yearly sunspot number. The total yearly sunspot number for the period of 1986–1996 peaked up two times, one at 211 and other at 203, while during all other periods, the total yearly sunspot number peaked only once and then possessed a continuous downfall in the number of sunspots.
6. One interesting fact to note about the total yearly sunspot number is that it had never been the same from 1976 to 2020.

Figure 5.5 shows the plot for the 27-day-averaged data for the sunspot number (SSN) versus 10.7 cm solar radio flux (in units of SFU) from the 1st day of 2020 to the 223rd day of 2020 (1 SFU = 10^{-22} W m^{-2} Hz^{-1}). Figure 5.6 shows the 27-day-averaged data for the sunspot number versus solar wind proton density (*n*/cc, *n* is the number of particles). The data for the 27-day-averaged of: the sunspot number (new version), 10.7 cm solar radio flux, and solar wind proton density have been collected from the OMNI Web Data Explorer and Space Physics Data Facility (SPDF) (https://omniweb.gsfc.nasa.gov/form/dx1.html).

From Fig. 5.5 it is clear that, the 10.7 cm solar flux is not varying significantly with the sunspot number in starting phase of solar cycle 25 while the solar wind proton density shows little variation with the sunspot number Fig. 5.6.

The plot in Fig. 5.7 shows how the sunspots varied every day from the 1st day of 2020 to the 223rd of 2020 (Jan 1, 2020 to August 10, 2020). The data for the daily total sunspot number is collected from the Sunspot Index and Long-Term Solar

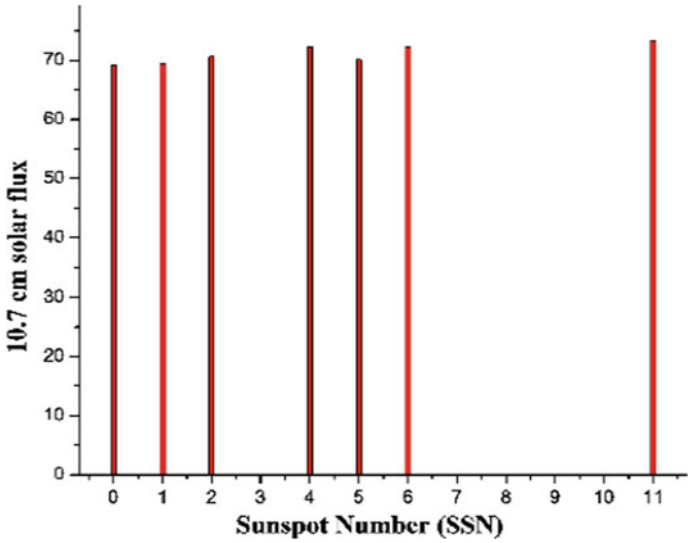

Fig. 5.5 Sunspot number versus 10.7 cm solar flux from 1st day of 2020 to 223rd day of 2020

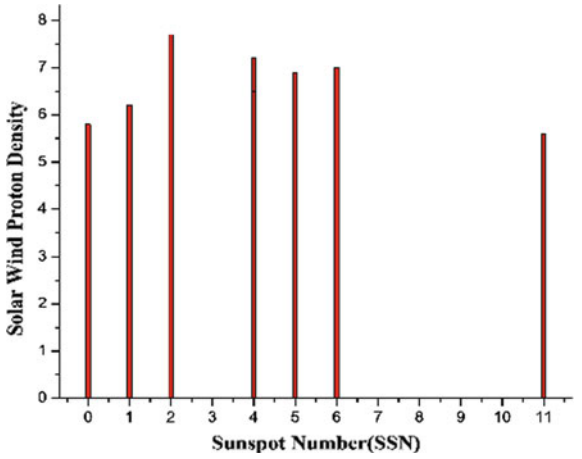

Fig. 5.6 Sunspot number versus solar wind proton density from 1st day of 2020 to 223rd of 2020

Observations (SILSO), Royal Observatory of Belgium, Brussels (https://wwwbis.sidc.be/silso/datafiles). The graph shows the Sun was almost quiet for most of the time in the start of 2020 ranging from zero to very few sunspots. The activity started to increase in June of 2020 with a little number of sunspots but again sunspots declined to zero. Sunspots finally started to rise in the late of July 2020, announcing that the Sun has entered into the solar cycle 25. In October 2020, from the sunspot region AR2776 erupted the B3-class solar flare. On the day, the sunspot number was only

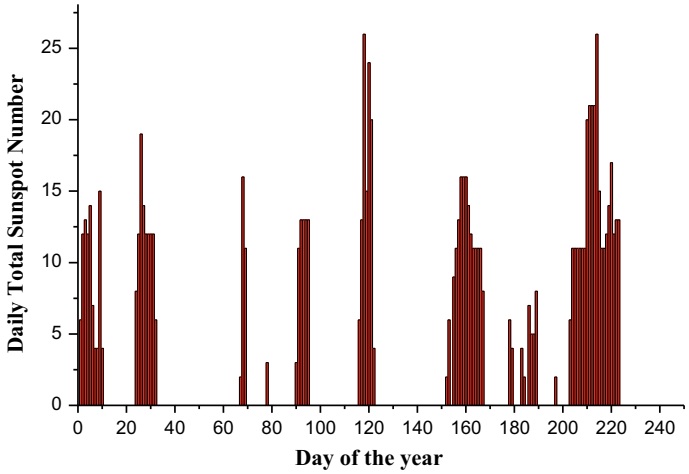

Fig. 5.7 Daily total sunspot number from 1st day of 2020 to 223rd day of 2020

14, but the solar wind speed exceeded up to 306 km/s [15]. Another M4.4 X-ray class solar flare, observed by the solar orbiter, occurred on November 29 2020 from the AR2786 at 12:34 UT [16].

5.3 Conclusion

We have studied how sunspots, CME and the different solar parameters, varied from the start of solar cycle 21 to the upcoming phase of solar cycle 25. We see that the sunspot counts and the rate of occurrence of solar activities vary on a yearly basis.

Acknowledgements We acknowledge the different astronomical observatories for providing free online data to carry out this work. The first author acknowledges the help and support provided for this study during the summer research program at K. S. Krishnan Geomagnetic Research Laboratory, Indian Institute of Geomagnetism. The first author also wants to thank the Physics department of Ewing Christian College for completion of this work.

References

1. A.K. Singh, D. Singh, R.P. Singh, Space weather. Physics, effects and predictability. Surv. Geophys. **31**, 581–638 (2010). http://doi.org/10.1007/s10712-010-9103-1
2. M. Moldwin, *An Introduction to Space Weather* (2008), pp. 1–142. http://doi.org/10.1017/CBO9780511801365

3. H.S. Hudson, J.L. Bougeret, J. Burkepile, Coronal mass ejections: overview of observations, in *Coronal Mass Ejections. Space Sciences Series of ISSI*, vol. 21 (Springer, New York, NY, 2006). http://doi.org/10.1007/978-0-387-45088-9_2
4. O.C. Christian, A statistical analysis of sunspot & CME parameters for the solar cycle 23. Phys. Astron. Int. J. **2**(4) (2018)
5. S.A. Hamouda, F.F. Alfarjani, F.Y. Elfituri, Sunspots production and relation to other phenomena: a review. Hum. J. Rev. **9**(4) (2018)
6. R. Cameron, Solar dynamo. in *Oxford Research Encyclopedia of Physics*. Retrieved 2 Sept 2021 (2021)
7. A. Balogh, H.S. Hudson, K. Petrovay et al., Introduction to the solar activity cycle: overview of causes and consequences. Space Sci. Rev. **186**, 1–15 (2014). https://doi.org/10.1007/s11214-014-0125-8(2014)
8. D.H. Hathaway, The solar cycle. Living Rev. Solar Phys. **12**, 4 (2015). http://doi.org/10.1007/lrsp-2015-4
9. H.V. Cane, I.G. Richardson, What caused the large geomagnetic storm of November 1978. J. Geophys. Res. **102**(A8), 17445–17449 (1997)
10. D.H. Boteler, A 21st century view of the March 1989 magnetic storm (2019). http://doi.org/10.1029/2019SW002278
11. Space Radiation Storm, NASA. https://www.swpc.noaa.gov/phenomena/solar-radiation-storm, last accessed 2021/10/02
12. Solar flare biggest since 89, Contra Costa Times. https://infoweb.newsbank.com/apps/news/document-view?p=WORLDNEWS&docref=news/1064A3E55B815DA8&f=basic, last accessed 2021/10/02
13. W.R. Webber, F.B. McDonald, J.A. Lockwood, B. Heikkila, The effect of the July 14, 2000 "Bastille Day" solar flare event on >70 MeV galactic cosmic rays observed at V1 and V2 in the distant heliosphere. Geophys. Res. Lett. **29**(10), 1377–1380 (2002)
14. C.-C. Wu, K. Liou, R.P. Lepping, L. Hutting, S. Plunkett, R.A. Howard, D. Socker, The first super geomagnetic storm of solar cycle 24: "The St. Patrick's day event (17 March 2015)" (2015)
15. Z.S. Hamidi, N.N.M. Shariff, The correlation between solar wind and active sunspot AR2776 in 25th solar cycle. J. Phys. Conf. Ser. **1936**, 012013 (2021)
16. G.M. Mason, C.M.S. Cohen, G.C. Ho, D.G. Mitchell, R.C. Allen, M.E. Hill, G. Bruce Andrews, L. Berger, S. Boden, S. Böttcher, I. Cernuda, E.R. Christian, A.C. Cummings, A.J. Davis, M.I. Desai, G.A. de Nolfo, S. Eldrum, R. Elftmann et al., Solar energetic particle heavy ion properties in the widespread event of 2020 November 29 (2021). http://doi.org/10.1051/0004-6361/202141310

Chapter 6
Theoretical Approach to Modify the Born–Mayer Parameters in Layered Superconductor

Hempal Singh

Abstract Since 1932, most of the scientists considered the coefficients (known as range and softening constants) of Born–Mayer potential as constants need in depth investigation. This has been explored in the form of Born–Mayer–Huggins (BMH) potential for the high temperature superconductors in a new frame work which enables to develop the expressions for Born–Mayer parameters, bulk modulus, and pressure. These investigations divulge that the Born–Mayer parameters for different interactions in high temperature superconductor are not simple quantities but depend upon various physical quantities like pressure, charges, volume, and Gruneisen parameter which is the measure of the strength of anharmonic affects in high temperature superconductors. The numerical computations have been performed for the various interactions of $YBa_2Cu_3O_{6+\delta}(YBCO)$ superconductor to adjudge the suitability of this formalism which is applicable to other high temperature and layered superconductors.

6.1 Introduction

The Ba–La–Cu–O was the first high temperature superconductor (HTS) with critical temperature 35 K stands as a landmark discovery by Bednorz and Muller in 1986 [1]. The fascinating area of high temperature superconductivity (HTSC) attracted the attention of scientific community which not only led to synthesize the HTSC at room temperature but also to investigate its various dynamical properties. Owing to the established that the HTS has layered structures with large number of atoms per unit cell, the requirement of a suitable potential becomes mandatory to study the various dynamical properties of layered systems. A newly developed Born–Mayer–Huggins (BMH) potential has been proposed to study the lattice spectrum of YBCO which is a combination of attractive and repulsive interactions and can be represented as [2–8]

H. Singh (✉)
Kirori Mal College, Department of Physics, University of Delhi, Delhi 110007, India
e-mail: physics.hempal@gmail.com

K. L. Pandey et al. (eds.), *Proceedings of the National Workshop on Recent Advances in Condensed Matter and High Energy Physics*, Springer Proceedings in Physics 278,
https://doi.org/10.1007/978-981-19-2592-4_6

$$V_{ij}(r) = a_{ij}\, e^{-b_{ij}r} + \frac{q_i\, q_j}{r} \tag{6.1}$$

Here, i and j label the ions $r_{ij} \equiv r$ distant apart and a_{ij}, b_{ij}, q_i, and q_j are the range parameter, softening parameter, charge on i and j ions, respectively. First term in BMH is the Born–Mayer term which is repulsive (weak, short-range) and keeps the atoms apart from collapsing. Second term is Coulomb term (strong, long-range) which can be attractive or repulsive depending upon the nature of the charges, and it works to save the crystal from expansion to unnatural dispersion.

6.2 Theoretical Background of the Present Work

To deal with the problem, we have taken the thermodynamic approach in which angular frequency depends upon the volume $\omega \propto V^{-\gamma}$ and well-known relation $\gamma = \mathrm{d}(\ln \omega)/\mathrm{d}(\ln V)$ [9], which leads to the form $\mathrm{d}\omega/\mathrm{d}V = -\gamma\omega/V$. Using the potential energy and pressure relation, i.e., $P = -\mathrm{d}V_{ij}(r)/\mathrm{d}V$ we can obtain

$$P = -\frac{\gamma r}{V}\frac{\mathrm{d}V_{ij}(r)}{\mathrm{d}r} \tag{6.2}$$

Equations (6.1) and (6.2) lead to the unique form of pressure in the following form

$$P = \frac{\gamma r}{V}\left[a_{ij}b_{ij}e^{-b_{ij}r} + \frac{q_i q_j}{r^2}\right] \tag{6.3}$$

This shows that Born–Mayer parameters are pressure dependent appearing as one of the main finding. Further, the volume compressibility $\beta = -V\mathrm{d}P/\mathrm{d}V$ is the key factor to evaluate the form of bulk modulus as

$$B = -\frac{\gamma^2 r}{V}\left[a_{ij}b_{ij}(1 - b_{ij}r)e^{-b_{ij}r} - \frac{q_i q_j}{r^2}\right] \tag{6.4}$$

The equilibrium condition $\mathrm{d}V_{ij}(r)/\mathrm{d}r\big|_{r=r_o} = 0$ applied to (6.1), leads to develop the Born–Mayer parameters in the following form [8]

$$b_{ij} = \left(\frac{r_o}{r}\right)\left[\frac{1}{r_o} + \frac{1}{r} - \frac{BV}{q_i q_j \gamma^2}\right] \tag{6.5}$$

$$a_{ij} = -\frac{q_i q_j}{r_o^2}\left(\frac{r + r_o}{r r_o} - \frac{BV}{q_i q_j \gamma^2}\right)^{-1} \exp\left[\frac{r_o^2}{r}\left(\frac{r + r_o}{r r_o} - \frac{BV}{q_i q_j \gamma^2}\right)\right] \tag{6.6}$$

The above expressions reveal that Born–Mayer parameters are not constant (as considered in earlier work) but depend upon various physical quantities.

6.3 Results and Discussions

To justify the obtained results, we have taken the representative-layered HTS YBCO for numerical computation. Considering the Y[1] ion at the center of the system, a mesh of 38 atoms/lattice sites (Ba[2], Cu[16] and O[20] ions) is observed for the model calculations in which Cu–O_2 plane has Cu[8] and O[8], Ba–O layer has Ba[2] and O[8], and Cu–O layer has Cu[8] and O[4] ions. The digits appearing in brackets with elements stand for their number taken up for numerical estimation.

The physical constants used in numerical computation are $a = 3.8$ Å, $b = 3.9$ Å, $c = 11.60$ Å, $V = 1.71912 \times 10^{-24}$ cm^3, $\gamma = 1.4$, and $B = 4.6 \times 10^{11}$ Dyne/cm^2 [10–12]. The nature of range parameter for Y–O(I) interaction (in CuO_2 plane), Y–Cu(+2) interaction (in CuO_2 plane), Y–Ba interaction (in Ba–O layer), and Y–O(II) interaction (in Ba–O layer) with interionic distances has been portrayed simultaneously in Fig. 6.1.

The critical investigations reveal that range parameter slightly changes for Y–O(I) interaction in the range $r < 2$ Å and saturated to the large interionic distances. For Y–Cu interaction, a_{ij} abruptly decreases in the region $r < 2$ Å and slightly increases (above 3 Å) for larger r. The interaction Y–Ba shows similar nature to the Y–Cu interaction. On the other hand, a_{ij} changes its nature 2 Å $< r <$ 5 Å and no dissipation if $r > 8$ Å is observed. The behavior of softening parameter for Y–O(I) interaction (in CuO_2 plane), Y–Cu(+2) interaction (in CuO_2 plane), Y–Ba interaction (in Ba–O layer), and Y–O(II) interaction (in Ba–O layer) with interionic distances is shown simultaneously in Fig. 6.2. It is evident from the curves that softening parameter for Y–O(I) falls off steadily in the range $r < 2$ Å and changes its nature drastically within the range 2 Å $< r <$ 8 Å. Whereas for interaction Y–Cu, b_{ij} start to dissipate near 2.5 Å and saturated after 13 Å. Furthermore, b_{ij} for Y–Ba interaction also start to change its nature $r < 2$ Å [as Y–O(I)] but saturated near 13

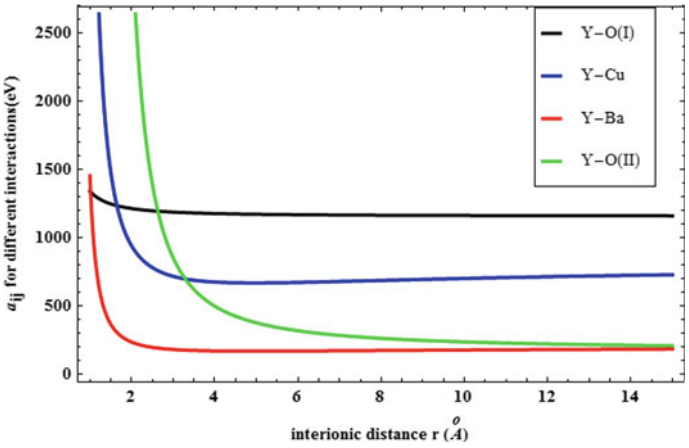

Fig. 6.1 Nature of range parameter with interatomic distance for different interactions

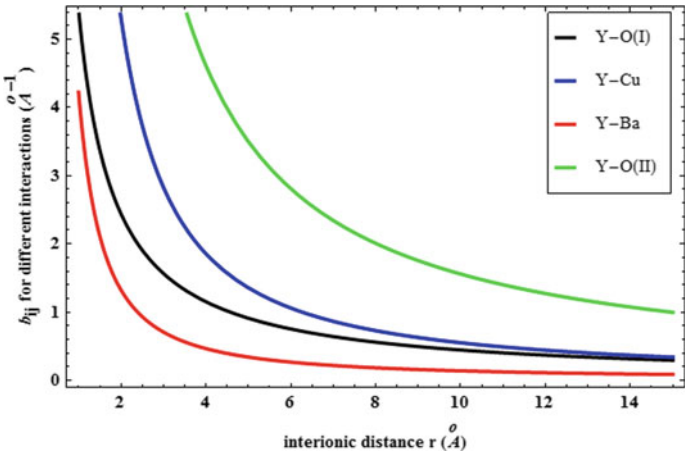

Fig. 6.2 Behavior of softening parameter with interionic distance for different interactions

Å. The saturation point of Y–O(II) interaction is largest 14 Å and falls rapidly in the range 3.5 Å < r < 13.5 Å. The variation of bulk modulus for Y–O(I) interaction (in CuO_2 plane), Y–Cu(+2) interaction (in CuO_2 plane), Y–Ba interaction (in Ba–O layer), and Y–O(II) interaction (in Ba–O layer) with interionic distances has been depicted simultaneously in Fig. 6.3. The deeper insights reveal that bulk modulus for both interactions Y–Cu and Y–Ba meet and start to dissipate near 1.25 Å. These interactions of B achieve their maximum at 2 Å and 2.25 Å, while saturated after 10 Å and 6 Å. The interaction Y–O(I) sharply down to its minimum near 6.5 Å and start to increase for large interionic distances.

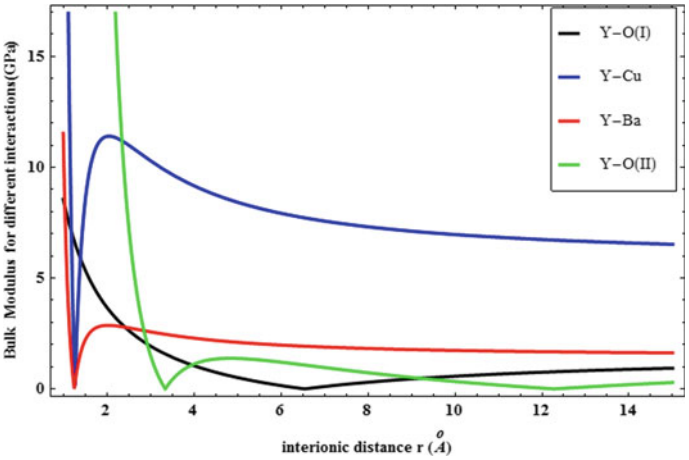

Fig. 6.3 Variation of B with interionic distance for different interactions

The nature of Y–O(II) interaction of B is different from others as it attain minimum at two points 3.4 Å and 12.4 Å and increases for large interionic distances.

6.4 Conclusions

The present study investigates that Born–Mayer parameters are not constant but depend upon various physical quantities. It also divulges that BMH potential is the best suitable potential high temperature and layered superconductors. This theory will be applicable to other high temperature and layered superconductors.

Acknowledgements I want to express lifetime gratitude to my supervisor Late Prof B. D. Indu for his valuable time to complete this research work.

References

1. J.G. Bednorz, K.A. Muller, Possible high T_C superconductivity in Ba-La-Cu-O system. Z. Phys. B **64**, 189–193 (1986)
2. M. Born, J.E. Mayer, Zur Gittertheorie der Ionenkristalle. Z. Phys. **75**, 1–18 (1932)
3. M. Born, K. Huang, *Dynamical Theory of Crystal Lattices*, 1st edn. (Oxford University Press, New York, 1954)
4. M.L. Huggins, J.E. Mayer, Interatomic distances in crystals of the alkali halides. J. Chem. Phys. **1**, 643–646 (1933)
5. T.P. Martin, NaCl polymers. J. Chem. Phys. **67**, 5207–5212 (1977)
6. J.P. Rose, R.S. Berry, Freezing, melting, nonwetting, and coexistence in $(KCl)_{32}$. J. Chem. Phys. **98**, 3246–3261 (1993)
7. J.M. Delaye, V. Louis-Achille, D. Ghaleb, Modeling oxide glasses with Born–Mayer–Huggins potentials: effect of composition on structural changes. J. Non-Cryst. Solids **210**, 232–242 (1997)
8. H. Singh, A. Singh, B.D. Indu, The Born Mayer Huggins potential in high temperature superconductors. Mod. Phys. Lett. B **30**, 1650283(1–10) (2016)
9. J.R. Hook, H.E. Hall, *Solid State Physics*, 2dn edn. (Wiley, New York, 1991)
10. D. Varshney, A. Yogi, N. Dodiya, I. Mansuri, Alkaline earth (Ca) and transition metal (Ni) doping on the transport properties of $Y_{1-x}Ca_xBa_2(Cu_{1-y}Ni_y)_3O_{7-\delta}$ superconductors. J. Mod. Phys. **2**, 922–927 (2011)
11. C. Haetinger, I. Abrego Castillo, J.V. Kunzler, L. Ghivelder, P. Pureur, S. Reich, Thermal expansion and specific heat of non-random YBCO/Ag composites. Supercond. Sci. Technol. **9**, 639–643 (1996)
12. D.P. Almond, E. Lambson, G.A. Saunders, W. Hong, An ultrasonic study of the elastic properties of the normal and superconducting states of $YBa_2Cu_3O_{7-\delta}$. J. Phys. F Met. Phys. **17**, L221–L224 (1987)

Chapter 7
Effect of Varying the Grating Length in an Optical Readout Scheme Based on Grated Waveguide Cantilever Cavity Resonance

Anil Kumar Singh, Renil Kumar, and Prem Prakash Singh

Abstract In our earlier work, a novel design of an optical readout scheme based on a grated waveguide (GWG) resonator for interrogating microcantilever sensor arrays is presented. An analytical modelling of the transfer function of this scheme is described and it reasonably matches with the FDTD numerical solution performed using open-source software MEEP. This readout scheme is designed on silicon optical bench platform which consists a monolithically integrated microcantilever in proximity to a grated waveguide (GWG). In analytical modelling, cavity formed between the microcantilever and the grated waveguide (GWG) is considered to be lossy, and it is studied using a Fabry-Perot (FP) interferometer model. An analytical expression is derived for the optical power transmission as a function of the grating length, periodicity of the grating, and grating efficiency. In this paper, effect of varying the grating length, FP cavity loss parameter, and reflectance parameter on power transmission is studied. Results show that analytical calculations reasonably match with FDTD numerical models.

7.1 Introduction

Microcantilever-based sensors offer a low-cost sensing platform for many types of applications viz., chemical sensing for environmental monitoring, detection of explosives, food quality testing owing to their high sensitivity, compactness, and mass production [1–3]. All microcantilever MEMS sensors operate in either static or dynamic mode. In the static mode, the external target molecule induces bending in the microcantilever upon surface binding, which introduces strain in the microcantilever. This strain can be sensed by different readout techniques [4–6]. In the dynamic mode,

A. K. Singh · P. P. Singh (✉)
Ewing Christian College, University of Allahabad, Prayagraj, India
e-mail: iiscprem@gmail.com

R. Kumar
RIKEN, Saitama, Japan

K. L. Pandey et al. (eds.), *Proceedings of the National Workshop on Recent Advances in Condensed Matter and High Energy Physics*, Springer Proceedings in Physics 278,
https://doi.org/10.1007/978-981-19-2592-4_7

the adsorption of a single external target molecule changes the resonant frequency of the microcantilever [7]. The mass of external target molecule can then be correlated to the shift in the resonant frequency. In order to determine the deflection or the frequency shift of a cantilever, different readout methods specifically capacitive method [8], piezoelectric method [9], and optical method [10] have been used by various research groups. Recently, optical interferometry-based readout schemes have drawn much attention in comparison with optical beam deflection technique [11]. In our earlier work, a novel optical readout scheme based on a grated waveguide resonator for the interrogation of microcantilever sensor arrays is presented [12], where the sensor (cantilever) and the detector element (grated waveguide) are monolithically integrated on the same chip leading to high-multiplexing capability.

In earlier work, S. V. Pham et al. reported an all optical GWG resonator-based readout scheme for the interrogation of a microcantilever for selective gas sensing [13]. In their design, the bending of a SiO_2 cantilever monolithically integrated in close proximity to a Si_3N_4 GWG creates an effective refractive index variation of the grating which changes the optical resonance. Measuring the resonance shift provides a means for the detection of cantilever bending since it is a sensitive function of the effective refractive index variation caused by the cantilever bending. In this structure, the modulation of the optical mode in the waveguide is due to the interaction of the cantilever with the evanescent field of the GWG, which requires the cantilever to be placed within the exponentially decaying evanescent field of the waveguide with fairly tight tolerances. In contrast, in the device proposed here, the coupling of cantilever mechanical motion and the propagating optical mode in the waveguide is non-evanescent in nature and arises from the interference between the propagating leaky mode in the waveguide with the light coupled out by the grating reflected and coupled back into the grated waveguide by the cantilever as shown in Fig. 7.1a. The opto-mechanical coupling, in this case, is strong even for cantilever-waveguide separations which are several times the wavelength of light used, as we show in this article, unlike evanescent coupling where the gap can only be a small fraction of the wavelength. This results in more relaxed fabrication tolerances as well as ease of integrating supporting structures such as those that may enhance the transport of analyte to the cantilever sensor. Design of the readout scheme is explained in

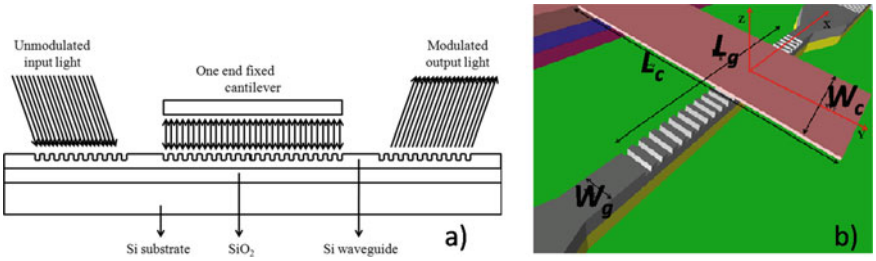

Fig. 7.1 **a** Shows the architecture for integrated optical readout of cantilever deflection using a grated waveguide (GWG) placed underneath and **b** shows the 3D view of the same

our previous work [12]. In our readout scheme, the microcantilever is monolithically integrated just above the grated waveguide, and schematically, it is shown in Fig. 7.1.

7.2 Analysis of the Grated Waveguide Cantilever Cavity

In the absence of the cantilever, the grating is characterized by a loss parameter, also referred to as the grating efficiency parameter, α, which denotes the efficiency of the grating to out-couple the light field propagating in the waveguide layer to a substrate or cover mode. The fraction of guided power after length L_g of the grating is

$$P(L_g)/P_0 = \exp(-2\alpha L_g) \tag{7.1}$$

which is the power transmission coefficient through a grating of length L_g and efficiency α. Power lost from the guided mode is coupled out of the guiding layer to the cover or substrate layer (cover layer, air, in this case) at coupling angles given by the phase matching condition,

$$\sin\theta = n_{\text{eff}} \pm m\frac{\lambda}{\Lambda} \tag{7.2}$$

where n_{eff} is the effective refractive index of the guided mode, λ is the free-space wavelength and Λ is the grating periodicity, and the order m takes on integer values.

If a cantilever is placed on top of the grating, Fabry-Perot cavity is formed. The mechanism is similar to the enhancement of coupling efficiency using a buried mirror under a grating coupler, which has been analyzed using scattering matrix formalism [14].

To account for multiple reflections and back-couplings into the GWG, so we divide the GWG along its length into several segments, as shown in Fig. 7.2, with periodicity (segment PQ in Fig. 7.2) Λ_g defined by the out-coupling angle θ, as, $\Lambda_g = 2g\tan\theta$, where g is the gap between the cantilever and the grated waveguide.

The cantilever changes the grating efficiency in the shaded region shown in Fig. 7.2. The grating efficiency remains α in the un-shaded region but changes to α_{pert} in the shaded region. In each segment, say segment m, the electric field amplitude along the length is denoted as $E_m{}^{\text{pert}}(x)$ where x ranges from 0 to Λ_g. From symmetry, we see that the cantilever couples back field amplitudes from its neighbours $E_{m\text{-}k}$, where k goes from 1 to $m-1$.

For any segment m, the propagation (7.3) is modified as

$$\begin{aligned}\frac{dE_m^{\text{pert}}(x)}{dx} = -\alpha\Big\{ & E_m^{\text{pert}}(x) + \gamma_1 e^{j\varphi} E_{m-1}^{\text{pert}}(x) + \gamma_2 r e^{2j\varphi} E_{m-2}^{\text{pert}}(x) \\ & + \gamma_3 r^2 e^{3j\varphi} E_{m-3}^{\text{pert}}(x) + \ldots\Big\}\end{aligned} \tag{7.3}$$

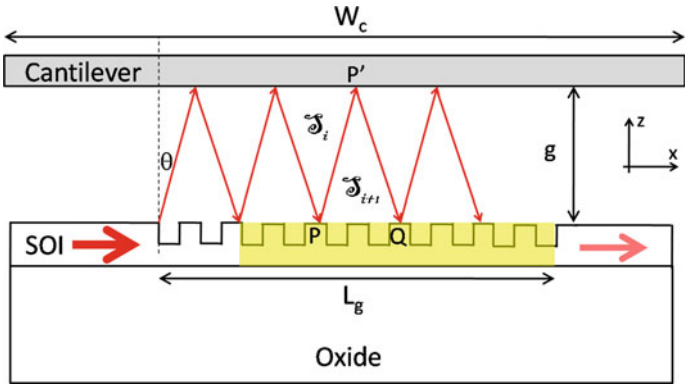

Fig. 7.2 Geometry of the device. The shaded region of the waveguide grating represents the region with "back-coupled" light reflected by the cantilever

where ϕ is the phase difference between the back-coupled field and the field propagating in the WG, and γ_k is the coupling fraction from the kth neighbour of the given segment, and r is the reflectance of the GWG, treated as a mirror forming the FP cavity.

With these assumptions, (7.4) becomes

$$\frac{dE_m^{\text{pert}}(x)}{dx} = -\alpha E_m^{\text{pert}}(x)\left\{1 + \gamma_0 \sum_{k=1}^{\infty} r^{k-1} e^{j\varphi} e^{-k\eta\Lambda_g}\right\} \tag{7.4}$$

The summation gives the value of the perturbed loss coefficient α pert as

$$\alpha_{\text{pert}} = \alpha\left(1 + \gamma_0 \frac{e^{-\eta\Lambda_g} e^{j\varphi}}{1 - re^{-\eta\Lambda_g} e^{j\varphi}}\right) \tag{7.5}$$

Here, $\eta = \beta - \alpha$.

The amplitude transmission is then given by

$$AT = \exp(-\alpha\Lambda_g)\exp\left(-\alpha_{\text{pert}}(L_g - \Lambda_g)\right) \tag{7.6}$$

and power transmission in dB is then

$$PT = 20\log(|AT|) \tag{7.7}$$

7.3 Results and Discussion

Figure 7.3 shows the comparison of the effect of varying the grating length using simple analytical model given by (7.7), with the FDTD numerical simulation performed using open-source software MEEP [15, 16]. A reasonable match between the numerical and analytical calculation is obtained. The structure which is used for the simulation consists of a varying grating length, L_g, with grating efficiency, α, of 0.11 μm^{-1}. The periodicity of the grating, Λ, is 630 nm, and the effective refractive index, n_{eff}, of the fundamental TE mode is 2.83, which gives the out-coupling angle θ, according to (7.2) as 13.6°. These parameters are used in the analytical model.

The free parameters that are used for fitting the numerical data are β, which has been taken as 3α and r, which has been taken as 0.3 and γ_0 which is taken as 1.4. The heuristic model described here cannot be used to estimate the values of these parameters. Coupling constants γ_k, etc., need to be found using more involved calculations such as the S-matrix method used to treat multilayer waveguide structures with loss and/or gain [16].

To understand the effects of the two main free parameters in the model, namely β and r, we show the effect of these parameters on the optical transmission in Fig. 7.4. As mentioned before, β is a Fabry–Perot (FP) cavity loss parameter. Increasing β will reduce the extent of back-coupling due to larger losses, for instance to the substrate and reduce the modulation depth as shown in Fig. 7.4a. The periodic oscillations in the optical transmission will damp out to their asymptotic value, $\exp(-2\alpha L_g)$, which is the transmission coefficient without the cantilever, faster with increasing B. In contrast, increasing r is analogous to increasing the reflectance of the mirrors forming an FP cavity, increasing r increases the modulation depth and also reduces the width of the dips, due to the increase in cavity finesse with increasing r. In practice, this means that the underside of the cantilever must have as high a reflectance as possible for increasing the modulation depth of the device. This is easily accomplished with a metal coating underneath.

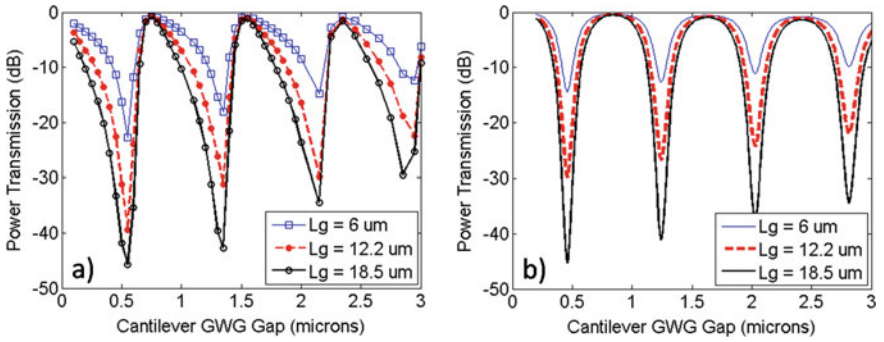

Fig. 7.3 **a** Shows MEEP FDTD simulations from GWGs with 3 different lengths and **b** shows the analytical calculations for the same GWGs indicating a reasonable match

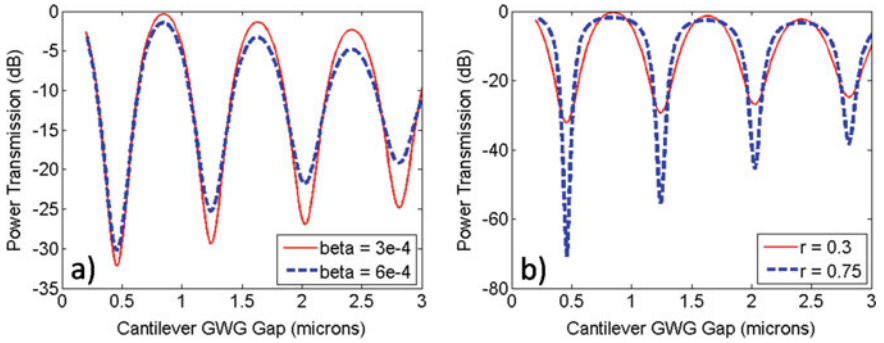

Fig. 7.4 Effect of model parameters **a**β and **b**r on the optical transmission

7.4 Conclusion

To summarize, we presented a simple lossy Fabry-Perot cavity model which captures many of the essential features of the numerical FDTD results obtained through MEEP. Although this model cannot be used to find the coupling fraction of the power into the waveguide and so on explicitly, it provides an intuitive picture to guide the design of the proposed device and understand the parameters that affect the performance of the realized device.

References

1. Z. Hu, T. Thundat, R.J. Warmack, Investigation of adsorption and absorption-induced stresses using microcantilever sensors. J. Appl. Phys. **90**(1), 427–431 (2001)
2. D.R. Baselt, B. Fruhberger, E. Klaassen, S. Cemalovic, C.L. Britton Jr., S.V. Patel, T.E. Mlsna, D. McCorkle, B. Warmack, Design and performance of a microcantilever-based hydrogen sensor. Sens. Actuators B **88**, 120–131 (2003)
3. C.L. Britton Jr., R.L. Jones, P.I. Oden, Z. Hu, R.J. Warmack, S.F. Smith, W.L. Bryan, J.M. Rochelle, Multiple-input microcantilever sensors. Ultramicroscopy **82**, 17–21 (2000)
4. Chri stiane Ziegler, Cantilever-based biosensors. Anal Bioanal Chem **379**, 946–959 (2004)
5. R. Raiteri, M. Grattarola, H.J. Butt, P. Skládal, Micromechanical cantilever-based biosensors. Sens. Actuators B**4010**, 115–126 (2001)
6. M. Godin, V. Tabard-Cossa, Y. Miyahara, T. Monga, P.J. Williams, L.Y. Beaulieu, R.B. Lennox, P. Grutter, Cantilever-based sensing: the origin of surface stress and optimization strategies. Nanotechnology **21**, 1–8 (2010)
7. A. Gupta, D. Akin, R. Bashir, Single virus particle mass detection using micro resonators with nanoscale thickness. Appl. Phys. Lett. **84**(11), 1976–1978 (2004)
8. J. Verd, G. Abadal, J. Teva, A. Uranga, N. Barniol, J. Esteve, M. Duch, F. Pérez-Murano, High-sensitivity capacitive readout system for resonant submicrometer-scale cantilevers based sensors, in *IEEE Proceedings* (2005)
9. M.S.K. Mutyala, D. Bandhanadham, L. Pan, V.R. Pendyala, H.-F. Ji, Mechanical and electronic approaches to improve the sensitivity of microcantilever sensors. Acta Mech. Sin. **25**, 1–12 (2009)

10. S.T. Koev, R. Fernandes, W.E. Bentley, R. Ghodssi, A cantile ver sensor with an inte grated optical readout for detection of enzymatically produced homocysteine. IEEE Trans. Biomed. Circ. Syst. **3**(6), 415–423 (2009)
11. L.J. Kauppinen, H.J.W.M. Hoekstra, M. Dijkstra, R.M. de Ridder, G.J.M. Krijnen, Grated waveguide optical cavity as a compact sensor for sub-nanometre cantilever deflections, Eindhoven, The Netherlands (2008)
12. P. Prakash, Renil Kumar, R. Pratap, Optical read-out scheme based on Grated Waveguide Cantilever cavity resonance for interrogation of cantilever sensor arrays, in *COMMAD*, Melbourne (2012)
13. S.V. Pham, L.J. Kauppinen, M. Dijkstra, H.A.G.M. van Wolferen, R.M. de Ridder, H.J.W.M. Hoekstra, Read-Out of cantilever bending with a grated waveguide optical cavity. IEEE Photon. Technol. Lett. **23**(4) (2011)
14. R. Orobtchouk, A. Layadi, H. Gualous, D. Pascal, A. Koster, S. Laval, High-efficiency light coupling in a sub-micrometric silicon-on-insulator waveguide. Appl. Opt. **39**(31) (2000)
15. G. Putrino, A. Keating, M. Martyniuk, L. Faraone, J. Dell, Model and analysis of a high sensitivity resonant optical read-out approach suitable for cantilever sensor arrays. J. Lightwave Technol. **30**(12) (2012)
16. A.F. Oskooi, D. Roundy, M. Ibanescu, P. Bermel, J. Joannopoulos, S.G. Johnson, Meep: aflexible free-software package for electromagnetic simulations by the FDTD method. Comput. Phys. Commun. **181**(3), 687–702 (2010)

Chapter 8
Synthesis and Characterization of MoO_3 Nanomaterials for Energy Storage Application

K. K. Tiwari, Atul Kumar Gupta, and Amit Kumar Verma

Abstract Nanomaterial are being adapted into a number of applications across multiple domains such as cosmetics, optical components, biology, physics, chemistry, polymer science, pharmaceutical drug manufacture, toxicology, and mechanical engineering. Molybdenum oxide (MoO_3) and its derivatives are widely used in industry as specific alloy and catalyst applications, electrochemical capacitors, display devices, sensors, smart windows, lubricants, battery electrodes, etc. Nanoparticles of MoO_3 were synthesized using the salvo thermal method and synthesized MoO_3 nanoparticles were characterized by using UV-Visible, XRD, SEM, and cyclic voltammetry analysis techniques at different temperatures. XRD analysis show that particle size increases as its temperature increases and the corresponding strain decreases also. SEM morphology shows its nanorods structure.

8.1 Introduction

In the recent years, energy storage is a big challenge to us due to its increasing demand by the modern society. Researchers try to develop a new device to store the energy for a very long time, and they found that super capacitors or electrochemical capacitors may be a suitable candidate for next generation energy storage device due to its high power density and fast recharging capabilities, long life, maintenance free, and environment friendly energy storage devices [1–5]. A super capacitor is a new type of energy storage device, different from a conventional capacitor and a rechargeable battery. Although scientists have made a lot of progress in electrode materials for super capacitor, which are still limited by low capacitance, like as carbon-based electrode. There are two types of super capacitors depending upon their charge transfer mechanism, one is electrical double layer capacitors and second is pseudocapacitors. In electrical double layer capacitors, the charge storage mechanism is non-faradic

K. K. Tiwari · A. K. Gupta (✉) · A. K. Verma
Department of Physics, Allahabad Degree College, University of Allahabad, Allahabad 211003, India
e-mail: atulkumar_physics@rediffmail.com

K. L. Pandey et al. (eds.), *Proceedings of the National Workshop on Recent Advances in Condensed Matter and High Energy Physics*, Springer Proceedings in Physics 278,
https://doi.org/10.1007/978-981-19-2592-4_8

and the charges are accumulated in the interface between the electrode and electrolytic solution while in pseudocapacitors, fast faradic redox reactions associated with the solid-state diffusion of electrolyte ions take place at the electrode surface in pseudocapacitors. So many transition metal oxides have the ability to fulfill the conditions of super capacitors [6–10]. Among these transition metal oxides, MoO_3 become more suitable for super capacitors due to its cost effective, non-toxicity, high electrochemical activity, availability of multiple oxidation states of its stable and meta stable polymorphous, having higher specific capacitance with good cycling stability and eco-friendly nature. Thus, in the present study, nanocrystalline MoO_3 has been synthesized by salvo thermal method and studied its phase, structure and electrochemical properties at different temperatures.

8.2 Experimental

All the chemicals were of AR grade and used without further purification. In a typical synthesis of MoO_3 nanocrystals, 2.47 g of ammonium molybdate tetrahydrate [$(NH4)_6Mo_7O_{24}.34H_2O$] was dissolved in deionized (DI) water (10 mL), and the solution was stirred for 30 min at room temperature for the complete dispersion. The solution was heated at 70 °C and introduced drop wise 3 mL nitric acid under stirring condition for 1 h. The final white mixture was taken out and washed with ethanol three times to remove impurities and loosely bonded atoms and dried in oven for 12 h at 60 °C. Further, the resultant synthesized product was annealed at different temperature such as 200 °C, 300 °C, 400 °C, and 500 °C for 3 h in order to characterization and application of MoO_3. The synthesized materials were named as M1, M2, M3, M4, and M5 for as synthesized, annealed at 200 °C, 300 °C, 400 °C, and 500 °C, respectively. The samples were characterized by X-ray diffraction (XRD), scanning electron microscope (SEM), UV–vis, and cyclic voltammetry.

8.3 Results and Discussion

8.3.1 XRD Analysis

The phase and crystalline nature of as-synthesized samples were characterized with a Rigaku X-ray diffractometer using Cu Kα radiation ($\lambda = 1.5406$ A°) operated at 40 kV and 30 mA, in the 2θ range of 10–70°. Figure 8.1a shows the XRD pattern of the samples M1, M2, M3, M4, and M5. XRD pattern confirms the hexagonal phases (h- MoO_3) for the samples M1, M2, and M3 (JCPDS file No-770354) and orthorhombic phases for the samples M4 and M5 with space group P_{bnm} (JCPDS file No-050508) and lattice parameters, $a = 3.954$, $b = 13.825$, and $c = 3.695$.

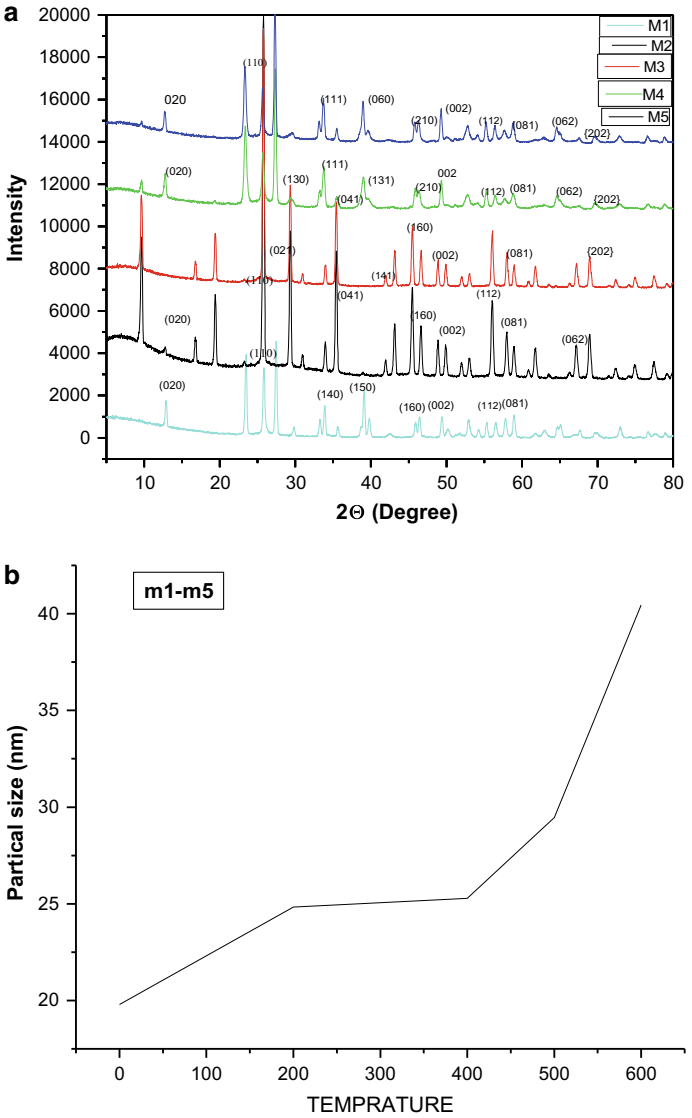

Fig. 8.1 **a** XRD pattern of MoO_3 samples M-1, M-2, M-3, M-4, and M-5, at room temperature, 200 °C, 300 °C, 400 °C, and 500 °C, respectively and **b** variation of particle size versus temperature

Phase of the material remains unchanged even after annealing at 400 °C. XRD result shows that there is sudden change from hexagonal phase to orthorhombic phase and crystallinity is also increase with temperature, i.e., stability increases and crystal strain decreases. Particle size, lattice strain, and bond lengths of the samples at different temperatures are given in the Table 8.1. The particle size of the MoO_3

Table 8.1 Particle size, strain, and bond lengths of the samples at different temperatures

S. No.	Samples	Particle size. (nm)	Lattice strain	Bond Length (nm)
1	M1	19.79	0.0083	4.3
2	M2	24.83	0.0065	4.5
3	M3	25.28	0.0060	4.3
4	M4	29.46	0.0052	4.8
5	M5	40.45	0.0038	4.4

nanomaterial is calculated by Scherer formula given by [11],

$$d = \frac{0.9\lambda}{\beta \cos\theta}$$

where d is the crystallite size, λ is the wavelength of radiation used, cos θ is the Bragg angle, and β is the full-width at half-maximum measured in radian. The average crystallite size of as-synthesized sample and annealed samples are given in Table 8.1.

The variation of particle size with temperature is also shown in Fig. 8.1b. Here, graph shows that particle size remains nearly constant between the temperature range 200–400 °C.

8.3.2 SEM Analysis

SEM image is taken by Zeiss EVO MA 15 Scanning Electron Microscope. The morphology of the samples was analyzed with the SEM which is shown in Fig. 8.2. Figure 8.2a shows the SEM image of the as prepared MoO_3. Figure 8.2b shows the high resolution SEM image of the MoO_3 at 300 °C with an average length of 29.72 μm and diameter 0.3 μm. Figure 8.2c shows the SEM image of the MoO_3 at 400°C. We see that as the temperature increases at 400 °C, and the morphology of the samples is changed due to temperature effect, and nanorods are converted into nanosheets which is also confirmed by XRD result.

8.3.3 UV-Vis Analysis

The UV-Vis absorption spectra were carried out by Shimadzu UV-2330 spectrometer in the spectral range of 200–800 nm. The samples were dispersed in double distilled water, and double distilled water is taken as reference. Figure 8.3 shows the optical absorption spectra of the samples. Generally, absorption in solids occurs by various mechanisms, in all of which the photon energy is absorbed either by the lattice or

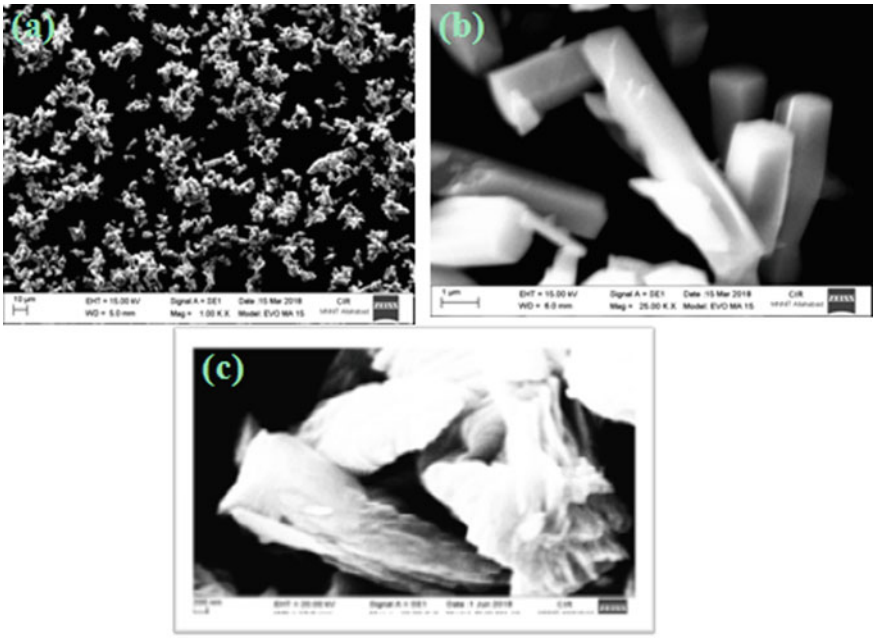

Fig. 8.2 **a** SEM image of as prepared sample, **b** high resolution SEM image of the sample at 300 °C, and **c** SEM image of the sample at 400 °C

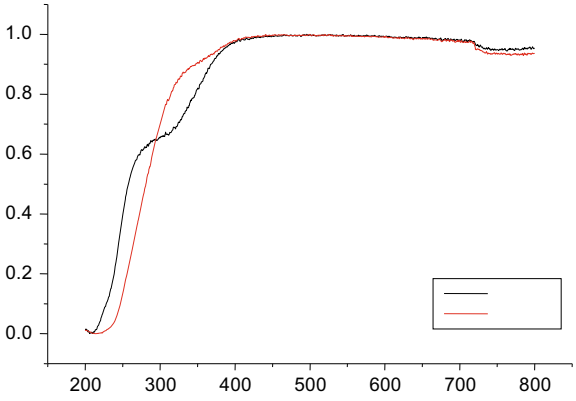

Fig. 8.3 Optical absorption spectra of as-synthesized sample and annealed sample at 400 °C

by electrons where the transferred energy is conserved. The lattice absorption will give information about the atomic vibrations involved. The higher energy parts of the spectrum particularly those associated with the interband electronic transition will provide the information about electron states. In this process, the electrons are excited from filled to an empty band by the photon absorption, as a consequence a

sharp increase in absorption coefficient will occur. The onset of this rapid change in absorption coefficient is called the fundamental absorption edge, and corresponding energy is defined as optical energy gap, E_g.

By knowing the value of absorbance, the optical band gap of MoO_3 nanomaterial is determined by the formula [11],

$$\alpha = \frac{A(hv - E_g)^m}{hv}$$

where α is the absorption coefficient, A is constant, E_g is the optical band gap, and m characterizes the nature of transition. The value of m may be 1/2, 2, 3/2, and 3 for allowed direct, allowed indirect, forbidden direct, and forbidden indirect transitions, respectively. The optical band gaps obtained are 4.5 eV and 4.2 eV for as-synthesized and annealed MoO_3 at 400 °C, respectively.

8.3.4 Electrochemical Analysis

The electrochemical properties of the samples were characterized using Metrohm Autolab PGST302N having three electrode, Ag/AgCl as reference electrode, Pt wire as a counter electrode and MoO_3 as a working electrode at room temperature. The cyclic voltammetry experiment was performed in 1 M Na_2SO_4 electrolyte at different scan rates as 5, 10, 20, 50, 100, and 200 mV/s. The working electrode was prepared by mixing 80 wt% active material (MoO_3), 15 wt% conducting agent (Carbon black) and 5 wt% polyvinylidene fluoride. These electrodes were used for cyclic voltammetry characterization to understand the electrochemical behavior of the MoO_3 nanomaterial. Figure 8.4 shows the cyclic voltammetry curves of the α-MoO_3 nanorods prepared at 400 °C (M4 sample) because this sample shows more conductivity than other samples. The cyclic voltammetry curves show faradic redox behavior which indicates the pseudocapacitive nature of the sample. The electrochemical Na^+ insertion process is given by the reaction as [12].

$$MoO_3 + xNa^+ + xe^- \leftrightarrow Na_xMoO_3$$

The areal current drawn under the cyclic voltammetry curve is maximum for scan rate 200 mv/s for the M4 sample. These curves show that the areal current areal current increases with respect to scan rate due to slower Na^+ ions transfer rate at higher scan rates. Specific capacitance of the samples is calculated by the formula given as [13]

$$C_s = \frac{1}{mv\Delta V}\int_{V_1}^{V_2} IdV$$

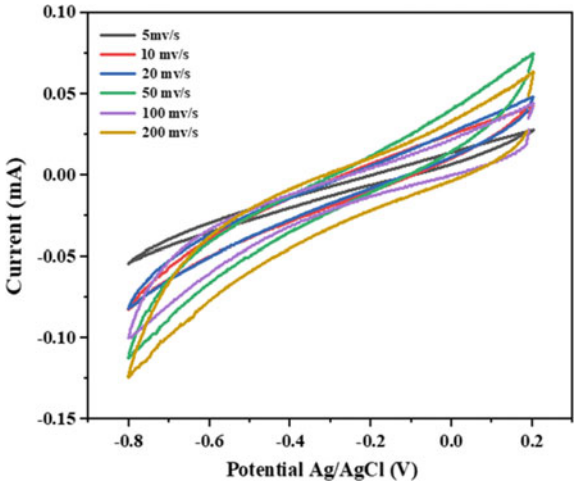

Fig. 8.4 Cyclic voltammetry curve of MoO_3 annealed at 400 °C

where m is the mass of the active material used in the electrodes, v is the scan rate, I is the current density, and ΔV is potential drop during discharge from V_1 to V_2. The measured specific capacitances of the samples prepared at room temperature, at 200 °C, 300 °C, 400 °C, and 500 °C are 105 F/g, 135 F/g, 160F/g, 185 F/g, and 90 F/g, respectively. The influence of current density on the electrode active area is mainly due to the effective utilization of active material for Na^+ ion insertion. The high specific capacitance of the sample prepared at 400 °C is due to uniform nanorod like surface morphology with the increased surface to volume ratio [14].

8.4 Conclusions

We have successfully synthesized MoO_3 nanorods by the salvo thermal method and improve the stability of crystallinity with annealing the samples. Strains are also decreased with temperature. The nanorod structure is confirmed at 400 °C by SEM analysis and cyclic voltammetry analysis confirm that the sample at 400 °C shows maximum specific capacitance than other samples. Thus, MoO_3 nanorods may be suitable for super capacitors.

Acknowledgements Authors are thankful to the Head, department of physics, M.N.N.I.T. Allahabad for providing XRD, SEM, UV-vis and cyclic voltammetry facilities.

References

1. X. Zhao, B.M. Sanchez, P.J. Dobson, P.S. Grant, The role of nanomaterial in redox-based supercapacitor for next generation energy storage devices. Nanoscale **3**, 839−855 (2011)
2. A. Gonzalez, E. Goikolea, J.A. Barrena, R. Mysyk, Review on supercapacitors: technologies and materials. Renew. Sustain. Energy Rev. **58**, 1189–1206 (2016)
3. Y. Liu, B. Zhang, Y. Yang, Z. Chang, Z. Wen, Y. Wu, Polypyrrole-Coated α-MoO3 nanobelts with good electrochemical performance as anode materials for aqueous supercapacitors. J. Mater. Chem. A **1**, 13582–13587 (2013)
4. Z.S. Iro, C. Subramani, S.S. Dash, A brief review on electrode materials for supercapacitor. Int. J. Electrochem. Sci. **11**, 10628–10643 (2016)
5. K.H. Chang, C.C. Hu, Oxidative synthesis of $RuO_2{\cdot}nH_2O$ with ideal capacitive characteristics for supercapacitors. J. Electrochem. Soc. **151**, A958–A964 (2004)
6. V. Kang, T. Yu, G.H. Lim, T. Koh, B. Lim, Facile synthesis of carbon supported, ultra small ruthenium oxide nanocrystals for supercapacitor electrode materials. Chem. Phys. Lett. **592**, 192–195 (2014)
7. N.A. Chernova, M. Roppolo, A.C. Dillon, M.S. Whittingham, Layered vanadium and molybdenum oxides: batteries and electrochromics. J. Mater. Chem. **19**, 2526–2552 (2009)
8. X. Xia, Q. Hao, W. Lei, W. Wang, H. Wang, X. Wang, Reduced-graphene oxide/molybdenum oxide/polyaniline ternary composite for high energy density supercapacitors: synthesis and properties. J. Mater. Chem. **22**, 8314–8320 (2012)
9. Y. Shi, B. Guo, S.A. Corr, Q. Shi, Y.-S. Hu, K.R. Heier, L. Chen, R. Seshadri, G.D. Stucky, Ordered mesoporous metallic MoO_2 materials with highly reversible lithium storage capacity. Nano Lett. **9**(12), 4215–4220 (2009)
10. Y. Zhu, X. Xu, G. Chen, Y. Zhong, R. Cai, L. Li, Z. Shao, Surfactant-free self assembly of reduced graphite oxide-MoO2 nanobelt composites used as electrode for lithium-ion batteries. Electrochim. Acta **211**, 972–981 (2016)
11. R. Kripal, A.K. Gupta, R.K. Srivastava, S.K. Mishra, Photoconductivity and photoluminescence of ZnO nanoparticles synthesized via co-precipitation method. Spectrochimica Acta Part A **79**, 1605–1612 (2011)
12. N.G. Prakasha, M. Dhananjaya, A.L. Narayana, D.P.M.D. Shaik, P. Rosaiahc, O.M. Hussain, High performance one dimensional α-MoO3 nanorods for supercapacitor applications. Ceram. Int. **44**(8), 9967–9975 (2018)
13. W. Zhang, Y. Tan, Y. Gao, J. Wu, B. Tang, J. Zhao, Amorphous nickel–boron and nickel–manganese– boron alloy as electrochemical pseudocapacitor materials. RSC Adv. **4**, 27800–27804 (2014)
14. C.C. Zhang, L. Zheng, Z.M. Zhang, R.C. Dai, Z.P. Wang, J.W. Zhang, Z.J. Ding, Raman studies of hexagonal MoO_3 at high pressure. Phys. Status Solidi B **248**(5), 1119–1122 (2011)

Chapter 9
Enhancement in Optical Absorbance of ZnO Nanoparticles by Introducing MoS_2 Nanosheets

Sarita Yadav

Abstract MoS_2 basically layered van der Walls material which have strong bonding between intralayer (Mo and S) and the weak bonding between interlayer, i.e. neighbouring planes of sulphur atoms, and therefore, these materials can easily exfoliate into few or monolayer. In this work, the nanosheets of MoS_2 are exfoliated using liquid exfoliation techniques followed by ultrasonication. Further, the exfoliated MoS_2 nanosheets are used to form the composite of MoS_2 and zinc oxide (ZnO). The formation of composite material is confirmed from the XRD. The band gap of ZnO nanoparticles is 3.2 eV. The ZnO/MoS_2 nanocomposite material shows less band gap (3.0 eV). The low band gap of composite material increases the absorption of light from ultraviolet to visible regime. The enhancement in light absorbance of composite material reveals that ZnO/MoS_2 has potential for highly active photocatalyst.

9.1 Introduction

The unusual properties of graphene created a tremendous breakthrough in 2D materials such as topological insulator, boron nitride, metal oxides and transition metal dichalcogenides (TMDs) [1–4]. Among TMDs, molybdenum disulphide (MoS_2) intensively studied due to its unique optical, chemical and electrical properties [5–7]. The layered structure of MoS_2 has weak van der Walls interaction between layers and strong in plane bonding, and therefore, it can easily exfoliate into few layers [8]. The bulk MoS_2 has indirect band gap which changed into direct band gap as the thickness of MoS_2 layers decreases from multilayers to monolayers. The transition in band gap of MoS_2 from indirect to direct band gap and high surface area with huge edge active sites in MoS_2 layers has great potential for photocatalyst [9, 10]. Photocatalysts are defined as materials that absorb light and produce charge carriers that enhance light induced reaction. A photocatalyst does not consumed in chemical reaction. Metal oxides, metal sulphides and oxysulphides are used as photocatalyst

S. Yadav (✉)
Physics Department, University of Allahabad, Prayagraj, India
e-mail: saritajnu@gmail.com

K. L. Pandey et al. (eds.), *Proceedings of the National Workshop on Recent Advances in Condensed Matter and High Energy Physics*, Springer Proceedings in Physics 278,
https://doi.org/10.1007/978-981-19-2592-4_9

[11–13]. Among of them the most popular photocatalysts are ZnO and TiO_2 due to its lower cost and higher stability. Particularly, nanoparticles and nanorods of ZnO are promising photocatalyst due to its direct band gap, high exciton binding energy and large charge carrier mobility. But in visible light irradiation, the photocatalytic activity is reduced due to wide-band gap and large recombination rate of photogenerated charge carriers. The limitation of absorption of visible light by ZnO can be overcome by synthesizing mixed material which increases the absorption of light resulting higher photocatalytic effect. MoS_2 has layered structure and narrow-band gap which absorb sunlight in visible region. Due to unique layered structure, MoS_2 sheets can be mixed with ZnO to form composite material. The low-band gap of composite material increases the light absorption in both visible and UV regime and enhances the charge separation ability of photogenerated charge carriers. Therefore, in this work, we have synthesized composite of ZnO nanoparticles with MoS_2 nanosheets to increases the absorption of sunlight from UV region to visible regime.

9.2 Experimental Details

9.2.1 Materials

MoS_2 powder (<2 μm, 99%), zinc acetate ($Zn(CH_3COO)_2$) and sodium hydroxide (NaOH) were purchased from Sigma Aldrich. Chemicals were used without any further purification.

9.2.2 Synthesis of Zinc Oxide Nanoparticles

Zinc acetate and sodium hydroxide were used for synthesis of ZnO nanoparticles. The solution of 0.125 M $Zn(CH_3COO)_2$ and 0.25 M NaOH was prepared in ethanol–water mixed (1:2) solution. The 60 ml NaOH solution was added dropwise in 30 ml $Zn(CH_3COO)_2$ solution at 60 °C under constant stirring. White precipitate occurred in solution after completion of reaction. The formed precipitated solution was centrifuged to separate the precipitate. The precipitate was washed several times with double distilled water. The obtained precipitate dried completely. Finally, the precipitate was crushed by mortar and the obtained fine powder which consists ZnO nanoparticles.

9.2.3 Synthesis of MoS_2 Nanosheets

Facile liquid exfoliation technique has been used for synthesis of MoS_2 nanosheet. For the synthesis of MoS_2 nanosheet, 200 mg MoS_2 powder was dissolve in 60 ml ethanol–water mixed solution and continuously ultra-sonicated for 6 h. The MoS_2 solution were centrifuged for 20 min at 5000 rpm. The supernatant consists MoS_2 nanosheets. Now, MoS_2 nanosheets solution were used for synthesis of composite material.

9.2.4 Synthesis of ZnO/MoS_2 Nanocomposite

The 15 mg ZnO nanoparticles were dispersed in 10 ml MoS_2 nanosheets solution and vigorously sonicated for an hour to obtain composite of ZnO nanoparticles and MoS_2 nanosheets. The obtained nanocomposite was dried at 80 °C and used for further characterization.

9.3 Characterization Techniques

UV-Visible absorption spectra of synthesized samples were recorded by Perkin Elmer Lambda-35 double beam spectrophotometer. The spectral range for absorption spectrum was 250 nm to 1000 nm. The purity and crystallinity of synthesized sample were analysed by PROTOA-XRD diffractometer. A filtered Cu K_α radiation ($\lambda = 1.54$ Å) was used as a X-ray source.

9.4 Results and Discussions

Figure 9.1 shows the XRD of synthesized ZnO nanoparticles, MoS_2 nanosheets and ZnO/MoS_2 nanocomposite. XRD data of the exfoliated MoS_2 nanosheets have one strong peak and a weak peak with no other peaks related to bulk MoS_2, which suggests the exfoliated MoS_2 has nanosheets.

The diffraction peak at 14.8° and 40.0° can be assigned to (002) and (103). The XRD pattern of ZnO shows strong diffraction peaks at 32.3°, 34.8°, 36.7° and 44.0° corresponding to (100), (002), (101) and (102) planes of hexagonal wurtzite structure of ZnO [14]. Moreover, the broad diffraction peaks indicate the ZnO product comprised of ZnO nano particles with small size [15]. Scherrer's formula is used to find out the average diameter (d) of ZnO particles. The Scherrer's formula is given below [16]

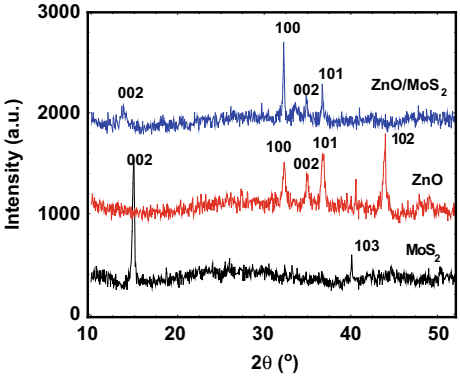

Fig. 9.1 XRD of synthesized MoS_2 nanosheets, ZnO nanoparticles and ZnO/MoS_2 nanocomposite

$$d = \frac{K\lambda}{\beta \cos\theta}$$

where λ (1.54 Å) is the wavelength of X-ray, K (0.89) is a shape factor, β is the full width at half maximum (FWHM) of diffraction peak and θ is the Bragg angle. The average diameter of ZnO particles is 19.3 nm. Figure 9.1 also shows the XRD pattern of ZnO/MoS_2 nanocomposite. A slight shift has been observed in diffraction peak of MoS_2 in nanocomposite but no change has been observed in diffraction peaks of ZnO nanoparticles. The XRD pattern of nanocomposite consists distinct lattice planes corresponding to MoS_2 nanosheets, and ZnO nanoparticles clearly reveal the existence of individual components of MoS_2 and ZnO in nanocomposite.

The UV-Vis spectra of synthesized ZnO nanoparticles, and ZnO/MoS_2 nanocomposites are shown in Fig. 9.2. In ZnO, nanoparticles mainly absorption occurs below 500 nm with absorption peak at 357.8 nm. MoS_2 can absorb the visible region of light due to its narrow-band gap. Therefore, the incorporation of MoS_2 nanosheets in ZnO nanoparticles increases the absorption of light from ultraviolet to visible region. Tauc plots for direct band gap of UV-V is spectra are shown in the inset of Fig. 9.2. Tauc plots clearly indicate that incorporation of MoS_2 nanosheets decreases the band gap of ZnO from 3.2 eV to 3.0 eV. The ZnO/MoS_2 nanocomposite could facilitate towards a good photocatalysts because the absorbance of ZnO/MoS_2 nanocomposite is larger than that of ZnO nanoparticles over the total UV-Visible region, and also the band gap of ZnO/MoS_2 nanocomposite is lower than that of ZnO nanoparticles.

9.5 Conclusions

In summary, in this work, we have successfully synthesized ZnO/MoS_2 nanocomposite. Liquid exfoliation is used to synthesize the nanosheets of MoS_2, and sol gel

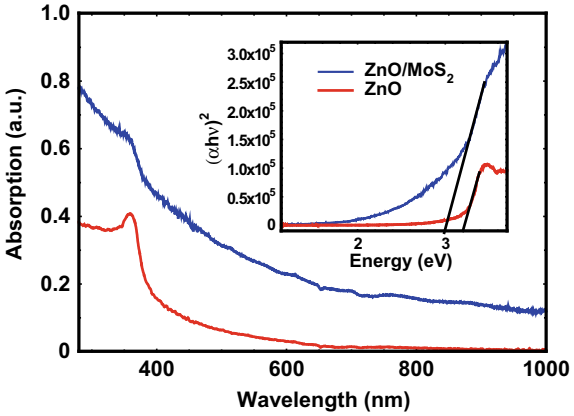

Fig. 9.2 UV-V is spectra of synthesized ZnO nanoparticles and ZnO/MoS_2 nanocomposite. Inset shows the Tauc plot of synthesized ZnO nanoparticles and ZnO/MoS_2 nanocomposite

method is used for synthesis of ZnO nanoparticles. The average size of ZnO nanoparticles is 19.3 nm. The presence of distinct diffraction planes of MoS_2 and ZnO in XRD pattern of ZnO/MoS_2 nanocomposite clearly reveals the existence of individual components of MoS_2 and ZnO. The UV-V is spectra of ZnO/MoS_2 nanocomposite and shows the enhancement in absorption in entire UV-V and is region compare to that of ZnO nanoparticles. Therefore, ZnO/MoS_2 nanocomposite have great potential for photocatalyst.

Acknowledgements This work is financially supported by Department of Science and Technology through Inspire Faculty award (DST/INSPIRE/04/2016/001600). SY gratefully acknowledge the instrument facilities available in Physics Department, University of Allahabad, Prayagraj.

References

1. S.-H. Choi, Unique properties of graphene quantum dots and their applications in photonic/electronic devices. J. Phys. D: Appl. Phys. **50**, 103002 (2017)
2. M.G. Rasul, A. Kiziltas, B. Arfaei, R. Shahbazian Yassar, 2D boron nitride nanosheets for polymer composite materials. npj 2D Mater. Appl. **5**, 56 (2021)
3. A.G.M. Ferrari, J. Rowley-Neale, C.E. Banks, Recent advances in 2D hexagonal boron nitride (2D-hBN) applied as the basis of electrochemical sensing platforms. Anal. Bioanal. Chem. **413**, 663 (2021)
4. P. Kumbhakar, et al., Emerging 2D metal oxides and their applications. Mater. Today **45**, 142 (2021)
5. G.A. Ermolaev, et al., Broadband optical properties of monolayer and bulk MoS_2. npj 2D Mater. Appl. **4**, 21 (2020)
6. S. Yadav, P. Chaudhary, K.N. Uttam, A. Varma, M. Vashistha, B.C. Yadav,Facile synthesis of molybdenum disulfide (MoS_2) quantum dots and its application in humidity sensing. Nanotechnology **30,** 295501 (2019)

7. X. Liab, H. Zhu, Two-dimensional MoS_2: properties, preparation, and applications. J. Materiomics **1**, 33 (2015)
8. C.Z. Magda, J. Peto, G. Dobrik, C. Hwang, L.P. Biro, L. Tapaszto, Exfoliation of large area transition metal chalcogenide single layer. Sci. Rep. **5**, 14714 (2015)
9. M. Sabarinathan, S. Harish, J. Archana, M. Navaneethan, H. Ikeda, Y. Hayakaw, Highly efficient visible-light photocatalytic activity of MoS_2–TiO_2 mixtures hybrid photocatalyst and functional properties. RSC Adv. **7**, 24754 (2017)
10. S. Huang, C. Chen, H. Tsai, J. Shayac, C. Lu, Photocatalytic degradation of thiobencarb by a visible light-driven MoS_2 photocatalyst. Sep. Purif. Technol. **197**, 147 (2018).
11. X. Chen, Z. Wu, D. Liu, Z. Gao, Preparation of ZnO Photocatalyst for the Efficient and Rapid Photocatalytic Degradation of Azo Dyes. Nanoscale Res. Lett. **2**, 143 (2017)
12. Y. Shiga, N. Umezawa, N. Srinivasan, S. Koyasu, E. Sakaia, M. Miyauchi, A metal sulfide photocatalyst composed of ubiquitous elements for solar hydrogen production. Chem. Commun. **52**, 7470 (2016)
13. Q. Wang, et al., Oxysulfide photocatalyst for visible-light-driven overall water splitting. Nat. Mater. **18**, 827 (2019)
14. S. Bhatia, N. Verma, Photocatalytic activity of ZnO nanoparticles with optimization of defects. Mater. Res. Bull. **95**, 468 (2017)
15. Z. Chen, X.X. Li, G. Dua, N. Chen, A.Y.M. Suen, A sol–gel method for preparing ZnO quantum dots with strong blue emission. J. Lumin. **131**, 2072 (2011)
16. N. Yadav, P. Chaudhary, K.K. Dey, S. Yadav, B.C. Yadav, R.R. Yadav, Non-functionalized Au nanoparticles can act as high performing humidity sensor. J. Mater. Sci. Mater. Electron. **31**, 17843 (2020)

Chapter 10
Effect of Different Ablation Time of ns-pulsed Laser on the Synthesis of Silver Nanoparticles in Liquid

Prahalad Prasad Paroha, Gaurav Kumar Yogesh, Birendra Singh, Kamlesh Yadav, and Anurag Tewari

Abstract In the present report, we have studied the effect of nanosecond pulsed laser irradiation time on the particle abundance, morphology, and optical properties of silver nanoparticles (Ag-NPs). High-resolution transmission electron microscopy, selected area diffraction pattern, and UV-visible absorption spectroscopy were used to characterize morphological, structural, and optical properties of the Ag-NPs. The prolonged laser irradiation above 60 min demonstrates the melting and diffusion-induced aggregation of Ag-NPs. The statistical evaluation of various particles under different irradiation durations reveals uniform and monodispersed particle distribution for only 60 min of ablation duration.

10.1 Introduction

The recent surge in the intensive investigation to obtain colloidal noble metal nanoparticles (NPs) arises due to the size-dependent optical, electrical, and physicochemical properties caused by the high surface-to-volume ratio [1, 2]. The red or yellow color indicates colloidal gold and Ag-NPs, observed by the naked eye even at pico-molar concentration, resulting from absorption and scattering of light through these gold and Ag-NPs [3]. Ag-NPs are widely explored in various areas such as optoelectronic, biological labeling, surface-enhanced Raman spectroscopy, clad-modified optical fiber sensors, antibacterial, and photocatalysis [2, 4–8]. Different chemical processes, including biological synthesis, ultrasonic treatment, microwave-assisted

P. P. Paroha · G. K. Yogesh (✉) · B. Singh · A. Tewari
Department of Basic Science and Humanities, Pranveer Singh Institute of Technology, Kanpur 209305, India
e-mail: yogeshgaurav26@gmail.com; gaurav.yogesh@psit.ac.in

G. K. Yogesh
Department of Physics, National Institute of Technology, Tiruchirappalli 620015, India

K. Yadav
Department of Physics, School of Basic Sciences, Central University of Punjab, Bathinda, Punjab 151401, India

K. L. Pandey et al. (eds.), *Proceedings of the National Workshop on Recent Advances in Condensed Matter and High Energy Physics*, Springer Proceedings in Physics 278,
https://doi.org/10.1007/978-981-19-2592-4_10

techniques, and solvothermal, have been explored in the last two decades [1, 5, 9]. Previously, several researchers employed the naturally occurring biological extract, micro-organisms such as bacteria, fungus, and Curcuma longa tuber powder as reductants and as surfactant molecules for producing Ag-NPs [1, 5, 7, 10]. A typical chemical method reduces silver salts under borohydride (strong reductants) and sodium citrate (weak reductants). The reductants usually show less control over the particle size distribution, such as borohydride results in smaller particle sizes but fail to increase the particle as expected. In comparison, sodium citrate demonstrates the converse effects as borohydride. Thus, a facile and green method is needed to obtain controlled growth, stable with unique functional properties colloidal nanoparticles.

Apart from the chemical methods, the physical method widely used for synthesizing Ag-NPs is pulsed laser ablation of solid or metal salt in solution [11]. The pulsed laser ablation in liquid (PLAL) is a well-known green, inexpensive, and facile physical method for fabricating ultrapure colloidal Ag-NPs [4, 12, 13]. Initially, the Ag-NPs were prepared by the laser ablating the solid target with/without a surfactant-containing solution. Later, pulsed laser ablation of silver salts in solution was used to generate Ag-NPs [4]. Although PLAL is regarded as easy and green technique. However, it also demonstrates uncontrollable growth, a significant amount of polydispersity in shape and size, etc. [11]. The recent investigation reveals that optmized laser irradiation parameters (ablation duration, solvent and laser wavelength) can effectively control the resizing and reshaping Ag-NPs through melting and fragmentation process .

This work aims to study the formation and resize Ag-NPs under the different laser irradiation duration of silver salt in the presence of surfactant. The dependence of particle growth and resizing was studied for different ablation durations of the silver salt aqueous solution under a constant surfactant solution.

10.2 Experiments

In the current studies, commercially available silver nitrate and sodium dodecyl sulfate SDS ($AgNO_3$, $NaC_{12}H_{25}SO_4$, Alfa Aesar, and spectrum India) were used without further purification in this study. 0.1 M (5 ml water) of SDS was mixed with 0.01 M (50 ml water) of silver nitrate to obtain a standard silver nitrate solution. Then, the silver nitrate solution was irradiated by an ns-pulsed laser. The silver nanoparticles were synthesized using Nd: YAG pulsed laser (Quanta Ray Spectra-Physics 230-10). The laser was operated at 1064 nm wavelength, pulse duration of 10 ns, and repetition rate of 10 Hz with constant output energy at 500 mJ of unfocussed beam calculated at the wall of the glass beaker. Four different samples were prepared at continuous energy (500 mJ) with 20, 40, 60, and 80 minutes of ablation duration of the same samples.

10.3 Characterization

The optical absorption spectra of colloidal Ag-NPs were recorded using a double beam spectrometer (JASCO, Model: V-670) from 200 to 700 nm. High-resolution transmission electron microscopic (HRTEM) (JEOL 2010, Model: JSM, 200 kV) analysis of colloidal CNPs was recorded for evaluating the average particles sizes. A few drops of colloidal CNPs were placed on the carbon-coated copper grid and allowed to evaporate at room temperature before analysis. The average particle size of Ag-NPs is estimated by evaluating various particles using ImageJ software.

10.4 Result and Discussion

Figure 10.1 shows the experimental schematic diagram of PLAL technique for the synthesized Ag-NPs. The inset of Fig. 10.1 shows the digital snapshot image of colloidal Ag-NPs under different ablation duration (0, 20, 40, 60, and 80 min). After the 20 min of laser ablation, the color of ablating silver nitrate solution transformed into the brownish-yellows, which confirms the formation of Ag-NPs. As further laser ablation progress, the intensity of colloidal Ag-NPs increases, which could arise to increase Ag-NPs concentration in colloidal solution (Fig. 10.1). Figure 10.2 demonstrates the HRTEM images of Ag-NPs synthesized under the different ablation duration. The morphological studies of as-synthesized Ag-NPs reveals the formation of uniform and monodispersed silver particles in the first 20 nm of laser ablation. In the next 40, 60, and 80 min of laser ablation, aggregation and transformation of Ag-NPs were observed. It is also evident from the HRTEM images that the Ag-NPs

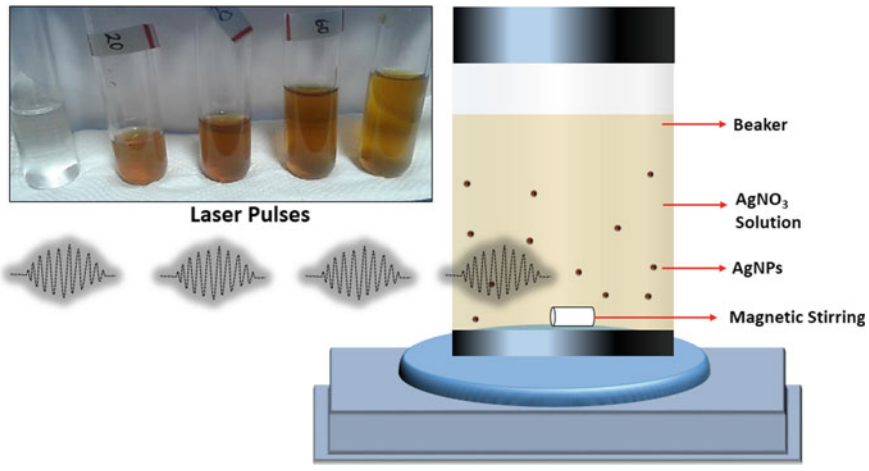

Fig. 10.1 Snapshot image of colloidal Ag-NPs synthesized by pulsed laser ablation in liquid

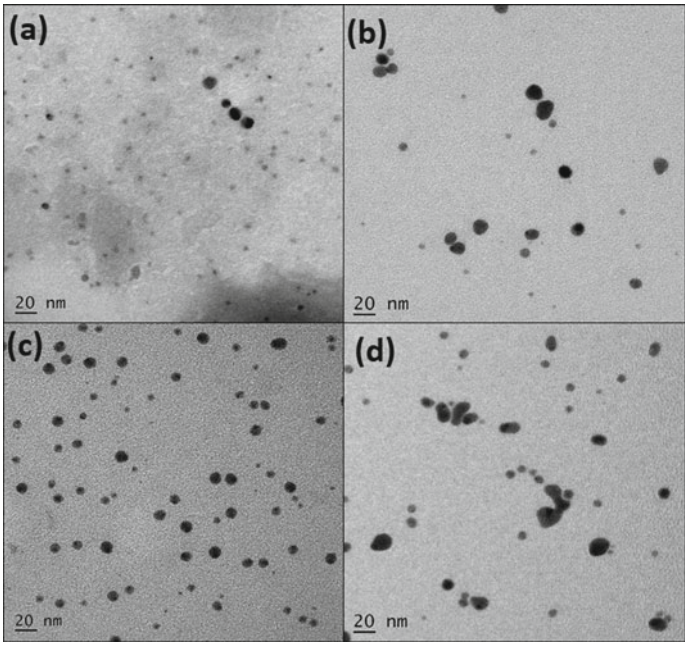

Fig. 10.2 HRTEM images of Ag-NPs synthesized under the different pulsed laser ablation duration **a** 20 min, **b** 40 min, **c** 60 min, and **d** 80 min

get aggregated through the melting and fusion of smaller size particles. The statistical evaluation of various particles reveals the average particle size is found to be around 2.5, 8.4, 7.3, and 11.7 nm, respectively. Thus, it was observed that an increased ablation duration increased in average particle size. However, for 40 of laser ablation duration, the average particle size of Ag-NPs is slightly higher than 60 min, except for the broad particle size distribution. While the Ag-NPs are under the 20 and 60 min ablation duration, the particle distribution is highly monodispersed and uniform. At the end of 80 min of ablation, the aggregated particles significantly increased. The selected area diffraction (SAED) pattern analysis of as-synthesized Ag-NPs reveals diffused ring that corresponds to the mixed amorphous or polycrystalline crystal structure (Fig. 10.4a–d) [10, 14]. The measured distance between the two reflection points in each SAED pattern is found to be around 0.75–0.80 nm^{-1}, which is close to the lattice spacing of 0.23 nm of the FCC crystal structure of Ag-NPs [10]. At the same time, the lattice spacing (0.25 ± 0.02 nm) was estimated from the SAED pattern displays a slightly larger than 17% (Table 10.1). In general, several researchers were also observed the expansion and contraction of lattice spacing in various kinds of nanostructure materials (Fig. 10.3).

Figure 10.5a shows the absorbance spectra of Ag-NPs for different ablation duration. It is noted that the intensity of absorbance gradually increases as the ablation

Table 10.1 SAED pattern analysis of Ag-NPs

	20 Min	40 Min	60 Min	80 Min
2R ring diameter (nm^{-1})	7.5	8.0	8.0	7.4
Interplanar spacing (nm)	0.26	0.25	0.25	0.27

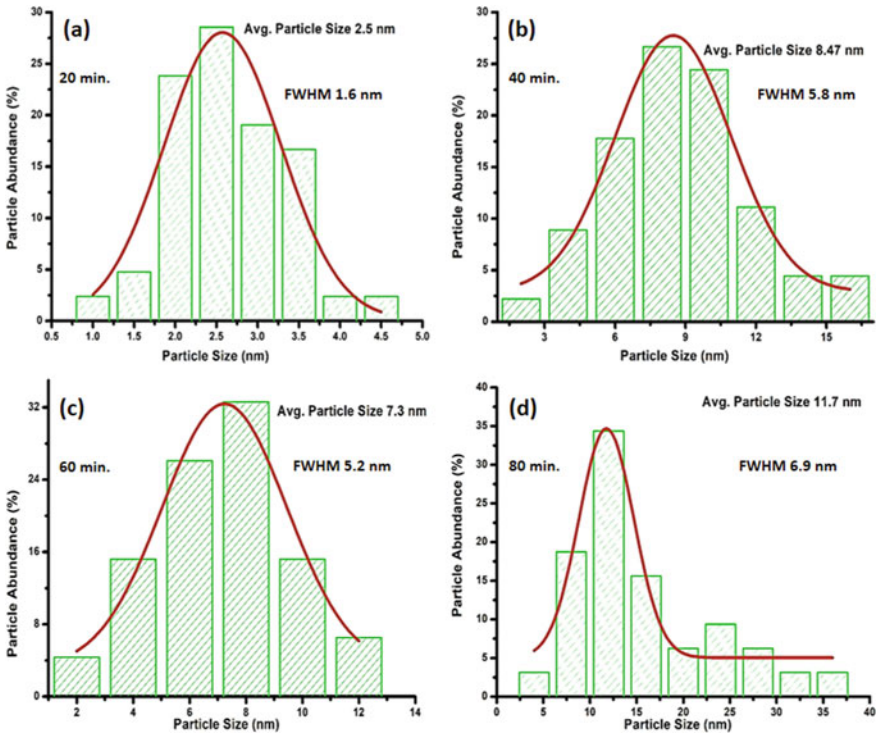

Fig. 10.3 Statistical evaluation of Ag-NPs synthesized under the different pulsed laser ablation duration **a** 20 min, **b** 40 min, **c** 60 min, and **d** 80 min

duration increases. The appearance of the single peak positioned at 410 nm corresponds to the longitudinal plasmon resonance indicated the nearly spherical shape of Ag-NPs [15, 16]. In the case of the non-spherical (ellipsoidal) nanoparticles, two peaks exist instead of a single peak [15]. The laser irradiation can effectively change the morphology of the nanoparticles, but such a thing does not appear in the UV absorption spectra. After the laser irradiation for 20, 40, 60, and 80 min, no such shift occurs absorbance band is observed. Thus, it indicated that the morphology of the nanoparticles had remained the same in all cases. The peak enhancement in the longitudinal direction supports the change in particles size with the increase in the irradiation time unless the dielectric constant of the media is kept constant. In PLA, the light is mainly scattered on the surface of the particles; therefore, the surface

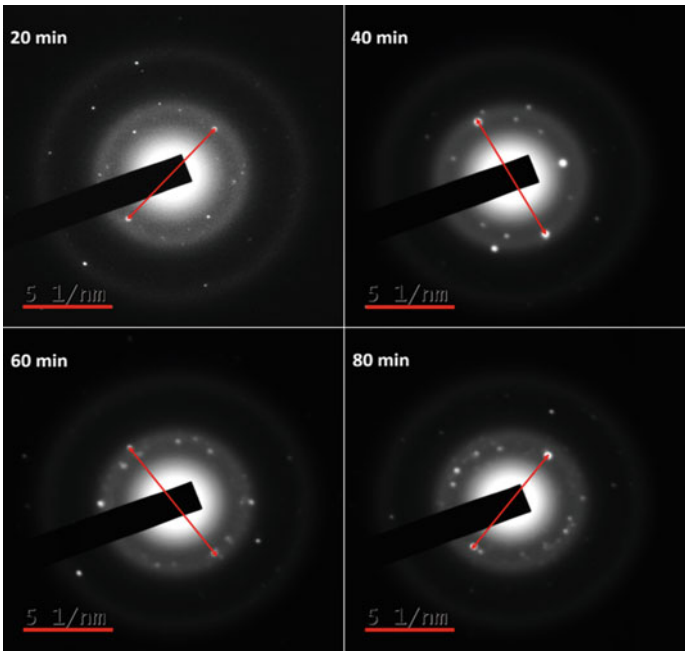

Fig. 10.4 SAED. Pattern analysis of Ag-NPs synthesized under different ablation durations

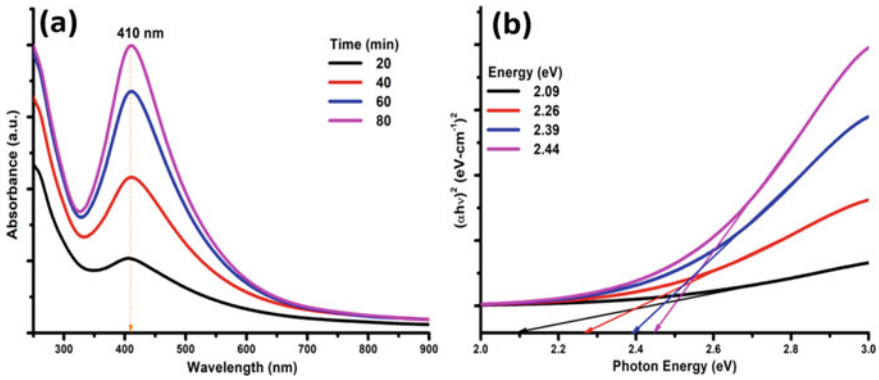

Fig. 10.5 **a** UV-Vis absorption spectra, **b** direct and indirect band of Ag-NPs synthesized at 20, 40, 60, and 80 min of laser ablation duration

plasmon frequency of the free electron oscillation is shifted from the UV region to the visible region of the spectrum. The plasmon frequency of nanoparticles is in the visible part only for the three metals Au, Ag, and Cu nanoparticles; for others, it shifts to the UV regions [17].

Figure 10.5b demonstrated Ag-NPs direct optical band gap, obtained from extrapolating the Tauc plot. The absorption coefficient of absorbance spectra is related to the optical band gap that has been calculated by using the relation

$$\alpha h\nu = A\left(h\upsilon - E_g\right)^{1/2}$$

where α is the absorption coefficient, $h\upsilon$ is the photon energy, h is the plank constant, and E_g is the direct optical band gap of Ag-NPs. Figure 5b shows the variation of $(\alpha h\nu)^2$ with the photon energy $h\upsilon$. The linear region of the curve was extrapolated at the energy axis to determine the band gap of Ag-NPs. The observed band gap of Ag-NPs is around 2.09 to 2.44 eV, which is concurrent with previously reported results [18].

10.5 Ag-NPs Formation in Solution

Over the decades, several researchers proposed the mechanism for forming Ag-NPs under the pulsed laser irradiation of silver salt in water [19, 20]. Figure 10.6 demonstrates the formation and transformation of Ag-NPs under the ns-pulsed laser ablation. The effect of ablation duration shows that the basic Ag-NPs formation

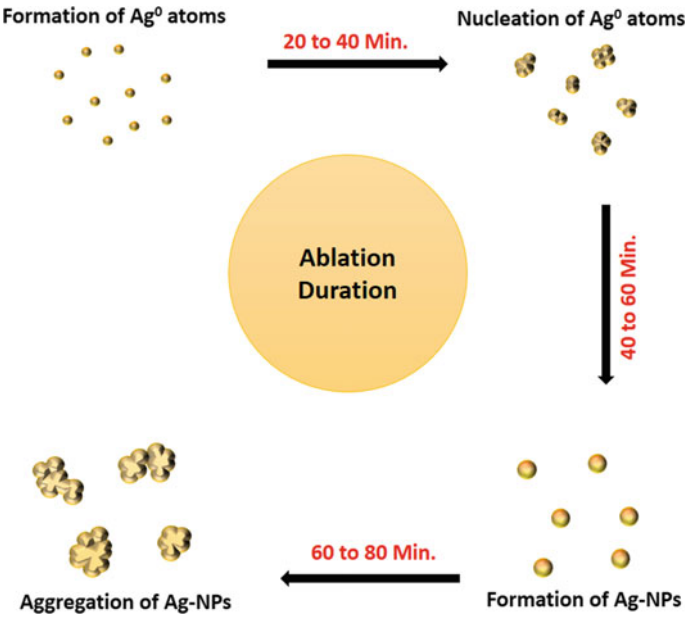

Fig. 10.6 Schematic diagram of formation and transformation of Ag-NPs under nanosecond pulsed laser

process proceeds sequentially. The dynamic formation mechanism of Ag-NPs under the PLAL method comprises of three stages (I) generation of silver plume consisting of silver atoms, (II) embryonic silver nuclei growth under the plasma plume, and (III) supply of silver atoms through diffusion along with capping of Ag-NPs surfactant [21]. The SDS surfactant covering over the Ag-NPs avoids the re-aggregation Ag-NPs. The neutral silver atoms were formed by absorbing the solvated electron and hydrogen radical ions during reducing silver ions. [19]. The photolysis of water molecules via the multiphoton absorption process had such solvated electron and hydrogen radicals. The absorbed energy (7 eV) exceeds the 6.7 eV due to water's photodecomposition into solvated e^{-}_{aq}, $OH_{aq,}$ and H_{aq} radical [22, 23]. These radical species are much shorter in their lifetime. However, these species can quickly reduce the silver ions into their zero valence state through the following scheme.

$$Ag^{+} + e^{-}_{aq} \rightarrow Ag^{0}$$
$$Ag^{+} + H^{\cdot} \rightarrow Ag^{0} + H^{+}$$

The silver nuclei absorb the nearest neutral silver ions supplied by the silver salt's laser reduction. Further, the growth of Ag-NPs competes with termination steps by absorbing SDS anions over the Ag-NPs [22]. Herein, the HRTEM micrograph images also reveal melting and diffusion of nearest Ag-NPs once the ablation process is inefficient to provide the continuous silver neutral atoms. Thus, the growth of silver nanoparticles superseded the typical silver neutral absorption process, which later proceeds through aggregation and silver nanoparticles.

10.6 Conclusion

This work sucessfully prepared Ag-NPs by nanosecond pulsed laser ablation in the liquid (PLAL) technique. The influence of laser ablation duration on morphological and optical properties has been thoroughly investigated. A typical laser ablation duration directly affects particle formation and morphology. Herein, the observed band gap of the materials shows the inverse relationship with the particle size.

Conflict of Interest There is no conflict of interest among the authors.

References

1. K.M.M.A. El-nour, A. Al-warthan, R.A.A. Ammar, Synthesis and applications of silver nanoparticles. 135–140 (2010). https://doi.org/10.1016/j.arabjc.2010.04.008

2. M. Mashayekh, D. Dorranian, Size-dependent nonlinear optical properties and thermal lens in silver nanoparticles. Optik (Stuttg). **125**, 5612–5617 (2014). https://doi.org/10.1016/j.ijleo.2014.07.066
3. D. Paramelle, A. Sadovoy, S. Gorelik, P. Free, J. Hobley, D.G. Fernig, A rapid method to estimate the concentration of citrate capped silver nanoparticles from UV-visible light spectra. Analyst. **139**, 4855–4861 (2014). https://doi.org/10.1039/c4an00978a
4. A. Resano-Garcia, Y. Battie, A. Koch, A. En Naciri, N. Chaoui, Influence of the laser light absorption by the colloid on the properties of silver nanoparticles produced by laser ablation in stirred and stationary liquid. J. Appl. Phys. **117** (2015). https://doi.org/10.1063/1.4915277
5. R. Sankar, P.K.S.M. Rahman, K. Varunkumar, C. Anusha, A. Kalaiarasi, K.S. Shivashangari, V. Ravikumar, Facile synthesis of Curcuma longa tuber powder engineered metal nanoparticles for bioimaging applications. J. Mol. Struct. **1129**, 8–16 (2017). https://doi.org/10.1016/j.molstruc.2016.09.054
6. S. Jaworski, M. Wierzbicki, E. Sawosz, A. Jung, G. Gielerak, J. Biernat, H. Jaremek, Ł. Witold, B. Wo, J. Wojnarowicz, L. Stobi, A. Ma, M. Mazurkiewicz-pawlicka, Ł. Maciej, N. Kurantowicz, A. Chwalibog, Graphene oxide-based nanocomposites decorated with silver nanoparticles as an antibacterial agent. (2018)
7. J. Puišo, D. Jonkuviene, I. Mačioniene, J. Šalomskiene, I. Jasutiene, R. Kondrotas, Biosynthesis of silver nanoparticles using lingonberry and cranberry juices and their antimicrobial activity. Colloids Surfaces B Biointerfaces. **121**, 214–221 (2014). https://doi.org/10.1016/j.colsurfb.2014.05.001
8. I. Ivanišević, S. Milardović, P. Kassal, Recent advances in (Bio)chemical sensors for food safety and quality based on silver nanomaterials. Food Technol. Biotechnol. **59**, 216–237 (2021). https://doi.org/10.17113/ftb.59.02.21.6912
9. H. Wang, X. Qiao, J. Chen, S. Ding, Preparation of silver nanoparticles by chemical reduction method. Colloids Surfaces A Physicochem. Eng. Asp. **256**, 111–115 (2005). https://doi.org/10.1016/j.colsurfa.2004.12.058
10. L. Devi, S. Joshi, Ultrastructures of silver nanoparticles biosynthesized using endophytic fungi. J. Microsc. Ultrastruct. **3**, 29 (2015). https://doi.org/10.1016/j.jmau.2014.10.004
11. G.K. Podagatlapalli, S. Hamad, M. Ahamad Mohiddon, S. Venugopal Rao, Effect of oblique incidence on silver nanomaterials fabricated in water via ultrafast laser ablation for photonics and explosives detection. Appl. Surf. Sci. **303**, 217–232 (2014). https://doi.org/10.1016/j.apsusc.2014.02.152
12. R. Kaimal, G.K. Yogesh, D. Sastikumar, J.J. Wu, S. Anandan, M. Ashokkumar, Laser-assisted decoration of carbon nanotubes with palladium nanoparticles for application in electrochemical methanol oxidation. Bull. Mater. Sci. **44**, 125–135 (2021). https://doi.org/10.1007/s12034-021-02428-z
13. G.K. Yogesh, S. Shukla, D. Sastikumar, P. Koinkar, Progress in pulsed laser ablation in liquid (PLAL) technique for the synthesis of carbon nanomaterials: a review. Appl. Phys. A. **127**, 810–850 (2021). https://doi.org/10.1007/s00339-021-04951-6
14. N. Nagar, V. Devra, A kinetic study on the degradation and biodegradability of silver nanoparticles catalyzed Methyl Orange and textile effluents. Heliyon **5**, e01356 (2019). https://doi.org/10.1016/j.heliyon.2019.e01356
15. F. Mafuné, J. Kohno, Y. Takeda, T. Kondow, H. Sawabe, Formation and size control of silver nanoparticles by laser ablation in aqueous solution. J. Phys. Chem. B. **104**, 9111–9117 (2000). https://doi.org/10.1021/jp001336y
16. K.L. Kelly, E. Coronado, L.L. Zhao, G.C. Schatz, The optical properties of metal nanoparticles: the influence of size, shape, and dielectric environment. J. Phys. Chem. B. **107**, 668–677 (2003). https://doi.org/10.1021/jp026731y
17. A.V. Simakin, V.V. Voronov, G.A. Shafeev, Nanoparticle formation during laser ablation of solids in liquids. Phys. Wave Phenom. **15**, 218–240 (2007). https://doi.org/10.3103/S1541308X07040024
18. A. Aziz, M. Khalid, M.S. Akhtar, M. Nadeem, Z.A. Gilani, H.M.N. Ul Huda Khan Asghar, J. Rehman, Z. Ullah, M. Saleem, Structural, Morphological and optical investigations of

silver nanoparticles synthesized by sol-gel auto-combustion method. Dig. J. Nanomater. Biostructures. **13**, 679–683 (2018)
19. J.P. Abid, A.W. Wark, P.F. Brevet, H.H. Girault, Preparation of silver nanoparticles in solution from a silver salt by laser irradiation. Chem. Commun. **7**, 792–793 (2002). https://doi.org/10.1039/b200272h
20. F. Mafuné, J.Y. Kohno, Y. Takeda, T. Kondow, H. Sawabe, Structure and stability of silver nanoparticles in aqueous solution produced by laser ablation. J. Phys. Chem. B. **104**, 8336–8337 (2000). https://doi.org/10.1021/jp001803b
21. F. Mafuné, J. Kohno, Y. Takeda, T. Kondow, H. Sawabe, Structure and stability of silver nanoparticles in aqueous solution produced by laser ablation. J. Phys. Chem. B. **104**, 8333–8337 (2002). https://doi.org/10.1021/jp001803b
22. A.K. Priya, G.K. Yogesh, K. Subha, V. Kalyanavalli, D. Sastikumar, Synthesis of silver nano-butterfly park by using laser ablation of aqueous salt for gas sensing application. Appl. Phys. A Mater. Sci. Process. **127**, 1–12 (2021). https://doi.org/10.1007/s00339-021-04370-7
23. A.K. Priya, S.K. Rao, G.K. Yogesh, R.P., D. Sastikumar, Green synthesis of silver nanoparticles by pulsed laser ablation using Citrus Limetta juice extract for clad-modified fiber optic gas sensing application. **54**, (2021). https://doi.org/10.1117/12.2597642

Chapter 11
Investigation of Thermodynamical and Electro-Optical Properties of Nematic Liquid Crystals Dispersed with Low wt% $BaTiO_3$ Nanoparticles

U. B. Singh, Dheeraj Kumar Pandey, M. B. Pandey, and K. L. Pandey

Abstract Composite was prepared by dispersing barium titanate nanoparticles ($BaTiO_3$–NPs) into a multi-component liquid crystalline material having wide range room temperature nematic phase. The thermodynamic and electro-optical properties of the composite sample were studied along with pristine materials. Effect of $BaTiO_3$–NPs dispersion on various display parameters of nematic liquid crystals, namely threshold voltage and splay elastic constant have been observed. The host liquid crystals have nematic ordering which supports alignment of $BaTiO_3$–NPs parallel to the liquid crystals director, which consequently improves electro-optical parameters of the composite system.

11.1 Introduction

Liquid crystals (LCs) are fascinating organic materials being unique in their properties such as directional anisotropy like crystals and fluidity-like ordinary liquids [1, 2]. LC materials appeared as smart fluids for dispersion of nanostructures because of its elastic-mediated interactions between the medium, and alien objects which are dispersed into it. This elastic-mediated interaction facilitates self-assembly of nanostructures along the director field of liquid crystals. This assembly of nanostructures and LCs could be reoriented by external force for example: by applying electric and magnetic fields. Hence, assembly and orientation of the nanostructures

U. B. Singh (✉)
Department of Physics, Azim Premji University, Bhopal 462039, India
e-mail: ubsksk12@gmail.com

D. Kumar Pandey · M. B. Pandey (✉)
Department of Physics, Vikramajit Singh Sanatan Dharama College, Kanpur 208002, India
e-mail: mbpandey@gmail.com

K. L. Pandey
Department of Physics, Ewing Christian College, Prayagraj 211003, India

K. L. Pandey et al. (eds.), *Proceedings of the National Workshop on Recent Advances in Condensed Matter and High Energy Physics*, Springer Proceedings in Physics 278,
https://doi.org/10.1007/978-981-19-2592-4_11

could be altered in LCs. Because of this extra-ordinary property, LCs nanostructures as composites emerge a multi-disciplinary field of research which has attracted attention of scientist working in soft matter and nanoscience. On the other hand, LCs nanostructures composites are also useful in electro-optic devices based on LCs. In the last fifteen years, a tiny inclusion of carbon nanotubes [3], nanoparticles [4, 5], and quantum dots [6, 7] into LCs medium has been studied. Composite materials consisting of LCs dispersed with nanoparticles (NPs) have indeed attracted considerable scientific and technological interest, mainly because the incorporation of NPs enhances the electro-optical properties of the liquid crystals itself with ease of alignment of composites [8–11]. There are studies in which inclusion of metal NPs in LCs have changed the electro-optic response and other physical properties of the host medium [12, 13]. There are some reports which show that inclusion of ferroelectric NPs in LCs have changed the electro-optic response and alter the surrounding molecular alignment [14, 15]. The suspension of ferroelectric NPs can lead to enhancement of the orientational order of the LC medium due to the electrostatic interactions between the NPs and the LC molecules. Therefore, dispersions of NPs having ferroelectric properties might improve physical parameters of LCs which could be used in electro-optic devices. On the other hand, assembly and reorientation of ferroelectric NPs could be achieved in LC medium by applying external stimulus, for example, electric field. In the present work, we have prepared a composite by dispersing ferroelectric barium titanate ($BaTiO_3$) NPs into a room temperature nematic liquid crystalline material and studied the alignment of $BaTiO_3$–NPs into LCs medium. Further, we have investigated the thermodynamic and electro-optic properties of the composite along with pristine LCs which is reported here.

11.2 Experimental Techniques

A multi-component nematic liquid crystalline material (MDA-02-3835) has been procured from Merck, India. $BaTiO_3$–NPs have been procured from Sigma-Aldrich and are used without further treatment. The sizes of dispersed $BaTiO_3$–NPs are less than 50 nm. The composite is prepared by adding a small weight percentage of $BaTiO_3$–NPs (0.01%) in the nematic liquid crystalline materials. The composite is stirred in the isotropic phase of host LCs at 55 °C by using a magnetic vibrator, to get homogenous dispersions. Homogenous dispersion of $BaTiO_3$–NPs in LCs matrix and their alignment are examined under a polarized optical microscope (POM) with magnification (×200). The transition temperatures of the pure and dispersed samples were determined with the help of differential scanning calorimeter (DSC) of NETZSCH model DSC-200-F3-Maia. For electro-optic and dielectric measurements, the pristine LCs and composite are filled in the cells by capillary action. The cells have been made in the form of parallel plate capacitor using indium tin oxide (ITO)-coated glass electrodes. The thickness of the used cell was 7.2 ± 0.2 μm. The inner surfaces of cells have been coated with polymer and parallel rubbed for planar

alignment with a pre-tilt angle of ~5° (made by Instec, USA). To measure the transmission intensity, white light was passed through the cell, and intensity was recorded by a photo-detector (made by Instec, USA), and corresponding photo-voltage was measured with a six and half digit multi-meter of Agilent (model-34410A).

11.3 Results and Discussion

11.3.1 Thermodynamic and Optical Textures Studies

DSC thermogram showing heat flow with temperature for pristine NLC and composite of $BaTiO_3$–NPs is shown in Fig. 11.1. In order to get stabilized thermodynamic parameters, DSC was run at rate of 5.0 °C/min in the range 0–60 °C for initial two cycles, and then, final thermograms were recorded with scan rate of 2.5 °C/min which is given in Fig. 11.1. Thermodynamic study suggests that clearing temperature, which is nematic-to-isotropic transition temperature (T_{NI}) is enhanced in the case of composite because of the π–π and anisotropic interaction between $BaTiO_3$–NPs and host LC molecules. These interactions also improved the ordering of the nematic phase in the case of composite. Homogenous dispersions of $BaTiO_3$–NPs in NLC matrix were examined under POM. In most parts of the textures, the $BaTiO_3$–NPs dispersed uniformly into LCs matrix; however, few agglomerations were also seen. The optical textures under planar orientations of pure and composite samples were shown in Fig. 11.2a, b, respectively.

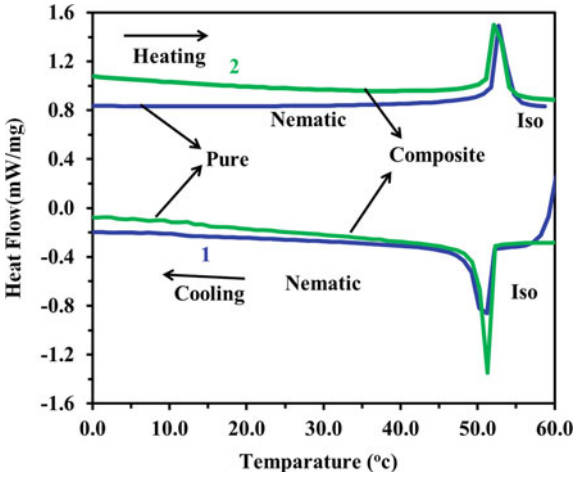

Fig. 11.1 DSC thermograms of the pristine (curve 1; blue) and 0.01 wt % $BaTiO_3$–NPs dispersed (curve 2; green) NLCs in the heating and cooling cycles at the scan rate of 2.5 °C/min

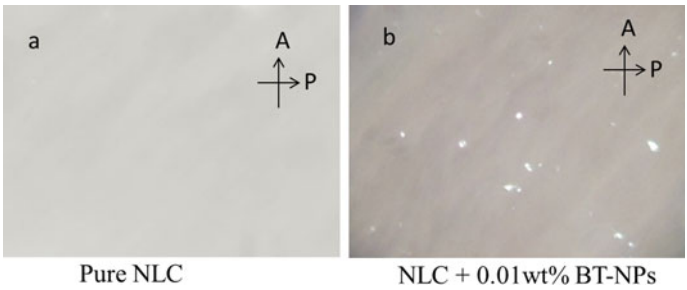

Fig. 11.2 Optical textures of pristine (**a**) and 0.01 wt % $BaTiO_3$–NPs dispersed NLCs (**b**) under crossed polarizer for planar anchoring of the samples at 30 °C

11.3.2 Electro-Optical Studies

The transmission–voltage (T–V) characteristics of the pristine NLCs and $BaTiO_3$–NPs dispersed system is carried out by applying an alternating voltage of 1 kHz with varying amplitude across the planar anchored cells (the molecular directors aligned parallel to the glass electrodes) and thereby measuring the intensity of transmitted light by a photo diode. By recording transmission intensity with applied field, T–V characteristics of the samples were drawn and shown in Fig. 11.3. Threshold voltage was determined from the drawn T–V curves. These experiments were performed at room temperature (30 °C). When the applied voltage was initially low, the LC molecules lie in the plane of the cell substrate because of the anchoring conditions and due to this bright state is obtained which corresponds to the maximum intensity

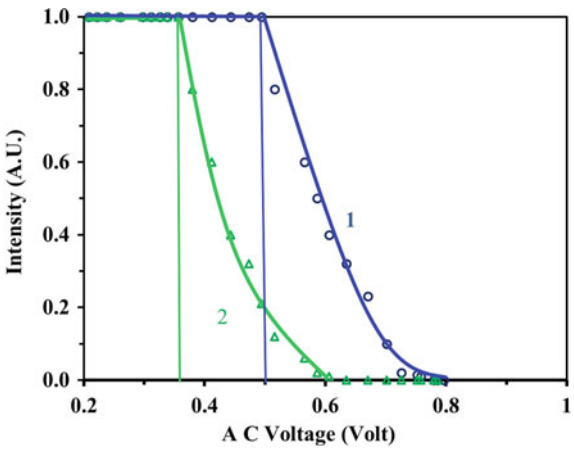

Fig. 11.3 Transmission–voltage (T–V) characteristic of the sample cell to the applied alternating voltage of frequency 1 kHz. Curves 1 (blue) and 2 (green) are corresponding to the pristine and 0.01 wt% $BaTiO_3$–NPs dispersed NLCs, respectively

Table 11.1 Transition temperature (T_{IN} in °C), threshold voltage (V_{th} in V), dielectric anisotropy ($\Delta\varepsilon'$), and splay elastic constant (K_{11} in pN) of pure NLCs and $BaTiO_3$–NPs dispersed sample

Sample	T_{IN}	V_{th}	$\Delta\varepsilon'$	K_{11}
NLCs pure	52.0	0.50	11.2	2.51
NLCs + 0.01 wt% $BaTiO_3$–NPs	56.0	0.35	11.6	0.94

on T–V curves. This state continues from low voltages up to 0.50 V for pure NLC and 0.35 V for 0.01% $BaTiO_3$–NPs composite. On further increasing the amplitude of applied voltage steadily, intensity of transmitted light reduces gradually, and finally, minimum intensity was observed. The minima of transmitted intensity are referred to the dark state for respective samples which happens due to the electrical switching or reorientation of LC molecules perpendicular to glass electrodes. This phenomenon is called Fredericks transition which is independent of sample thickness. Threshold voltage (V_{th}) of LC molecules depends on splay elastic constant (K_{11}) and dielectric anisotropy ($\Delta\varepsilon'$). It is always independent of the cell thickness and is expressed by Mishra et al. [10]:

$$V_{th} = \pi\left(\frac{K_{11}}{\varepsilon_0 \Delta\varepsilon'}\right)^{\frac{1}{2}} \tag{11.1}$$

Where ε_0 (=8.85 pF/m) is the permittivity of free space. From above equation, it can be seen that squire of V_{th} is proportional to the ratio of $K_{11}/\Delta\varepsilon'$. It is observed that V_{th} decreases significantly ~30% for $BaTiO_3$–NPs dispersed sample. From Fig. 11.3, it is apparent that steepness of the T–V curve is also improving for composite (see Table 11.1) which is desirable for energy efficient devices and other application point of view. This might be due to the proportionate decrease of splay elastic constant of dispersed samples. According to Gorkunov and Osipov theory, the anisotropic nature of $BaTiO_3$–NPs in the matrix of nematic liquid crystalline molecules (spherical NPs in the matrix of rod shaped LCs host) is responsible for the decrease of K_{11} [16].

11.4 Conclusions

The inclusion of small amount of $BaTiO_3$–NPs in the nematic matrix of host increases nematic-isotropic transition temperature and stabilizes nematic phase as evident from thermodynamic and dielectric studies. It decreases threshold voltage required for switching of molecules from planar (bright state) to homeotropic (dark state) configuration. As well, the steepness of T–V curves also improve for composite sample which might be useful for new electro-optic and display devices. The nematic ordering of host medium increased due to dispersion of $BaTiO_3$–NPs which causes increasing the nematic transition temperature of composite. The prepared composite is promising for the future energy efficient display and electronic devices based on NPs and LCs.

Acknowledgements We express our deep sense of gratitude to The Head, Department of Physics and Principal, V.S.S.D. College Kanpur for their encouragement and support. One of us (MBP) thanks, Science and Engineering Research Board (SERB) DST, Govt. of India for financially supporting vide project no. FTP/PS-60/2008.

References

1. P.G. De Gennes, J. Prost, *The Physics of Liquid Crystals*, 2nd edn. (Oxford Science Publications, Oxford, 1993)
2. S. Chandrasekhar, *Liquid Crystals*, 2nd edn. (Cambridge University Press, Cambridge, 1994)
3. D. Singh, U.B. Singh, M.B. Pandey, R. Dabrowski, R. Dhar, Improvement of orientational order and display parameters of liquid crystalline material dispersed with single-wall carbon nanotubes. Mater. Lett. **5**, 216 (2018)
4. H.Y. Jung, H.J. Kim, S. Yang, Y.G. Kang, B.Y. Oh, H.G. Park, D.S. Seo, Enhanced electro-optical properties of Y_2O_3 (yttrium trioxide) nanoparticle-doped twisted nematic liquid crystal devices. Liq. Cryst. **39**, 789 (2012)
5. S.K. Prasad, M.V. Kumar, T. Shilpa, C.V. Yelamaggad, Enhancement of electrical conductivity, dielectric anisotropy and director relaxation frequency in composites of gold nanoparticle and a weakly polar nematic liquid crystal. RSC Adv. **4**, 4453 (2014)
6. S. Kumar, L.K. Sagar, CdSe quantum dots in a columnar matrix. Chem. Commun. **47**, 12182 (2011)
7. U.B. Singh, A.S. Pandey, R. Dhar, R. Dabrowski, M.B. Pandey, Electro-optical and dielectric properties of CdSe quantum dots and 6CHBT liquid crystals composites. AIP Adv. **4**, 117 (2014)
8. R. Basu, Effect of carbon nanotubes on the field-induced nematic switching. Appl. Phys. Lett. **103**, 241906 (2013)
9. S. Pandey, T. Vimal, D.P. Singh, S.K. Gupta, P. Tripathi, C. Phadnis, S. Mahamuni, A. Srivastava, R. Manohar, $Cd_{1-x}Zn_xS$/ZnS core/shell quantum dot ferroelectric liquid crystal composite system: analysis of faster optical response and lower operating voltage. Liq. Cryst. **41**, 1811 (2014)
10. M. Mishra, R. Dabrowski, R. Dhar, Thermodynamical, optical, electrical and electro-optical studies of 4-pentyl4′-cyanobiphenyl liquid crystal dispersed with barium titanate nano particles. J. Mol. Liq. **213**, 247 (2016)
11. D.P. Shcherbinin, E.A. Konshina, Ionic impurities in nematic liquid crystal doped with quantum dots CdSe/ZnS. Liq. Cryst. **44**, 648 (2017)
12. U.B. Singh, R. Dhar, R. Dabrowski, M.B. Pandey, Influence of low concentration silver nano particles on the electrical and electro-optical parameters of nematic liquid crystals. Liq. Cryst. **40**, 774 (2013)
13. A.S. Pandey, R. Dhar, S. Kumar, R. Dabrowski, Enhancement of the display parameters of 4-pentyl-4-cyanobiphenyl due to the dispersion of functionalized gold nano particles. Liq. Cryst. **38**, 115 (2011)
14. U.B. Singh, R. Dhar, R. Dabrowski, M.B. Pandey, Enhanced electro-optical properties of a nematic liquid crystals in presence of $BaTiO_3$ nanoparticles. Liq. Cryst. **41**, 953 (2014)
15. U.B. Singh, D. Singh, S. Kumar, R. Dhar, M.B. Pandey, The optical properties of quantum dots in anisotropic media. J. Mol. Liq. **241**, 1009 (2017)
16. M.V. Gorkunov, M.A. Osipov, Mean-field theory of a nematic liquid crystal doped with anisotropic nanoparticles. Soft. Matter. **74**, 348 (2011)

Chapter 12
Elastic and Mechanical Investigation of High-temperature Ir_xRe_{1-x} Alloys

Ajit Kumar Maddheshiya, Navneet Yadav, P. S. Yadav, and R. R. Yadav

Abstract The hexagonal structured inclusion material Ir_xRe_{1-x} ($0.1 \leq \times \leq 0.7$) alloys are utilized in an on-orbit communication satellite. The higher-order elastic constants at ambient temperature are used to explore the characteristics of high-temperature alloys Ir_xRe_{1-x} ($0.1 \leq \times \leq 0.7$). The higher-order elastic constants of the alloys are first determined using a Lennard–Jones potential model. Other elastic moduli, elastic stiffness constants, and hardness parameters are computed at ambient temperature for elastic and mechanical characterization using these other elastic moduli. The obtained data is analysed in order to explore more about the properties of Ir_xRe_{1-x} ($0.1 \leq \times \leq 0.7$) alloys.

12.1 Introduction

The compelling demand of materials capable to sustained use at temperature greater than about 1500 °C, there are challenging task for material scientists and engineers to developed a high-temperature materials [1, 2]. High-temperature alloys paved the way to overcome this difficulty. High temperature alloys have very high melting point and exhibits improved resistance to oxidation at higher-temperature regime [3]. These alloys are used to manufacture of flight-type rockets, turbine blades, and other compounds of jet engine. Unfortunately, the materials which have higher melting point are rapidly oxidized in the environments. Iridium (Ir) has very high melting point (2454 °C), so it is the most promising materials for applications in high-temperature environments [4]. Since, iridium is quite expensive element compared with other elements used in high-temperature applications. The incorporation of rhenium (Re) into iridium-containing alloys overcome this difficulty because Re has also higher melting point like Ir, but generally, Re is less expensive in comparison to Ir. Iridium–rhenium (Ir–Re) alloys are very economic and used to make thruster chamber in an on-orbit communication satellite.

A. K. Maddheshiya · N. Yadav (✉) · P. S. Yadav · R. R. Yadav
Department of Physics, University of Allahabad, Allahabad 211002, India
e-mail: navneetyadav@allduniv.ac.in

K. L. Pandey et al. (eds.), *Proceedings of the National Workshop on Recent Advances in Condensed Matter and High Energy Physics*, Springer Proceedings in Physics 278,
https://doi.org/10.1007/978-981-19-2592-4_12

For any cast restoration to be successful, it must understand the fundamental aspects such as mechanical deformation and structural stability of the materials. The linear elastic properties of the materials can be understood with the knowledge of second-order elastic constants (SOECs). In past few years, nondestructive evaluation technique has been developed, which provides the important diagnostic for microstructural properties as well as deformation processes in a material. Ir–Re alloys have attracted great attention as a high-temperature structural material due to its excellent hardness, superior high-temperature tensile and creep rupture strength (up to 2000 °C), and good chemical and physical compatibility [4].

In present work, we have made the effort to explore the ultra-superior mechanical properties for Ir_xRe_{1-x} ($0.1 \leq \times \leq 0.7$) alloys. For that, we have calculated the higher-order elastic constants, elastic stiffness constants for chosen alloys at room temperature. The related mechanical properties such as Young's modulus (Y), bulk modulus (B), shear modulus (G), Pugh's ratio (B/G), Poisson's ratio (σ), and hardness (H_V) are also evaluated and discussed for these alloys.

12.2 Computational Method

There are several ways to calculate the elastic constant of a condensed material. In this first-principles method based on density functional theory (DFT) in generalized gradient approximation (GGA), GW, and quasi-harmonic approximation (QHA) are mainly used to calculate elastic constants. In these DFT theories, there are many approximations for estimating higher-order elastic constants. The interaction potential model approach is also one of the most well established theories for determining higher-order elastic constants for materials with hexagonal closed packing (HCP) and hexagonal wurtzite structure [6]. In this work, interaction potential model approach has been used for calculation of higher-order elastic constants. The formulations of higher-order elastic constants have been obtained by the second- or third-order strain derivative of elastic energy density.

A generalized definition of nth order elastic constant is the partial derivatives of the thermodynamic potential of the medium subjected to finite deformation and mathematically given by following expression as [5]:

$$C_{ijklmn\ldots} = \frac{\partial^n F}{\partial \eta_{ij} \partial \eta_{kl} \partial \eta_{mn} \cdots} \tag{12.1}$$

where F and η_{ij} represent free energy density and Lagrangian strain component tensor, respectively. F can be expanded in terms of strain η using Taylor series expansion as:

$$F = \sum_{n=0}^{\infty} F_n = \sum_{n=0}^{\infty} \frac{1}{n!} \left(\frac{\partial^n F}{\partial \eta_{ij} \partial \eta_{kl} \partial \eta_{mn} \cdots} \right) \eta_{ij} \eta_{kl} \eta_{mn} \cdots \tag{12.2}$$

Thus, the free energy density up to cubic term is written as:

$$F_2 + F_3 = \frac{1}{2!} C_{ijkl}\eta_{ij}\eta_{kl} + \frac{1}{3!} C_{ijklmn}\eta_{ij}\eta_{kl}\eta_{\mathrm{mn}} \tag{12.3}$$

For HCP material, the basis vectors are $a_1 = a\left(\frac{\sqrt{3}}{2}, \frac{1}{2}, 0\right)$, $a_2 = a(0, 1, 0)$ and $a_3 = a(0, 0, c)$ in Cartesian system axes. Here, a and c are the unit cell parameter. The unit cell of HCP material consists of two nonequivalent atoms: six atoms in basal plane and three-three atoms above and below the basal plane. Thus, both first and second neighbourhood consists of six atoms. The $r_1 = a(0, 0, 0)$ and $r_2 = \left(\frac{a}{2\sqrt{3}}, \frac{a}{2}, \frac{c}{2}\right)$ are the position vectors of these two type of atoms.

The potential energy per unit cell up to second nearest neighbour is written as follows:

$$U_2 + U_3 = \sum_{I=1}^{6} U(r_I) + \sum_{J=1}^{6} U(r_J) \tag{12.4}$$

where I refers to atoms in the basal plane and J refers to atoms above and below the basal plane.

The energy density is considered to be function of Lennard–Jones potential (many body interactions potential) and given as [9, 10]:

$$\phi(r) = -\frac{a_0}{r^m} + \frac{b_0}{r^n} \tag{12.5}$$

where a_0 and b_0 are constants, m and n are integers, and r is the distance between atoms. The interaction considered up to second nearest neighbours. Developing the interaction potential model leads to calculate six SOECs of the HCP material and can be written as the following set of equations [7–10]:

$$\left.\begin{array}{ll} C_{11} = 24.1p^4C' & C_{12} = 5.918p^4C' \\ C_{13} = 1.925p^6C' & C_{33} = 3.464p^8C' \\ C_{44} = 2.309p^4C' & C_{66} = 9.851p^4C' \end{array}\right\} \tag{12.6}$$

where $p = c/a$: axial ratio; $C' = \chi\, a/p^5$. In present study, we have expanded the theory for theoretical computation of parameter χ. The potential energy can be expanded in the powers of changes in the squares of distances. The expansion up to cubic term can be written as:

$$\phi = \phi_0 + \psi \sum_{i=1}^{2} \left[\Delta r_i^2\right]^2 + \chi \sum_{i=1}^{2} \left[\Delta r_i^2\right]^3 \tag{12.7}$$

According to the (12.7), χ can be written as:

$$\chi = \frac{1}{2!}\left[\frac{d^2\phi(r)}{d(r^2)^2}\right] \tag{12.8}$$

By solving (12.7) and (12.8) for hexagonal structured materials, we have:

$$\chi = (1/8)[\{nb_0\,(n-m)\}/\{a^{n+4}\}] \tag{12.9}$$

The χ can be calculated using (12.9) and appropriate values of m, n, and b_0. Since our potential model takes very few data (lattice parameter) as initial, avoids approximations as required in first-principles calculations and gives good results of higher-order elastic constants, hence it is better than the other model.

Calculation of bulk modulus (B) and shear modulus (G) has been done using Voigt and Reuss's approaches [11, 12]. Young's modulus (Y) and Poisson's ratio (σ) are determined using the values of B and G [13, 14]. The following expressions (12.10) have been used for the calculation of Y, B, G, and σ.

$$\left.\begin{array}{ll} M = C_{11} + C_{12} + 2C_{33} - 4C_{13}; & C^2 = (C_{11} + C_{12})C_{33} - 4C_{13} + C_{13}^2; \\ B_R = \frac{C^2}{M}; & B_V = \frac{2(C_{11}+C_{12})+4C_{13}+C_{33}}{9}; \\ G_V = \frac{M+12(C_{44}+C_{66})}{30}; & G_R = \frac{5C^2C_{44}C_{66}}{2[3B_VC_{44}C_{66}+C^2(C_{44}C_{66})]}; \\ Y = \frac{9GB}{G+3B}; \quad B = \frac{B_V+B_R}{2}; & G = \frac{G_V+G_R}{2}; \quad \sigma = \frac{3B-2G}{2(3B+G)} \end{array}\right\} \tag{12.10}$$

12.3 Results and Discussion

The unit cell parameter (a) and axial ratio (p) for the Ir_xRe_{1-x} ($0.1 \leq \times \leq 0.7$) alloys at room temperature is taken from literature [3]. The calculated values of Lennard–Jones parameter (b_0) for the Ir_xRe_{1-x} ($0.1 \leq \times \leq 0.7$) alloys evaluated under equilibrium condition is 4.93×10^{-65} erg-cm^7. The values of m, n are $m = 6$, $n = 7$ for these alloys. The calculated values of SOCEs for Ir_xRe_{1-x} ($0.1 \leq \times \leq 0.7$) alloys at room temperature are presented in Table 12.1.

The SOECs are also well connected with the material's hardness, compressibility, ductility, brittleness, toughness, and bonding nature. Table 12.1 indicates that among these Ir_xRe_{1-x} alloys, $Ir_{0.7}Re_{0.3}$ when compared to other alloys in the same group, it had the greatest elastic constant value, indicating superior mechanical performance. Clearly, the five independent elastic constants must meet the well-known Born stability criterion for a stable hexagonal structure. [13, 14], i.e. $C_{11} - |C_{12}| > 0$, $(C_{11} + C_{12})\,C_{33} - 2C^2{}_{13} > 0$ and $C_{44} > 0$. It is obvious from Table 12.1, all these compounds are mechanically stable because all the values of elastic constants are positive and

Table 12.1 SOEC (in 10^{10}Nm^{-2}) for $\text{Ir}_x\text{Re}_{1-x}$ ($0.1 \leq \times \leq 0.7$) alloys

Elastic constants	$\text{Ir}_{0.7}\text{Re}_{0.3}$	$\text{Ir}_{0.6}\text{Re}_{0.4}$	$\text{Ir}_{0.5}\text{Re}_{0.5}$	$\text{Ir}_{0.4}\text{Re}_{0.6}$	$\text{Ir}_{0.3}\text{Re}_{0.7}$	$\text{Ir}_{0.2}\text{Re}_{0.8}$	$\text{Ir}_{0.1}\text{Re}_{0.9}$
C_{11}	698.7	666.1	672.6	661.3	651.0	642.0	637.9
C_{12}	171.5	163.5	165.1	162.4	159.8	157.6	156.6
C_{13}	143.7	134.1	135.8	133.2	131.6	130.6	131.2
C_{33}	666.4	608.9	617.9	604.5	599.6	598.7	608.4
C_{44}	172.4	160.9	162.9	159.7	157.9	156.6	157.4
C_{66}	274.0	261.2	263.7	259.3	255.3	251.7	250.1

satisfy the Born's mechanical stability constraints. The SOECs of $\text{Ir}_x\text{Re}_{1-x}$ have not been compared due to lack of data in literature.

The elastic stiffness of the materials determines the response of the crystal to an externally applied strain (or stress) and provides information about the structural and mechanical stability. The elastic constants C_{11} and C_{33} represent stiffness against principal strains. The stiffness of the material is the display of the resistance against uniaxial tensions and determine by Young's modulus [6, 13]. Similarly, the bulk modulus relates to strain response of a crystal to hydrostatic stress. It involves change in volume without change of shape. On the other hand, the shear modulus describes the strain response of a body to torsional shear or stress, involving change of shape without change in volume. The values of Young's modulus (Y), shear modulus (G), and bulk modulus (B) for $\text{Ir}_x\text{Re}_{1-x}$ ($0.1 \leq \times \leq 0.7$) alloys at room temperature are computed using (12.9) and presented in Table 12.2.

Young's, shear, and bulk moduli of all alloys are found smaller than those of $\text{Ir}_{0.7}\text{Re}_{0.3}$ (Table 12.2). Thus, all the alloys comprise little stiffness and bonding with respect to $\text{Ir}_{0.7}\text{Re}_{0.3}$. Pugh's ratio ($B/G$) and Poisson's ratio ($\sigma$) define brittleness and ductility of a solid. A solid is usually brittle in nature with $\sigma \leq 0.26$ and $B/G \leq 1.75$; otherwise it is ductile in nature [6, 14]. In our evaluation, it is clear from Fig. 12.1 the low values of Poisson's and Pugh's ratio with respect to their critical values indicate that all the chosen alloys have brittle in nature at room temperature.

The hardness of HCP structured material can be obtained by the relation $H_v = 2(k^2G)^{0.585} - 3$. It is obvious from Fig. 12.2, the value of hardness constant (H_V) of $\text{Ir}_{0.7}\text{Re}_{0.3}$ is higher in magnitude in comparison with other alloys of same group. Thus, $\text{Ir}_{0.7}\text{Re}_{0.3}$ is comparatively harder material in compression to other $\text{Ir}_x\text{Re}_{1-x}$ alloys at room temperature.

Therefore, all the mechanical behaviour of a material can be described with help of the knowledge of these elastic moduli.

12.4 Conclusions

The theory based on Lennard–Jones potential model for the calculation second-order elastic constants is supported for $\text{Ir}_x\text{Re}_{1-x}$ ($0.1 \leq \times \leq 0.7$) alloys. At ambient

Table 12.2 Voigt–Reuss constants (M and C^2), Young's modulus (in $10^{10}\mathrm{Nm}^{-2}$), bulk modulus (in $10^{10}\mathrm{Nm}^{-2}$), and shear modulus (in $10^{10}\mathrm{Nm}^{-2}$) for $\mathrm{Ir_xRe_{1-x}}$ ($0.1 \leq \times \leq 0.7$) alloys

Elastic constants	$\mathrm{Ir_{0.7}Re_{0.3}}$	$\mathrm{Ir_{0.6}Re_{0.4}}$	$\mathrm{Ir_{0.5}Re_{0.5}}$	$\mathrm{Ir_{0.4}Re_{0.6}}$	$\mathrm{Ir_{0.3}Re_{0.7}}$	$\mathrm{Ir_{0.2}Re_{0.8}}$	$\mathrm{Ir_{0.1}Re_{0.9}}$
M	1628.2	1511.0	1530.3	1499.9	1483.6	1474.6	1486.5
C^2	538,601.9	469,177.8	480,731.6	462,442.2	451,518.6	444,607.8	448,946.9
B_R	330.7959	310.5082	314.142	308.3153	304.3398	301.5108	302.0161
G_v	232.8333	219.2067	221.65	217.5967	214.7333	212.4733	212.55
B_v	331.2889	311.6111	315.1667	309.4111	305.2889	302.2556	302.4667
G_R	221.3296	207.7099	210.1243	206.1767	203.608	201.6429	202.0559
B	331.0424	311.0596	314.6543	308.8632	304.814	301.8832	302.2414
G	227.0815	213.4583	215.8872	211.8867	209.1707	207.0581	207.3029
Y	554.4645	521.1625	527.1099	517.3547	510.6951	505.5832	506.1814
G/B	0.685959	0.686229	0.686109	0.686021	0.686223	0.685888	0.685885

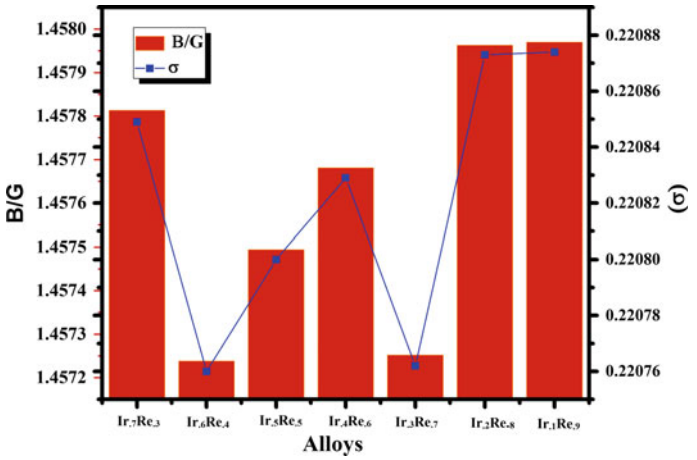

Fig. 12.1 Variation of Pugh's and Poisson's ratio with various alloys composition

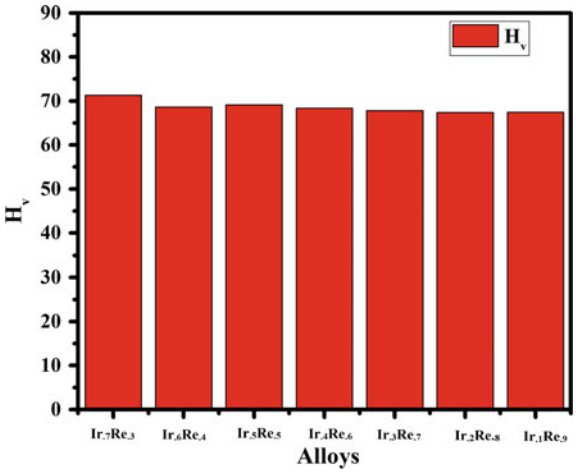

Fig. 12.2 Variation of hardness with various alloys composition

temperature, $Ir_{0.7}Re_{0.3}$ shows better mechanical properties than that of Ir_xRe_{1-x} alloys due to lager values of stiffness and elastic constants for $Ir_{0.7}Re_{0.3}$. These compounds have higher value of brittleness and hardness. The study may be fruitful for the online characterization and processing of these alloys. These findings will provide a base for further investigation of crucial thermophysical properties in the field of high-temperature alloys.

Acknowledgements The authors are thankful to Dr. P.K. Yadawa, Asso. Professor and Dr. Shakti Pratap Singh, Post-doctoral fellow Prof. Rajendra Singh (Rajju Bhaiya) Institute of Physical

Sciences for Study and Research, V. B. S. Purvanchal University, Jaunpur for fruitful discussion and suggestions during the preparation of the manuscript.

References

1. M.M. Kenisarin, High-temperature phase change materials for thermal energy storage. Renew. Sustain. Energy Rev. **14**, 955–970 (2010). https://doi.org/10.1016/j.rser.2009.11.011
2. D. Laing, T. Bauer, N. Breidenbach, B. Hachmann, M. Johnson, Development of high temperature phase-change-material storages. Appl. Energy **109**, 497–504 (2013). https://doi.org/10.1016/j.apenergy.2012.11.063
3. K.V. Yusenko, Phase diagram of the iridium-rhenium system. Platinum Metals Rev. **57**, 43–51 (2013). https://doi.org/10.1595/147106713X659064
4. L. Zhu, S. Bai, H. Zhanga, Y. Ye, W. Gao, Long-term high-temperature oxidation of iridium coated rhenium by electrical resistance heating method. Int. J. Refractory Metals Hard Mater. **44**, 42–48 (2014). https://doi.org/10.1016/j.ijrmhm.2014.01.010
5. K. Brugger, Thermodynamic definition of higher order elastic coefficients. Phys. Rev. A. **133**, 1611–1612 (1964). https://doi.org/10.1103/PhysRev.133.A1611
6. C.P. Yadav, D.K. Pandey, D. Singh, Ultrasonic study of Laves phase compounds $ScOs_2$ and YOs_2. Indian J. Phys. **93**, 1147–1153 (2019). https://doi.org/10.1007/s12648-019-01389-8
7. S.P. Singh, G. Singh, A.K. Verma, P.K. Yadawa, R.R. Yadav, Ultrasonic wave propagation in thermoelectric ZrX_2 (X = S, Se) compounds. Pramana J. Phys. **93**, 83 (2019). https://doi.org/10.1007/s12043-019-1846-8
8. D.K. Pandey, R.R. Yadav, Temperature dependent ultrasonic properties of aluminium nitride. Appl. Acoust. **70**, 412–415 (2009). https://doi.org/10.1016/j.apacoust.2008.05.011
9. D.K. Pandey, P.K. Yadawa, R.R. Yadav, Ultrasonic properties of hexagonal ZnS at nanoscale. Mater. Lett. **61**, 5194–5198 (2007). https://doi.org/10.1016/j.matlet.2007.04.028
10. P.K. Dhawan, S. Upadhyaya, S.K. Verma, M. Wan, R.R. Yadav, B. Joshi, Size and temperature dependent ultrasonic properties of thermoelectric nanowires. Mater. Lett. **114**, 15–18 (2014). https://doi.org/10.1016/j.matlet.2013.09.104
11. W. Voigt, Lehrbuch der kristallphysik (mitausschluss der kristalloptik) (Leipzig Berlin, B.G. Teubner) (1928)
12. A. Reuss (1929) Berechnung der Fliessgrenze von Mischkristallen auf Grund der Plastizitätsbedingung für Einkristalle. ZAMM—J. Appl. Math. Mech./Zeitschrift für Angewandte Mathematik und Mechanik, **9**, 49–58 (1929) https://doi.org/10.1002/zamm.19290090104
13. N. Turkdal, E. Deligoz, H. Ozisik, H.B. Ozisik, First-principles studies of the structural, elastic, and lattice dynamical properties of $ZrMo_2$ and $HfMo_2$. Phase Transitions **90**, 598–609 (2017). https://doi.org/10.1080/01411594.2016.1252979
14. P.F. Weck, E. Kim, V. Tikare, J.A. Mitchell, Mechanical properties of zirconium alloys and zirconium hydrides predicted from density functional perturbation theory. Dalton Trans. **44**, 18769–18779 (2015). https://doi.org/10.1039/C5DT03403E

Chapter 13
Comparative Study of Photocatalytic Activity of ZnS and CuS Nanoparticles for Dye Degradation Under Visible Light Irradiation

Pooja Dwivedi and Pratima Chauhan

Abstract As we all know that sun is the naturally abundant source of energy. Using this environment friendly source for energy production and harmful waste remediation has been an intensive area of research. In this research article, we have synthesized the ZnS and CuS nanoparticles (NPs). These samples were characterized using various analytical techniques to confirm the formation and study their morphology, structure, and bandgap. The average crystallite size of ZnS and CuS NPs was found to be in range of 2–4 nm and 8–10 nm, respectively. The photocatalytic activity has been investigated for their dye degradation potential under visible light irradiation.

13.1 Introduction

Metal sulfides (MSs) are promising semiconductor with multiple uses in several fields due to their properties such as a tunable narrow optical bandgap (absorption in the infrared region), fluorescence, and magnetic, structural, and thermal stability at the nanometric scale [1–5]. Among various metal sulfides, ZnS and CuS are important class of photocatalysts due to their unique physical and chemical properties. ZnS is

P. Dwivedi (✉) · P. Chauhan
Department of Physics, University of Allahabad, Prayagraj 211002, India
e-mail: poojadwivediau@gmail.com

K. L. Pandey et al. (eds.), *Proceedings of the National Workshop on Recent Advances in Condensed Matter and High Energy Physics*, Springer Proceedings in Physics 278,
https://doi.org/10.1007/978-981-19-2592-4_13

an important II–VI class of semiconductor having theoretically superior properties than TiO_2 as a photocatalyst [6, 7]. CuS NPs have attracted great interest due to its versatile properties and applications. The stoichiometry of CuS varies from Cu_2S at the copper-rich side to CuS_2 at the copper-deficient side. The covellite CuS is one of the most intensively studied copper sulfides due to its exceptional physical and chemical properties and its potential applications in many fields such as photocatalysis [8]. The potentially effective and eco-friendly approach is utilization of naturally abundant solar energy for wastewater treatment, energy production, air purification, and hazardous waste remediation, which have attracted much attention of researchers. Dye (is a colored substance that imparts permanent stain which is not removable by washing with water or detergent) is one of those substances that pollute our environment and make it toxic. The dyes are being used in several industries such as leather, paints, textile, cosmetics, plastic, food, and rubber. [9, 10]. The presence of such dye in water reduces the transmission of light through it and thus affects aquatic lives [11]. Even a small quantity of dye in water can pollute it to be toxic. Therefore, the removal of dye from waste water is important for environments. Photocatalysis plays a crucial role in water purification. The process of photocatalysis mainly involves the production of electron–hole pairs by irradiation of light with suitable energy of a semiconductor material. The performance of photocatalytic degradation of toxic dye in presence of photoactive materials depends on various factors like the amount of catalyst, surface area, number of production of electron–hole pair, and their recombination time [12, 13]. Various metal sulfides have been investigated and reported as photoactive catalysts for various dye degradation. In this article, we have synthesized the ZnS and CuS NPs and investigated their photocatalytic activities for methylene blue (MB) dye degradation under visible light irradiation. A comparative study has been done for their photocatalytic performance.

13.2 Experimental Techniques

ZnS and CuS NPs were synthesized by chemical co-precipitation method which is a cost-effective method. For synthesis of CuS NPs, an appropriate amount (10 mmol) of $[Cu(NO_3)_2 3H_2O]$ was dissolved in 100 mL of double distilled water (solution 1), and solution was ultrasonicated for 30 min; Sodium sulfide (15 mmol) was separately dissolved in another 100 mL of DI water (solution 2) and ultrasonicated for 30 min. Appropriate amount of CTAB (1 mmol) was mixed into solution 1. Solution 2 is then added drop wise into solution1 under vigorous magnetic stirring. The mixture was stirred continuously for 3 h. The resulting solution was left for 24 h and allowed to settle down. CuS NPs (black precipitate) were taken out after centrifuge. The product was washed several times with distilled water and ethanol to remove impurities and loosely bonded ions and then filtered. The filtered sample was dried at room temperature. For synthesis of ZnS NPs, we have followed the same stated procedure by replacing the copper nitrate with zinc acetate $[Zn(CH_3COO)_2 2H_2O]$. Finally, we obtained ZnS (white precipitate) NPs after centrifugation. Thus, the obtained material

was finally used for further characterization and their application as catalyst for MB dye degradation.

13.3 Characterizations

To obtain the crystallographic information of synthesized sample, XRD spectra were recorded, using a Rigakusmart laboratory X-ray diffractometer with monochromatized Cu Kα radiation ($\lambda = 1.543$ Å) were used as an X-ray source and operated at 40 kV and 30 mA. Diffraction pattern was recorded over the 2θ range of 15° to 80°. UV–Vis absorption spectra were recorded by Avaspec Avantes fiber optic spectrometer. Spectral range from 180 to 350 nm was used for UV–Vis measurement.

13.4 Dye Degradation Experiments

Methylene blue (MB, Sigma-Aldrich) dye was chosen as a test pollutant in the aqueous solution. MB (also known as methylthioninium chloride), a cationic dye, is a chemical compound. The molecular formula of MB dye is $C_{16}H_{18}N_3ClS$. The chemical structure of MB dye has shown in Fig. 13.1a. The dye solution was made in distilled water as shown in Fig. 13.1b.

We have conducted the photocatalysis reaction using a custom-built photocatalytic reactor. The photocatalytic reactor consisted of a light source, reaction container, and magnetic stirrer. The aqueous solution of MB dye mixed with photocatalysts is exposed to visible light. A halogen lamp of 500 W was used as a visible light source. During experiments, the reaction container was placed on a magnetic stirrer for proper mixing of the catalyst with dye. The distance between the light source and reaction container was approximately 50 cm. 20 mg of catalysts was used in 50 ml

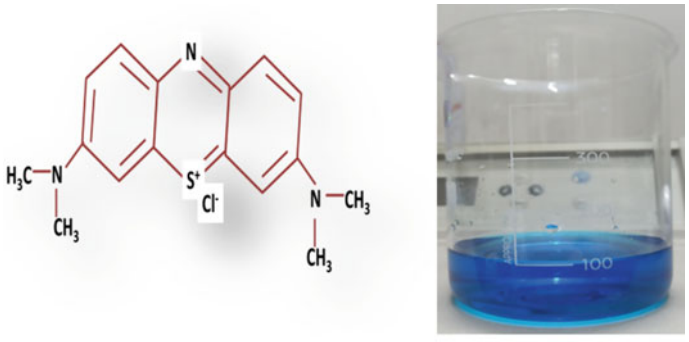

Fig. 13.1 **a** Chemical structure and **b** aqueous solution of MB dye

of 30 ppm MB dye solution. The reaction mixture was stirred for 10 min in the dark before being subjected to light irradiation for the reaction to occur. 5 mL of solution was taken out from the suspension at a certain interval of time and centrifuged to separate the catalyst.

The degradation of dye was monitored by analyzing the UV–visible spectra of dye. The UV–visible absorption spectrum was recorded in the range of 325–800 nm using Avaspec Avantes fiber optic spectrophotometer. The percentage of dye degraded has been calculated using the formula.

$$D(\%) = \frac{A_0 - A_t}{A_0} * 100 = \frac{C_0 - C_t}{C_0} * 100 \tag{13.1}$$

where A_0, A_t, C_0, and C_t are the absorbance values and concentrations of MB at time 0 and t, respectively; t is the irradiation time in seconds.

The rate constant of catalysts for MB dye degradation has been calculated using a pseudo-first-order equation as follows:

$$\ln(C_0/C_t) = kt \tag{13.2}$$

where k is the apparent rate constant ($k_{(app)}$, min^{-1}) for photocatalytic dye degradation. The slope of linear fitting of $\ln(C_0/C_t)$ versus irradiation time provides the rate constant.

13.5 Results and Discussions

13.5.1 X-Ray Diffraction (XRD) Pattern Analysis

The XRD patterns of ZnS and CuS NPs are shown in Fig. 13.2. The strong diffraction peaks appeared around 28°, 47°, and 56° correspond to (111), (220), and (311) planes, respectively, of cubic phase of ZnS (JCPDS no-050,566). For CuS sample, the intense peaks appeared around $2\theta = 27°$, 29°, 31°, 47°, and 59° correspond to (101), (102), (103), (107), and (203) planes, respectively, and matched well with the hexagonal phase of CuS (JCPDS no-060,464).

No impurity peaks (peaks corresponding to CuO and ZnO) were found in the XRD pattern of the synthesized samples. This confirms the formation of ZnS and CuS NPs. The broad diffraction peaks present in XRD pattern of ZnS NPs reflect the small crystallite size of ZnS NPs. The peaks of CuS were relatively narrower than the peaks of ZnS, which results the larger crystallite size of CuS NPs.

The crystallite size was determined by the well-known Scherrer formula [14]:

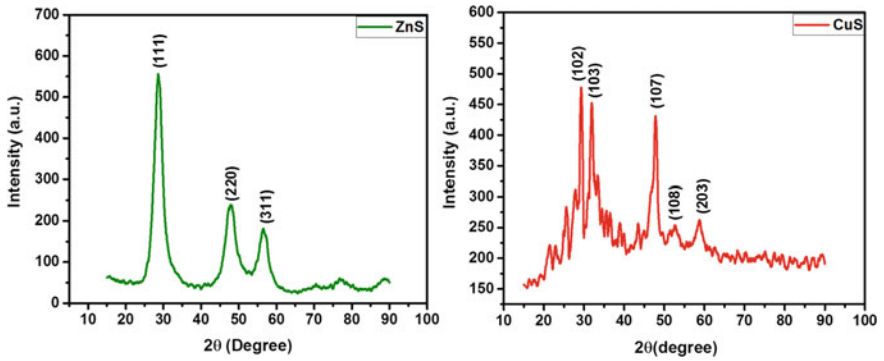

Fig. 13.2 XRD pattern of pure ZnS and CuS NPs

$$D = \frac{(K\lambda)}{(\beta \cos\theta)} \tag{13.3}$$

where K is shape factor having value 0.90, D is the crystallite size, λ is the wavelength of radiation (1.543 Å) used in X-ray diffraction, θ is the Bragg angle, and β is the full width at half maximum (FWHM) measured in radian. The average crystallite size as estimated is lying in the range 2–4 nm for ZnS and 8–10 nm for CuS nanoparticles.

13.5.2 UV–Visible Spectra Analysis

The UV–visible spectra of synthesized NPs have shown in Fig. 13.3. In crystalline and amorphous materials, the absorption coefficient (α) depends upon the incident

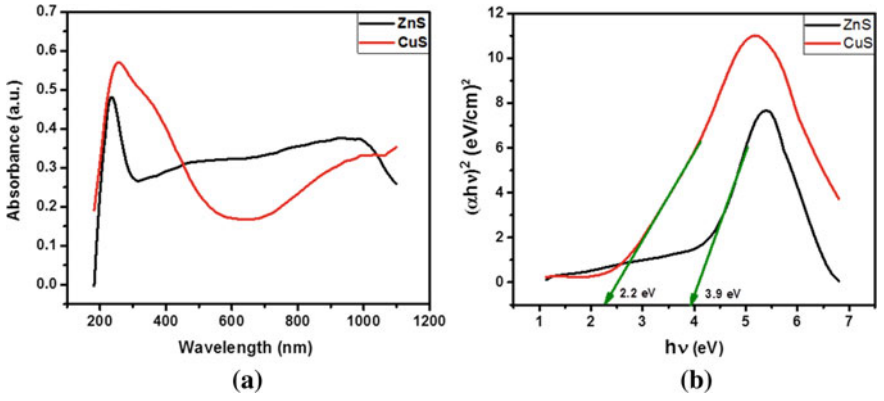

Fig. 13.3 **a** UV–Vis spectra and **b** Tauc plot of synthesized ZnS and CuS nanoparticles

photon energy and expressed by the following relation [15].

$$\alpha h\nu = A\left(h\nu - E_g\right)^n \tag{13.4}$$

where A is energy independent constant, E_g is the energy bandgap of material and exponent 'n' depends on the type of transition. As ZnS and CuS have direct allowed transition, therefore $n = 1/2$.

Bandgap of synthesized nanoparticles was calculated by Tauc plot method. From the slope of the plot, we have calculated the bandgap 3.9 eV, and 2.2 eV for ZnS and CuS NPs, respectively.

13.5.3 Dye Degradation

The absorbance spectra during the photocatalytic degradation of MB dye have shown in Fig. 13.4. The intensity of the absorption peaks of MB dye has not significantly decreased with increasing the irradiation time in absence of catalysts (Fig. 13.4a). We have observed that with CuS NPs, the dye degraded more than with ZnS NPs. Figure 13.4 (b and c) shows the degradation efficiency of the catalysts (ZnS, CuS) with time. In 150 min, the dye degradation efficiency of ZnS and CuS samples has been observed to 27.89 and 53.88, %, respectively. There are many factors like bandgap, morphology, size, electron–hole pair generation, and their recombination time, etc., that affect the photocatalytic performance of materials toward the degradation of pollutants [12, 13, 16].

The lowest degradation of MB dye with ZnS NPs is due to its large bandgap (3.9 eV), corresponding to a wavelength less than 320 nm. Thus, a very small portion of irradiated light could be absorbed by the catalyst (ZnS) to perform photodegradation. Due to the small bandgap of CuS NPs (2.2 eV), it has a strong affinity to absorb light. Therefore, more light could be absorbed that generate more electron–hole pair due to which we observed better photodegradation of MB dye.

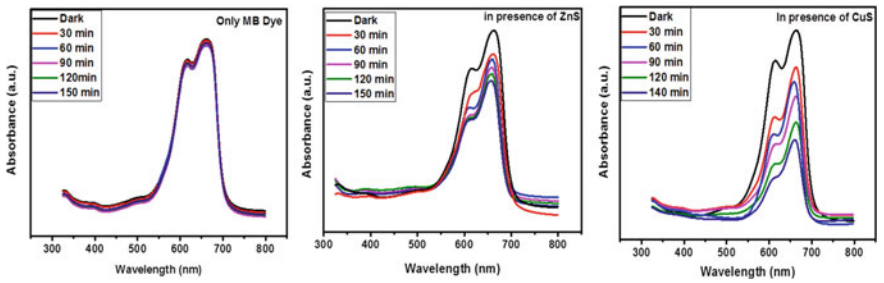

Fig. 13.4 UV–visible absorbance of MB dye as a function of exposure time with different catalysts

13.5.4 PhotoDegradation Mechanism

The possible mechanism for photodegradation of MB dye pollutants can be explained as follows. The photocatalytic reaction started when the suitable wavelength of light incident on the semiconductor, electron–hole pair generates (13.5). Electron excited from valance band to conduction band while the hole remains in the valence band of the semiconductor. This electron and hole pair ($e^- + h^+$) undergo the subsequent reduction and oxidation reactions with the reactants that get adsorbed on the surface of the semiconductor. The electrons in conduction band react with the molecules of oxygen and convert them to oxygen radicals (13.6). Meanwhile, the hole in valance band reacts with the hydroxyl ions and produces hydroxyl radicals (13.7). Proton then neutralizes the oxygen radicals (13.8) and further formation of H_2O_2 (13.9) takes place. By reduction, the dissolved H_2O_2 decomposes and further generates more hydroxyl radicals (13.10). These reactive species (O_2^* and OH^*) (13.11 and 13.12) initiate the degradation of dye into a nontoxic product. The key steps involved in the photodegradation process of dye are summarized in the following equations:

$$\text{catalyst} + hv \rightarrow e_{CB}^- + h_{VB}^+ \tag{13.5}$$

$$O_2 + e_{CB}^- \rightarrow O_2^{*-} \tag{13.6}$$

$$H_2O\left(H^+ + OH^-\right) + h_{VB}^+ \rightarrow H^+ + OH^* \tag{13.7}$$

$$O_2^{*-} + H^+ \rightarrow HO_2^* \tag{13.8}$$

$$2HO_2^* \rightarrow H_2O_2 + O_2 \tag{13.9}$$

$$H_2O_2 + e^- \rightarrow 2OH^* \tag{13.10}$$

$$O_2^* + \text{dye} \rightarrow \text{product} \tag{13.11}$$

$$OH^* + \text{dye} \rightarrow \text{product} \tag{13.12}$$

The better photodegradation of MB dye in the case of CuS NPs is due to its better absorption of light in visible region that allow to offered more photoinduced charge carriers to participate in photodegradation of dye pollutants.

13.6 Conclusion

In summary, we have successfully synthesized CuS and ZnS NPs. The synthesized NPs have been successfully used as catalysts. The XRD pattern of ZnS and CuS sample confirms the formation of respective nanoparticles. CuS NPs proved to have a better photocatalytic response than ZnS NPs under visible light irradiation. This behavior was expected due to their respective bandgap. Thus, the results prove the promising prospect of the synthesized CuS/ZnS nanostructures as visible-light-sensitive photocatalyst with high photocatalytic efficiency for large-scale practical application in wastewater handling. Also, the effect of concentration CuS and ZnS NPs may also have significant effect on its catalytic performance.

Acknowledgements The authors are grateful to the University Grants Commission (UGC), New Delhi, Government of India, for financial support. The instrument facilities available in the Department of Physics, University of Allahabad, Prayagraj, are highly acknowledged.

References

1. M.P. Vena, M. Jobbáígy, S.A. Bilmes, Microorganism mediated biosynthesis of metal chalcogenides; a powerful tool to transform toxic effluents into functional nanomaterials. Sci. Total Environ. **565**, 804–810 (2016)
2. Z.H. Ge, L.D. Zhao, D. Wu, X. Liu, B.P. Zhang, J.F. Li, J. He, Low-cost, abundant binary sulfides as promising thermoelectric materials. Mater. Today **19**, 227–239 (2015)
3. D.J. Vaughan, J.R. Craig, *Mineral Chemistry of Metal Sulfides* (Cambridge University Press, 1978)
4. C. Wadia, A.P. Alivisatos, D.M. Kammen, Materials availability expands the opportunity for large-scale photovoltaics deployment. Environ. Sci. Technol. **43**, 2072–2077 (2009)
5. S.A. Dahoumane, E.K. Wujcik, C. Jeffryes, Noble metal, oxide and chalcogenide-based nanomaterials from scalable phototrophic culture systems. Enzyme Microb. Technol. **95**, 13–27 (2016)
6. A.A. Alshatwi, P.V. Subbarayan, E. Ramesh, A.A. Al-Hazzani, M.A. Alsaif, A.A. Alwarthan, Food Additives Contaminants: Part A **30**(1), 1–10 (2013)
7. E. Radziun, J.D. Wilczynska, I. Ksiazek, K. Nowak, E.L. Anuszewska, A. Kunicki, A. Olszyna, T. Zabkowski, Toxicol. In Vitro **25**(8), 1694–1700 (2011)
8. Z. Hosseinpour, S. Hosseinpour, Mater. Sci. Semicond. Process. **72**, 32–36 (2017)
9. M. Chincholi, P. Sagwekar, C. Nagaria, S. Kulkarni, S. Dhokpande, Int. J. Eng. Sci. Res. 835–840 (2014)
10. M.T. Yagub, T.K. Sen, S. Afroze, H.M. Ang, Adv. Coll. Interface. Sci. **209**, 172–184 (2014)
11. M.S. Chiou, P.Y.H.Y. Ho, J. Li, Dyes Pigm. **60**(1), 69–84 (2004)
12. A. Singh, B. Ahmed, A. Singh, A.K. Ojha, Spectrochim. Acta Part A Mol. Biomol. Spectrosc. **204**, 603–610 (2018)
13. T.H. Chiang, P.Y. Ho, S.Y. Chiu, A.C. Chao, J. Alloy. Compd. **651**, 10–113 (2015)
14. B.D. Cullity, S.R. Stock, *Elementary of X-ray Diffraction, Englewood Cliffs*, 3rd edn. (Prentice-Hall, New Jersey, 2001)
15. P. Żółczyk, E. Miller, M. Przybyt, ZnS Cu-doped quantum dots. Biotechnol. Food Sci. **78**(1), 53–69 (2014)
16. B. Ahmed, S. Kumar, A.K. Ojha, P. Donfack, A. Materny, Spectrochim. Acta Part A Mol. Biomol. Spectrosc. **175**, 250–261 (2017)

Chapter 14
Microstructural Properties of Palladium-Doped Tin Oxide Thick Film

Ajaya Kumar Sharma, Ankit Kumar Vishwakarma, and Lallan Yadava

Abstract In the present study, we fabricate undoped and 1 wt% palladium (Pd)-doped tin oxide (SnO_2) films were deposited on alumina substrate using screen-printing technology. The deposited film is characterized, and its microstructural properties are studied using X-ray diffraction (XRD) and atomic force microscope (AFM). XRD measurement reveals that the crystallite size was ~23.5 nm and ~19.2 nm for undoped and Pd-doped SnO_2 film, respectively. The morphology analysis shows that grain size and roughness parameter reduce with Pd doping.

14.1 Introduction

Nanotechnology is a bright platform to provide a broad range of novel used and advanced technology toward physical, sensing, chemical, and biological pharmaceutical analysis [1–3]. The nanocrystalline metal oxide is an important multifunctional material with various applications such as gas sensors, thin film, thick film, electrochemical sensor, solar cell, and photocatalytic [4, 5]. In the gas sensor devices, there are various metal oxide materials, viz. SnO_2, TiO_2, ZnO, WO_3, etc. SnO_2 is one of the most important semiconductor metal oxides synthesized by various technologies such as the thermal evaporation method [6] screen printing [7], PVD method [8], etc. SnO_2 has an n-type semiconductor with a wide bandgap (3.6 eV) at room temperature [9]. Several researchers developed SnO_2-based thin or thick film and investigated the structural, morphological, and sensing behavior [10–13]. In the present investigation, we reported undoped and 1 wt% Pd-doped SnO_2 thick film. Pd-doped SnO_2 thick films were deposited on alumina substrate using screen-printing technology. The deposited films are characterized, and their microstructural properties were studied using XRD and AFM. The crystallite size, grain size, and roughness were reduced

A. K. Sharma · A. K. Vishwakarma · L. Yadava (✉)
Thin Film Laboratory, Department of Physics, Deen Dayal Upadhyaya Gorakhpur University, Gorakhpur, Uttar Pradesh 273009, India
e-mail: ncfm16@gmail.com

K. L. Pandey et al. (eds.), *Proceedings of the National Workshop on Recent Advances in Condensed Matter and High Energy Physics*, Springer Proceedings in Physics 278,
https://doi.org/10.1007/978-981-19-2592-4_14

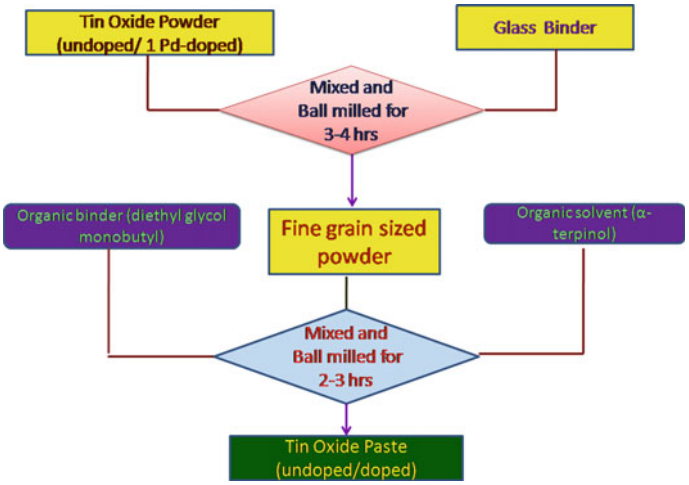

Fig. 14.1 Flowchart of fabrication of SnO_2

with Pd doping. The enhancement of crystallinity and roughness lead to improve sensing behavior toward the ethanol gas.

14.2 Experimental

14.2.1 Fabrication of SnO_2 Thick Films

Undoped and 1 wt% Pd-doped SnO_2 paste were prepared using ball mixing. The fabrication steps of undoped and 1 wt% Pd-doped SnO_2 thick film sensor are demonstrated in Fig. 14.1. The detailed fabrication process was previously reported by Vishwakarma et al. [7]. The prepared past was pasted on a designed alumina substrate (with finger electrode pattern and heater) to make a sensor. The fabricated gas sensor using a thick film screen-printing process is shown in Fig. 14.2.

14.2.2 Characterization

The microstructural properties of the fabricated undoped and 1 wt% Pd-doped SnO_2 films were studied using XRD and AFM. XRD pattern was obtained by D8-advanced equipped with Cu $K\alpha_1$ radiation with wavelength 0.15406 nm used as a source. The surface morphology of the fabricated films was investigated using AFM. The AFM image was recorded with digital instrument Nanoscope-IV, with Si_3N_4 100 μm cantilever, 0.58 N/m force constants in contact mode. The response of the fabricated

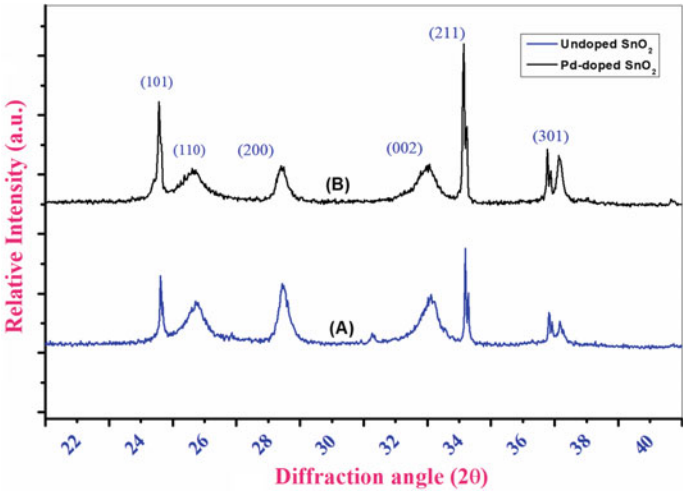

Fig. 14.2 XRD pattern of undoped SnO_2 and Pd-doped SnO_2 thick film

Pd–SnO_2 thick film sensor was measured with varying concentrations of ethanol gas (0–5000 ppm) at 200 °C temperature.

14.3 Result and Discussion

14.3.1 XRD Analysis

The XRD pattern of undoped SnO_2 and Pd-doped SnO_2 thick films are shown in Fig. 14.2. The intensity of the XRD pattern was increased with Pd doping and also crystallite size was decreased from ~23.5 to ~19.2 nm. The crystallite size was calculated using the Scherer formula [13–15].

$$D = \frac{k \cdot \lambda}{\beta \cdot \mathrm{Cos}\,\theta} \tag{14.1}$$

where D is the average size of crystallite assuming it to be K = shape factor and it is ~0.94, $\lambda = 1.5418$ Å, β = full-width half maxima (FWHM) of diffraction peak, and θ is the angle of diffraction. In the XRD peak at diffraction angle 2θ, ~25.58 for the plane (101) the average crystallite size is ~23.5 nm for undoped SnO_2 and ~19.2 nm for 1 wt% Pd-doped SnO_2.

14.3.2 Surface Analysis

The surface morphology of the deposited sample was presented by AFM at room temperature in non-contact mode. The roughness parameter and grain size of the fabricated SnO_2 film were studied using AFM. AFM data were plotted using WSxM.5.0 develop-8.3 software. AFM 2D and 3D structure for undoped SnO_2 and 1 wt% Pd–SnO_2 structure are presented in Fig. 14.3. The average grain size and roughness parameter have been obtained by statistical fitting of the distribution of the Gaussian function. The histogram of the fabricated film was shown in Fig. 14.4. We observed from Fig. 14.4 that the grain size of undoped SnO_2 and Pd-doped SnO_2 was ~64 nm and ~47 nm, respectively. The roughness parameter is reduced from ~18.33 nm to ~11.0 nm. Earlier, Srivastava et al. [5] reported the sensing mechanism of the Pd–SnO_2 sensor for LPG detection. They reported that the crystallite size of SnO_2 was a small change (1%) increased with Pd doping (0.25, 1 wt%) tin oxide; however, in the present investigation, we found that 1 wt% Pd-doped SnO_2 showed a large reduction (43.8%) in crystallite size than undoped SnO_2. The large reduction

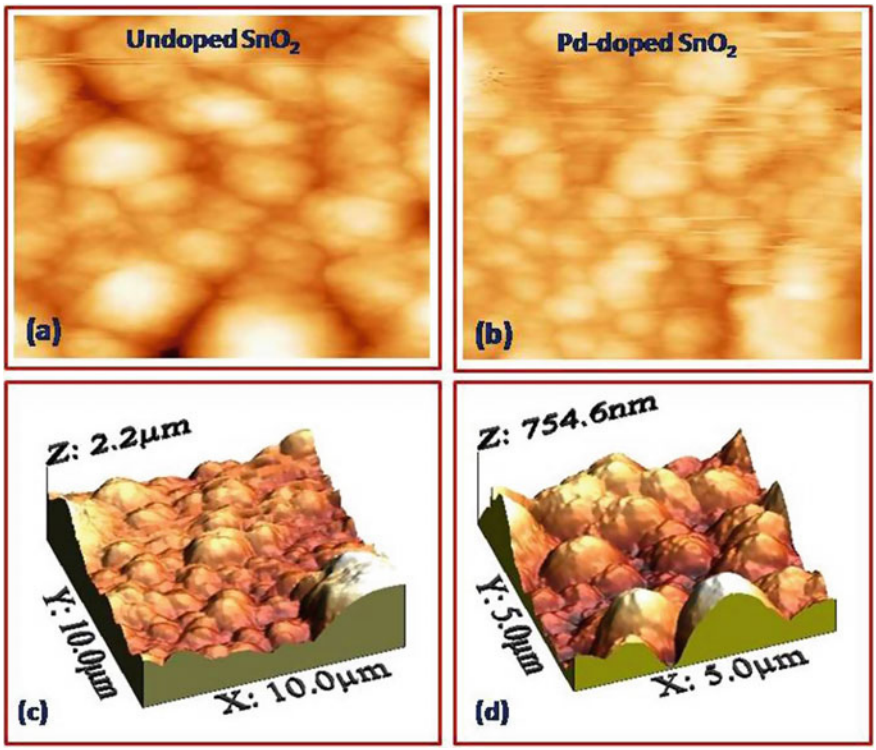

Fig. 14.3 AFM 2-dimensional structures **a** for undoped SnO_2, **b** 1 wt% Pd-doped SnO_2 and 3-dimensional structures, and **c** for undoped SnO2, **d** 1 wt% Pd-doped SnO_2

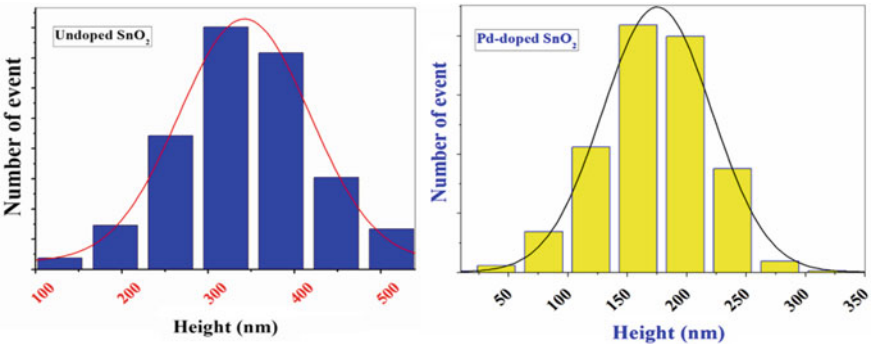

Fig. 14.4 AFM histogram structures for undoped SnO_2, 1 wt% Pd-doped SnO_2

Table 14.1 Crystallite size, grain size, roughness, response, and response/recovery time for undoped and 1 wt% Pd-doped SnO_2 thick film gas sensor

Sample	Crystallite size (nm)	Grain size (nm)	Roughness (nm)
Undoped SnO_2	23.5	64	18.33
Pd-doped SnO_2	19.2	47	11.03

in crystallinity plays an efficient role in enhancing the sensing behavior of test gas ethanol (Table 14.1).

14.4 Conclusion

We fabricate two kinds of thick film such as undoped and 1 wt% palladium (Pd)-doped tin oxide (SnO_2) films. It was deposited on an alumina substrate using screen-printing technology. The deposited film is characterized and its microstructural properties are studied using X-ray diffraction (XRD) and atomic force microscope (AFM). XRD measurement reveals that the crystallite size was ~23.5 nm and ~19.2 nm for undoped and Pd-doped SnO_2 film, respectively. The morphology analysis shows that grain size and roughness parameter reduce with Pd doping. The microstructural properties such as XRD and AFM are investigated. The maximum change in a reduction in the crystallite size of SnO_2 with Pd content has modified the surface of the Pd/ SnO_2 structure.

Acknowledgements The authors are thankful to UGC-DAE CSR, Indore for providing XRD and AFM measurements.

References

1. R. Sadegi, H. Karimire, A. Bahari, M. Taghvi, Anal. Methods **8**, 1780 (2016)
2. A.K. Vishwakarma, L. Yadava, Detection of propanol gas using titanium dioxide-based thick film. IOP Conf. Series: Mater. Sci. Eng. **404**, 012020 (2018)
3. A.K. Sharma, A.K. Vishwakarma, L. Yadava, Sensing and structural characteristics of TiO_2 thick film for LPG sensor. Mater. Today: Proc. **38**(5), 2123–2126 (2021)
4. J.K. Srivastava, P. Pandey, V.N. Mishra, R. Dwivedi, Structural and microstructural studies of PbO-doped SnO_2 sensor for detection of methanol, propanol, and acetone. J. Nat. Gas Chem. **20**, 179–183 (2011)
5. J.K. Srivastava, P. Pandey, V.N. Mishra, R. Dwivedi, Sensing Mechanism of Pd-doped SnO_2 sensor for LPG detection. Solid State Sci. **11**, 1602–1605 (2009)
6. A.J. Haider, A.J. Mohammed, S.S. Shaker, K.Z. Yahya, M.J. Haider, Sensing characteristics of nanostructured SnO_2 thin films as a glucose sensor. Energy Procedia **119**, 473–781 (2017)
7. A.K. Vishwakarma, L. Yadava, Structural and sensing properties of ethanol gas using Pd-doped SnO_2 thick film gas sensor. Environ. Sci. Pollut. Res. **28**(4), 3920–3927 (2021)
8. A.K. Vishwakarma, L. Yadava, Fabrication and characterization of nano TiO_2 thin film using physical vapor deposition method. Adv. Sci. Eng. Med. **10**, 723–726 (2018)
9. L. Yadava, R. Verma, R. Dwivedi, Sensing properties of CdS-doped tin oxide thick film sensor. Sens. Actuators, B: Chem. **144**, 37–47 (2010)
10. P. Yadav, A.K. Sharma, S.K. Yadav, A.K. Vishwakarma, L. Yadava, Sensing response of toluene gas and structural properties of CdS-SnO_2 thick films sensor. Mater. Today: Proc. **38**(5), 2792–2796 (2021)
11. A.K. Vishwakarma, N.K. Yadav, A.K. Sharma, P. Yadav, S.K. Yadav, L. Yadava, Morphological and electronic properties of titanium dioxide thin film. Mater. Today: Proc. **42**, 1642–1646 (2021)
12. A.K. Vishwakarma, A.K. Sharma, L. Yadava, Theoretical modeling of Pd-SnO_2 based ethanol gas sensor. J. Phys: Conf. Ser. **1921**, 012118 (2021)
13. A.K. Vishwakarma, A.K. Sharma, N.K. Yadav, L. Yadav, Development of CdS-doped TiO_2 nanocomposite as acetone gas sensor, vacuum **191** , 110363 (2021)
14. A.K. Vishwakarma, S.S. Majid, L. Yadava, XANES analysis and structural properties of CdS-doped TiO_2. Vacuum **165**, 239–245 (2019)
15. A.K. Vishwakarma, L. Yadava, Fabrication and characterization of CdS doped ZnO nano thick film. Vacuum **155**, 214–218 (2018)

Chapter 15
PVDF-Based Nanocomposite Polymer Electrolyte for Enhancement in Stability of Dye-Sensitized Solar Cells

Priyanka Chawla, Kumari Pooja, and Mridula Tripathi

Abstract Dye-sensitized solar cells (DSSCs) based on redox electrolyte solution set the limitation and restriction on its fabrication. Moreover, when this redox electrolyte comes in contact with photoanode causes its corrosion. The finding of ionic conductivity in polymer material complex with salt has given a breakthrough in the formation of DSSC devices. Polymer electrolytes, especially Polyvinylidene fluoride (PVDF), have attained considerable interest due to its some exceptional properties like thermal stability, chemical resistance, and excellent mechanical strength. In the present work, dye-sensitized solar cell has been assembled using electrolyte system composed of PVDF as host polymer, Ethylene Carbonate as plasticizer, LiI: I_2 as redox, and couple and graphite as filler; TiO_2 modified with CuO photoanode in order to provide inherent energy barrier and natural cocktail dye as sensitizer. The obtained solar cell conversion efficiency was about 2.27% with using an irradiation of 100 mW/cm^2 at 25 °C.

15.1 Introduction

Dye-sensitized solar cells (DSSCs) are third generation solar cells based on dye molecules which absorb light energy and convert into electrical energy. These cells are gaining lot of attention due to their low cost and easy fabrication. The main components of DSSCs are semiconductor electrode (TiO_2, ZnO, or SnO_2), counter electrode (Pt or C), dye as sensitizers, and electrolyte as redox mediator [1, 2]. Scientists are doing lot of research on improving its components and optimization so that efficiency comparable to silicon-based solar cell can be achieved.

The commonly used redox electrolyte used for DSSCs comprises iodide/triiodide (I^-/I_3^-) redox couple in an organic solvent. But it suffers from major drawback as the organic solvent used leaks and vaporizes with time. Therefore, scientists are focusing their attention in the solidification of electrolyte such as inorganic or

P. Chawla · K. Pooja · M. Tripathi (✉)
Department of Chemistry, CMP Degree College, University of Allahabad, Prayagraj 211002, India
e-mail: mtcmpau@gmail.com

K. L. Pandey et al. (eds.), *Proceedings of the National Workshop on Recent Advances in Condensed Matter and High Energy Physics*, Springer Proceedings in Physics 278,
https://doi.org/10.1007/978-981-19-2592-4_15

organic hole conductors, ionic liquids, and polymer electrolyte. Various polymers such as polyethylene oxide (PEO) and polyvinyl alcohol (PVA). are being employed as electrolyte in DSSCs [3, 4]. In the present study, we have prepared polymer electrolyte based on Polyvinylidene fluoride (PVDF) with graphite as filler to improve the conductivity of the electrolyte. Polyvinylidene fluoride (PVDF) can be considered as a suitable for forming polymer electrolyte as it has some exceptional properties like thermal stability, chemical resistance, excellent mechanical strength, and photo-electrochemical stability under potential application [5, 6].

Generally synthetic dyes based on heavy metals have been employed as sensitizers to achieve high efficiency. However, these dyes have expensive production and complicated synthesis. Moreover, heavy metals used in their production causes environmental pollution. Therefore use of environmental friendly dyes such as natural dyes as photosensitizers in DSSC is gaining lot of attention. Natural pigments containing carotenoids, chlorophyll, betalains, and flavonoids which are found in various parts of plants such as vegetable, fruits, flowers, and leaves have been successfully used as photosensitizer in DSSCs [7, 8].

The photoanode is another very important component of DSSCs and is generally made up of nanocrystalline semiconductor. Generally TiO_2 is widely used to make photoanode as it is nontoxic, low cost, and widely available. But TiO_2 suffers from major drawback as it large band gap of 3.2 eV, so it can utilize only 6% of the total solar radiation. Studies have shown that the addition of various metal oxides like SnO_2, ZnO, WO_3, CeO_2, etc., can improve the photocatalytic or photoelectrolytic activities of TiO_2 [9, 10]. Due to the interesting physical properties of CuO, it has received considerable interest. The wide application of CuO as a gas sensor, and photochromic and electrochromic material makes it an interesting candidate for the modification of the TiO_2 photoelectrode [11].

In the present work, we fabricated DSSC with polymer electrolyte system composed of PVDF as a host polymer, LiI: I_2 as a redox couple, EC as plasticizer, graphite as filler with cocktail dye, and CuO modified TiO_2 photoanode. The properties like short-circuit photocurrent density (J_{SC}), open circuit voltage (Voc), fill factor (ff) conversion efficiency, and stability of the fabricated DSSC have been studied.

15.2 Experimental

15.2.1 Materials

For the preparation of natural dye, fresh black grapes and spinach leaves were purchased from the local market. Titanium Isopropoxide (Ti [OCH $(CH_3)_2]_4$), Copper (II) Chloride ($CuCl_2 \cdot 6H_2O$), Ethylene Carbonate (EC), Propylene Carbonate (PC), Lithium iodide, and Iodine were purchased from Sigma Aldrich. Co. Ltd. Analytical grade solvents like Ethanol, Propanol were purchased from Merck Ltd.

15.2.2 Preparation of Polymer Electrolyte

For the preparation of polymer electrolyte film, we have employed well-known solution cast technique. To prepare thin films, appropriate amount of PVDF was dissolved in the solvent. LiI: I_2 was also dissolved in the same polymeric solution. Tetrahydrofuran (THF) and dimethylsulphoxide (DMSO) in a suitable ratio was used as common solvent and stirring medium. The polymeric solution with salt and graphite filler along with Ethylene Carbonate was casted in the glass petridish. The graphite powder was synthesized by ball milling machine for 48 h at rotation speed of 300 rpm. For the evaporation of solvent, petridish was closely packed for 40 h at room temperature then a thick viscous solution was obtained, which was further dried at room temperature for 8 h. This film was further dried in incubator for controlled evaporation followed by vacuum drying to obtain the solvent free standing film.

15.2.3 Synthesis of TiO_2–CuO Photoelectrode

The TiO_2 and CuO nanopowders were prepared by sol–gel process. First, TiO_2 colloidal solution was prepared by adding Ti $[OCH(CH_3)_2]_4$ to propanol drop by drop, and then, deionized water was added for the duration of 10 min. A white precipitate was formed during addition, and then, 1 ml of 70% HNO_3 was added to the mixture. The mixture was then stirred for 15 min at 80 ºC, and at the same time, propanol together with some water was allowed to evaporate resulting in TiO_2 colloidal solution. For the preparation of CuO, colloidal solution $CuCl_2 \cdot 6H_2O$ (0.2 M) and 1 ml of glacial acetic acid are added to the aqueous solution and heated to 100 ºC with constant stirring. Then in this heated solution, 8 M NaOH is added till pH value reaches 7. The large amount of precipitate is formed quickly, resulting in a CuO colloidal solution. For the preparation of TiO_2–CuO admixed nanopowder, CuO solution was slowly added to the TiO_2 colloidal solution under vigorous stirring condition for 6 h. The resulting gel was dried and calcinied at 450 ºC to get TiO_2–CuO nanopowder.

ITO conductive glass plates with a sheet resistance of 15–20 Ω/cm^2 were first cleaned in a detergent solution using an ultrasonic bath for 15 min, rinsed with water and ethanol, and then dried. In order to obtain TiO_2–CuO film, TiO_2–CuO nanopowder pastes were deposited on the ITO conductive glass by doctor-blade technique. The film on the substrate was annealed in oven at 150 °C for 5–10 min.

15.2.4 Extraction and Purification of Dye

The cocktail dye was extracted from black grapes, and the chlorophyll dye was extracted from spinach leaves. The black grapes and spinach leaves were cut into

pieces washed and soaked separately in ethanol for one week, and then, it was crushed. Solutions were filtered out, and filtrates were concentrated in rotavapor at 40 °C. After that prepared extracts were refined by chromatogram method, and the extracts were blended at volume ratio of 1:1 to serve as natural cocktail dye sensitizer for DSSC. Chromatogram technique was used for the purification of dye.

15.2.5 Structural Characterization

The structural and morphological characterization of TiO_2–CuO nanomaterial was carried out through XRD by employing a Philips PW 1710 diffractometer (CuKα radiation) equipped with a graphite monochromater and scanning electron microscope (JEOL-JXA-8100 EPMA).

In order to explore the spectral response, the absorption spectra of cocktail dye-coated TiO_2–CuO on quartz glass substrates was carried out through double-beam spectrophotometer (Systronics 2201).

The XRD pattern of the prepared polymer electrolyte film was recorded between 2θ values 20–80° at room temperature using Phillips PW 1710 diffractometer. The optical micrograph of the film was recorded using computer-controlled polarizing microscope (LEICA DMLP).

Impedance measurements were carried out using Biologic SP-150. During all the measurements, humidity level was maintained at ~55% (constant).

Fabrication and cell performance measurement of DSSC—TiO_2–CuO-based electrode—was immersed in an ethanol solution containing a natural cocktail dye for 10–12 h. Dye-sensitized working electrode and counter electrode were assembled to form a solar cell by sandwiching a chitosan-based polymer electrolyte containing redox couple. All electrochemical measurements were carried out by a Biologic SP-150. A Xenon-Mercury lamp (Oriel Corporation, USA) was used as illumination source the intensity of which was adjusted and fixed at 100 mW/cm^2.

15.3 Results and Discussion

The XRD pattern of 99 {80 PVDF- 20 LiI: I_2}: 1 graphite film prepared by solution cast technique is shown in Fig. 15.1 (normalized). The XRD pattern of pure PVDF film shows sharp and intense peaks at 18.3º, 19.9º, and 26.6º, respectively. However, for pure graphite film, it is at 25º. From the comparative study of the XRD patterns, it is clear that the addition of graphite in the polymer matrix reduces the intensity of the main peak followed by broadening of the peak area, which is an indication of increase in the degree of amorphousity. This provides a better medium for fast protonic conduction of ions resulting in better conductivity of the film. The intercalation of the polymer chain with filler increases the interlayer spacing which results in increase in the amorphous nature of the film.

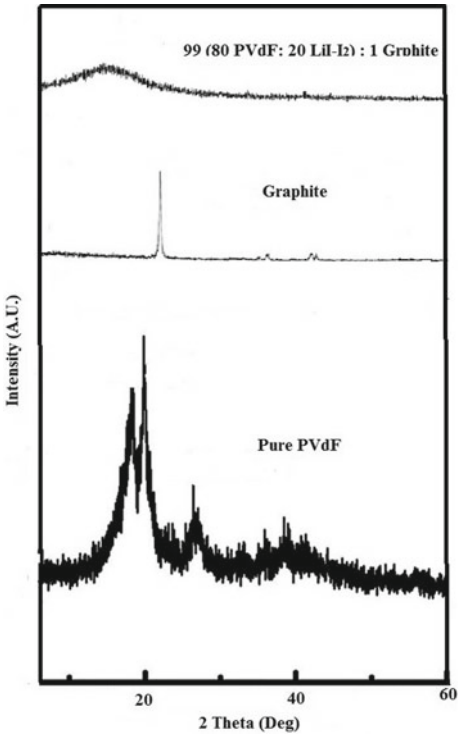

Fig. 15.1 XRD pattern of polymer electrolyte system

The optical micrograph of pure PVDF and 99 {80 PVDF - 20 LiI: I_2}: 1 graphite film prepared by solution cast technique at 80X magnification are shown in Fig. 15.2a, b. In pure PVDF film, several pores with a lamellar distribution can be seen. The addition of salt and filler drastically changed the microstructure of PVDF. The addition of filler connects these pores to each other due to lower surface energy resulting

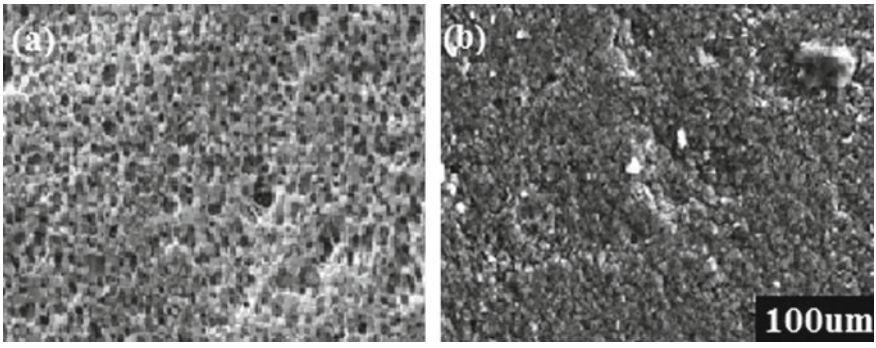

Fig. 15.2 Optical micrograph of the polymer electrolyte film, **a** pure PVDF and **b** 99 {80 PVDF-20 LiI: I_2}: 1 graphite

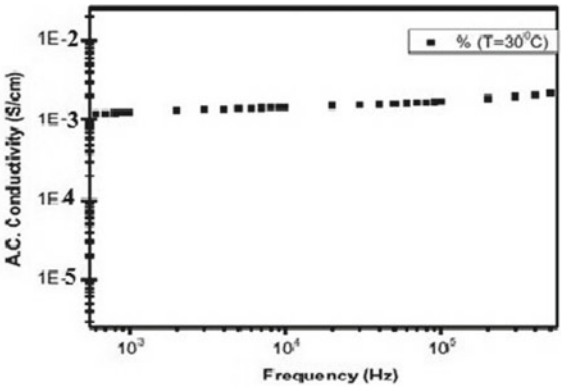

Fig. 15.3 Variation of ac conductivity of the film with frequency

in smooth surface of the film. The disappearance of these pores is advantageous for interfacial contact between the polymers and salt. The connectivity of the pores is favorable for the transportation of proton and thus resulting in improved ionic conductivity.

Figure 15.3 shows that the ambient ac conductivity of the PVDF-based polymer electrolyte reaches 10^{-3} S/cm. The conductivity increases linearly up to 5 kHz. According to well-known power law the ac conductivity of the sample depends on the frequency

$$\sigma^{ac} = A\omega^{\rho}$$

where A is constant and ρ is the frequency exponent ($\rho < 1$). The ω^{ρ} power law is very frequently observed in a wide range of materials among which is polymer.

The crystal structure and surface morphology of the prepared TiO_2–CuO nanoparticles were investigated by XRD and SEM analyses. X-ray diffraction pattern of the prepared TiO_2–CuO nanoparticles is shown in Fig. 15.4. The particles are found to be nanocrystalline in nature, and the crystallite size is obtained by the well-known Debye–Scherrer's equation. The crystallite size obtained using this formula is 20–35 nm.

The SEM image of the fabricated TiO_2–CuO nanoparticles is shown in Fig. 15.5, the SEM image reveals the highly porous nature of the resulting nanoparticles having grain size 20–35 nm. The small grain size offers large surface area, which offers many docking sites for the dye molecules and these molecules can anchor numerously and harvest immense amount of light.

The absorption spectra of the cocktail dye-coated TiO_2–CuO photoelectrode is shown in Fig. 15.6. The absorption peak is shifted toward the longer wavelength region which helps in improving the efficiency of the cell.

Figure 15.7 shows the cell performance of the PVDF-based DSSC with TiO_2–CuO photoelectrode sensitized with cocktail dye. The photocurrent (Isc) was found to be 9.86 mA/cm^2, and photovoltage (Voc) is 0.435 V. The conversion efficiency

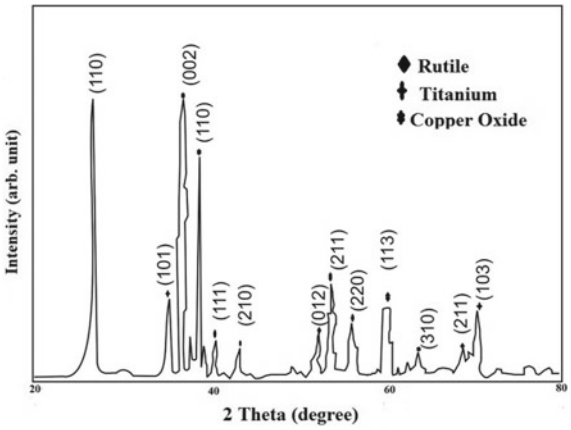

Fig. 15.4 XRD pattern of TiO_2–CuO nanopowder

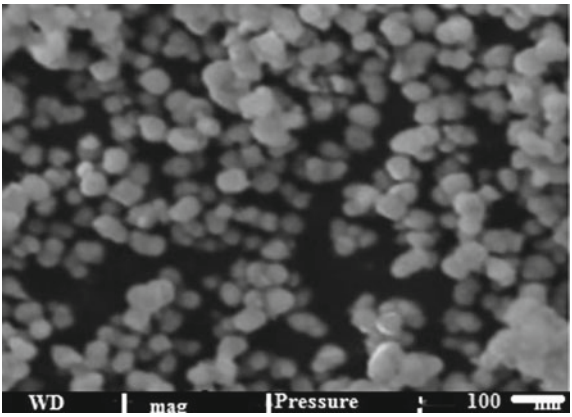

Fig. 15.5 Scanning electron micrograph of ns TiO_2–CuO

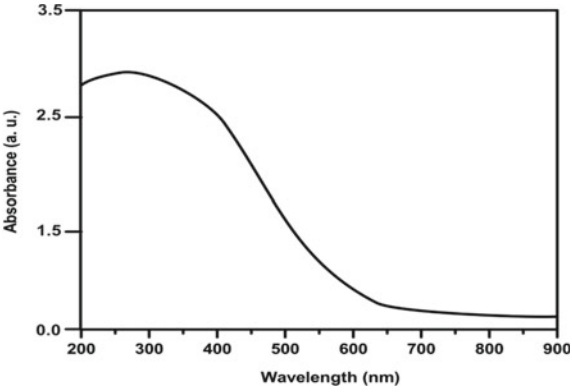

Fig. 15.6 Absorption spectra of cocktail dye-coated TiO_2–CuO photoelectrodeon ITO glass

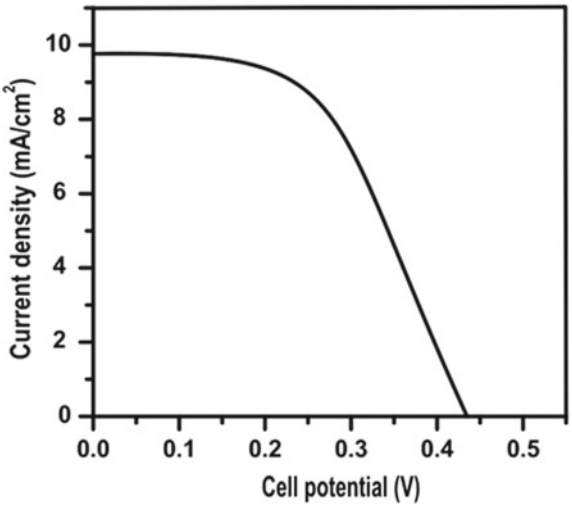

Fig. 15.7 Current–voltage characteristic curve of cocktail dye-coated TiO_2–CuO photoelectrode-based DSSC

and fill factor of cocktail dye-coated TiO_2–CuO photoanode were found to be 52% and 2.27%, respectively.

15.4 Conclusion

In the present work, we employed PVDF-based thin and mechanically stable polymer electrolyte for natural dye-sensitized-based DSSC. Ionic conductivity of the prepared electrolyte was found in the range of 10^{-5} S/Cm. The addition of graphite filler helped in improving the conductivity of the electrolyte. We have used TiO_2–CuO photoelectrode for DSSC. TiO_2 with CuO helps in improving the cell performance due to the reduced recombination rate of photoinjected electrons. In the present work, we have also explored the use of cocktail dye in DSSC. The cocktail dye prepared by 1:1 volume mixture of anthocyanin and chlorophyll dye obtained from black grapes and spinach leaves showed high absorption in the visible part of the solar spectrum. The dye showed better complexation with the photoelectrode, which aided in better charge transfer between the dye and the photoelectrode. Then, the cell performance of the TiO_2–CuO coated DSSC is investigated. The photocurrent (Isc) was found to be 9.86 mA/cm^2, and photovoltage (Voc) is 0.435 V. The conversion efficiency and fill factor of cocktail dye-coated TiO_2–CuO photoanode were found to be 52% and 2.27%, respectively.

Acknowledgements One of the authors is thankful to CSIR-India for the financial support in the form of Research Associate (RA).

References

1. R. Sastrawan, J. Beier, U. Belledin, S. Hemming, A. Hinsch, R. Kern, C. Vetter, F.M. Petrat, A. Prodi-Schwab, P. Lechner, W. Hoffmann, A glass frit sealed dye sensitized solar cell module with integrated series connections. Solar Energy Mater. Solar Cells **90**, 1680–1691 (2006)
2. I. Dincer, C. Acar, A review on clean energy solutions for better sustainability. Int. J. Energy Res. **39**(5), 585–606 (2015)
3. P. Chawla, M. Tripathi, Nanocomposite polymer electrolyte for enhancement in stability of Betacyanin dye sensitized solar cell. ECS Solid State Lett. **4**(1), 21–23 (2015)
4. Z. Seidalilir, R. Malekfar, H.P. Wu, J.W. Shiu, E.W.G. Diau, High performance and stable gel state dye sensitized solar cells using anodic TiO_2 nanotube arrays and polymer based gel electroly. ACS Appl. Mater. **23**, 12731 (2015)
5. S. Denizalti, A.K. Ali, C. Ela, M. Ekmekci, S.E. Ela, Dye sensitized solar cells using ionic liquids as redox mediators. Chem. Phys. Lett. **691**, 373–378 (2018)
6. R. Wang, B. Ahmed, S.K. Raghuvanshi, Siddhartha, N.P. Sharma, J.B.M. Krishna, M.A. Wahab, Prog. Nanotechnol. Nanomater. **2**, 42 (2013)
7. M. Kokkonen, P. Talebi, J. Zhou, S. Asgari, S.A. Soomro, F. Elsehrawy, J. Halme, S. Ahmad, A. Hagfelt, S.G. Hashmi, Advanced research trends in dye sensitized solar cells. J. Mater. Chem. A **9**, 10527–10545 (2021)
8. F. Kabir, M.M.H. Bhuiyan, M.S. Rahaman, M.A. Khan, T. Ikegami, Development of dye sensitized solar cell based on combination of natural dyes extracted from Malabar spinach and red spinach. Results Phys. 102474 (2019)
9. R. Vittal, K.C. Hou, Zinc oxide based dye sensitized based solar cells: a review. Renew. Sustain0 Energy Rev. 920–935
10. P. Chawla, M. Tripathi, CeO_2–TiO_2 photoanode for solid state dye sensitized solar cell. Ionics **21**(2), 541–546 (2015)
11. M. Tripathi, K. Pandey, S.D. Kumar, Surface modification of semiconductor photoelectrode for improved solar cell performance. Solar Energy Mater. Solar Cells **91**, 1663–1668 (2007)

Chapter 16
Morse Potential in Y-123 High Temperature Layered Superconductors

Hempal Singh

Abstract Adopting the Morse (combination of short-range repulsive and long-range attractive) potential, the stability, nature, and ranges of interactions for representative high temperature cuprate superconductor $YBa_2Cu_3O_{6+\delta}$(Y-123) have been investigated. The study of various interactions in Y-123, like Y–O, Y–Ba, and Y–Cu, has been incorporated as a function of inter-atomic distance. The results resemble with the earlier findings with deeper insight of short- and long-range interactions in the layered systems. This work is applicable to all the layered and high temperature superconductors.

16.1 Introduction

The advent of new era of high temperature superconductivity (HTSC) begun with the breakthrough discovery of first high temperature superconductor (HTS) ceramics Ba–La–Cu–O in 1986 by Bednorz and Muller [1]. These cuprate HTS are known for their layered structures with large number of atoms per unit cell, which mandatorily enforces the requirement of a suitable potential to study various dynamical properties of such systems. Many physicists attempted to describe various properties of layered superconductors adopting different types of potentials like Morse potential (MP) [2–4], Lennard–Jones potential [5, 6], Mie potential [7], and Born–Mayer–Huggins potential (BMH) [8]. Of these various potential, the present work deals analytically with the details and suitability of Morse potential in a new framework taking the case of Y-123 HTS with a comparison with Born–Mayer–Huggins potential.

H. Singh (✉)
Kirori Mal College, Department of Physics, University of Delhi, Delhi 110007, India
e-mail: physics.hempal@gmail.com

K. L. Pandey et al. (eds.), *Proceedings of the National Workshop on Recent Advances in Condensed Matter and High Energy Physics*, Springer Proceedings in Physics 278,
https://doi.org/10.1007/978-981-19-2592-4_16

16.2 The Morse Potential

Morse potential shows excellent outlay of repulsive and attractive forces which makes it one of the most suitable potential to study the layered systems and can be expressed in the following form [2–4]:

$$V_{ij} = D\left[e^{-2\,a(r-r0)} - 2\,e^{-\,a(r-r0)}\right] \tag{16.1}$$

where D and $r0$ are dissociation energy and inter-planer spacing, respectively. Two terms in the potential represent short-range repulsive (first term) and long-range attractive (second term) interactions.

16.3 Crystal Structure of Y-123 Superconductor

The layered structured Y-123 superconductor depicts the critical temperature 90–100 K and is highly anisotropic in nature. This contains two layers of Cu–O, two layers of Ba–O, two layers of CuO_2, and one layer of $\boldsymbol{Y}$. It bears orthorhombic crystal structure with $\vec{a} = \mathbf{3.82 \times 10^{-10} m}$, $\vec{b} = \mathbf{3.89 \times 10^{-10} m}$, $\vec{c} = \mathbf{11.6802 \times 10^{-10} m}$, and $\boldsymbol{\alpha = \beta = \gamma = 90°}$. In $YBa_2Cu_3O_{6+\delta}$, δ has range $0 < \delta < 1$ and if $0 < \delta < 0.4$ the sample exhibits an insulating state and for $0.4 < \delta < 1$ the sample remains in superconducting state. The details of layers and unit cell structure are depicted in Fig. (16.1) [9].

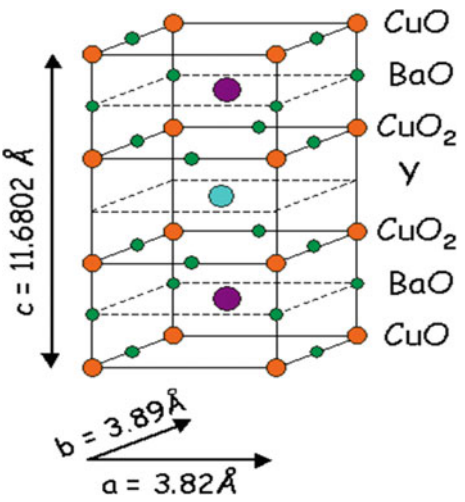

Fig. 16.1 Structure of unit cell of Y-123

16.4 Results and Discussions

Here, we focus the investigations to the representative high temperature superconductor layered crystal of Y-123 to study various response of Morse potential in the present framework. Considering Y(1) ion at the center of the system, a network of 38 ions/lattice site Cu(16), Ba(2), and O(20) is taken for numerical computation in which Ba–O layer has Ba(2) and O(8), CuO_2 plane has O(8) and Cu(8), and Cu–O layer O(4) and Cu(8) ions. The digits appearing with elements show the number of ions/lattice site used for the computation. The lattice constants are $a = 3.8$Å, $b = 3.9$Å, and $c = 11.60$Å, and other parameters are $D = 2.5635 \times 10^{-12}$ erg, $a = 1.3588\,\text{cm}^{-1}$[10]. The nature of Morse potential is compared with that of Born–Mayer–Huggins potential (total, combination of like and unlike charges and for various interactions) Y–Cu(I) and Y–O(I) (in CuO_2 plane), Y–O(II) and Y–Ba (in Ba–O layer), and Y–Cu(II) and Y–O(III) (in Cu–O layer) with interionic distances which has been portrayed in Figs. (16.2, 16.3 and 16.4). Here, we have taken the following form of Born–Mayer–Huggins potential:

$$V_{ij}(r) = a_{ij}\, e^{-b_{ij} r} + \frac{q_i\, q_j}{r} \tag{16.2}$$

The comparative study of MP and BMH potential for the interactions of total, unlike charges [combination of Y–O (I), Y–O(II) II and Y–O(III)] and like charges [combination of Y–Ba, Y–Cu (I) and Y–Cu (II)] has been portrayed in Fig. (16.2). It is

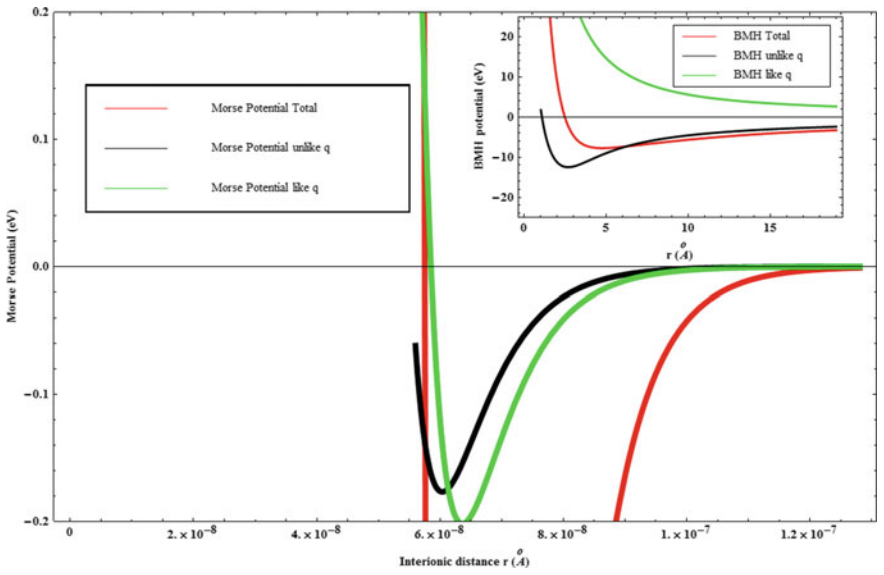

Fig. 16.2 Comparison of Morse potential with Born–Mayer–Huggins potential (interactions of combination of like and unlike charges) with interionic distance for Y-123 superconductor

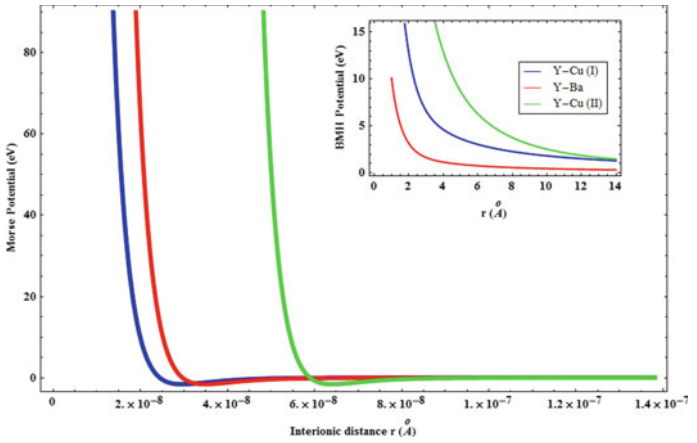

Fig. 16.3 Comparison of Morse potential with Born–Mayer–Huggins potential (interactions of like charges only) with interionic distance for Y-123 superconductor

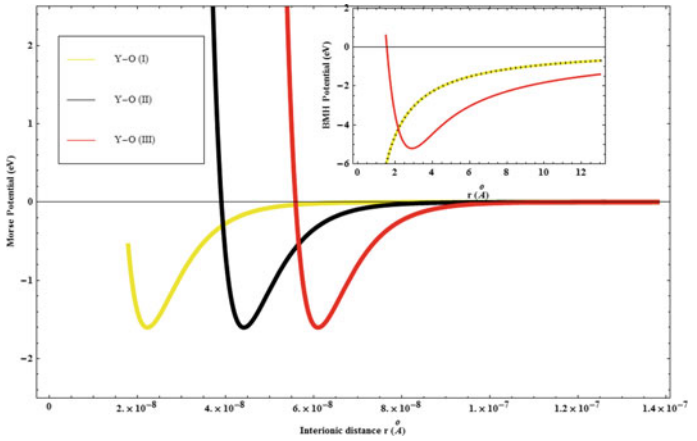

Fig. 16.4 Comparison of Morse potential with Born–Mayer–Huggins potential (interactions of unlike charges only) with interionic distance for YBCO superconductor

clearly observed that MP presents excellent outlay of repulsive as well as attractive and drastically changes its nature near 6.2Å, whereas BMH potential changes its nature around 4.5Å. The MP for the combinations of all the unlike interactions has attractive in nature and start to rise after 6Å, while BMH potential abruptly increases near 2.5Å. Again the MP for the combination of all the interactions of like charges shows the both type of nature attractive and repulsive and abruptly grows at 6.25Å, and on the contrary, BMH potential is repulsive throughout. The MP and BMH (for like charge interactions) have been depicted simultaneously in Fig. (16.3).

It is investigated that the interactions for MP are repulsive and attractive both, with a sharp change in their nature at 2Å[Y–Cu (I)], 2.5Å[Y–Ba], and 5.5Å[Y–Cu (II)] interactions, whereas for BMH potential these interactions are repulsive throughout and start to dissipate near 3.5Å, 2Å, and 5, respectively. Again, the comparison of MP with BMH for various unlike interactions is shown in Fig. (16.4). It is noticed that for MP different interactions have the nature Y–O(I) (repulsive), Y–O(II) (attractive and repulsive), and Y–O(III) (attractive and repulsive) and hastily change their character at 2Å, 4.25Å, and 6Å, respectively, while for BMH potential two interactions Y–O(I) and Y–O(II) have the same attractive nature and start to increase at 1.5Å. The Y–O(III) interaction is the only which shows attractive and repulsive both type of behavior and start to soar at 2.75Å.

16.5 Conclusions

The present investigations divulge that Morse potential may be taken as one of the suitable potential to study the stability, nature, and ranges of interactions. The obtained results are resembled with the earlier findings with deeper insight of short- and long-range interactions in the layered systems. This potential can be adopted to describe various dynamical properties of high temperature and layered superconductors.

References

1. J.G. Bednorz, K.A. Muller, Possible high T_C superconductivity in Ba–La–Cu–O system. Z. Phys. B **64**, 189 (1986)
2. P.M. Morse, Diatomic molecules according to the wave mechanics. II. Vibrational levels. Phys. Rev. **34**, 57 (1929)
3. R.N. Costa Filho, G. Alencar, B.-S. Skagerstam, J.S. Andrade Jr, Morse potential derived from first principles. Eur. Phys. Lett. **101**, 10009 (2013)
4. A.S. Shirinyana, Yu.S. Bilogorodskyy, Atom-Atom interactions in continuous metallic nanofilms. Phys. Met. Metallo. **113**, 823 (2012)
5. M.T. Dove, *Introduction to Lattice Dynamics*, 2st edn. (Cambridge University Press, New York, 1993)
6. A. Bizjak, T. Urbiˇc, V. Vlachy, Phase diagram of the Lennard-Jones system of particles from the cell model and thermodynamic perturbation theory. Acta Chim. Slov. **56**, 166 (2009)
7. R. Lesar, *Introduction to Computational Materials Science: Fundamentals to Applications*, 1st edn. (Cambridge University Press, New York, 2013)
8. H. Singh, A. Singh, B.D. Indu, The Born Mayer Huggins potential in high temperature superconductors. Mod. Phys. Lett. B. **30**, 1650283(1–10) (2016)
9. M.K. Wu, J.R. Ashburn, C.J. Torng, P.H. Hor, R.L. Meng, L. Gao, Z.J. Huang, Y.Q. Wang, C.W. Chu, Superconductivity at 93 K in a new mixed phase Y–Ba–Cu–O compound system ambient pressure. Phys. Rev. Lett. **58**, 908 (1987)
10. V. Ashokan, B.D. Indu, Renormalization effects and phonon density of states in high temperature superconductors. AIP Adv. **3**, 022108 (2013)

Chapter 17
Effect of Dispersion of Thiol-Capped AuNPs in Room-Temperature Discotic Material

Rahul Uttam, Sandeep Kumar, and Ravindra Dhar

Abstract Discotic liquid crystals (DLCs) are of enormous scientific interest due to their extraordinary unidirectional charge migration property and application in wide viewing liquid crystal display (LCD) devices. The unique geometry of columnar mesophases formed by disk-shaped molecules is important to study the one-dimensional charge and energy migration in nano-dispersions. In the present study, we have dispersed a low concentration of synthesized gold nanoparticles in a liquid crystal having a discotic columnar hexagonal mesophase at room temperature. These nanoparticles have been surface-stabilized using the thiol group to avoid aggregation. This also contributes in enhancing the stability of the dispersed nanocomposite. The dispersed system does not show any effect of dilution in the discotic mesophase and hence the thermodynamical property of nanocomposite such as transition enthalpy is increased. Textural observations of the pure and dispersed system confirms a well-ordered arrangement of gold nanoparticles inside the discotic matrix.

17.1 Introduction

Liquid crystals (LCs) exhibit a surfeit of distinguishing and remarkable properties that can be successfully modified for diverse inventive applications beyond the spectrum of displays [1, 2]. Discotic liquid crystalline mesophases are exhibited by disk-like molecules having an aromatic core to which are attached, via ester or ether linkages, usually six-to-eight alkyl chains of the same length [3]. Discotic molecules

R. Uttam (✉) · R. Dhar
Centre of Material Sciences, University of Allahabad, Prayagraj 211002, India
e-mail: ruttam95@gmail.com

R. Dhar
e-mail: rdhar@allduniv.ac.in

S. Kumar
Raman Research Institute, C.V. Raman Avenue, Sadashivanagar, Bengaluru 560080, India

Department of Chemistry, Nitte Meenakshi Institute of Technology, Bengaluru 560064, India

K. L. Pandey et al. (eds.), *Proceedings of the National Workshop on Recent Advances in Condensed Matter and High Energy Physics*, Springer Proceedings in Physics 278,
https://doi.org/10.1007/978-981-19-2592-4_17

have been shown to form both nematic and columnar mesophases. In a typical columnar mesophase, the molecules stack to form columns which in turn form a two-dimensional array, leading to various types of columnar mesophases such as hexagonal (D_h), rectangular (D_r), and oblique (D_{ob}) mesophase. A simple model for the formation of a discotic mesophase involves disordering of the side chains to attain a liquid-like state at the crystal-to-mesophase transition temperature, while the cores remain stacked and become disordered only at the isotropic temperature [4, 5]. The columnar organic liquid crystals were paid considerable attention due to their unique structures and properties such as extended π-stacking arrays which are favorable for transporting charge carriers along the columnar axis (unidirectional) and hence exhibiting the broad application in thin-film transistors, organic semiconductors, organic light-emitting diodes, and photovoltaic devices, etc. [6–10]. Rufigallol is an electron-deficient discotic molecule with six hydroxyl groups. By altering the soft alkyl chains linked via hydroxyl group with the anthraquinone core, different kinds of rufigallol-based columnar liquid crystals can be prepared [6]. These molecules have an elongated core with a twofold symmetry axis and are colored exhibiting polymorphism. The core is electron-deficient and thermodynamically stable [7, 8, 11]. More details can be found in our previous publications [7–10, 12, 13]. In the present work, we report the mesomorphic properties of alkanethiol-capped gold nanoparticles dispersed in the rufigallol-based discotic liquid crystal at a small concentration ($c = 0.4\%$ w/w). Hexanethiolate-stabilized gold nano-entities were prepared by following the reported method [14]. This procedure furnished 1.6 nm core diameter nanoparticles with an average composition of $Au_{140}[S(CH_2)_5CH_3]_{53}$ [14].

17.2 Experimental Techniques

RTAQ was prepared and purified as reported in the literature [11]. The liquid crystals–nanoparticles (LCs–NPs) composite was prepared by adding a small weight percentage of capped AuNPs in the host DLC. The capping around the Au core not only restricts the agglomeration of synthesized nanoparticles but also contributes to the stabilization and self-assembling of dopants in the dispersed mesophase. The synthesized alkanethiol-capped nanoparticles were characterized using an ultraviolet-visible spectrophotometer (Shimadzu UV-1800) with chloroform as a common solvent and Fourier transform infrared measurement (PerkinElmer Spectrum TWO spectrometer) in the range 400–4000 cm^{-1} at a resolution of 4 cm^{-1} using potassium bromide (KBr) as substrate. Textural studies of the pure and dispersed nanocomposite were performed using Polarized Light Microscope (PLM) coupled with a heating stage (Instec model HS-1) and temperature controller (Instec model mK 2) at a magnification of 100× and cooling rate of 0.1 °C/min. The thermal characterization of the columnar mesophase was done using Differential Scanning Calorimeter (NETZSCH model DSC-200-F3-Maia) at different scanning rates from 15.0 to 2.5 °C/min, in both heating and cooling cycles.

17.3 Results and Discussion

The pure DLC and prepared AuNPs-DLC nanocomposite were characterized using Polarized Light Microscopy, Differential Scanning Calorimetry, UV–visible spectroscopy, and Small-angle X-ray diffraction technique for the textural, thermodynamical, and optical characterization of the columnar mesophase respectively. The molecular overview (ball and stick model) of RTAQ is given in Fig. 17.1. Figure 17.2 shows the recorded optical and surface characterizations for the synthesized AuNPs. The formation of AuNPs was confirmed by UV–vis spectroscopy with a surface plasmon resonance peak close to 521 nm in the visible region (Fig. 17.2a). FTIR measurements show peaks at 670 and 721 cm^{-1} of the thiol group, band at 1632 cm^{-1} representing C=O stretching vibration frequency of COOH group, and band between 2800 and 3000 cm^{-1} signifying C–H stretching. Some other bands in the region 3000–3800 cm^{-1} are also observed [15, 16]. Figure 17.2b confirms the presence of thiol capping around the Au core. For studying the textural variations of pure DLC and nanocomposite due to dispersion, the microscope is kept in the cross-polarized state. Pure RTAQ shows pseudo focal conic type textures in the columnar phase (Fig. 17.3(a, b)) [17]. A uniform dark region is observed in the isotropic state for both systems. However, in the columnar phase, bright and dark domains signifying molecular planes slightly tilted and homeotropically aligned to the glass substrate were observed. The dispersed nanocomposite system also shows similar type of texture with no signs of aggregation (Fig. 17.3(c, d)). This confirms the presence of columnar hexagonal mesophase at room temperature in the nanocomposite. A monolayer of thiol capping around the Au core interacts strongly with aromatic cores of discotic molecules through π-π interactions. These are primarily responsible for holding the nanoparticles in the columnar mesophase. UV spectra of pure DLC and nanocomposite were recorded in the range 190–1000 nm. Pure RTAQ shows

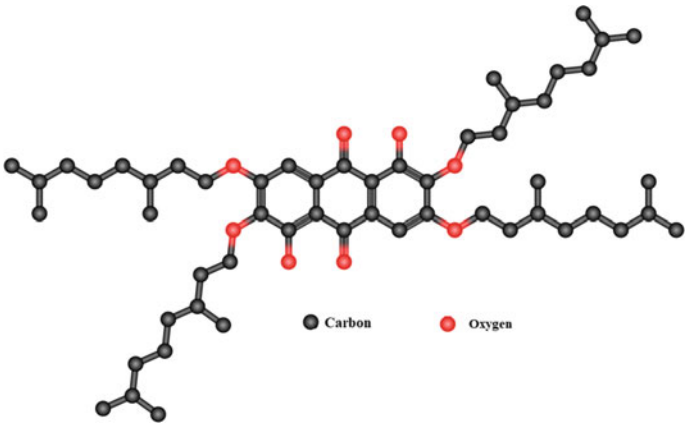

Fig. 17.1 Schematic representation of host DLC RTAQ (IUPAC name: 1,5-dihydroxy-2,3,6,7-tetrakis(3,7-dimethyloctyloxy)-9,10-anthraquinone)

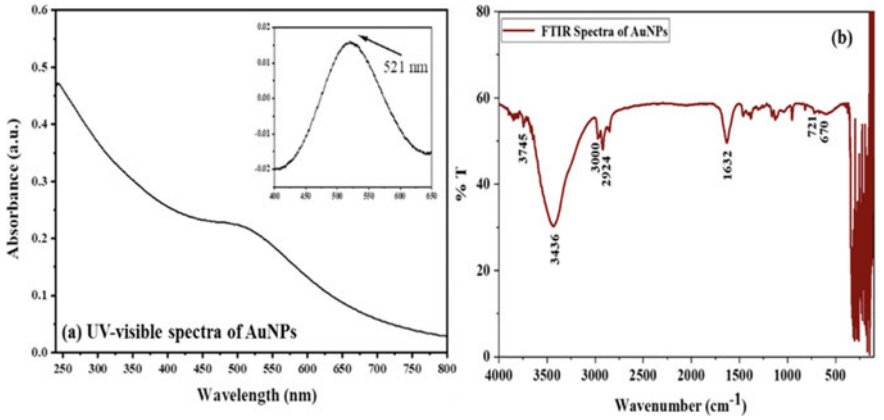

Fig. 17.2 Recorded, (**a**) ultraviolet-visible absorbance spectra and (**b**) Fourier transform infrared transmittance spectra of thiol-capped gold nanoparticles (AuNPs)

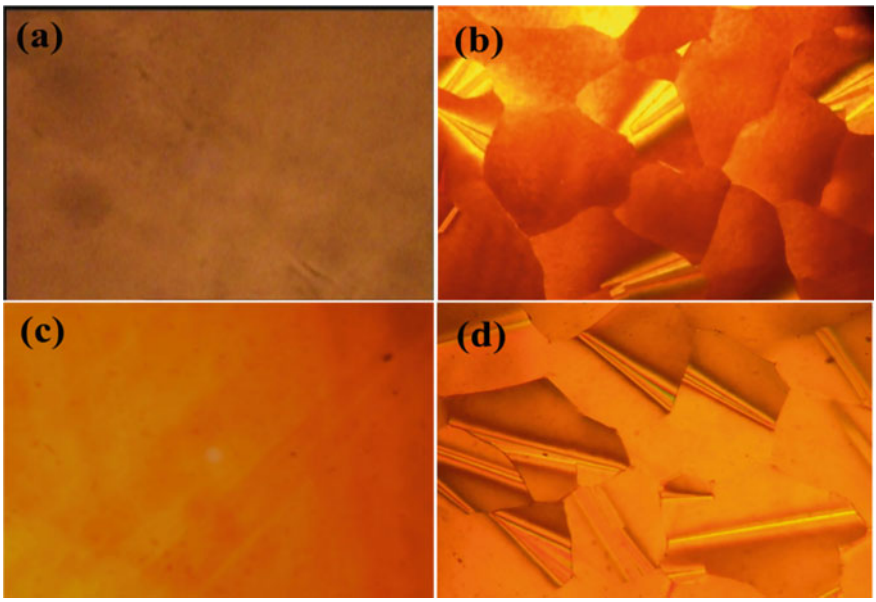

Fig. 17.3 Recorded optical textures for (**a**, **b**) pure RTAQ and (**c**, **d**) doped nanocomposite in the isotropic ($T = 125\,^{\circ}\mathrm{C}$) and columnar hexagonal ($T = 30\,^{\circ}\mathrm{C}$) phase under cross-polarized condition

absorption at 248.5, 347.0, and 434.0 nm with a direct bandgap of 3.5 eV (Fig. 17.4). The absorbance spectra of nanocomposite are similar to pure. This suggests a strong correlation between host molecules and dispersed nano-entity. The size of the used nanoparticle is almost similar to the size of a disk. Hence, the dispersion of AuNPs

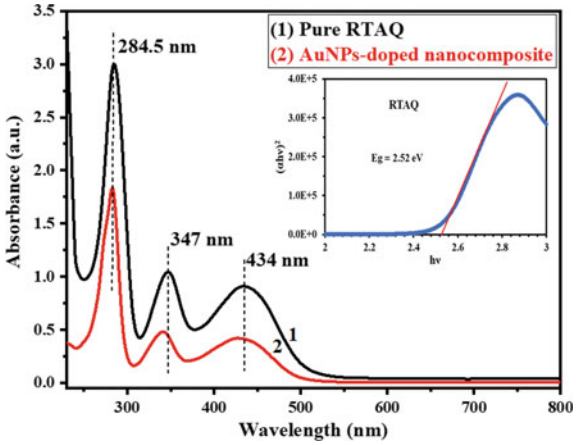

Fig. 17.4 Recorded absorbance spectra of pure RTAQ and AuNPs-dispersed nanocomposite. Inset shows Tauc plot for pure RTAQ

in the host matrix does not affect the columnar arrangement of disks, and occupies a position in between two discotic columns. The structure so formed has more packing efficiency as compared to that of pure. Thermodynamic study also confirms this result. A thermal study was performed from −30 °C to 130 °C at different scanning rates. On heating and cooling both the samples, peaks signifying columnar hexagonal-isotropic (Col_h–I) and isotropic-columnar hexagonal (I–Col_h) transitions appear. Under the condition of thermal equilibrium, both the transitions are supposed to occur at the same temperature. However, the observed transition temperature (T_p) is higher during the heating cycle and lower than the actual transition temperature during the cooling cycle. Hence, to determine the actual transition temperature, we extrapolate the scan rate versus transition temperature plot for both heating and cooling cycles. The extrapolated value of transition temperature for both the systems is 112.2 and 112.0 °C. Using NETZSCH thermal analysis software (Proteus), thermodynamic variables of the system such as transition enthalpy (ΔH), transition entropy (ΔS), the width of transition ($T_s \sim T_e$), and height of transition peak (h) for both the systems can also be determined. The incorporation of AuNPs in the host matrix led to the marginal decline of transition temperature value as compared to pure. This is due to the impurity/dilution effect of the non-liquid crystalline component (AuNPs) in the host matrix. The value of ΔH has increased for nanocomposite as compared to pure from 5.8 J/g to 6.1 J/g in the cooling scan. Similarly, ΔS also gets increased from 15.1 mJ/g-K for pure to 15.8 mJ/g-K in the cooling scan. This is because of the introduction of capped nano-entity in the host lattice which tries to strengthen the intercolumnar binding forces of hosts. However, the height of the transition peak has decreased while the width of the transition peak has increased for the nanocomposite. This implies that the transition process becomes a bit slow due to the presence of nanoparticles. Meanwhile, thermodynamic results confirm the presence of the Col_h

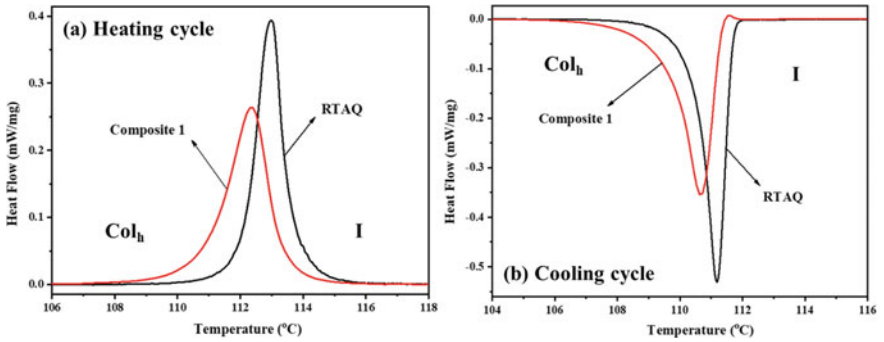

Fig. 17.5 Differential thermogram in the heating and cooling scans for pure RTAQ and AuNPs-doped DLC (scan rate = 2.5 °C/min)

mesophase at room temperature for both the systems and the absence of any crystallization process till −30 °C, as reported in our earlier publications [9, 12, 13] (Fig. 17.5).

17.4 Conclusion

We have experimentally shown that when a small quantity of surface-capped gold nanoparticles is dispersed in a room temperature discotic liquid crystal, AuNPs make a positive impact on the DLC's physical properties. Optical and surface characterization of synthesized nanoparticles confirms the formation of well-dispersed nanoparticles with thiol capping around the core. Optical, textural, and thermal studies confirm well-ordered columnar mesophase as compared to pure. Negligible aggregation or phase separation is also confirmed by the textural study. Thermodynamic results also confirm an increase in the transition enthalpy for the dispersed sample. Such dispersions make the present material (RTAQ) more applicable for use in electronic and electro-optical devices.

References

1. M. Kumar, S. Varshney, S. Kumar, Emerging nanoscience with discotic liquid crystals. Polym. J. **81**(1), 113–128 (2008)
2. R. Termine, A. Golemme, Charge mobility in discotic liquid crystals. Int. J. Mol. Sci. **22**(2), 877–928 (2021)
3. S. Chandrasekhar, Discotic liquid crystals A brief review. Liq. Cryst. **14**(1), 3–14 (1993)
4. E. Fontes, P.A. Heiney, M. Ohba, J.N. Haseltine, A.B. Smith III., Molecular disorder in columnar-phase discotic liquid-crystal strands. Phys. Rev. A **37**(4), 1329–1334 (1988)
5. D.M. Collard, C.P. Lillya, Control of thermal phase behavior of disklike molecules by modification of side-chain structure1. J. Armenian Chem. Soc. **111**, 1829–1830 (1989)

6. X. Zhang, H. Feng, M. Yan, H. Guo, F. Yang, The novel rufigallol-based liquid crystals with cholesterol units: synthesis, mesomorphic and photophysical properties. Liq. Cryst. **46**(5), 787–796 (2019)
7. R. Dhar, M. Gupta, V.K. Agrawal, S. Kumar, Characteristic dielectric parameters of columnar discotic hexa-*n*-alkoxyanthraquinones. Phase Transitions **81**(5), 459–469 (2008)
8. R. Dhar, S. Kumar, M. Gupta, V.K. Agrawal, Thermodynamic, optical and dielectric studies of the homologous members of columnar discotic compound Rufigallol hexa-n-alkoxylates. J. Mol. Liq. **141**, 19–24 (2008)
9. N. Yadav, S. Kumar, R. Dhar, Cadmium selenide quantum dots to ameliorate the properties of a room temperature discotic liquid crystalline material. RSC Adv. **5**(96), 78823–78832 (2015)
10. M. Bajpai, N. Yadav, S. Kumar, R. Srivastava, R. Dhar, Bulk heterojunction solar cells based on self-assembling disc-shaped liquid crystalline material. Liq. Cryst. **43**(3), 305–313 (2016)
11. H.K. Bisoyi, S. Kumar, Microwave-assisted synthesis of rufigallol and its novel room-temperature liquid crystalline derivatives. Tetrahedron Lett. **48**, 4399–4402 (2007)
12. R. Uttam, N. Yadav, S. Kumar, R. Dhar, Strengthening of columnar hexagonal phase of a room temperature discotic liquid crystalline material by using ferroelectric barium titanate nanoparticles. J. Mol. Liq. **294**, 111609 (2019)
13. R. Uttam, S. Kumar, R. Dhar, Magnified charge carrier conduction, permittivity and mesomorphic properties of columnar structure of a room temperature discotic liquid crystalline material due to the dispersion of low concentration ferroelectric nanoparticles. Phys. Rev. E **102**, 052702 (2020)
14. S. Kumar, V. Lakshminarayanan, Inclusion of gold nanoparticles into a discotic liquid crystalline matrix. Chem. Commun. **10**(14), 1600–1601 (2004)
15. A. Sharma, B.P. Singh, A.K. Gathania, Synthesis and characterization of dodecanethiol-stabilized gold nanoparticles. Indian J. Pure Appl. Phys. **52**(02), 93–100 (2014)
16. C. Fernandez-Ponce, J.P. Munoz-Miranda, D.M. de los Santos, E. Aguado, F. Garcia-Cozar, R. Litran, Influence of size and surface capping on photoluminescence and cytotoxicity of gold nanoparticles. J. Nanopart. Res. **20**, 305 (2018)
17. S. Kumar, Hierarchical discs. Liq. Cryst. Today **18**(1), 2–27 (2009)

Chapter 18
Neutrinos Properties and Its Detection

V. Singh, S. Karmakar, and M. K. Singh

Abstract Neutrino is one of the most elusive particles present in the universe. It also possess many puzzling nature. Many of its properties are still a mystery like the mass ordering, nature of neutrino, i.e., whether it is Dirac or Majorana type, and many other things. From oscillation experiments, we can have the idea of mass squared difference, but exact mass of flavor of neutrino is remains a mystery. Till date, we did not have the evidence for Neutrino less double beta decay, this phenomena have the potential to give the idea about the effective Majorana mass. Also neutrino nucleus coherent scattering can tell us about some interesting features about the neutrinos. In this paper, we will discuss different aspects of neutrino physics and the reach of some recent experiments. Also we will discuss some of the future planned experiments in the neutrino sector and the limit up to which they can reach.

18.1 Introduction

Neutrino plays an important role in the understanding of physics beyond standard model (BSM) [1–3]. Neutrino physics for the past several decades has advanced at a great pace. Various experiments running all over the world to understand the puzzle and to resolve the confusions related to the neutrino physics. It is now well known that three flavors of neutrinos can couple to the $W^{\pm}$ and Z^0 bosons [4]. Electroweak eigenstates for these neutrinos can be written as linear combinations of mass eigenstates [5]. Search of neutrino flavor oscillation is now well established and has the consequence that neutrinos possess a little but nonvanishing mass [5]. However, from the prediction of standard model physics, neutrinos are massless

V. Singh (✉)
Department of Physics, School of Physical and Chemical Sciences, Central University of South Bihar, Gaya 824236, India
e-mail: venkaz@yahoo.com; venktesh@cusb.ac.in

S. Karmakar · M. K. Singh
Department of Physics, Institute of Applied Sciences and Humanities, GLA University, Mathura 281406, India

K. L. Pandey et al. (eds.), *Proceedings of the National Workshop on Recent Advances in Condensed Matter and High Energy Physics*, Springer Proceedings in Physics 278,
https://doi.org/10.1007/978-981-19-2592-4_18

and flavor oscillation is thus forbidden. Oscillation experiments give us idea about the mass squared difference but not about the absolute mass [2–5]. Some unknown parameters in neutrino physics like the sign of largest mass squared difference which leaves the door open for the two possible mass ordering of the neutrino, corresponding to the two signs. Other unknown parameters are the value of a possible CP-violating phase in the neutrino mixing matrix, and the Dirac or Majorana nature of neutrinos [4–6].

18.2 Neutrino Properties and Its Detection

The study of neutrino interaction will reveals the mystery of neutrino. So we can look at some phenomena like neutrinoless double beta decay [7], oscillation of neutrino flavor [5], neutrino nucleus coherent scattering [8], interaction of neutrino as a millicharged candidate [9], etc. These interactions have the ability to check the correct mass ordering of neutrinos, they can also tell us whether neutrino is Dirac or Majorana in nature, etc. Here, we will discuss some of the above-mentioned phenomena and the limit up to which different collaborations have reached.

18.2.1 Neutrinoless Double Beta Decay

Search of $0\nu\beta\beta$ decay could be one of the best ways to answer problems related to lepton number violation, nature of neutrino, i.e., Dirac or Majorana, mass hierarchy of neutrino, matter antimatter asymmetry, etc. Physicists were doing active work for more than 75 years. At first, it originates as a nuclear physics problem and then along with the progress in physics it becomes a relevant problem in particle physics. In 1930, Wolfgang Pauli proposed neutrinos, in order to explain the continuous spectrum of β decay. Fermi in 1932 was introducing neutrino in his theory of beta decay. M. Goeppert-Mayer in 1935 introduces the concept of double beta decay after that W. H. Furry suggested that zero neutrino double beta decay is possible if neutrino is Majorana particle [10, 11]. From this time searching facility has developed, at first, geochemical and radiochemical technique have used latter on direct detection technique has used. In 1987, M. K. Moe and coworkers have reported the $2\nu\beta\beta$ decay for the first time. Germanium-based detection for $0\nu\beta\beta$ is well developed now [12]. Germanium can be used as the source as well as the detector for the search of $0\nu\beta\beta$ which increases the chance of the event detection. After giving many significant results, GERDA [13] and Majorana demonstrator [14] have merged to build a ton scale experiment with enriched ^{76}Ge. Their signal discovery sensitivity is expected to be greater than 10^{28} yr for $0\nu\beta\beta$ half-life [15]. Other experimental collaboration working on this field is CUORE they have focused with tellurium oxide. They were also not able to find $0\nu\beta\beta$ decay evidence and have put limit for ^{130}Te with 90% credibility interval Bayesian lower limit to 3.2×10^{25} yr [16]. Xe-based double beta

decay experiments have also a good impact like KamLAND-Zen 400, they are also planning to go for ton size experiments with Xe in there KamLAND2-Zen experiment [17].

18.2.2 Electromagnetic Properties of Neutrino

We can probe BSM another way by looking at the electromagnetic (EM) property of the neutrino. With the study of the EM property, we can get idea about Dirac or Majorana nature of neutrinos [18]. Basically, cosmological and astrophysical source of neutrino is a good tool to look at as they pass through intense magnetic field [19]. To study this types of interaction, one of the prime need is detector with sub-keV threshold. So in this detection, high-purity germanium-based detection technology is one of best proved technology [19–22]. Different collaborations have studied neutrino as a millicharged particle and also able to put limits. GEMMA and TEXONO are doing some of the world leading experiments. Using germanium detector with 300 eV threshold, TEXONO collaboration has set the limit on millicharge (with respect to electronic charge) 1.0×10^{-12} with 90% confidence limit [9]. GEMMA collaboration has also put upper limit on neutrino millicharge $<2.7 \times 10^{-12}$ e_0 with 90% CL where e_0 is the absolute value of the electronic charge [23]. These collaborations have also put limits on the magnetic moment of the neutrinos [9, 23], now they are focusing in lowering the detection threshold to enhance the detection.

18.2.3 Neutrino Nucleus Coherent Scattering

Elastic scattering of neutrino with nucleus (νA_{el}) is also a good tool to study the neutrino characteristics as well as BSM [24]. This process is well defined in the standard model of particle physics as weak interaction process. We can study different phenomena like density distributions of neutron, also we can look at supernova neutrinos, quantum–mechanical coherent effect in electroweak interactions also we can put a compact small-sized neutrino detectors for nuclear reactors real-time monitoring. The main background in the study of the future dark matter experiment is the νA_{el} events from atmospheric and solar neutrinos [24–27]. After its predication, various collaborations have started to search for this decay. As the other interaction of the neutrino, this also has very low cross-section of detection. The small rate of interaction and very little recoil are the main point of concern. COHERENT collaboration has detected coherent neutrino nucleus scattering (CEvNS) for the first time in history with the help of CsI[Na] scintillator detector in 2017 [8]. Neutrino from nuclear reactor have very high flux and their energy is also capable of elastically scatter from detector nuclei. TEXONO collaboration is also working on the νA_{el} searches with high-purity point contact germanium detector with the Kuosheng

nuclear reactor. They have also reached ~200 eV_{ee} threshold with the electro-cooled PCGe detector [28, 29].

18.3 Different Detection Technology Used in Neutrino Search

Till now, we have seen that detection of neutrino by different interaction channel is a tedious task. As the interaction rate is very much low, we need very much optimized detector and background-free environment to study neutrinos. Direct dark matter experiments with recent upgradation can also involve in neutrino searches. Neutrino will basically interact by scattering elastically from electron also it can coherently scattered of the detector nucleus [24–28, 30–33]. Due to this, a very low amount of recoil will be produced. Recoil can be observed in terms of scintillation or ionization produced by the neutrino in the detector element. Various detectors were used by different collaborations like inorganic scintillator detector, semiconductor detectors, noble liquid, superconductor detectors, etc. CsI detectors have a benefit in CEvNS detection as it have large cross-section also it can produce enough scintillation for the detection. Sub-keV germanium detector has also a good potential in the study of the neutrino physics, like TEXONO is using it in search of millicharge and magnetic moment of neutrino [28, 29]. Also germanium detector is used in the $0\nu\beta\beta$ search as it can be used to large ton sized detector. It also have good resolution at the required energy [9, 15, 23].

18.4 Conclusion and Future Outlooks

So we can see from the above that various experiments are running on the search to unzip the hidden mystery in the neutrino sector. Detection of neutrino less double beta decay can give us the answer about the nature of the neutrino with ton size future experiments. Also neutrino nucleus coherent scattering can give the idea about mass and many other properties of neutrino, so we are looking forward for the outcome of the future experiments.

Acknowledgements The authors are thankful to the DST, New Delhi, and grateful to the Ministry of Human Resource Development (MHRD), New Delhi, for the financial support through the scheme for Promotion of Academic and Research Collaboration (SPARC) project No. SPARC/20182019/P242/SL.

References

1. T.B. Cleveland et al., Measurement of the solar electron neutrino flux with the home stake chlorine detector. Astrophys. J. **496**, 505–526 (1998)
2. T. Kajita, Neutrino oscillations: discovery, current status, future directions. Int. J. Mod. Phys. A **24**, 3437–3446 (2009)
3. S.T. Petcov, Leptonic CP violation and lipogenesis, in *Proceedings of the Conference in Honour of the 90th Birthday of Freeman* (2014), pp. 179–201
4. H.E. Fisk et al., Charged current neutrino interactions. Annu. Rev. Nucl. Part. Sci. **32**, 499–573 (1982)
5. C. Giganti et al., Neutrino oscillations: the rise of the PMNS paradigm. Prog. Part. Nucl. Phys. **98**, 1–54 (2018)
6. S. Pakvasa, CP violation in the neutrino sector. J. Phys.: Conf. Ser. **556**, 012060 (2014)
7. K. Zuber, Double beta decay experiments. J. Phys. G: Nucl. Part. Phys. **39**, 124009 (2012)
8. D. Akimov et al., Observation of coherent elastic neutrino-nucleus scattering. Science **357**(6356), 1123–1126 (2017)
9. J.W. Chen et al., Constraints on millicharge neutrinos via analysis of data from atomic ionizations with germanium detectors at sub-keV sensitivities. Phys. Rev. D **90**, 011301(R) (2014)
10. W.H. Furry, On transition probabilities in double beta-disintegration. Phys. Rev. **56**, 1184–1193 (1939)
11. S. Dell'Oro et al., Neutrinoless double beta decay: 2015 review. Adv. High Energy Phys. **2016**, 2162659 (2016)
12. S.R. Elliott et al., Direct evidence for two-neutrino double-beta decay in ^{82}Se. Phys. Rev. Lett. **59**(18), 2020 (1987)
13. M. Agostini et al., Probing Majorana neutrinos with double-decay. Science **365**(6460), 1445–1448 (2019)
14. S.I. Alvis et al., Search for neutrinoless double-β decay in ^{76}Ge with 26 kg yr of exposure from the MAJORANA DEMONSTRATOR. Phys. Rev. C **100**, 025501 (2019)
15. N. Abgrall et al., The large enriched germanium experiment for neutrinoless double beta decay (LEGEND). AIP Conf. Proc. **1894**, 020027 (2017)
16. D.Q. Adams et al., Improved limit on neutrinoless double-beta decay in ^{130}Te with CUORE. Phys. Rev. Lett. **124**, 122501 (2020)
17. Y. Gando et al., First results of KamLAND-Zen 800. J. Phys.: Conf. Ser. **1468**, 012142 (2020)
18. J.W. Chen et al., Constraining neutrino electromagnetic properties by germanium detectors, arXiv:1411.0574v1 (2014)
19. A.K. Soma et al., Characterization and performance of germanium detectors with sub-keV sensitivities for neutrino and dark matter experiments. Nucl. Instrum. Methods Phys. Res. A **836**, 67–82 (2016)
20. H.T. Wong et al., Research program towards observation of neutrino-nucleus coherent scattering. J. Phys. Conf. Ser. **39**, 266–268 (2006)
21. M.K. Singh et al., Background rejection of TEXONO experiment to explore the sub-keV energy region with HPGe detector. Indian J. Phys. **91**(10), 1277–1291 (2017)
22. M.K. Singh et al., Study of the inactive layer of sub-keV point contact germanium detector. J. Sci. Res. **65**(1), 237–243 (2021)
23. V.B. Brudanin et al., New bounds on neutrino electric millicharge from GEMMA experiment on neutrino magnetic moment. Nucl. Part. Phys. Proc. **273–275**, 2605–2608 (2016)
24. D.Z. Freedman, Coherent effects of a weak neutral current. Phys. Rev. D **9**, 1389 (1974)
25. S. Kerman et al., Coherency in neutrino-nucleus elastic scattering. Phys. Rev. D **93**, 113006 (2016)
26. D.A. Sierra et al., Impact of form factor uncertainties on interpretations of coherent elastic neutrino-nucleus scattering data. J. High Energy Phys. **2019**, 141 (2019)
27. J. Monroe et al., Neutrino backgrounds to dark matter searches. Phys. Rev. D **76**, 033007(2007)

28. H.B. Li et al., Differentiation of bulk and surface events in p-type point-contact germanium detectors for light WIMP searches. Astropart. Phys. **56**, 1–8 (2014)
29. H. Jiang et al., Measurement of the dead layer thickness in a p-type point contact germanium detector. Chin. Phys. C **40**(9), 096001 (2016)
30. M. Drees et al., Review of particle physics. Phys. Rev. D **98**, 030001:396 (2018)
31. V. Sharma et al., Coherency in neutrino-nucleus elastic scattering. J. Phys.: Conf. Ser. **1468**, 012149 (2020)
32. V. Sharma et al., Studies of Quantum-Mechanical Coherency Effects in Neutrino-Nucleus Elastic Scattering, arXiv:2010.06810v1
33. H.B. Li et al., Limits on spin-independent couplings of WIMP dark matter with a p-type point-contact germanium detector. Phys. Rev. Lett. **110**(26), 261301 (2013)

Chapter 19
Identified Charged Particle Production in Pb + Pb Collisions at $\sqrt{s_{NN}} = 2.76$ TeV Using Tsallis Distribution Function

P. Kumar, P. K. Khandai, K. Saraswat, and V. Singh

Abstract In the proceeding, we show the transverse momentum (p_T) spectra of identified charged particles such as pion and kaon in Pb + Pb collisions at $\sqrt{s_{NN}}$ = 2.76 TeV using Tsallis distribution function. The power law of Tsallis/Hagedorn distribution function gives very good description of the hadron spectra in p_T range from 0.2 to 300 GeV/c in p + p collisions. Here, we use Tsallis distribution function as a fitting function to the data of invariant yield versus p_T of pion and kaon at various centralities in Pb + Pb collisions. These published data are taken from ALICE collaboration at mid-rapidity region. The Tsallis parameter T governs the soft bulk contribution to the spectra, and the parameter q shows the nonthermalization of the system. The data/fit shows deviations of the data from the Tsallis distribution. The parameters of such fittings are studied as a function of centralities.

19.1 Introduction

One of the primary objectives of heavy ion collisions is to create a novel phase of matter, known as quark–gluon plasma (QGP), where quarks and gluons are no longer confined inside the hadrons. This type of situation was formed in the beginning of the universe just after the Big Bang. The heavy ion collisions are performed at relativistic heavy ion collider (RHIC), BNL (USA) [1], and at large hadron collider (LHC),

P. Kumar
Department of Physics, Banaras Hindu University, Varanasi 221005, India

P. K. Khandai (✉)
Department of Physics, Ewing Christian College, Prayagraj 211003, India
e-mail: pkkhandai@gmail.com

K. Saraswat
Institute of Physics, Academia Sinica, Taipei, Taiwan

V. Singh
Department of Physics, Institute of Applied Science and Humanities, GLA University, Mathura 281406, India

K. L. Pandey et al. (eds.), *Proceedings of the National Workshop on Recent Advances in Condensed Matter and High Energy Physics*, Springer Proceedings in Physics 278,
https://doi.org/10.1007/978-981-19-2592-4_19

CERN (Switzerland) [2], where QGP [3] is produced under special conditions of temperature and pressure. The QGP is a thermalized state of matter which behaves like a perfect fluid, and hence a collective behavior of quarks and gluons is observed here [4]. The RHIC is designed to collide heavy ions such as Au + Au, Cu + Cu, U + U, Cu + Au along p + p and d + Au with center of mass energies ranging from $\sqrt{s_{\mathrm{NN}}} = 7.7$ to 200 GeV, whereas the LHC is designed to collide heavy ions such as Pb + Pb, Xe + Xe along with p + p and p + Pb with center of mass energies ranging from $\sqrt{s_{\mathrm{NN}}} = 0.9$ to 7 TeV even more.

The study of transverse momentum (p_{T}) spectra of hadrons is one of the important tools in high-energy collisions. This is because the transverse motion is generated during the collision and hence is sensitive to the collision dynamics. In heavy ion collisions, collective behavior is expected due to the large number of multi-particle scatterings [4]. The transverse momentum (p_{T}) spectra of identified particles can be used to study the collective properties [4] as well as the particle production mechanism in p + p and heavy ion (A + A) collisions. Some additional final state effects such as recombination [5] and jet-quenching [6] in different p_{T} ranges are observed in heavy ion collisions.

The Tsallis distribution [7] function successfully describes hadron p_{T} spectra in terms of only two parameters such as T and q. The parameter T signifies the freeze-out temperature, and the parameter q shows the degree of nonthermalization. The functional form of the Tsallis distribution, which describes near-thermal systems, is essentially the same as the Hagedorn power law function it is applicable to QCD hard scatterings [8]. There are various studies which show that the Tsallis/Hagedorn distribution gives an extremely good explanation of p_{T} spectra of all identified hadrons measured in p + p collisions at RHIC and LHC energies [9, 10]. When it is coming to heavy ion collisions, the Tsallis distribution function is not that much useful, so various modifications of Tsallis distribution have been done [11]. The current paper presents a study of the Tsallis distribution for p_{T} spectra of identified charge particle such as pions (π^+, π^-) and kaons (K^+, K^-) produced in Pb + Pb collisions at $\sqrt{s_{\mathrm{NN}}}$ = 2.76 TeV. The statistical and systematic errors are added in quadrature and are used in the fits. The parameters of such fittings are studied as a function of center of centralities. We use the published data of ALICE [11] collaboration at mid-rapidity regions and parameterize the data with Tsallis distribution to study the p_{T} spectra of pions and kaons in different centralities of Pb + Pb collisions.

19.2 Tsallis Distribution Function

The Tsallis distribution function describes thermal system in terms of two parameters, one is temperature T and another is q which measures the degree of nonthermalization. Tsallis distribution function given as

$$E\frac{d^3N}{dp^3} = C_n m_T \left(1 + (q-1)\frac{m_T}{T}\right)^{\frac{-1}{(q-1)}} \tag{19.1}$$

Here, C_n is the normalization constant, m_T is the transverse mass, T is the Tsallis temperature, and $q = (1 + n)/n$ is called nonextensive parameter that measures the temperature fluctuation inside the system. This form same as the QCD-inspired Hagedorn function. The Hagedorn function describes the transverse mass ($m_T = \sqrt{p_T^2 + m^2}$) distribution of particles produced in hadronic collisions. QCD-inspired Hagedorn function summed power law [10] given as

$$E\frac{d^3N}{dp^3} = A\left(1 + \frac{m_T}{nT}\right)^{-n} \tag{19.2}$$

This function describes both the particles produced in QCD hard scatterings reflected in the high p_T region and bulk spectra in the low pT region. Both (19.2) and in (19.1) have similar mathematical forms with $n = 1/(q - 1)$ and $p_0 = nT$. Larger values of n correspond to smaller values of q. Both n and q have been interchangeably used in Tsallis distribution. Phenomenological studies suggest that, for quark point scattering, $n \sim 4$, which grows larger if multiple scattering centers are involved. The study in [12] suggests that both the forms given in (19.1) and in (19.2) give equally good fit to the hadron spectra in p + p collisions. We use (19.2), in case of Pb + Pb collisions to obtain the p_T spectra of pions and kaons.

19.3 Results and Discussions

Figures 19.1 and 19.3 show the p_T spectra of pions and kaons as a function of p_T for different centralities of Pb + Pb collisions at $\sqrt{s_{NN}} = 2.76$ TeV and Figs. 19.2 and 19.4 show the data/fit as a function of p_T for different centralities of Pb + Pb collisions at $\sqrt{s_{NN}} = 2.76$ TeV. Here, we observe that the Tsallis distribution holds good for heavy ion collisions at low p_T region.

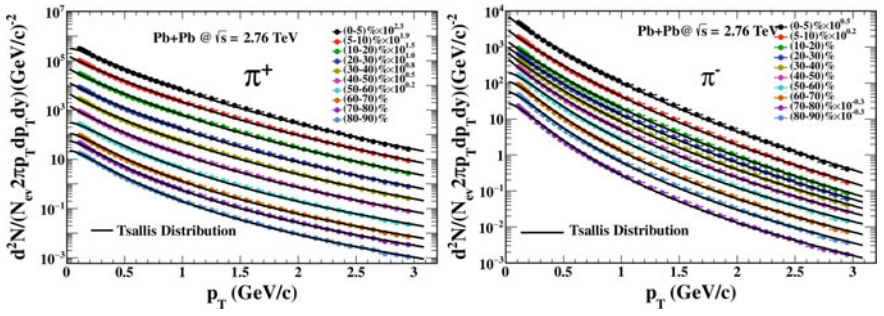

Fig. 19.1 Invariant yields of the pions (π^+ and π^-) as a function of transverse momentum p_T for Pb + Pb collision at $\sqrt{s_{NN}} = 2.76$ TeV measured by the ALICE experiment [11] at different centrality class. The solid curves are the fitted Tsallis distributions

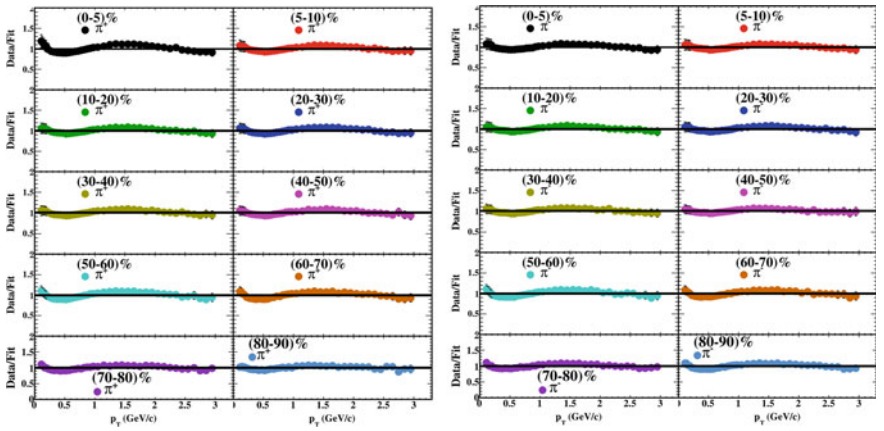

Fig. 19.2 Ratio of pion (π^+ and π^-) data and the fit function (Tsallis distribution 19.2) as a function of transverse momentum p_T for Pb + Pb collisions at $\sqrt{s_{NN}} = 2.76$ TeV data used in the fit for different centrality classes. The solid curves are the fitted Tsallis distributions. The left panel is for positive pions and the right panel is for negative pions. Here it is clearly noticed that the Tsallis distribution function fits perfectly with the data

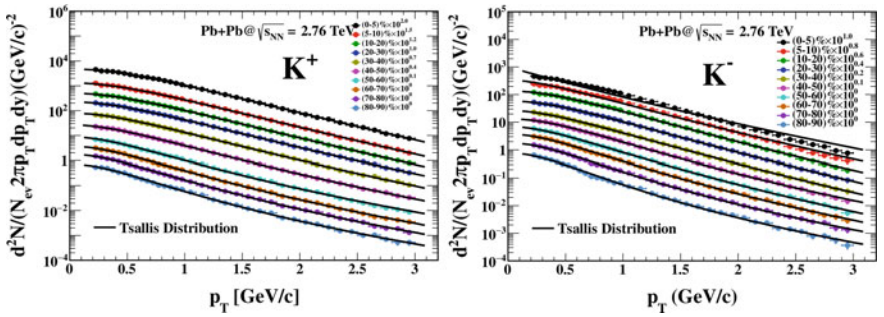

Fig. 19.3 Invariant yields of the positive and negative kaons (k^+ and k^-) as a function of transverse momentum p_T for Pb + Pb collision at $\sqrt{s_{NN}} = 2.76$ TeV measured by the ALICE experiment [11] at different centrality class. The solid curves are the fitted Tsallis distributions. The left panel is for positive kaons and the right panel is for negative kaons

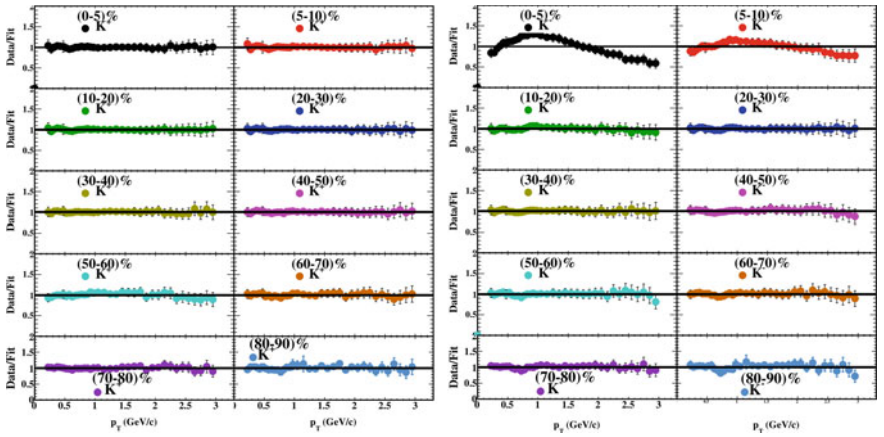

Fig. 19.4 Ratio of kaons (k^+, k^-) data and the fit function (Tsallis distribution 19.2) as a function of transverse momentum p_T for Pb + Pb collisions at $\sqrt{s_{NN}} = 2.76$ TeV data used in the fit for different centrality classes. The solid curves are the fitted Tsallis distributions. The left panel shows the data/fit of positive kaons and the right panel shows the data/fit of negative kaons. Here it is clearly seen that the fitting function fits the data perfectly

19.4 Conclusion

In this work, we have studied the transverse momentum spectra of pion and koan in the Pb + Pb collisions at $\sqrt{s_{NN}} = 2.76$ TeV using Tsallis distribution function. This function gives very good description of measured data from ALICE collaboration.

Acknowledgements We are thankful to all the members of the organizing committee of ACFP-2022, GLAU, and the AIP committee for selecting our proceedings.

References

1. K. Adcox et al. (PHENIX), Nucl. Phys. A **757**, 184–283 (2005), J. Adams et al. (STAR), Nucl. Phys. A **757**, 102–183 (2005)
2. N. Armesto et al. (LHC), J. Phys. G **35**, 054001 (2008)
3. E.V. Shuryak, Quantum chromodynamics and the theory of superdense matter. Phys. Rep. **61**, 71–158 (1980)
4. I.G. Bearden et al. (NA44), Phys. Rev. Lett. **78**, 2080–2083 (1997)
5. D. Prorok et al., Eur. Phys. J. A **55**, 37 (2019)
6. X.N. Wang, Phys. Lett. B **579**, 299 (2004)
7. C. Tsallis, J. Stat. Phys. **52**, 479 (1988)
8. R. Hagedorn, Riv. Nuovo Cim. 6N10 1 (1983)
9. P.K. Khandai, P. Sett, P. Shukla, V. Singh, Int. J. Mod. Phys. A **28**, 1350066 (2013)

10. P.K. Khandai, P. Sett, P. Shukla, V. Singh, J. Phys. G **41**, 025105 (2014). arXiv:1310.4022 [nucl-th]
11. B. Abelev et al., Phys. Rev. C **88**, 044910 (2013). arXiv:1303.0737 and references therein
12. H. Zheng, L. Zhu, A. Bonasera, Phys. Rev. D **92**, 074009 (2015). arXiv:1506.03156 [nucl-th]

Chapter 20
Multiplicity Features of the Grey Particles Emerged in $^{84}Kr_{36}$ + Em Interaction at 1 GeV per Nucleon

M. K. Singh, P. K. Khandai, and V. Singh

Abstract In this manuscript, we have focus on the target dissolution (mainly grey particles) emerged from the interactivity of the $^{84}Kr_{36}$ and nuclear emulsion detector (NED). NED is a composite target detector. In this analysis, we have used NIKFI-BR-2 emulsion plates. This analysis shows that the emission feature of the grey particle is not depending on the projectile mass and strongly depends on the various types of target groups of NED participating in the collisions.

20.1 Introduction

Nuclear disintegration is a key of experimental phenomenon in nucleus–nucleus collision at relativistic energy [1–3]. The PS model is the base model for the study of nucleus–nucleus collisions at relativistic energy [4–6]. Based on PS model, two interacting nuclei in high-energy nucleus–nucleus interaction can be split into three main regions. The overlapping region of two interacting nuclei known as participant region and other parts which is not taking part in collision is known as projectile and target spectator region. The sketch diagram of PS model is drawn in Fig. 20.1.

In this analysis, we have reported the multiplicity features of the grey particles emerged in the interactivity of ^{84}Kr projectile with Em (composite target detector) at incident kinetic energy 1 GeV per nucleon (i.e. total incident kinetic energy is 84 GeV).

M. K. Singh (✉)
Department of Physics, Institute of Sciences and Humanities, GLA University, Mathura 281406, India
e-mail: singhmanoj59@gmail.com

P. K. Khandai
Department of Physics, Ewing Christian College, Allahabad 211003, India

V. Singh
Department of Physics, Institute of Science, Banaras Hindu University, Varanasi 221005, India

K. L. Pandey et al. (eds.), *Proceedings of the National Workshop on Recent Advances in Condensed Matter and High Energy Physics*, Springer Proceedings in Physics 278,
https://doi.org/10.1007/978-981-19-2592-4_20

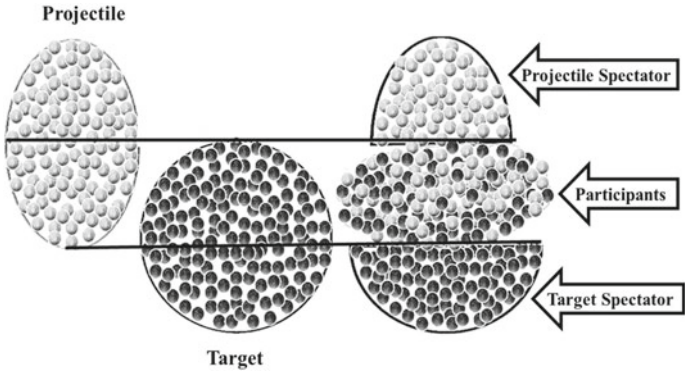

Fig. 20.1 The sketch diagram of the PS model [7]

20.2 Experimental Details

The NIKFI BR-2 emulsion plates was developed horizontally with ^{84}Kr as projectile having 1 A GeV at the SIS synchrotron, GSI, Darmstadt, Germany. The NED plates having volume 9.8 × 9.8 × 0.06 cm^3 [8]. The schematic diagram of the NED plate with ^{84}Kr as projectile is shown in Fig. 20.2. To search the event of interest, we have used transmitted light-binocular microscope (Olympus BH-2) having 100× oil emersion objectives as well as 15× eyepieces. The photo of Olympus BH-2 microscope is shown in Fig. 20.3 [8].

To scan the event of interest, we have adopted two standard methods one is line scanning method in which we follow the incident beam until they interact or escape from the NED plate, while in volume scanning, we scan the event of interest strip-by-strip. In low-energy region where the numbers of events are less, volume scanning is more useful in compare to line scanning. After the collection of the event of

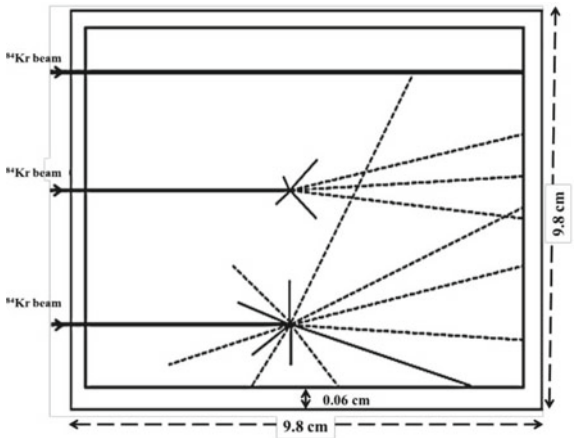

Fig. 20.2 The sketch diagram of the NED plate [8]

Fig. 20.3 The photograph of binocular microscope [8]

interest by following above two mentioned scanning methods, we distinguish them into different categories based on their properties such as track range (L) of the events in NED plate, relative velocity of the events in NED plate (β) and normalized grain density (g^*) of the events. Shower particles (N_s) are single charged particles which have velocity $\beta \geq 0.7$ and $g^* < 1.4$. Grey particles (N_g) have range $L > 3$ mm in NED plate, $0.3 < \beta < 0.7$ and $1.4 < g^* < 6.0$. Black particles (N_b) have range $L < 3$ mm in NED plate, $\beta < 0.3$ and $g^* > 6.0$. The sum of black and grey particles is known as heavily ionized charged particles ($N_h = N_b + N_g$). Based on the N_h values, the composite target detector NED is split into three main groups AgBr target group ($N_h \geq 8$), CNO target group ($2 \leq N_h \geq 7$) and H target group (N_h value 0 or 1).

20.3 Results and Discussion

The emission features of the grey particles emerged in the interactivity of the ^{16}O (60 A GeV) [9] and $^{84}Kr_{36}$ (1 A GeV) projectiles from AgBr target group of the NED is shown in Fig. 20.4. From Fig. 20.4, it is clear that the emission probability of the events showing independent behaviour on the incident energy as well as the mass of the projectiles.

Figure 20.5 shows the emission features of the grey particles emerged in the interactivity of the ^{16}O (60 A GeV) [9] and ^{84}Kr (1 A GeV) projectiles from CNO target group of the NED. Figure 20.5 reveals that the probability of the event emission

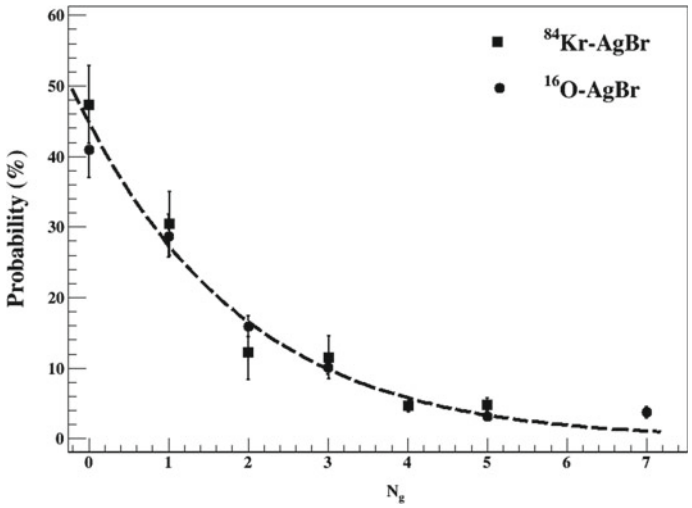

Fig. 20.4 Emission features of the grey particles produced in the interactivity of ^{16}O (60 A GeV) [9] and $^{84}Kr_{36}$ (1 A GeV) projectiles with AgBr target group of NED

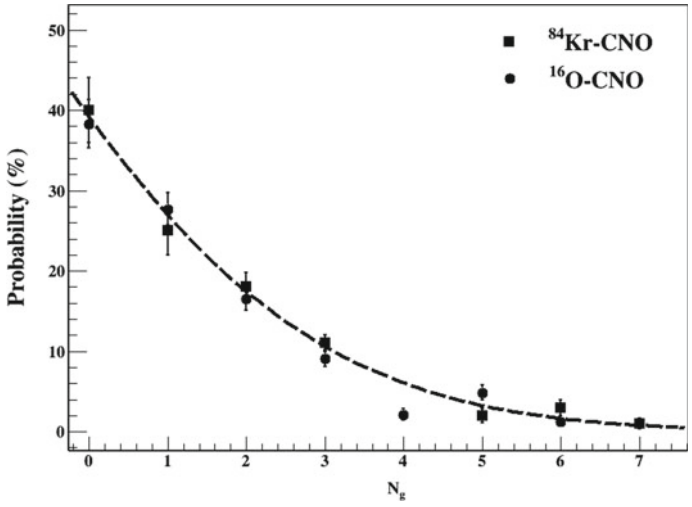

Fig. 20.5 Emission features of the grey particles produced in the interactivity of ^{16}O (60 A GeV) [9] and $^{84}Kr_{36}$ (1 A GeV) projectiles with CNO target group of NED

showing independent behaviour on the incident energy as well as the mass of the projectile. From Figs. 20.4 and 20.5, it is also clear that the emission probability in the interaction with AgBr target group is higher as compared to the emission probability in the interaction with CNO target group of the NED.

20.4 Conclusion

In the present analysis, we have presented our studies on the multiplicity feature of the grey particles emerged in the interactivity of ^{84}Kr with a nuclear emulsion (a composite target detector) at 1 GeV per nucleon (i.e. total incident energy of the projectile is 84 GeV). The analysis shows that the emission feature of grey particles does not depend on the projectile mass and strongly depends on the different target groups of the NED. The emission probability of the grey particles is more if the projectile interacts with AgBr target group of NED in comparison with the interactivity of projectile from CNO target group of NED.

Acknowledgements The authors are grateful to the all members of GSI, Germany, for exposing the NED with $^{84}Kr_{36}$ as projectile at 1 A GeV.

References

1. M.A. Jilany, Fast helium production in interactions of 3.7 A GeV ^{24}Mg with emulsion nuclei. Eur. Phys. J. A **22**, 471–480 (2004)
2. A. Andronic et al., Excitation function of elliptic flow in Au + Au collisions and the nuclear matter equation of state. Phys. Lett. B **612**, 173–180 (2005)
3. M.K. Singh et al., Characteristics of alpha projectile fragments emission in interaction of nuclei with emulsion. Indian J. Phys. **84**(9), 1257–1273 (2010)
4. F.H. Liu, Multiplicity distribution of relativistic charged particles in oxygen-emulsion collisions at 3.7 A GeV. Chin. J. Phys. **41**(5), 486–496 (2003)
5. M.K. Singh et al., Two source emission behavior of projectile fragments alpha in ^{84}Kr interactions at around 1 GeV per nucleon. Indian J. Phys. **85**(10), 1523–1533 (2011)
6. J. Knoll, Nonlinear phenomena in multiplicity distributions from nucleus-nucleus collisions at high-energy? Nucl. Phys. A **308**, 500–512 (1978)
7. M.K. Singh et al., Emission characteristics of the grey particles produced in the interaction of the $^{84}Kr_{36}$ with nuclear emulsion detector at 1 A GeV. Eur. Phys. J. Plus **135**, 740(1–8) (2020)
8. U. Singh et al., Emission characteristics of charged particle production in interactions of ^{84}Kr with the nuclear emulsion detector at relativistic energy. J. Korean Phys. Soc. **76**(4), 297–300 (2020)
9. A. Abdelsalam et al., Sensibility of grey particle production system to energy and centrality in 60 A and 200 A GeV ^{16}O–nucleus interactions. Int. J. Mod. Phys. E **25**(6), 1650034 (2016)

Chapter 21
Quantifying the Performance of Multilayer Insulation Technique for Cryogenic Application

D. Singh, M. K. Singh, and V. Singh

Abstract Multilayer insulation (MLI) is an important thermal protection system which is used in space cryogenic programs as well as on the ground experiments also. For the continuous and reliable functioning of a cryostat, it is desired to have a minimum heat load to the inner wall of the cryostat, and the need of minimum heat load (radiation heat load in particular) can be well fulfilled by using the MLI technique. It is used to reduce the radiation heat load mainly in the cryostats by placing the radiation shields and spacers in the gap between the two walls (hot and cold surfaces) of the cryostat. The present work is focused on investigation of the suitable reflective layer and spacer materials in MLI systems. In our analysis, Perforated Double-aluminized Mylar (DAM) with Dacron, Unperforated DAM with Silk-net, and Perforated DAM with Glass-tissue have been selected for their evaluation as the reflective layer as well as spacer materials in MLI technique. Current work would discuss the effect of layer density to optimize the layer density and the effect of the number of layers on the heat load. Knowing the key parameters of MLI, the heat load generation in spherical as well as cylindrical cryostats has been compared and the different effect of shielding of the cryostat placing a single layer near the inner or near the outer wall of the cryostat.

D. Singh (✉)
Department of Physics, Institute of Science, Banaras Hindu University, Varanasi 221005, India
e-mail: damini.singh13@bhu.ac.in

M. K. Singh
Institute of Physics, Academia Sinica, Taipei 11529, Taiwan

V. Singh
Physics Department, School of Physical and Chemical Sciences, Central University of South Bihar, Gaya 824236, India

K. L. Pandey et al. (eds.), *Proceedings of the National Workshop on Recent Advances in Condensed Matter and High Energy Physics*, Springer Proceedings in Physics 278,
https://doi.org/10.1007/978-981-19-2592-4_21

21.1 Introduction

MLI technique is an important method for insulation based on the principle of multiple radiation reflection by placing the radiation shields between the vacuum space of the two walls of the cryostats. This is used to prevent heat transmission entering from the outer wall of the cryostats. To reduce the coming radiation by reflection, the radiation shields are made by highly reflecting materials. Since these radiation shields are made up of highly reflecting material (metals like Aluminium or Gold, but mostly Aluminium is used due to low cost), so there may always be a chance of solid conduction due to thermal short between the radiation shields. To reduce the solid conduction between the radiation shields, spacers are the low-thermal conductivity materials which are placed side-by-side near the radiation shields, so that thermal contact between the radiation shields can be removed and hence the solid conduction too. This work focuses on the low-temperature applications of the MLI technique, i.e., in the basic physics research experiments like dark matter searches and neutrinoless double β-decay searches. Therefore, there is a need to check the best materials to be used in the MLI technique. For the testing and analysis purpose, three material combinations are selected for being used as radiation shields and spacers which are Unperforated DAM with Silk-net and Perforated DAM with Glass-tissue and Perforated DAM with Dacron [1].

21.2 Heat Transfer Analysis for a Cryostat

It is known that there is always a chance of heat load in between the two walls of the cryostat. There are three types of heat load, at very low temperature that may take place in a cryostat, which are solid conduction, residual gas conduction, and thermal radiation. In fact, thermal radiation is the most important and heavy part of the total heat load, which is produced in the cryostats. Solid conduction can be minimized by making a suitable and appropriate choice of the material. Residual gas conduction can be minimized by creating a suitable vacuum in between the outer (hot) and inner (cold) surfaces of the cryostat. Thermal radiation can be minimized by placing radiation shields with spacers in between the cold and hot surfaces of the cryostat [1]. For the consideration of spherical and cylindrical shape cryostats, the heat flux without any intermediate layer can be expressed as [1]:

$$q_{1-2} = \frac{\sigma A_2\left(T_1^4 - T_2^4\right)}{\frac{1}{\varepsilon_2} + \frac{(1-\varepsilon_1)}{\varepsilon_1}\left(\frac{A_2}{A_1}\right)} \tag{21.1}$$

Here σ is the Stefan–Boltzmann's constant which is taken as 5.675×10^{-8} W m^{-2} K^{-4}, A_1 and A_2 are the surface areas of the outer and inner walls, respectively. The temperatures of hot boundary and cold boundary surfaces are taken as T_1

and $T_{2,}$ respectively, and ε_1 and ε_2 are the emissivities of the outer and inner walls of the cryostat.

After inserting a single layer of radiation shield of the same material which is kept at temperature T_3, the average temperature of the hot boundary and cold boundary surfaces, with surface area A_3, emissivity ε_3, and the heat flux may be expressed as [1]:

$$q_{1-2} = \frac{\sigma A_2\left(T_1^4 - T_2^4\right)}{\frac{1}{\varepsilon_2} + \frac{(1-\varepsilon_1)}{\varepsilon_1}\left(\frac{A_2}{A_1}\right) + 2\left(\frac{1}{\varepsilon_3} - 1\right)\left(\frac{A_2}{A_3}\right) + \frac{A_2}{A_3}} \tag{21.2}$$

These two expressions (21.1) and (21.2) are helpful to make clear about the reduction of the heat load with insertion of the third layer in between the space of two walls of cryostat. In this sequence, one can use many radiation shields in order to reduce the heat load coming from the outer surface of the cryostat, but using a large number of radiation shields within a fixed available space results in the increment of thermal short [2]. Thus, it is important to optimize the number of radiation shields within a fixed thickness of insulating blanket. For this purpose, two analytical models are proposed to optimize the layer density. First one is the Modified Lockheed equation and the second one is the Layer-by-layer approach developed by McIntosh. Both of these models have been incorporated with all the three modes of heat transfer as given in the expression [2]:

$$q_{\text{total}} = q_{\text{radiation}} + q_{\text{solid conduction}} + q_{\text{gas conduction}} \tag{21.3}$$

Here, Modified Lockheed equation is used to optimize the layer density as well as for the analysis also. The generalized expression for the Modified Lockheed equation is given as [2]:

$$q_{\text{total}} = \frac{C_R\varepsilon\left(T_1^{4.67} - T_2^{4.67}\right)}{N} + \frac{C_S\bar{N}^{2.63}\left(T_1^2 - T_2^2\right)}{2(N+1)} + \frac{C_G P\left(T_1^{0.52} - T_2^{0.52}\right)}{N} \tag{21.4}$$

In this expression, $\bar{N}$ and N are the layer density and number of layers, respectively, the terms C_{S}, $C_{\text{R,}}$ and C_{G} are the empirical constants which are known as solid conduction coefficient, radiation coefficient, and gas conduction coefficient, respectively. The symbol P represents the residual gas pressure and ε is the emissivity of the radiation shield. This expression (21.4) is only applicable for the Unperforated DAM with Silk-net and Perforated DAM with Glass-tissue and it is conduction term got improved for Perforated DAM with Dacron. This modification is done because in the original Lockheed equation the used spacer material was Glass-tissue with different sizes of shield's perforation; whereas, during testing the used spacer was Dacron material with dissimilar sizes of shield's perforation [2]. Therefore, the Modified Lockheed equation for perforated DAM with Dacron is expressed as [2]:

$$q_a = \frac{C_R \varepsilon \left(T_1^{4.67} - T_2^{4.67}\right)}{N} + \frac{C_G P \left(T_1^{0.52} - T_2^{0.52}\right)}{N} \tag{21.5a}$$

$$q_b = \frac{2.4 * 10^{-4}\left(0.017 + 7 * 10^{-6}(800 - T) + 0.0228 \ln(T)\right)\bar{N}^{2.63}(T_1 - T_2)}{N} \tag{21.5b}$$

$$q_{\text{total}} = q_a + q_b \tag{21.6}$$

In this expression (21.6), the solid conduction term is got improved for Perforated DAM with Dacron.

21.3 Results and Discussion

A stable thermal performance of the cryostat can be achieved by reducing the heat load coming from the outer hot boundary surface of the cryostat. For current analysis, the selected combinations of reflecting shields and spacers have been used. For the testing purpose of the thermal performance of MLI technique, the value of ε is taken to be 0.043; for Aluminized radiation shields [2, 3], optimum vacuum pressure P is taken as 10^{-4} T [2], residual gas is Nitrogen. The values of T_1 and T_2 are taken as 300 K for water and 77 K for LN_2, respectively. The values of all the empirical constants [1] are given in Table 21.1.

21.3.1 Effect of Layer Density and Optimization of the Layer Density

It is clear in Sect. 21.2 that, by using more radiation shields heat load decreases, but the use of more radiation shields within a fixed thickness of MLI blanket results in the increment of the heat load. Here, the effect of layer density is observed, for all the three material combinations at constant $N = 40$, in light of expression (21.4) and (21.6) and all the empirical constants are taken form Table 21.1.

After the analysis, the result is shown in Fig. 1a. This increment in the heat load is because of the increment of solid conduction through the spacers due to the reduced

Table 21.1 Radiation shields and spacers with their empirical constants

Materials	C_R	C_S	C_G
Unperforated DAM with Silk-net	5.39×10^{-10}	8.95×10^{-8}	1.46×10^{-4}
Perforated DAM with Glass-tissue	7.07×10^{-10}	7.30×10^{-8}	1.46×10^{-4}
Perforated DAM with Dacron	4.94×10^{-10}	Updated in (21.6)	1.46×10^{-4}

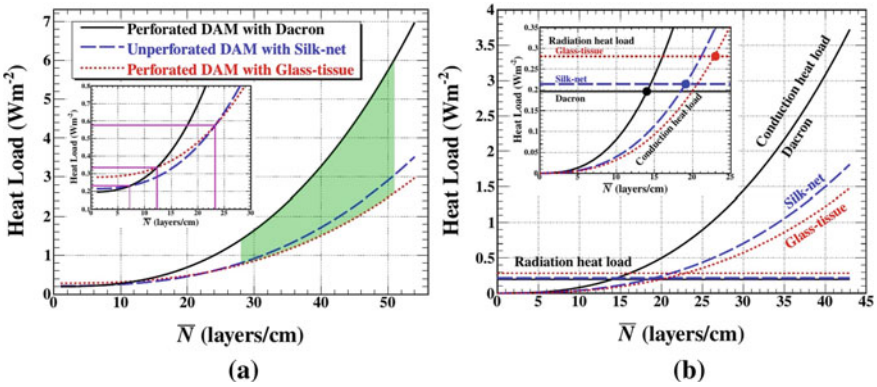

Fig. 21.1 **a** Heat load variation with layer density at a constant value of $N = 40$. **b** Optimum value of layer density at a constant value of $N = 40$

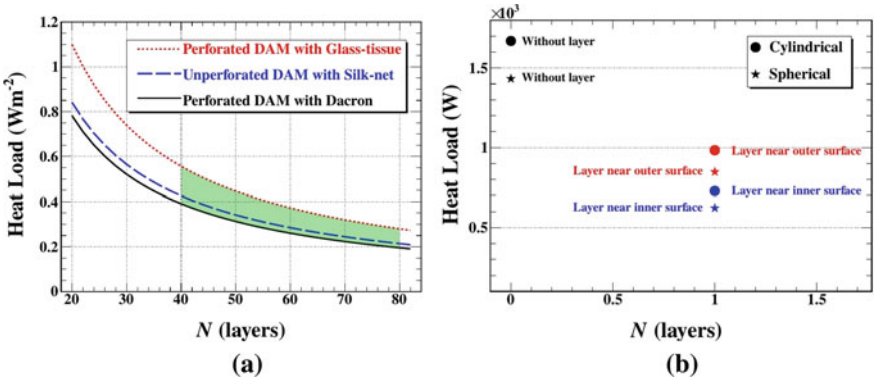

Fig. 21.2 **a** Heat load variation with N at optimized layer density. **b** Comparison of the geometry of the cryostats with respect to heat load

thickness of the spacers. Thus, it is necessary to optimize the layer density. The value of layer density is optimized by the equilibrium point between the radiation and conduction heat loads at the same constant value of N. The optimized layer density for all the three material combinations is shown in Fig. 2b.

21.3.2 Effect of Number of Layers and Shape Comparison

After knowing the optimal values of $\bar{N}$ for all the three material combinations, further the effect of N on heat load is investigated. By using the Modified Lockheed equation, taking all the constants from Table 21.1, the observed result is represented in Fig. 2a. This figure explains the 50% decrement in heat load with the 100%

increment in the value of N. In this sequence, appropriate geometry for a cryostat is very important because the geometry also affect the heat load. Cylindrical and spherical shapes with two enclosed envelopes are the shape of interest in the cryostat design. Assuming the parameters of the cryostat used in GERDA experiment and scaling the radius according to volume (64 m^3) of the cryostat, the heat load for both the geometries has been calculated with the help of expressions (21.1) and (21.2) in three different scenarios, i.e., without layer, with one layer near the inner surface of the cryostat, and with one layer near the outer surface of the cryostat. The observed result is represented in Fig. 2b which clears that the spherical geometry is the most appropriate configuration because of the lower heat load due to the minimum surface area to volume ratio, but cylindrical geometry is commonly being used in many experiments because of it is easy formation and most economical configuration [4].

References

1. D. Singh, Heat radiation reduction in cryostats with multilayer insulation technique, 2020 JINST 15 P07032
2. A. Hedayat et al., Variable density multilayer insulation for cryogenic storage, in *36th AIAA/ASME/SAE/ASEE Joint Propulsion Conference and Exhibit* (2000)
3. C.W. Keller et al., Thermal performance of multi-layer insulations, final report, contract NAS3-14377 (Lockheed Missiles & Space Company, Sunnyvale, CA, USA, 1974)
4. G.B. Thapa, Design of a laboratory nitrogen liquefier cum cryostat based on closed cycle refrigerator, Master thesis, National Institute of Technology, Rourkela, India, 2013

Chapter 22
Identification of Bulk and Surface Event in Point Contact Germanium Detector at Sub-keV Energy Region

S. Karmakar, M. K. Singh, V. Singh, and H. T. Wong

Abstract Germanium detector is one of the principal detection technologies in the study of dark matter physics, neutrino physics, etc. Among different configurations of germanium detector, point contact configuration is an apt in the study of the low-energy neutrino and low-mass WIMPs. There are two types of point contact configuration, i.e., n-type point contact detectors and p-type point contact detectors, in which p-type point contact germanium detectors possess an inactive layer of few mm thickness and give rise to anomalous surface events. These events are not able to give the correct information about the interaction due to partial charge collection. In order to interpret the accurate result, we have to remove these anomalous surface events from the bulk events, whereas n-type point contacts germanium detectors are free from these anomalous events. Here, we present two different methods to discriminate these events that arise from the surface layer of the p-type point contact germanium detectors.

22.1 Introduction

Understanding of neutrino and dark matter is one of the long-standing problems in physics. Germanium detector technology with a sub-keV detection threshold is a widely used in the search of low-mass (1–10 GeV) WIMPs, which is a prime candidate for dark matter [1–4]. The point contact configuration of the germanium detector has a very low threshold and good resolution due to which various collaborations have used this configuration [5, 6]. Point contact configuration is available in two

S. Karmakar (✉) · M. K. Singh
Department of Physics, Institute of Applied Sciences and Humanities, GLA University, Mathura 281406, India
e-mail: shuvadeepk@gmail.com

V. Singh
Department of Physics, Central University of South Bihar, Gaya 824236, India

H. T. Wong
Institute of Physics, Academia Sinica, Taipei 115201, Taiwan

K. L. Pandey et al. (eds.), *Proceedings of the National Workshop on Recent Advances in Condensed Matter and High Energy Physics*, Springer Proceedings in Physics 278,
https://doi.org/10.1007/978-981-19-2592-4_22

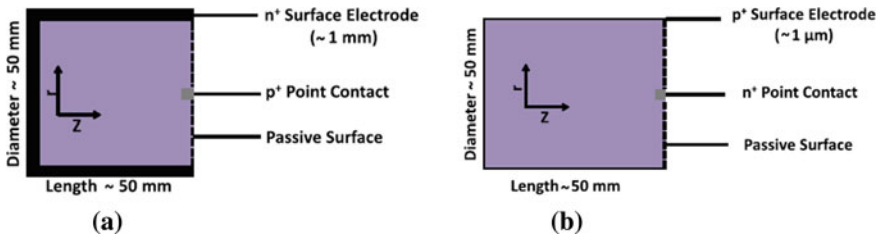

Fig. 22.1 **a** P-type point contact germanium detector, **b** N-type point contact germanium detector [4]

types, one is p-type point contact (pPCGe), and the other one is n-type point contact (nPCGe) as shown in Fig. 22.1, and in pPCGe detector, there is a presence of n^+ surface layer induced by the lithium diffusion [7]. The thickness of this layer is of the few mm order. In nPCGe, the p^+ layer is formed by the boron implantation and order of μm thickness [4]. The surface layer of the pPCGe gives rise to anomalous surface behavior, whereas the nPCGe does not give rise to any such kind of behavior [8, 9]. Due to the presence of this surface (S) layer, whenever an electron–hole pair will be created by the interaction, they will first try to diffuse through the layer and then drifted to the electrode [10]. Electron–hole pairs created at the surface layer in pPCGe are subjected to a lesser drift field than those in the bulk (B) volume of the detector [10–12]. Some of these electron–hole pairs will induce physics signals, and other pairs will recombine. The signal originated from this will be weaker and slower due to partial charge collection and high pulse rise time (τ) from the B events. The charge collection efficiency as a function of the depth of the surface was recently measured and simulated in [10]. If experimental data was not rectified from these events, then these events can mimic physics events which may lead to a false interpretation of the result. As a result, the wrong sensitivity and limit will be reported [13].

22.2 Experimental Setup

At the Jinshan district of Taiwan, the Kuo–Sheng Neutrino Laboratory (KSNL) is situated. It consists of two reactor cores, 2.9 GW is the average thermal power output from each. Basically, KSNL is situated at a distance nearly 28 m and 102 m from first core and the second core, respectively. The laboratory is placed at first floor of the seven-story building [5]. A diagram of the Kuo-Sheng Nuclear power station (KSNP) along with the KSNL is shown in Fig. 22.2a.

To reduce the background level, various shielding layer have been used. Among them, some are used for data taking and to tag events, known as active shielding. Shielding is not used for data taking purpose known to be passive shielding [5]. Active shielding poses two components. There were 16 plastic scintillator detectors

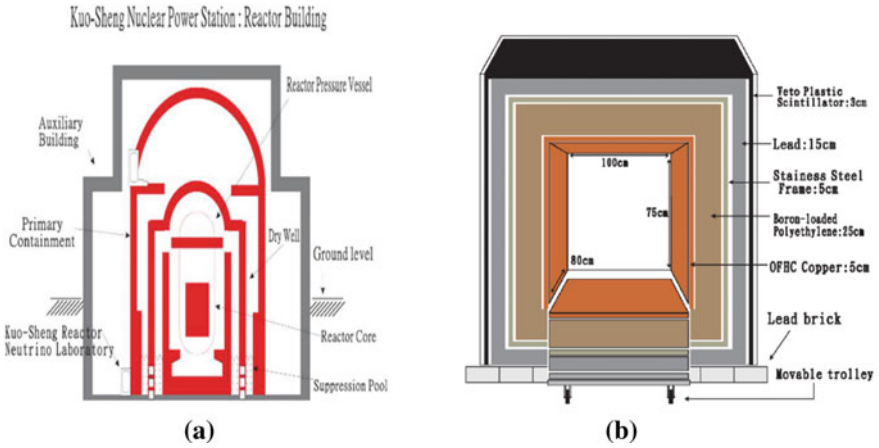

Fig. 22.2 **a** Schematic diagram of the KSNP, **b** Shielding of the detector cryostat in different layers [5]

acting as cosmic ray (CR) veto detector shown in Fig. 22.2b. Anti-Compton (AC) detector is the second component of the active shielding. NaI (TI) crystal acts as AC veto detector and provides 4Π covering to the target germanium detector [5].

There are four layers in passive shielding, arranged in such a manner that the background will be minimum from different shielding material. The inner space has a dimension of 100 cm × 80 cm × 75 cm shown in Fig. 22.2b. In the shielding, the outermost layer has 15 cm thick lead bricks to stop ambient photons. Then, frame of 5 cm stainless steel is kept to produce the structural support. After that, boron-loaded polyethylene of 25 cm thick is kept to prevent the neutron flux. In the most inner part of the shielding, 5 cm thick oxygen-free high conductivity (OFHC) copper is to reduce the contamination from the intrinsic radioactivity [5].

22.3 Different Processes to Differentiate the Anomalous Surface Events

There are mainly two processes to separate anomalous surface events in the pPCGe in which spectral shape method is used previously in the data analysis, but due to some issues, a new process is adopted in data analysis and is known as the ratio method [10–15].

22.3.1 Spectral Shape Method

This is a cut-based algorithm designed to perform bulk surface differentiation (BSD) in light WIMPs search with the data of TEXONO collaboration. In this technique, two main parameters of interest are bulk signal retaining efficiency (ε_{BS}) and the surface background suppression efficiency (λ_{BS}). To determine this two unknown parameters ε_{BS}, λ_{BS}, we required to have minimum two familiar source whose B to S event ratio is different but known [9, 14]. GEANT-4 simulation is used to get the real B spectrum. Then with the corresponding measured event, ε_{BS}, λ_{BS} were estimated. Then with this ε_{BS}, λ_{BS}, WIMP candidate data can be corrected. There are several limitations of this method discussed briefly in our previous works [9–13].

22.3.2 Ratio Method

The aim of the analysis is to draw out the information of B and S event distribution indicated by $N_{Bi}(E, \tau)$ and $N_{si}(E, \tau)$, respectively, which are the functions of energy (E) and rise time (τ). These distributions are related to the real B and S events, respectively, as shown in (22.1) [13] (Fig. 22.3),

$$B_{ri}(E) = \int_{\text{all } \tau} N_{Bi}(E, \tau)\mathrm{d}\tau \quad \text{and} \quad S_{ri}(E) \int_{\text{all } \tau} N_{Si}(E, \tau)\mathrm{d}\tau \tag{22.1}$$

In particular, B_{ri} would be the neutrino- and WIMP-induced possible spectra which correspond to the data sample surviving from different cuts. We can also write the distribution as shown in (22.2) [13],

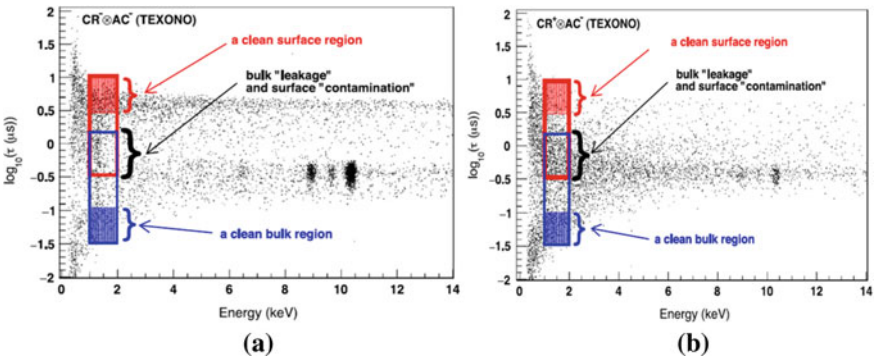

Fig. 22.3 Rise time versus energy plot with TEXONO data: **a** Neutrino and WIMPs-induced events, **b** Cosmic ray-induced events [13]

$$N_{Bi}(E,\tau) = \beta_i(E) f_{\mathrm{B}}(E,\tau) \quad \text{and} \quad N_{\mathrm{Si}}(E,\tau) = \xi_i(E) f_{\mathrm{S}}(E,\tau) \tag{22.2}$$

where β_i and ξ_i are τ independent scaling factors.

The measured events is therefore can be expressed as,

$$\begin{aligned} N_i(E,\tau) &= N_{\mathrm{Bi}}(E,\tau) + N_{\mathrm{Si}}(E,\tau) \\ &= \beta_i(E) f_{\mathrm{B}}(E,\tau) + \xi_i(E) f_{\mathrm{S}}(E,\tau) \end{aligned} \tag{22.3}$$

Now, the value of the $N_{\mathrm{Bi}}(E,\tau)$, $N_{\mathrm{si}}(E,\tau)$ can be found from (22.3) by χ^2 minimization [11] with different sources having various bulk-to-surface event ratio. Here for this analysis, absolute value of the β_i and ξ_i is not important, but the $\beta_i(E) f_{\mathrm{B}}(E,\tau)$ and $\beta_i(E) f_{\mathrm{B}}(E,\tau)$ are the quantity of interest. We are not bounded in the choice of the value of β_i and ξ_i, till they obey (22.2) which is equivalent to the τ independent ratio as shown in (22.4), and this is the basis of the ratio method.

$$\frac{N_{\mathrm{Bi}}(E,\tau)}{N_{\mathrm{Bj}}(E,\tau)} = \frac{\beta_i(E)}{\beta_j(E)} \quad \text{and} \quad \frac{N_{\mathrm{Si}}(E,\tau)}{N_{\mathrm{Sj}}(E,\tau)} = \frac{\beta_i(E)}{\beta_j(E)} \tag{22.4}$$

In the uncontaminated region, β_i and ξ_i are selected as discussed in our previous work [11], they also satisfy (22.2) and (22.4) and provide required scaling factors to solve the solution of (22.3) by χ^2 minimization. For contaminated region ($E <$ 2 keV), β_i and ξ_i could be derived by successive approximation and then the real B and S rates are calculated [13].

22.4 Conclusion and Future Out Look

In the present report, we have discussed two different methods to distinguish bulk and surface events in pPCGe. These two methods are helpful to crosscheck the results. Ratio method eliminates the need of the external γ source for the low-energy calibration. Further, we are looking for optimizing the technique for the low-energy range near the desired detector threshold which may lead to better efficiency for BS event separation.

References

1. S.K. Liu et al., Constraints on axion couplings from the CDEX-1 experiment at the China Jinping Underground Laboratory. Phys. Rev. D **95**(5), 052006 (2017)
2. Q. Yue et al., Detection of WIMPs using low threshold HPGe detector. High Energy Phys. Nucl. Phys. **28**(8), 877 (2004)
3. H.T. Wong et al., Research program towards observation of neutrino-nucleus coherent scattering. J. Phys. Conf. Ser **39**, 266–268 (2006)

4. A.K. Soma et al., Characterization and performance of germanium detectors with sub-keV sensitivities for neutrino and dark matter experiments. Nucl. Instrum. Methods Phys. Res. A **836**, 67–82 (2016)
5. M.K. Singh et al., Background rejection of TEXONO experiment to explore the sub-keV energy region with HPGe detector. Indian J. Phys. **91**(10), 1277–1291 (2017)
6. W. Zhao et al., Search of low-mass WIMPs with a p-type point contact germanium detector in the CDEX-1 experiment. Phys. Rev. D **93**(9), 092003 (2016)
7. H. Jiang et al., Measurement of the dead layer thickness in a p-type point contact germanium detector. Chin. Phys. C **40**(9), 096001 (2016)
8. M.K. Singh et al., Study of the inactive layer of sub-keV point contact germanium detector. J. Sci. Res. **65**(1), 237–243 (2021)
9. H.B. Li et al., Differentiation of bulk and surface events in p-type point-contact germanium detectors for light WIMP searches. Astropart. Phys. **56**, 1–8 (2014)
10. S. Karmakar et al., Energy calibration of the sub-keV germanium detector. Int. J. Contemp. Res. Eng. Technol. **10**(1), 1–4 (2020)
11. R.D. Martin et al., Determining the drift time of charge carriers in p-type point-contact HPGe detectors. Nucl. Instrum. Methods Phys. Res. A **678**, 98–104 (2012)
12. J.L. Ma et al., Study of inactive layer uniformity and charge collection efficiency of a p-type point-contact germanium detector. Appl. Radiat. Isot. **127**, 130–136 (2017)
13. L.T. Yang et al., Bulk and surface event identification in p-type germanium detectors. Nucl. Instrum. Methods Phys. Res. A **886**, 13–23 (2018)
14. Q. Yue et al., Limits on light weakly interacting massive particles from the CDEX-1 experiment with a p-type point-contact germanium detector at the China Jinping Underground Laboratory. Phys. Rev. D **90**(9), 091701 (2014)
15. H.B. Li et al., Limits on spin-independent couplings of WIMP dark matter with a p-type point-contact germanium detector. Phys. Rev. Lett. **110**(26), 261301 (2013)

Chapter 23
Fragmentation Characteristics of the Projectile Fragments Emitted in $^{84}Kr_{36}$ + Em Interaction at 1 A GeV

M. K. Singh and S. Karmakar

Abstract Study of the nucleus–nucleus interactivity at relativistic energy is one of the prime interests since the past in nuclear physics. It provides the information of reaction mechanism of heavy-ion interactivity with fundamental physics. In the present article, we have focused on the fragmentation characteristics of the projectile fragments (PF) with various target groups of the NED for the events emerged in the interactivity of $^{84}Kr_{36}$ + Em at 1 GeV per nucleon. The result of the present analysis is found to be consistence with other experimental results which was performed at relativistic energy.

Keywords RHIC · NED · PF

23.1 Introduction

By the time of the prediction of QGP as a new phase of matter, interest in the study of nucleus–nucleus (A–A) as well as hadronic–nucleus (h–d) collisions at relativistic energy increased at a great peace [1, 2]. At relativistic energy, study of heavy-ion collisions yields to look at the interactivity of particle production mechanism. Variation of reaction properties with respect to the geometry of collision is the matter of prime interest. After the discovery of NED, its utilization in the experimental field of particle physics and nuclear physics becomes inevitable for the new particle search. NED is proved to be a good tool due to its compact size; detection capability 4π, resolution of position is also very high for this. On the basis of the impact parameter, collision between the target nucleus and projectile nucleus is divided into three classes.

I. **Peripheral collision**: In this type of collision, the value of the transfer momentum is very much low.

M. K. Singh (✉) · S. Karmakar
Department of Physics, Institute of Applied Sciences and Humanities, GLA University, Mathura 281406, India
e-mail: singhmanoj59@gmail.com

K. L. Pandey et al. (eds.), *Proceedings of the National Workshop on Recent Advances in Condensed Matter and High Energy Physics*, Springer Proceedings in Physics 278,
https://doi.org/10.1007/978-981-19-2592-4_23

II. **Quasi-central collision**: In this type of collision, the number of participant nucleon is more compared to the peripheral one.
III. **Central collision**: In this type of collision, transverse momentum transfer and energy transfer are much higher. Also, the target nuclei and the projectile nuclei get completely destructed.

The region of interest of the various type of collisions as mentioned above can be divided in three main regions [3–5] as stated below:

I. **Projectile spectator region**: This is one of the important parts as the PF is produced from this part, but this region does not take participation in the interactivity.
II. **Target spectator region**: Target fragment is generated from this region. This part also does not participate in the interactivity. Velocity of this region with respect to laboratory frame is zero.
III. **Participant region**: The most important part of the interactivity is this. It is the region from where new particles are generated due to the violent collision of the two nuclear objects.

Here in this article, we have focused on the fragmentation characteristics of the alpha PF with various target groups of the NED for the events emerged in the interactivity of $^{84}Kr_{36}$ + Em at 1 GeV per nucleon.

23.2 Experimental Details

One of the best composite detectors used in particle and nuclear physics is NED. Components of these detector are roughly a varying percentage of ^{1}H (hydrogen), ^{12}C (carbon), ^{14}N (nitrogen), ^{16}O (oxygen), ^{80}Br (bromine) with ^{108}Ag (silver). The amount is varied basically as per the experimental need. In our present analysis, NIKFI-BR2 NED plate is used. The general content of the NIKFI-BR2 NED, used in the current study, is ^{1}H (3.150), ^{12}C (1.410), ^{108}Ag (1.028), ^{80}Br (1.028), ^{16}O (0.956), ^{14}N (0.395) with minute mixture fluorine and iodine [6, 7]. The beam of ^{84}Kr was used as a projectile beam having incident kinetic energy 1 GeV/nucleon. In the passage through the NED medium, the projectile beam interacts with the target nuclei present in the NED plate and the information of the collision collected in the NED. The NED plate thickness was around 600 μm. At GSI Darmstadt, Germany, the NED plate was made with ^{84}Kr as projectile beam. Data collection was made with assistance of the Olympus BH-2, which is a transmitted light-binocular microscope. It consists 100× of oil emersion objective with 15× eyepieces. Two scanning methods are used to find the event of interest, which are volume scanning and line scanning. In volume scanning, strip-by-strip search was performed, whereas in line scanning, search is done along the track of the event till the interactivity point was found.

All the out comings of the interactivity are categorized on the basis of the range (L), relative velocity (β), and normalized density of grains (g^*):

I. **Shower particles**: These are the type of particles produced mainly in the participant region, having $\beta > 0.7$ with $g^* < 1.4$. Pions and a small fraction of kaons basically come in this type.
II. **Gray particle**: The particle emerges from the target spectator region known as gray particle. These particles basically have $L > 3$ mm in NED, associated with β (0.3–0.7) and g^* (1.4–6.0) [8, 9].
III. **Black particle**: The production of this kind of particle is basically from the target spectator region with $L < 3$ mm, $g^* > 6.0$ and $\beta < 0.3$.
IV. **Heavily ionized charged particles**: This is the sum of black and gray particles.

The PF is produced from the projectile spectator region having $Z \geq 1$ and is divided mainly in three groups. The particles having single charge ($Z = 1$), double charge ($Z = 2$) are known as single charge (SC) and double charge (DC) PF. DC PF are also known as alpha PF. The PF which has charge more than two is known as multiple charges PF [10–14].

23.3 Result and Discussion

Figure 23.1 showing the normalized space angle distribution of the SCPF and DCPF for the events emerged from the interactivity of $^{84}Kr_{36}$ with AgBr target group of emulsion detector. From Fig. 23.1, it is clear that the mean of the emission angle for SCPF is higher as compared to that of the DCPF. Thus, it is clear that the SCPF emerged in wider space angle, while DCPF emitted in narrow space angle, which

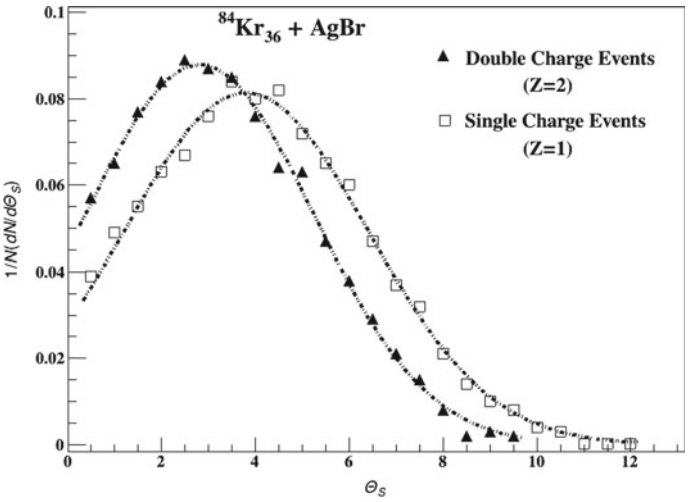

Fig. 23.1 Variation of the normalized space angle distribution for the SCPF and DCPF for the events emerged in the interactivity of the $^{84}Kr_{36}$ with AgBr target group of the emulsion detector

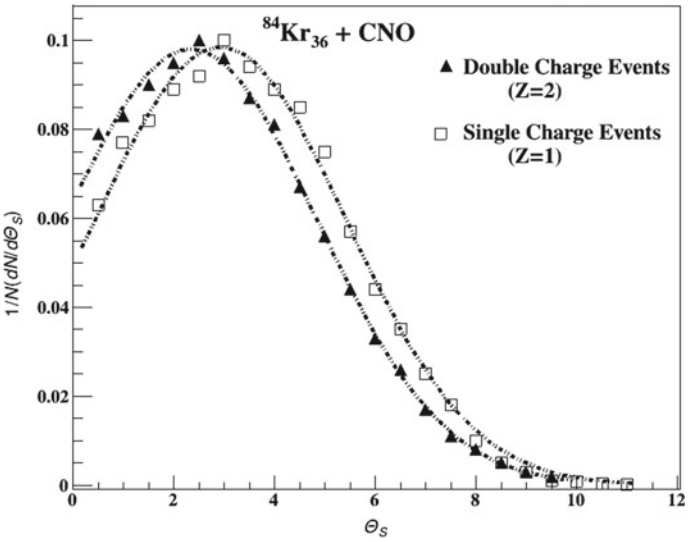

Fig. 23.2 Variation of the normalized space angle distribution for the SCPF and DCPF for the events emerged in the interactivity of the $^{84}Kr_{36}$ with CNO target group of the emulsion detector

shows that during the collision, SCPF gets more energy and momentum as compared to DCPF.

The normalized space angle distribution of the SCPF and DCPF for the events emerged from the interactivity of $^{84}Kr_{36}$ with CNO target group of emulsion detector is shown in Fig. 23.2. From Fig. 23.2, we can see that the mean of the emission angle for SCPF is higher as compared to that of the DCPF but not as higher as compared to the events emerged in the interactivity with AgBr target. Thus, it is clear that the SCPF emerged in wider space angle as compared to the DCPF. It reveals that the space angle distribution is depending on the various types of the target group of the emulsion detector.

23.4 Conclusion

The studies of the space angle distribution for PF with various types of target groups of emulsion detector reveal the emission characteristics of the PF. In the present studies, it is clear that the space angle distribution of the various charged PF (SCPF and DCPF) are depending on the various types of target groups of emulsion detector.

Acknowledgements Author is thankful to all the technical staff of GSI Darmstadt, Germany, for exposing NED using $^{84}Kr_{36}$ projectile at 1 A GeV.

References

1. W.H. Barkas, *Nuclear Research Emulsion* (Academia, London, 1963)
2. M.K. Singh, Energy dependence study of projectile fragmentation of $^{84}Kr_{36}$ + emulsion interactions, Ph.D. Thesis, VBS Purvanchal University, 2014
3. F.H. Liu, Multiplicity distribution of relativistic charged particles in oxygen-emulsion collisions at 3.7 A GeV. Chin. J. Phys. **41**(5), 486–496 (2003)
4. F.H. Liu, Emission of relativistic light fragments in nucleus-emulsion collisions at high energy. Chin. J. Phys. **38**(6), 1063–1073 (2000)
5. M.K. Singh et al., Two source emission behavior of projectile fragments alpha in ^{84}Kr interactions at around 1 GeV per nucleon. Indian J. Phys. **85**(10), 1523–1533 (2011)
6. M.K. Singh et al., Characteristics of alpha projectile fragments emission in interaction of nuclei with emulsion. Indian J. Phys. **84**(9), 1257–1273 (2010)
7. M.K. Singh et al., Charge measurement/estimation techniques in nuclear emulsion detector. J. Sci. Res. **63**, 249–264 (2019)
8. M.K. Singh et al., Emission characteristics of the grey particles produced in the interaction of the $^{84}Kr_{36}$ with nuclear emulsion detector at 1 A GeV. Eur. Phys. J. Plus **135**, 740(1–8) (2020)
9. M.K. Singh et al., Characteristics of the grey particles emission at relativistic energy. Eur. Phys. J. Plus **136**, 115 (2021)
10. M.K. Singh et al., Projectile fragmentation study in peripheral collision for the interaction of the ^{84}Kr with nuclear emulsion at relativistic energy. Int. J. Mod. Phys. E **28**(8), 1950063(1–7) (2019)
11. M.K. Singh et al., Emission characteristics of charged particle production in interactions of ^{84}Kr with the nuclear emulsion detector at relativistic energy. J. Korean Phys. Soc. **76**(4), 297–300 (2020)
12. M.K. Singh et al., Study of emission characteristics of the projectile fragments produced in the interaction of $^{84}Kr_{36}$ with nuclear emulsion detector at 1 GeV. Chin. J. Phys. **67**, 107–112 (2020)
13. U. Singh et al., Projectile multifragmentation study in the interaction of ^{84}Kr with nuclear emulsion detector at relativistic energy. Indian J. Pure Appl. Phys. **58**(5), 368–370 (2020)
14. M.K. Singh et al., Emission characteristics of intermediate mass fragments by the $^{84}Kr_{36}$ projectile in nuclear emulsion detector at 1GeV per nucleon. Eur. Phys. J. Plus **135**, 373(1–8) (2020)

Chapter 24
Study of the Multiplicity Characteristics for Target Fragments Produced in $^{84}Kr_{36}$ + Em Interaction at Relativistic Energy

Babita Kumari, M. K. Singh, and R. Singh

Abstract Study of the N–N and N–A interaction for relativistic energy (RE) is one of the supreme interests since the birth of the nuclear physics. It gives physics behind the reaction process of heavy-ion interactions. In this manuscript, we have focused on the multiplicity characteristics of the target fragments produced in the interactivity of the ^{84}Kr + Em on 1 GeV per nucleon. In this manuscript, we have used total charge Q of the outgoing projectiles (forward cone $\theta_c \leq 3^0$) of non-interacting projectile nucleon for the differentiation of the various type of collisions instead of impact parameter.

24.1 Introduction

Nuclear emulsion detector (NED) is antique technique of use in experimental nuclear physics [1]. Nucleus–nucleus interaction provides important information about the nature of heavy-ion interactivity process [1, 2]. Participant spectator (PS) model [3–5] explains the interactivity techniques of two interacting nuclei. Based on PS model, the overlapping area of two interacting nuclei is called participant area (PR), the particles ejected from this area are known as shower particles, while the other two areas which are not participating in the interactivity are known as target spectator (TS) and projectile spectator (PS) areas, and the events emitting from these areas are called target fragments (TF) and projectile fragments (PF), respectively [5, 6]. In this analysis, we have mainly looked on the properties of the target fragments with non-interacting projectile nucleons for the events emerged from the interactivity of $^{84}Kr_{36}$ − Em at 1 GeV per nucleon.

B. Kumari · M. K. Singh (✉) · R. Singh
Department of Physics, Institute of Applied Sciences and Humanities, GLA University, Mathura 281406, India
e-mail: singhmanoj59@gmail.com

K. L. Pandey et al. (eds.), *Proceedings of the National Workshop on Recent Advances in Condensed Matter and High Energy Physics*, Springer Proceedings in Physics 278,
https://doi.org/10.1007/978-981-19-2592-4_24

24.2 Experimental Details

NED plates used in the present study were processed at GSI, Darmstadt (Germany), and the scanning of the NED plates to search for the physics events was performed at Banaras Hindu University (BHU), Varanasi, India [7]. NED is a mixed target detector containing H, C, N, O, Ag, Br, and few percent of S and I [8]. In the evolution of the NED plates, ^{84}Kr with incident kinetic energy 1 A GeV was used as a projectile [2]. To search the physics events, we have used Olympus BH-2 microscope with 15× eyepieces and 100× oil immersion objective [2, 9]. In the scanning of events, we have followed two (line and volume) scanning methods [2, 7]. After the collection of events of interest by scanning the NED plates, we have further differentiate all the events into various groups based on the properties such as range (L), normalized grain density (g^*), and relative velocity (β) [2, 7]. ***Black particles***: These events have $\beta < 0.3$, $L < 3$ mm, and $g^* > 6.0$, and they are ejected from the TS area. It is represented by N_b. ***Gray particles***: These events have $0.7 < \beta > 0.3$, $6.0 > g^* > 1.4$, $L > 3$ mm, and they are ejected from the TS area. It is represented by N_g [10]. **Shower particles**: These events have $g^* < 1.4$, $\beta > 0.7$, and they are ejected from the PR. It is represented by N_s [9]. Heavily charged particle: The sum of N_b and N_g (i.e., $N_h = N_b + N_g$) is called as heavily charged particle. The projectile fragments having charge $Z \geq 1$ are divided into three main groups. ***Singly charged PF***: The PF has single charge and represented by $N_{Z=1}$. ***Doubly charged PF***: The PF has double charge and represented by $N_{Z=2}$. ***Multiple charged PF***: The PF has more than two charge and represented by $N_{Z>2}$ [11–14].

24.3 Result and Discussion

To understand the nucleus–nucleus interaction process, we need to study the multiplicity characteristics of the secondary charged particles [15]. A lot of experimental results on nucleus–nucleus interactions at RE have been studied over the last few years [3–15]. As we know that in heavy-ion collision, the type of interaction plays an important role to understand the reaction process. On the basis of interaction geometry, two colliding nuclei can be separated into three type of collisions, which are peripheral collision (PC), central collision (CC), and quasicentral collision (QCC). In the present study, we have used different parameter instead of impact parameter to classify the types of collisions, which is total charge Q of the outgoing projectile fragments or total charge of the non-interacting projectile nucleons (TCNPN) [15]. For each interaction, $Q = \sum Z_{PF}$ [15]. In current analysis, $Q = 0$ represents the events emerged in central collisions and $Q = 1$ the events emerged from the peripheral collisions [15]. In current analysis, the main focus was on the peripheral events (i.e., $Q = 1$) emerged in the interaction of ^{84}Kr with emulsion at around 1 A GeV. For this study, we have used 300 events out of 700 events. From Figs. 24.1 and 24.2, we can see that the values of $<N_b>$ and $<N_g>$ are showing the linear variation with values

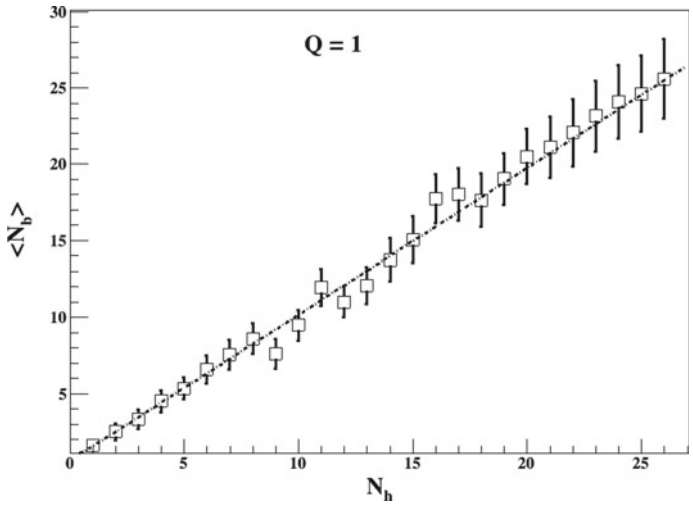

Fig. 24.1 Variation of $<N_b>$ with N_h for $Q = 1$ events. The fitting line is just to show the linear behavior of data points

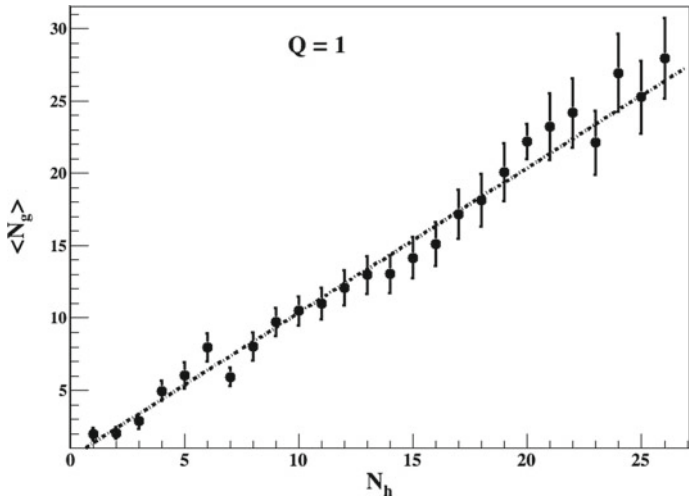

Fig. 24.2 Variation of $<N_g>$ with N_h for $Q = 1$ events. The fitting line is just to show the linear behavior of data points

for the events emerged in the interactivity ^{84}Kr with emulsion for peripheral collision at 1 A GeV. The results observed in this study are also consistence with other experimental observations performed at RE, which show that this linear behavior is strongly depending on the types of collision of two colliding nuclei as compared to incident kinetic energy [15].

24.4 Conclusion

In this study, we have used different parameter instead of impact parameter to classify the types of collisions, known as total charge Q of the outgoing projectile fragments or TCNPN. Here, we have looked on the peripheral events (i.e., $Q = 1$) emerged in the interactivity of ^{84}Kr with emulsion at around 1 A GeV. From this study, we have found that the values of $<N_b>$ and $<N_g>$ are showing the linear behavior with N_h, and the variation is strongly depending on the type of collision of two interacting nuclei.

Acknowledgements Authors would like to give thanks to all the technical staff of GSI Darmstadt, Germany, for developing NED with $^{84}Kr_{36}$ at 1 A GeV.

References

1. W.H. Barkas, *Nuclear Research Emulsion* (Academia, London, 1963)
2. M.K. Singh, Energy dependence study of projectile fragmentation of $^{84}Kr_{36}$ + emulsion interactions, Ph.D. Thesis, VBS Purvanchal University, 2014
3. F.H. Liu, Multiplicity distribution of relativistic charged particles in oxygen-emulsion collisions at 3.7 A GeV. Chin. J. Phys. **41**(5), 486–496 (2003)
4. F.H. Liu, Emission of relativistic light fragments in nucleus-emulsion collisions at high energy. Chin. J. Phys. **38**(6), 1063–1073 (2000)
5. M.K. Singh et al., Two source emission behavior of projectile fragments alpha in ^{84}Kr interactions at around 1 GeV per nucleon. Indian J. Phys. **85**(10), 1523–1533 (2011)
6. M.K. Singh et al., Charge measurement/estimation techniques in nuclear emulsion detector. J. Sci. Res. **63**, 249–264 (2019)
7. M.K. Singh et al., Characteristics of alpha projectile fragments emission in interaction of nuclei with emulsion. Indian J. Phys. **84**(9), 1257–1273 (2010)
8. M.K. Singh et al., Projectile fragmentation study in peripheral collision for the interaction of the ^{84}Kr with nuclear emulsion at relativistic energy. Int. J. Mod. Phys. E **28**(8), 1950063(1–7) (2019)
9. M.K. Singh et al., Emission characteristics of charged particle production in interactions of ^{84}Kr with the nuclear emulsion detector at relativistic energy. J. Korean Phys. Soc. **76**(4), 297–300 (2020)
10. M.K. Singh et al., Emission characteristics of the grey particles produced in the interaction of the $^{84}Kr_{36}$ with nuclear emulsion detector at 1 A GeV. Eur. Phys. J. Plus **135**, 740(1–8) (2020)
11. M.K. Singh et al., Characteristics of the grey particles emission at relativistic energy. Eur. Phys. J. Plus **136**, 115 (2021)
12. M.K. Singh et al., Study of emission characteristics of the projectile fragments produced in the interaction of $^{84}Kr_{36}$ with nuclear emulsion detector at 1 GeV. Chin. J. Phys. **67**, 107–112 (2020)
13. U. Singh et al., Projectile multifragmentation study in the interaction of ^{84}Kr with nuclear emulsion detector at relativistic energy. Indian J. Pure Appl. Phys. **58**(5), 368–370 (2020)
14. M.K. Singh et al., Emission characteristics of intermediate mass fragments by the $^{84}Kr_{36}$ projectile in nuclear emulsion detector at 1 GeV per nucleon. Eur. Phys. J. Plus **135**, 373(1–8) (2020)
15. M. Mohery et al., The multiplicity characteristics of ^{7}Li-Em interactions as a function of noninteracting projectile nucleons. Int. J. Mod. Phys. E **29**(8), 2050063 (2020)

Chapter 25
Characteristics of the High-Purity Germanium Detectors in Dark Matter and Neutrino Sector

S. Karmakar, M. K. Singh, V. Singh, and H. T. Wong

Abstract To look at different modern sectors of physics like the study of dark matter interaction, different properties of neutrino and other exotic particle interaction, detectors having a very low threshold of the order of eV_{ee} (electron equivalent) are one of the prime needs. Germanium ionization detector is one of the apt technologies with good resolution and low threshold. Various configurations of a highly pure germanium detector have been used by various collaboration to look at the above-mentioned properties. Among them, the point contact and ultra-low energy detector configurations have shown a very promising energy threshold near the desired range. Ultra-low energy detectors also have a very good resolution, but their low mass is a point of concern in scaling up the detector. Whereas coaxial configuration has a large mass, but the resolution is not that much good. All the advantages and the disadvantages of the highly pure germanium detector technology based on different configurations will be discussed here.

Keywords Point contact germanium detector · Neutrino physics · Dark matter physics

25.1 Introduction

High-purity germanium (HPGe) detectors have very wide application in different field of physics from dark matter detection to search of neutrino less double beta decay also it has application in the search of electromagnetic property of the neutrino

S. Karmakar (✉) · M. K. Singh
Department of Physics, Institute of Applied Sciences and Humanities, GLA University, Mathura 281406, India
e-mail: shuvadeepk@gmail.com

V. Singh
Department of Physics, Central University of South Bihar, Gaya 824236, India

H. T. Wong
Institute of Physics, Academia Sinica, Taipei 115201, Taiwan

K. L. Pandey et al. (eds.), *Proceedings of the National Workshop on Recent Advances in Condensed Matter and High Energy Physics*, Springer Proceedings in Physics 278,
https://doi.org/10.1007/978-981-19-2592-4_25

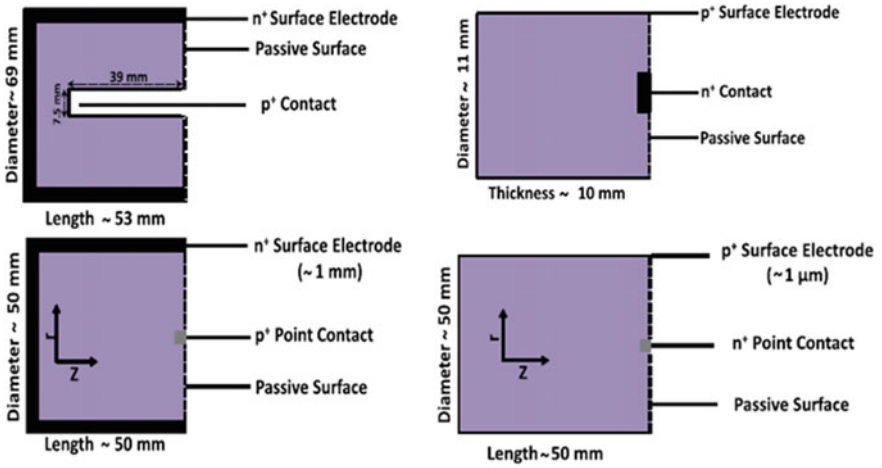

Fig. 25.1 Coaxial configuration (up left), ULGe (up right), p-type point contact germanium detector (down left), n-type point contact germanium detector (down right) [5]

[1–6]. Exposure of ton yr order is one of the prime needs of these types of physics experiment, in which HPGe detectors are very much prominent, due to its ultra-low internal radioactive background, lower detection threshold, high resolution [1–3]. HPGe crystals have two classes, n-type and p-type. If the doping impurity atoms provides free electrons, then it becomes n-type, and if the impurity provides free holes, then it becomes p-type. Basically, the level of the impurity in the HPGe crystal has very low value of 10^{10} atoms/cm^3 [2, 3]. Taiwan EXperiment On NeutrinO (TEXONO) collaboration has used different HPGe detector configurations by the time [4–6] and is shown in Fig. 25.1.

Also while doing work with the HPGe detector in sub-keV region, we always have to very much concern about the external background [6, 7]. There are numerous number of sources like muons from cosmic ray, photons arises from radioactive decay channels, and the neutron emitting sources are explained briefly in our previous work [6].

25.2 Experimental Setup

The Kuo–Sheng Neutrino Laboratory (KSNL) is located at the Jinshan district on the northern shore of Taiwan. It has two boiling water reactor cores, with an average thermal power output of 2.9 GW each. The KSNL is located at a distance of 28 m from the first core and 102 m from the second core. The KSNL is situated on the first floor of the seven-story reactor building and 12 m below the sea level [6]. A schematic diagram of the Kuo-Sheng Nuclear Power Station is depicted in Fig. 25.2a.

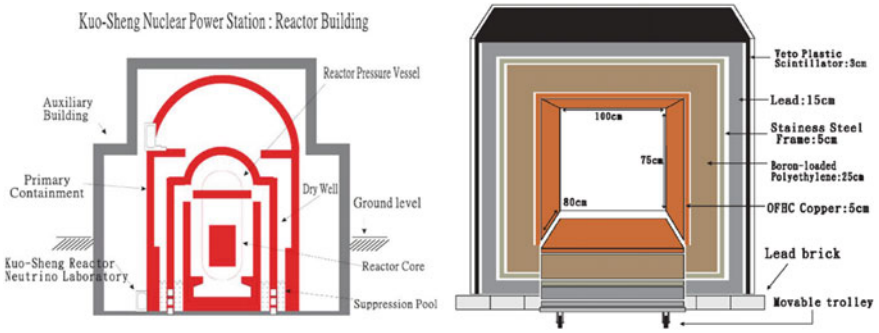

Fig. 25.2 **a** Schematic diagram of the Kuo-Sheng Nuclear Power Station. **b** Different layers of shielding's of the detector cryostat [6]

Taiwan EXperiment On NeutrinO (TEXONO) is one of the world's leading experiments in dark matter physics and low-energy nuclear reactor neutrino. To suppress the background, various shieldings have used [6]. Among these shielding, some of them are used to collect data and tag various events, and these are known as active shielding and shieldings which are not used in data taking known as passive shielding [6].

Here, active shielding has two components. Firstly, 16 plastic scintillator detectors act as the cosmic ray (CR) veto detector as shown in Fig. 25.2b. Anti-Compton (AC) detector acts as the second component of the active shielding. A total of 40 kg of NaI(TI) crystal acts as the AC veto detector and provides 4Π covering to the target detector. The NaI(TI) provides time information of events like CR veto detectors. In addition to time information, the NaI(TI) also provides information on the energy deposition [6].

Passive shielding has many components and oriented in four layers. It is oriented in such a way so that the background arising from different shielding material will be minimum. The total weight of passive shielding is nearly 50 t. The inner space as shown in Fig. 25.2b has a dimension of 100 cm × 80 cm × 75 cm; in this space, the detector is kept. In the shielding, the outermost layer consists of 15 cm thick lead bricks that absorb the ambient γ photons. After that, the next 5 cm stainless steel frame is placed which gives the structural support, reduces the γ-ray flux, also it slows down the fast neutron. The next inner layer of 25 cm thick boron-loaded polyethylene helps to reduce the neutron flux from outside. The most inner part of the passive shielding is the 5 cm thick wall of oxygen-free high conductivity (OFHC) copper which absorbs photons from intrinsic radioactive contamination and excited state of nuclei induced by neutron or cosmic ray in the lead and polyethylene [6–8].

25.3 Results and Future Outlook

In this section, we have focused the aspects of the different setup of germanium detectors in details based on the analysis made by the TEXONO collaboration [5]. Coaxial germanium detector configuration was used by TEXONO collaboration in the earlier time for the study of the neutrino magnetic moment $\mu_{\bar{\upsilon}e}$ [9]. The HPGe crystal used in this configuration has mass of nearly 1.06 kg. It proved to have a good potential in the study of neutrino magnetic moment due to its good resolution, low threshold, and stability [9]. The detection threshold achieved by this configuration is 5 keV [5]. In 2003, TEXONO has published their limit on neutrino magnetic moment $\mu_{\bar{\upsilon}e} < 1.3 \times 10^{-10}\ \mu_B$ [9] with 90% confidence level. In 2007, they have improved the limit of neutrino magnetic moment $\mu_{\bar{\upsilon}e} < 7.4 \times 10^{-11}\ \mu_B$ [10] with 90% confidence level. Ultra-low-energy germanium detectors have also used by TEXONO collaboration. They have used four detectors each of having mass nearly 5 g. In terms of resolution, this configuration is very good in the study of spin-independent and spin-dependent interaction of low mass WIMPs with the germanium detector [11]. Also, this detector is good in the study of neutrino nucleus coherent scattering [7–10]. Various limits also updated in this sector with this detector configuration. Now, point contact germanium detector is one of the best in terms of low threshold as well for the mass of the detectors. Many physics were studied with this detector for both n-type and p-type point contact configurations. Various new limits on the millicharged particle [12, 13], spin-independent coupling with WIMPs are also given with PCGe [11]. Physics threshold of nearly 200 eV_{ee} is achieved with point contact detector.

As we can see from above, various configurations of germanium detectors have different usefulness like coaxial configuration is very much helpful when we look for physics below 100 keV, and with this configuration, magnetic moment was studied. N-type point contact detectors have also used in neutrino magnetic moment studies and have provided some good limits [13]. In terms of detection threshold, ULGe detectors are quite good. So, we can see that point contact configurations have the potential to fulfill the future experimental needs. Further, R&D is going on to improve the detector noise edge and background by improving hardware as well as by optimizing software analysis tool.

References

1. M.-S. Raut et al., Characterization of High-Purity Germanium (Ge) Crystals for Developing Novel Ge Detectors. arXiv:2002.07706v2
2. G. Wang et al., Development of large size high-purity germanium crystal growth. J. Cryst. Growth **352**, 27–30 (2012)
3. J. Li, et al., HPGe detector field calculation methods demonstrated with an educational program, GeFiCa. arXiv:2001.02762v1
4. H.T. Wong et al., Research program towards observation of neutrino-nucleus coherent scattering. J. Phys. Conf. Ser. **39**, 266–268 (2006)

5. A.K. Soma et al., Characterization and performance of germanium detectors with sub-keV sensitivities for neutrino and dark matter experiments. Nucl. Instrum. Methods Phys. Res. A **836**, 67–82 (2016)
6. M.K. Singh et al., Background rejection of TEXONO experiment to explore the sub-keV energy region with HPGe detector. Indian J. Phys. **91**(10), 1277–1291 (2017)
7. M.K. Singh et al., Study of the inactive layer of sub-keV point contact germanium detector. J. Sci. Res. **65**(1), 237–243 (2021)
8. S. Karmakar et al., Energy calibration of the sub-keV germanium detector. Int. J. Contemp. Res. Eng. Technol. **10**(1), 1–4 (2020)
9. H.B. Li et al., Limit on the electron neutrino magnetic moment from the Kuo-Sheng reactor neutrino experiment. Phys. Rev. Lett. **90**(13), 131802 (2003)
10. H.T. Wong et al., Search of neutrino magnetic moments with a high-purity germanium detector at the Kuo-Sheng nuclear power station. Phys. Rev. D **75**, 012001 (2007)
11. S.T. Lin et al., New limits on spin-independent and spin-dependent couplings of low-mass WIMP dark matter with a germanium detector at a threshold of 220 eV. Phys. Rev. D **79**, 061101(R) (2009)
12. J.-W. Chen et al., Constraints on millicharged neutrinos via analysis of data from atomic ionizations with germanium detectors at sub-keV sensitivities. Phys. Rev. D **90**, 011301(R) (2014)
13. L. Singh et al., Constraints on millicharged particles with low-threshold germanium detectors at Kuo-Sheng Reactor Neutrino Laboratory. Phys. Rev. D **99**, 032009 (2019)